

*Thermo-magnetic Instabilities in Nb<sub>3</sub>Sn Superconducting  
Accelerator Magnets*

*Ph.D. Thesis*

*Author:*

*Bernardo Bordini*

*Advisors:*

*Prof. Fabio Fineschi*

*(Pisa University)*

*Prof. Bruno Montagnini*

*(Pisa University)*

*Dr. Sandor Feher*

*(Fermilab)*



# Contents

<b>Chapter 1 – Introduction.....</b>	<b>1</b>
1.1 Introduction.....	1
1.2 Superconductivity .....	4
1.2.1 Relevant type II superconductors.....	5
1.2.2 Critical current density & critical surface.....	7
1.2.3 Transition of the superconductor at a fixed temperature and magnetic field ....	7
1.2.4 Critical state model .....	8
1.2.5 Magnetization of a superconductor.....	9
1.2.6 Impact of the superconductor magnetization on wire layout.....	12
1.3 Critical current measurements of superconducting strands .....	12
1.4 Basic properties of Nb <sub>3</sub> Sn superconductor .....	13
1.5 Manufacturing processes of Nb <sub>3</sub> Sn composite strands.....	15
1.5.1 The bronze process .....	15
1.5.2 The internal tin process.....	15
1.5.3 The Powder In Tube process.....	16
1.5.4 The Modified Jelly Roll and Restack Rod processes.....	18
1.6 Rutherford-type superconducting cables .....	21
1.7 Typical superconducting accelerator magnets.....	22
1.8 Current state of the art Nb <sub>3</sub> Sn accelerator magnets .....	25
1.9 High Field Magnet program at Fermilab .....	26
1.10 Scope of the thesis .....	32
<b>Chapter 2 – Superconducting magnet instabilities.....</b>	<b>33</b>
2.1 Degradation and training.....	33
2.2 Type of disturbances.....	35
2.3 Disturbances origins.....	40
2.3.1 Mechanical instabilities .....	41
2.3.2 Thermo-magnetic instabilities in type II superconductors.....	41
2.4 Thermo-magnetic instabilities: the adiabatic criteria.....	43
2.5 Thermo-magnetic instabilities: the dynamic effect on the stability criteria. ....	45

2.5.1 Thermo-magnetic instability: linearization of the equations .....	46
2.5.2 Stability criteria and the role of $\tau$ .....	48
2.5.3 Design of stable strand .....	49
2.5.4 Non linear electric conductivity and dynamic effect .....	50
2.6 Stability of a magnet made of an unstable superconductor .....	51
<b>Chapter 3 – Magnet test results .....</b>	<b>55</b>
3.1 Vertical Magnet Test Facility .....	56
3.1.1 Vertical dewar .....	56
3.1.2 30 kA power supply system .....	58
3.2 Instrumentation and software .....	60
3.3 Voltage Spike Detection System .....	61
3.3.1 Hardware .....	62
3.3.2 Software .....	63
3.4 Test Results .....	64
3.4.1 Quench studies of Fermilab Nb <sub>3</sub> Sn Magnets .....	64
3.4.2 Flux jump observations .....	66
3.4.3 Instability studies using small racetrack .....	70
3.4.4 Quench performance of FNAL dipoles based on PIT strands .....	82
3.5 Conclusions .....	87
<b>Chapter 4 – Strand test results .....</b>	<b>91</b>
4.1 Short Sample Test Facility .....	94
4.2 Voltage Spike Detection System at the SSTF .....	99
4.3 Sample preparation and test procedure .....	103
4.4 Data analysis steps and tools .....	105
4.4.1 Critical current measurements .....	105
4.4.2 Critical current estimate at low field using a scaling law .....	107
4.4.3 Analysis of voltage spikes measurements .....	110
4.5 Test results .....	115
4.5.1 Quench current of Nb <sub>3</sub> Sn strand during V-I measurements .....	115
4.5.2 Quench current of Nb <sub>3</sub> Sn strand during V-H measurements .....	123
4.5.3 Voltage spikes in superconducting strands .....	133

4.5.4 Discussion .....	146
4.6 Conclusions .....	150
<b>Chapter 5 Thermo-magnetic instabilities in strands: calculation of the minimum quench current .....</b>	<b>153</b>
5.1 Geometry of the 1 mm MJR strand.....	154
5.2 Volumetric specific heat of Nb <sub>3</sub> Sn T<T <sub>c</sub> .....	156
5.3 Volumetric specific heat of the MJR composite T<T <sub>c</sub> .....	160
5.4 Critical current of the 1 mm MJR strand .....	160
5.5 Energy dissipated in a magnetized sub-element during a complete flux jump: the ‘magnetization’ energy .....	162
5.6 Energy dissipated in a not magnetized strand with transport current during a complete flux jump: the ‘Self field’ energy .....	165
5.7 Enthalpy calculation and quench criterion.....	167
5.8 Minimum quench current based on Self field energy.....	167
5.9 Minimum quench current based on Self field and Magnetization energy .....	170
5.10 Self Field in the strand sample.....	171
5.11 Magnetization in the strand sample due to self field .....	172
5.12 Comparison with experimental results.....	176
5.13 Conclusions.....	178
<b>Chapter 6 – Conclusions.....</b>	<b>179</b>
<b>Appendix A – V-I characteristic of type II superconductor .....</b>	<b>183</b>
<b>Appendix B – Critical current parameterization.....</b>	<b>185</b>
<b>References.....</b>	<b>189</b>
<b>Acknowledgments .....</b>	<b>199</b>



# Chapter 1 – Introduction

The advance of High Energy Physics research using circulating accelerators strongly depends on increasing the magnetic bending field which accelerator magnets provide. To achieve high fields, the most powerful present-day accelerator magnets employ NbTi superconducting technology however, with the start up of Large Hadron Collider (LHC) [1] in 2007, NbTi magnets will have reached the maximum field allowed by the intrinsic properties of this superconductor.

A further increase of the field strength necessarily requires a change in superconductor material; the best candidate is Nb<sub>3</sub>Sn. Several laboratories in the US and Europe are currently working on developing Nb<sub>3</sub>Sn accelerator magnets, and although these magnets have great potential, it is suspected that their performance may be fundamentally limited by conductor thermo-magnetic instabilities: an idea first proposed by the Fermilab High Field Magnet group early in 2003 [2].

This thesis presents a study of thermo-magnetic instability in high field Nb<sub>3</sub>Sn accelerator magnets. In this chapter the following topics are described:

- the role of superconducting magnets in High Energy Physics;
- the main characteristics of superconductors for accelerator magnets;
- typical measurements of current capability in superconducting strands;
- the properties of Nb<sub>3</sub>Sn;
- a description of the manufacturing process of Nb<sub>3</sub>Sn strands;
- superconducting cables;
- a typical layout of superconducting accelerator magnets;
- the current state of the art of Nb<sub>3</sub>Sn accelerator magnets;
- the High Field Magnet program at Fermilab; and,
- the scope of the thesis.

## **1.1 Introduction**

High Energy Physics (HEP), also known as particle physics, is the branch of science dedicated to the pursuit of the fundamental nature of matter. In order to study the structure of matter experimentally, HEP employs energetic particles analogous to the

light source of a microscope; the performance of the particle "microscope" however, is dependent on the energy of the particles and the luminosity of the beams in collision. In order to probe shorter and shorter distances, the energy (or momentum) of the particles has to increase. Also, since the strong interaction acts only at very short distances, the collision cross-section of high energy particles is usually small and requires a high luminosity of colliding particles in order to study these interactions.

HEP was and still is the main driving force pushing particle accelerator development to the technological limit, thereby providing the incentive for the accelerator community to build higher and higher energy accelerators with higher particle luminosity.

The current state of this advancement is embodied by the Large Hadron Collider (LHC) [1], that will accelerate protons up to 7 TeV energy at  $10^{34} \text{ cm}^{-2}\text{s}^{-1}$  particle luminosity, with an average beam current of 0.85 A.

Achieving such high energies and luminosities is not a trivial task. It requires the building of complex accelerator systems. For accelerating protons (or anti-protons) to high energies, the circulating accelerator technique has proved the most successful.

The basic idea of a circular accelerator [3] is to keep charged particles circulating around in a ring. At short straight sections of the ring the particles are accelerated by specially tuned cavities in which a radio-frequency (RF) wave is applied. The component of this wave closest to the beam has an electric field aligned such that the charged particles get a boost in the right direction at that time. This type of acceleration works like a swing that is periodically given a push at the proper phase of its (harmonic) cycle. After many revolutions, the particles will gain significant amounts of energy. The key to achieving high energy therefore is to have many revolutions of the particles without losing them.

The particles are kept in a circular orbit by bending the beam with a homogeneous magnetic field that is perpendicular to the direction of the beam. This is only possible if the beam has no transverse momentum spread; any small impulse (kick) in the transverse direction will cause the particle spiral away from the beam orbit. Since all beams have some non-zero momentum spread, keeping the particles on a circular orbit therefore requires both bending and focusing forces which can be generated by magnetic fields.

To reach high magnetic fields while keeping the operational costs acceptable is impossible using conventional magnets. For this reason the bending (dipole) and focusing (quadrupole) magnets in high energy circular accelerators typically utilize superconducting materials. The vanishing electrical resistance substantially reduces the operating costs. In the Super Proton Synchrotron at CERN a power of 52 MW is needed to power the normal conducting magnets to reach 315 GeV energy of protons compared to HERA at DESY which needs of a 6 MW cryogenic power plant to cool the superconducting magnets for the 820 GeV proton accelerator [4].

The first high energy particle accelerator based on superconducting magnet technology was the Tevatron at Fermilab, which began operation in 1983 [5]. The Tevatron has 774 dipoles and 180 quadrupoles for a total circumference of 6.3 km. Since then, other superconducting accelerators, where the basic magnetic structure has remained the same, were built successfully, Tab. 1-1. In these accelerators, all the coils were wound using multifilament strands based on NbTi superconductor (details in next section) [6].

Although over the years the current carrying capability of NbTi superconducting strands increased significantly (from 1800 A/mm<sup>2</sup>, at the start of Tevatron conductor fabrication, to 3100 A/mm<sup>2</sup> at 5 T/4.2 K currently for mass production [4]), it still remains the bottleneck to achieving magnetic fields higher than 10 T due to the intrinsic material properties of the superconductor (see next section for details).

Today there are many new superconductor materials which can operate at magnetic fields higher than 10 T; however, manufacturing multifilamentary strands suitable for magnet applications using these materials is still challenging. Among these 'next generation' superconductors Nb<sub>3</sub>Sn is the only conductor available in multifilamentary stabilized strands, made in long lengths, and capable of high current densities at 10-15 T fields [7,8,9]. Consequently the current state of the art accelerator magnet technology has been focused on the development of Nb<sub>3</sub>Sn magnets.

**Tab. 1-1 Accelerators based on high field superconducting magnets around the world**

Project	Lab	Energy [TeV/beam]	Tunnel length [Km]	Operating dipole field [Tesla]	Status
TEVATRON <sup>†</sup>	FNAL	0.98	6.3	4.4	Operated in 1983
HERA <sup>*</sup>	DESY	0.92	6.3	5.3	Operated in 1989
SSC	SSCL	20	87	6.7	Cancelled in 1993
RHIC <sup>‡</sup>	BNL	0.1/nucleon	3.8	3.4	Operated in 1999
LHC	CERN	7	27	8.3	Operation in 2007

<sup>†</sup>0.98 TeV were reached in 2001

<sup>\*</sup>0.92 TeV were reached in 1998

<sup>‡</sup> heavy ion accelerator

## 1.2 Superconductivity

The liquefaction of helium was first achieved in 1908 by H. Kamerlingh Onnes [10] at the University of Leiden, in the Netherlands. This was a breakthrough in low temperature physics since the availability of liquid helium made it possible to study material properties at and even below 4.2 K (boiling temperature of liquid helium at atmospheric pressure) relatively easily.

Shortly after this major cryogenic breakthrough, in 1911, superconductivity was discovered at the same university in the laboratory headed by H. K. Onnes. A graduate student was measuring resistivity of the mercury as a function of the temperature when he observed that at specific temperature (later known as transition temperature or critical temperature  $T_c$ ) around 4.2 K, the measured resistance suddenly went to zero. Onnes himself was the first who realized that mercury below a transition temperature is in a different state and called this state “superconducting”.

In 1933 W. Meissner and R. Ochsenfeld discovered that superconducting materials completely expel from its interior a weak magnetic field when cooled down below  $T_c$  [11]. This phenomenon is now known as the Meissner effect. They also observed that in strong fields superconductivity broke down and the material changed back to the normal state.

The magnetic field value at which the superconducting material passes to normal state is named *critical field*  $B_c$ .  $B_c$  is decreasing with the temperature similar to  $T_c$  decreasing with increasing magnetic field.

The Meissner effect could not be explained in the frame work of Classical Electrodynamics. The full understanding of this phenomenon occurred with the advent of the BCS microscopic theory of superconductivity by J. Bardeen, L. N. Cooper and J. R. Schrieffer [12]. This research was published in 1957.

Another important event was the discovery of superconductors which remain superconducting at relatively high magnetic fields. In these superconductors, the magnetic field can penetrate into the bulk of the superconductor. After this discovery, superconductors were divided into two types: type I and type II superconductors. Type I materials have only one superconducting state, the Meissner state characterized by complete field expulsion. Type II materials have two superconducting states: the Meissner state and the mixed state at higher fields. The magnetic field at which the superconductor passes from the Meissner to the mixed state is called *lower critical field*  $B_{c1}$ . By increasing the field higher than  $B_{c1}$  the magnetic field will penetrate into the superconductor until the *upper critical field*  $B_{c2}$  then by further increasing the field superconductivity vanishes.

Also  $B_{c1}$  and  $B_{c2}$  are function of the superconductor temperature. Generally speaking, the terms upper critical field and critical temperature are referred to the upper critical field at 0 K,  $B_{c20}$ , and to the critical temperature at vanishing magnetic field,  $T_{c0}$ .

The magnetic field penetration into the superconductor was explained by the theory of the mixed state of type-II superconductors by A. A. Abrikosov, who, by analogy with super-fluidity in helium II, introduced the concept of magnetic vortices or fluxoids [13]. This theory was published in 1957 as well.

### **1.2.1 Relevant type II superconductors**

The most commonly used superconductor is a ductile metallic alloy of niobium and titanium (NbTi) whose critical temperature is about 9 K. The first detailed study on NbTi was published in 1961 [14]. The success of this material is due to both its good superconducting and mechanical properties.

In 1954 another now commercially available superconductor was discovered which is an intermetallic compound of niobium and tin,  $\text{Nb}_3\text{Sn}$  [15]. Its critical temperature is about 18 K. Brittleness and manufacturing difficulties of  $\text{Nb}_3\text{Sn}$  were the reasons that it has been used only for specific high-field applications.

In 1972 the superconductivity of ternary molybdenum sulfides [16] was discovered. These compounds, now referred to as Chevrel phases, have a critical temperature between 2 and 14 K, and are interesting because of their relatively high upper critical magnetic field. The most promising is  $\text{PbMo}_6\text{S}_8$ , which has a critical temperature of 14 K and an upper critical field of about 50 T at 4.2 K. Despite a lot of effort, the production of multifilament wires based on  $\text{PbMo}_6\text{S}_8$  has never reached an industrial scale.

A real breakthrough in the superconducting world happened in 1986 when J. G. Bednorz and K. A. Muller observed the superconductivity of a sample Ba-La-Cu-O at a relatively high temperature of about 30 K. The results were published the same year [17] and earned the two scientists the Nobel Prize in Physics in 1987.

This discovery started a worldwide search for superconducting copper oxide ceramics whose critical temperature turned out to be in the 90-120 K range. These materials are named High Temperature Superconductors (HTS); among them the most interesting are the Y-Ba-Cu-O compounds discovered in 1987 [18] and the Bi-Sr-Ca-Cu-O compound discovered in 1988 [19]. Although the quality of commercially available products is steadily increasing, HTS are still not yet competitive in the traditional markets of NbTi and  $\text{Nb}_3\text{Sn}$ .

The most recent surprising discovery happened in 2001 when it was found that  $\text{MgB}_2$ , an intermetallic compound, becomes superconducting just below 40 K [20]. At first, for the low cost, the high critical temperature and, an upper critical field similar to NbTi, it was thought that  $\text{MgB}_2$  was the natural replacement of NbTi. However, it has been recently demonstrated that the introduction of strong impurity scattering could even increase significantly the upper critical field (beyond that of Nb-based superconductors). This opens new possibilities for the use of  $\text{MgB}_2$  which have yet to be explored [21].

## 1.2.2 Critical current density & critical surface

For applications in accelerator magnets, a superconducting wire must be able to carry a large current in the presence of fields typically higher than 5 Tesla [4]. This is possible only for type II superconductor.

At a fixed temperature and magnetic field a type II superconductor can carry a current density with a vanishing electrical resistivity up to a certain value called the *critical current density*,  $j_c$ . Above this value the superconductor starts returning to the normal state and its resistivity increases drastically.

The  $j_c$  is a function of the temperature and of the transverse magnetic field, hence a superconductor is characterized by its *critical surface*. Fig. 1-1 shows the critical surface for the NbTi superconductor.

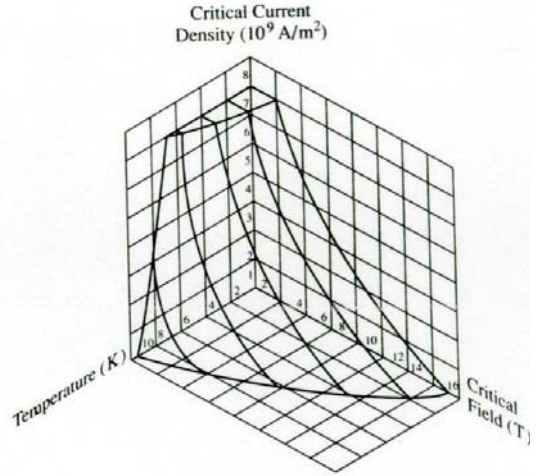


Fig. 1-1 Critical surface for NbTi [22]

The critical surface is the border between the superconducting and the normal state. When a conductor passes from the superconducting state to the normal state it is said to be *quenching* [4]. In general, the word *quench* can be referred to any superconducting device and indicates an irreversible transition from a non-resistive to a resistive state.

## 1.2.3 Transition of the superconductor at a fixed temperature and magnetic field

The increase of the resistivity and of the electric field once  $j_c$  is approached can be parameterized with a power law [4, 22]:

$$\rho(j) = \rho_c \left( \frac{j}{j_c} \right)^n \quad \text{eq. 1-1}$$

$$E(j) = E_c \left( \frac{j}{j_c} \right)^{n+1} \quad \text{eq. 1-2}$$

$$\rightarrow \quad \tilde{\rho} \equiv \frac{dE}{dj} = (n+1) \rho_c \left( \frac{j}{j_c} \right)^n \quad \text{eq. 1-3}$$

where  $\rho_c$  and  $E_c$  are respectively, the resistivity and the electric field in the superconductor when it reaches the critical current density. The parameter  $n$ , named *n-value*, describes the steepness of the increase of the resistivity and the electric field as a function of the current density.

The derivative of the electric field respect to the current density is named *differential resistivity*  $\tilde{\rho}$  and its inverse *differential conductivity*  $\tilde{\sigma}$ . The differential conductivity value is a relevant parameter for the thermo-magnetic instability of the superconductor (chapter II).

The development of the electric field can be also parameterized using the following formula [23]:

$$\boxed{E(j) = E_c e^{\frac{j-j_c}{j_i}}} \quad \text{eq. 1-4}$$

These parameterizations are valid only when the electric field within the superconductor does not pass a certain threshold value  $E_f$  ( $\sim 10^{-4}$  V/m). Increasing the electric field beyond  $E_f$  the superconductor enters in the *flux-flow regime* characterized by a constant differential resistivity  $\tilde{\rho}_f$  [23]. The differential resistivity in the flux flow regime is of the order of  $10^{-6}$  -  $10^{-7}$   $\Omega$  m while at  $E_c$  ( $10^{-5}$  -  $10^{-6}$  V/m) it is of the order of  $10^{13}$   $\Omega$  m [23].

### 1.2.4 Critical state model

The steep increase of the resistivity for current densities higher than  $j_c$  allowed Bean [24, 25] and London [26] to formulate the concept of the *critical state*. According to this concept when an electric field is applied in a type II superconductor, the involved region responds by establishing a critical state in which the current density is equal to  $j_c(T, B)$ . This means that in the superconductor the current density will be equal either to 0 or to  $j_c(T, B)$ . For a non vanishing electric field the relationship between the electric field  $E$  and the current density  $j$  is:

$$\vec{j} = j_c(T, B) \frac{\vec{E}}{E}$$

The critical state model which is the most accepted model presently incorporated into macroscopic electrodynamics of type II superconductors [23].

### 1.2.5 Magnetization of a superconductor

In a superconductor under influence of a changing magnetic field, electric currents are induced to flow in such a way as to shield the interior of the superconductor from the changing field. The distribution and the magnitude of these currents are well described by the critical state model.

Let us assume an infinite superconducting slab of width equal to  $2a$  initially not magnetized and then exposed to an increasing magnetic field parallel to the slab surface. Fig. 1-2 shows: *i*) the slab, the magnetic field and current directions, *ii*) the distribution of the magnetic field and, *iii*) of the current inside the slab at different times (1,2, and 3) at increasing external field values  $B_{ext}$ .

This distribution is drawn directly from Maxwell equations and Bean's model of the critical state (critical state + critical current density as a function of the temperature and external magnetic field).

The increasing magnetic field  $B_y$  induced screening currents  $\pm j_z$  to flow in the slab. According to the critical state model  $j_z = j_c$ . From the Maxwell equation in one dimension:

$$\frac{\partial B_y}{\partial x} = -\mu_0 j_z = -\mu_0 j_c \quad \text{eq. 1-5}$$

Thus the magnetic field within the slab (*ii*) at first ( $B_{ext1}$ ) falls-off from the surface until the field reaches zero at the interior, after which the current density becomes zero and the field does not change. By increasing the external field, the regions of  $\pm j_c$  extend further into the slab until they reach the center, at which point the slab is said to be *fully penetrated*. Further increasing the field will generate no change in the current pattern, simply a general increase in the field throughout the slab.

If now the external field is reduced, Fig. 1-3, the currents will progressively change direction ( $B_{ext4}$ ) starting from the slab surfaces. In the slab inner part, the magnetic field distribution will remain unchanged until the original current is completely wiped out ( $B_{ext5}$ ). From this point on, further reducing the field will not change the current distribution anymore, and the field value will change in the whole slab ( $B_{ext6}$ ).

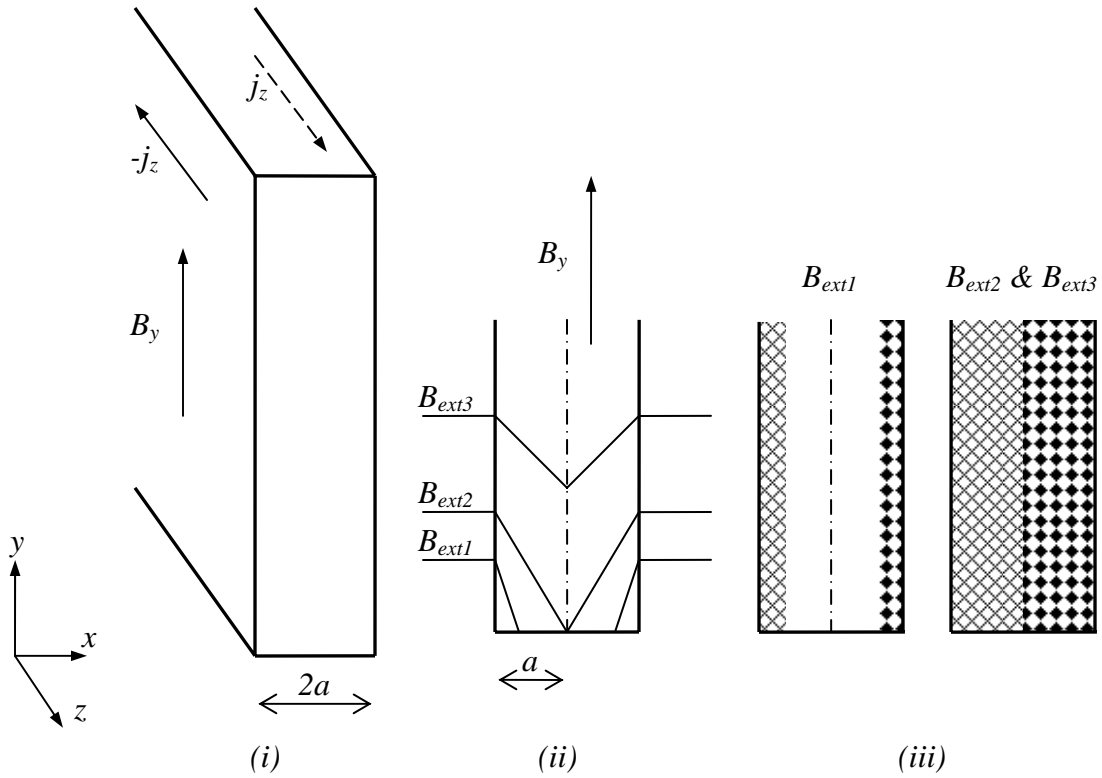


**Fig. 1-2 Magnetization of a infinite superconducting slab while ramping up the field  $B_y$  at different times (1,2, and 3) at increasing external field values  $B_{ext}$ : (i) magnetic field and current direction; (ii) distribution of the magnetic field; (iii) distribution of the current.**

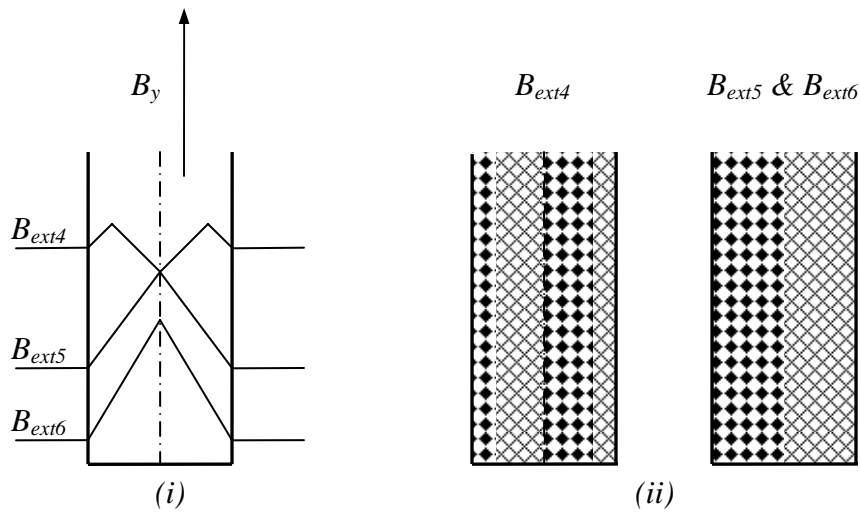


**Fig. 1-3 Magnetization of a infinite superconducting slab while ramping down the field  $B_y$  at different times (4,5, and 6) at decreasing external field values  $B_{ext}$ : (i) distribution of the magnetic field; (ii) distribution of the current.**

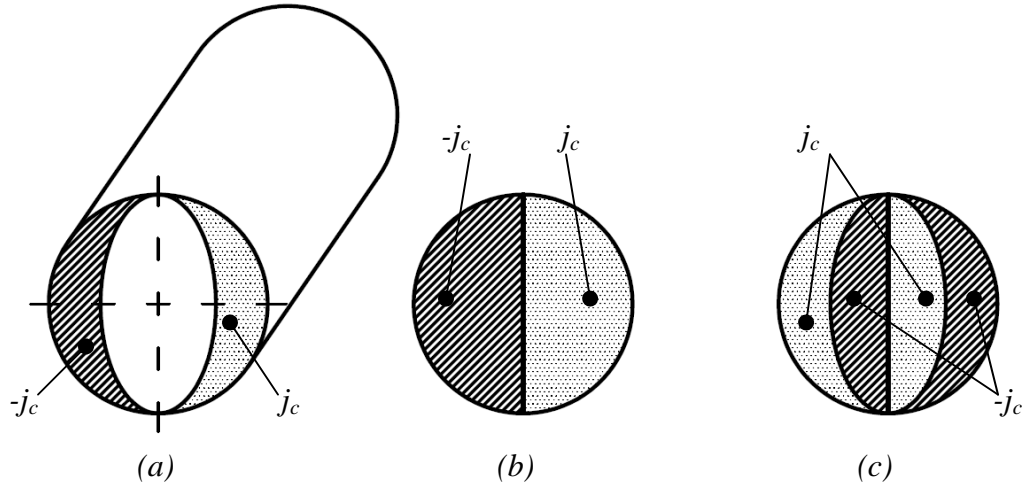


**Fig. 1-4 Current distribution in a cylindrical superconducting wire exposed to a transverse magnetic field: a) the field is ramped up, the wire is initially not magnetized; b) at certain field value the wire is fully penetrated; c) the field is ramped down.**

The currents induced in the superconductor by a changing magnetic field are named *persistent currents*; even if the magnetic field stops changing, these current will persist (the decay time constant is incredibly long) [27, 28].

The persistent currents produce a magnetic moment per unit volume (generally named *magnetization*). With a current distribution like the case  $B_{ext2}$  &  $B_{ext3}$  in Fig. 1-2, the magnetization  $M_{slab}$  is [29]:

$$M_{slab} = -\frac{j_c a}{2} \quad eq. 1-6$$

Changing the current polarity (case  $B_{ext5}$  &  $B_{ext6}$  of Fig. 1-3) the formula is the same but with a different sign.

For the more practical case of a cylindrical wire aligned perpendicular to the field, Fig. 1-4, the calculation of the magnetization  $M_{cyl}$  for the current distribution indicated by *b* in the figure, gives the result [29]:

$$M_{cyl} = -\frac{4}{3\pi} j_c a \quad eq. 1-7$$

where  $a$  is the radius of the wire.

## 1.2.6 Impact of the superconductor magnetization on wire layout

Superconductor magnetization has three harmful effects on magnet performance: production of field distortions [30, 31], power dissipation which heats up the magnet coil [26], and thermo-magnetic instability of the superconductor [22]. The field quality degradations are mainly of concern for accelerator magnets and require elaborate correction schemes to control beam optics [32, 33]. The power dissipation due to magnetization is mostly a problem for pulsed magnets which have to have carefully designed cooling to prevent degrading magnet performance. This issue is of particular concern for the magnets of nuclear fusion reactors. Thermo-magnetic instabilities are dangerous for any type of magnet because they can also limit the magnet performance. Thermo-magnetic instabilities will be discussed in the second chapter.

The superconductor magnetization is proportional to the superconductor diameter (*eq. 1-7*). In order to reduce magnetization effects, all magnet conductors are made with the superconductor divided into fine filaments. These fine filaments are embedded in a matrix of normal metal. Present superconducting strands mainly utilize copper for its good electrical and thermal conductivity and its ductility which is very useful in the fabrication process. As chapter two will show, a good electrical and thermal conductivity is useful in reducing thermo-magnetic instabilities; it also helps to protect the conductor from burn-out if the magnet quenches. However it has the effect of coupling the superconducting filaments together and making act them as a much bigger filament. In order to solve this problem the filaments are twisted [22]. All the SC accelerator magnets built to date have twisted filaments with a diameter of  $\sim 6 - 20 \mu\text{m}$ .

## 1.3 Critical current measurements of superconducting strands

The critical current  $I_c$  of superconducting strands is generally obtained through a measurement of the voltage between the ends of the sample while ramping the current at a fixed temperature and magnetic field (V-I measurements).

Two different criteria are used to evaluate the  $I_c$  from V-I measurements: the critical electric field and the resistivity [34]. In the first case the  $I_c$  is reached when the voltage drop between two points of the strand is:

$$V_c = E_c \cdot l$$

where  $l$  is the strand length between the two points and, the critical field  $E_c$  is equal to 10  $\mu\text{V/m}$ . In the resistivity criterion case, the  $I_c$  is reached when the voltage drop is:

$$V_c = I \cdot \rho_c \frac{l}{S}$$

where  $S$  is the strand cross section area and  $\rho_c$  is  $10^{-14} \Omega\text{m}$ . At Fermilab this second criterion is usually adopted. The critical current density is then calculated dividing  $I_c$  by the value of the superconductor area in the strand section. Actually in  $\text{Nb}_3\text{Sn}$  strands, where the strand cross section is composed not only of copper and superconductor but also of bronze, the critical current density is defined as the ratio between the  $I_c$  and the non-copper area.

Another value measured during critical current measurements is the quality factor  $n$ . At Fermilab the  $n$ -value is extrapolated using the following parameterization:

$$\boxed{\rho(I) = \rho_c \left( \frac{I}{I_c} \right)^n} \quad \text{eq. 1-8}$$

where  $\rho$  is the average resistivity of the whole strand.

A homogeneous strand has a sharper transition since all the filaments reach the critical limit for the current at the same time. Hence the  $n$ -value is a good parameter for the strand quality. Typical  $n$ -values for high quality  $\text{Nb}_3\text{Sn}$  superconducting strands are of the order of 40 at 12 T.

The  $n$ -value is a function of the magnetic field at which the V-I measurement is performed: the higher the magnetic field, the lower the  $n$ -value.

## **1.4 Basic properties of $\text{Nb}_3\text{Sn}$ superconductor**

The present NbTi magnets have reached the maximum magnetic field they can produce; the nominal operating field of the LHC is 8.4 T at 1.9 K (superfluid helium). In order to increase the operating field level it is necessary to use a superconductor which can withstand a higher magnetic field with a high current density (critical current density,  $j_c$ ) [35].

The best candidate to fulfill this requirement is  $\text{Nb}_3\text{Sn}$ . Fig. 1-4 shows the critical current density of high current density superconductors as a function of the magnetic field.  $\text{Nb}_3\text{Sn}$  has much better superconducting properties compared to NbTi: a  $j_c$  equal to

1000 A/mm<sup>2</sup> is reached by the NbTi at ~11 T and ~1.9 K versus Nb<sub>3</sub>Sn at ~15-17 T and 4.2 K. Moreover, above 11T the  $j_c$  of NbTi drops drastically while above 15-17 T the  $j_c$  reduction for Nb<sub>3</sub>Sn is much more gradual.

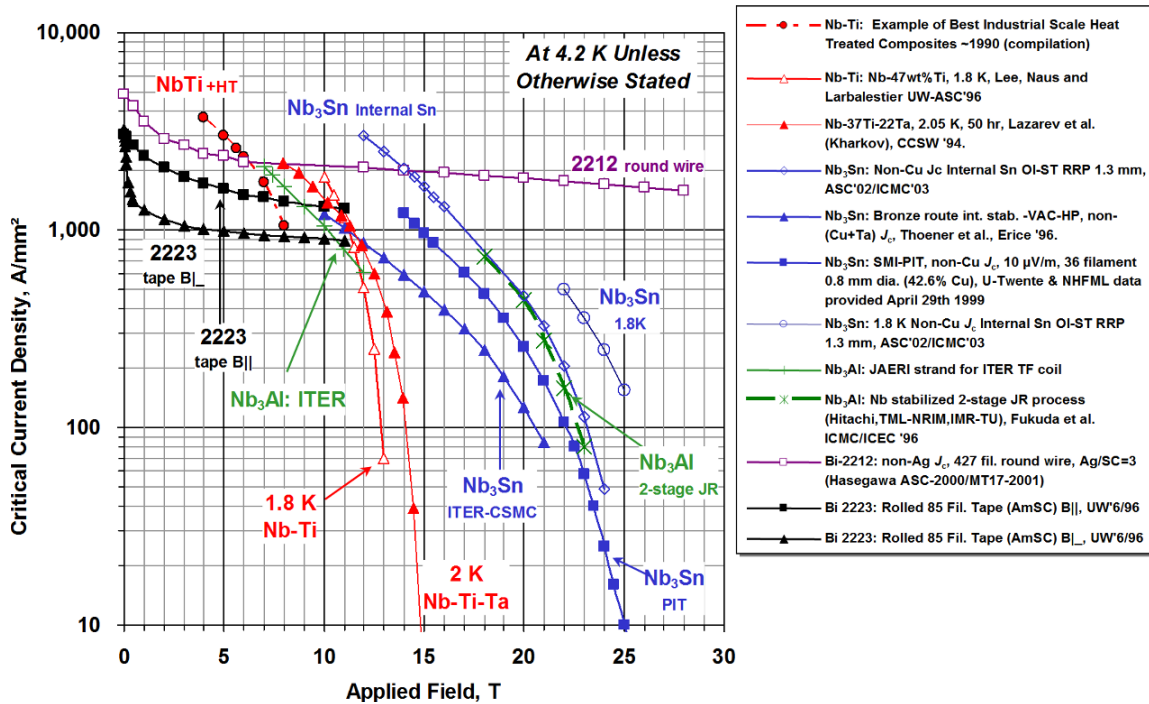


Fig. 1-5 Critical current density of superconducting materials; courtesy Applied Superconductivity Center, University of Wisconsin

Nb<sub>3</sub>Sn is an inter-metallic compound with a cubic A-15 structure. More precisely, it consists of a body-centered lattice of Sn atoms, with two Nb atoms on each face of the cube. Many of the A-15 materials are known to be superconducting, among them Nb<sub>3</sub>Sn is the most commonly used because it is the easiest to produce in a form suitable for large magnets. From the mechanical point of view, Nb<sub>3</sub>Sn is not as easy to handle as NbTi, because of its brittleness.

Nb<sub>3</sub>Sn conductors for magnet fabrication are made of superconducting sub-elements embedded in a copper matrix. The copper matrix is for magnet protection and for strand stabilization. Sub-elements are composed by Nb<sub>3</sub>Sn fine filaments embedded in a bronze matrix.

Before being heat treated, the sub-elements do not contain Nb<sub>3</sub>Sn. At this stage, the strand is still ductile and can be used to produce cables.

The Nb<sub>3</sub>Sn is formed during a heat treatment at ~650°C, by solid diffusion of Sn into Nb, through the bronze matrix. The copper in the sub-elements works as a catalytic agent for the preferential growth of the Nb<sub>3</sub>Sn phase reducing the heat treatment time.

### ***1.5 Manufacturing processes of Nb<sub>3</sub>Sn composite strands***

Different manufacturing processes for Nb<sub>3</sub>Sn have been tested and developed over time by different companies. The most important ones are the bronze process, the internal tin process (IT) and the powder in tube process (PIT). Fig. 1-6 shows a schematic of these processes.

#### **1.5.1 The bronze process**

In the bronze process, a sub-element is made by assembling a billet where rods of pure ductile Nb or Nb containing a small amount of Ta or Ti are inserted in a bronze matrix. A large bronze matrix is required to provide sufficient tin to the niobium rods since the tin content in the bronze matrix is limited to about 13.5wt% (limit for a ductile bronze alloy).

The initial billet is made of hundreds of Nb rods and it is drawn into a hexagonal shaped element. The hexagonal rods are cut and reassembled in a second billet whose matrix is made of OFHC copper. The copper has to be protected from the diffusion of the bronze-tin by a tantalum or niobium barrier. This second billet is extruded, annealed and drawn to the final wire size.

The bronze process requires frequent annealing steps because bronze work hardens rapidly. If precautions are not taken, these multiple anneals result in pre-reaction between the Sn in the bronze and the Nb, with formation of Nb<sub>3</sub>Sn during fabrication [36].

#### **1.5.2 The internal tin process**

The Internal Tin (IT) process was introduced to overcome the main limit of the bronze method, which is a limited tin content of 13.5wt% in the matrix. A higher concentration of tin produces higher critical current densities in the Nb<sub>3</sub>Sn layer [37].

The idea was to locate a tin source in the center of each sub-element. A Cu tube containing several Nb rods around a central hole is first hot extruded, then filled with Sn

and drawn into hexagonal sub-elements, which are shortened and reassembled into a new billet. This billet contains an outer stabilizing Cu ring protected from Sn diffusion by a tantalum barrier. The billet is then drawn to the final wire size without intermediate annealing.

Since this process does not involve intermediate anneals during wire fabrication, the billets are free from pre-reaction problems. Factors like the amount of Nb and Sn, the filament size and the sub-element number characterize the conductor properties.

This method suffers from ‘bridging’ problems [36]. Since the Nb filaments around the Sn rod within a sub-element are close together, they join or “bridge” during reaction when their volume increases (38%) after the conversion of Nb into the more voluminous Nb<sub>3</sub>Sn. This leads to a so-called *effective filament diameter* much larger than the filament itself with flux jumps (chapter 2) and large magnetization. This problem could be solved by spacing the filaments more widely apart. However, this would lower the overall  $J_c$ , thus invalidating one of the chief advantages of the process.

### 1.5.3 The Powder In Tube process

The Powder in Tube (PIT) process was first developed by the Netherlands Research Foundation [38, 39] and is presently implemented by the Shape Metal Innovation Company (SMI) [40].

The basic idea is to fill hollow Nb tubes with fine granulated Nb<sub>2</sub>Sn powder and then place them into a Cu matrix.

Compared to other methods, a large portion of the non-active bronze content can be replaced by superconductor elements or stabilizing Cu. The non-reacted part of the outer Nb tube acts as barrier between Cu and Nb<sub>3</sub>Sn.

The development of this technique has allowed producing long 36 and 192 filament strands. Factors like the number of sub-elements, the quality of the powders and the presence of a ternary element characterize the conductor properties.

Voids in the center of the Nb<sub>3</sub>Sn parts are inherent to this method. Fig. 1-7 shows a 1 mm PIT strand and the Nb<sub>3</sub>Sn distribution in a sub-element after reaction. The filament size for this process is the Nb tubes dimension. In the case of a 1mm PIT strand by SMI with 192 filaments, the filament size is about 50 μm.

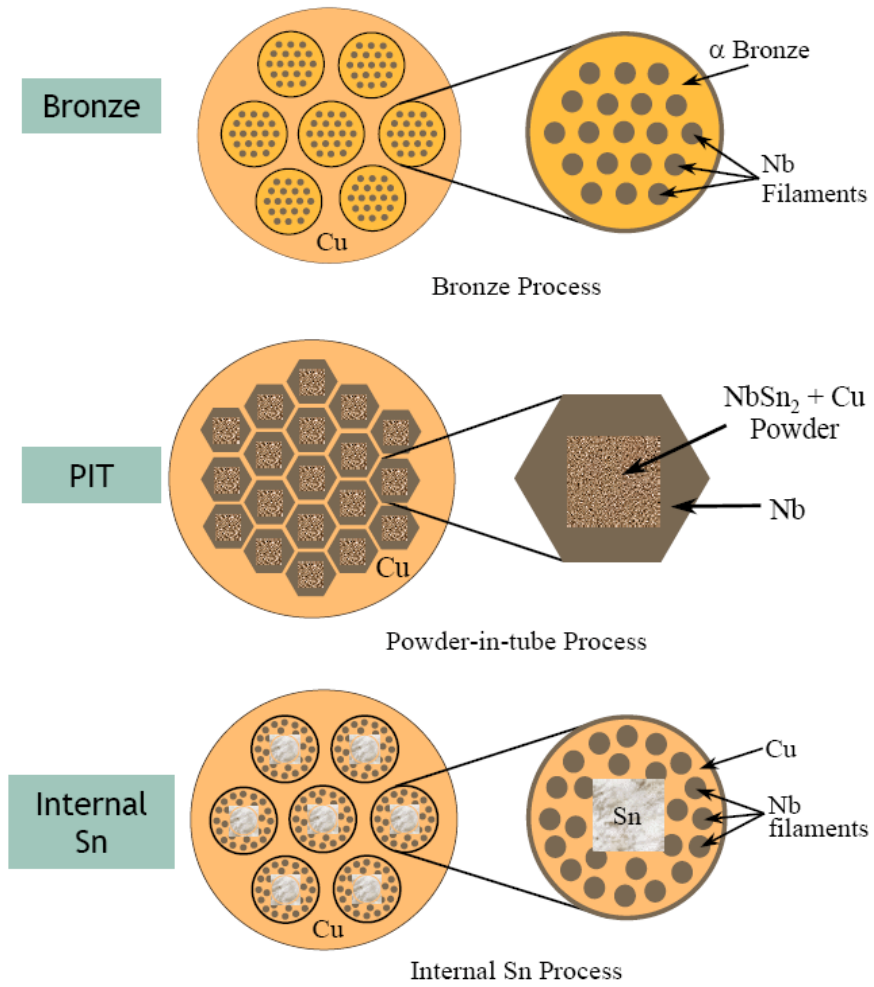


Fig. 1-6 Most important processes to build Nb<sub>3</sub>Sn superconducting strands

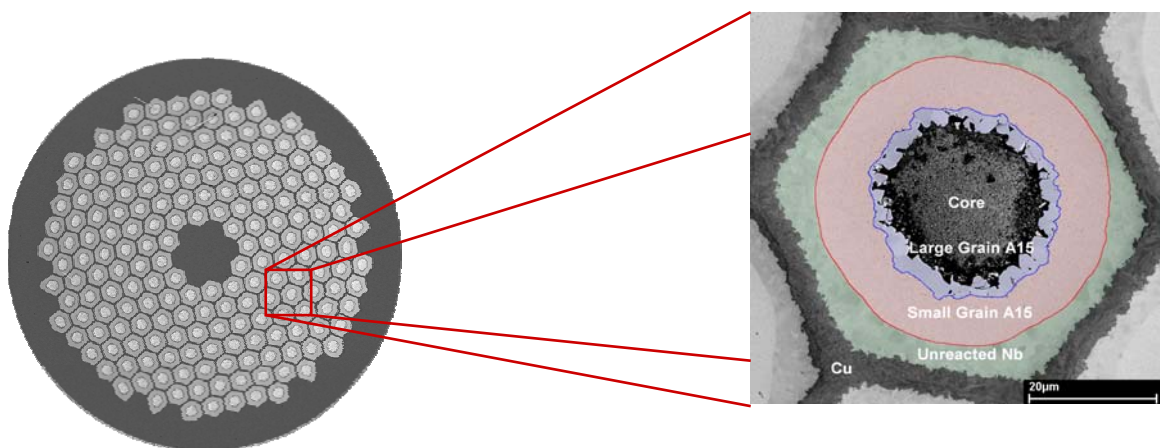


Fig. 1-7 1mm PIT strands (by SMI); from Fisher MS thesis, University of Wisconsin 2002

### 1.5.4 The Modified Jelly Roll and Restack Rod processes

The original internal tin process has had two evolutions the modified jelly roll (MJR) and the restacked rod process (RRP).

The Modified Jelly Roll (MJR) is a variant of the internal tin method pursued by Teledyne Wah Chang company in the US [41]. At present the patent is used by Oxford instrument Superconducting Technology (OST) [42].

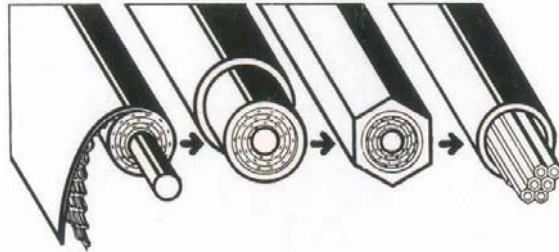


Fig. 1-8 Modified jelly roll process

The central part of the sub-element is composed by two overlapped sheets of niobium and copper rolled around a tin rod wrapped with a copper sheet. This roll is then wrapped with a niobium sheet which prevents the tin from diffusing out of the roll. The final component of the sub-element is a copper tube where the roll is inserted to form a billet. With respect to the internal tin process, this solution allows an increase of the niobium content in the non copper area by 35%. The billet is then drawn; during drawing the billet cross section is reduced by  $\sim 750$  times and shaped as a hexagonal rod. Copper rods with the same geometrical dimensions are also made.

The final billet is assembled by inserting the two types of rods into a Cu tube. The Nb rods are placed around a central part made of Cu rods. This new billet is then drawn to the final wire size.

Fig. 1-8 illustrates the main steps of the process. Fig. 1-9 shows the standard cross section of a 1mm MJR strand by OST; the strand has 54 sub-elements and 61 bundles (54+7 Cu central rods). The dimension of the sub-element is about 100  $\mu\text{m}$ .

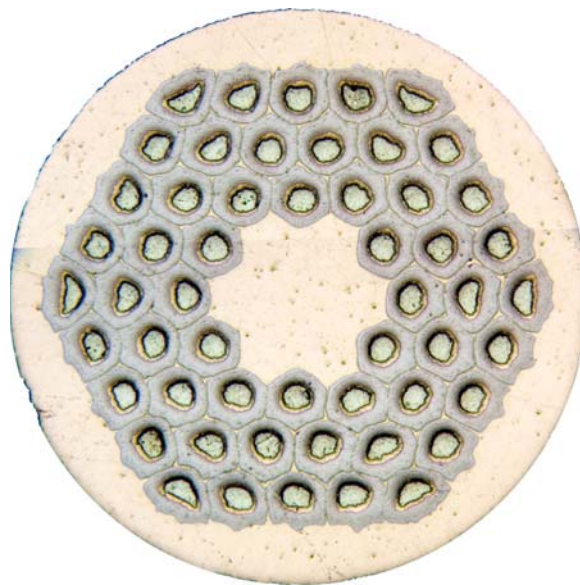


Fig. 1-9 Layout of a 54 subelements MJR/RRP OST strand

No annealing is required during the process. The same factors as in the IT method characterize the conductor properties [36].

Like the IT process, this technology also suffers from filament “bridging”. Due to the bridging the effective filament size is about the sub-element size.

Recently the “restack rod” process has been developed by Oxford Instruments to replace their MJR strands [43]. The main difference between the two processes is the composition of the sub-elements. In RRP, extruded Nb filaments surrounded by a Cu cladding and drawn to hexagonal form substitute the sheets of Nb and Cu used in the MJR process. Fig. 1-10 shows the process of the sub-element fabrication in the restack rod process. In Fig. 1-11 a comparison is shown between a RRP and a MJR sub-element before the heat treatment.

The new process allows better  $j_c$  performance, and moreover, the use of rods and extrusion instead of sheer and all-cold drawing makes yield more predictable. As for the MJR strands, the effective filament size for RRP strands is about the sub-element size. Since OST did not change the sub-element layout passing from MJR to RRP strands, for a 1mm strand with 54 sub-elements the effective filament size is about 100  $\mu\text{m}$ .

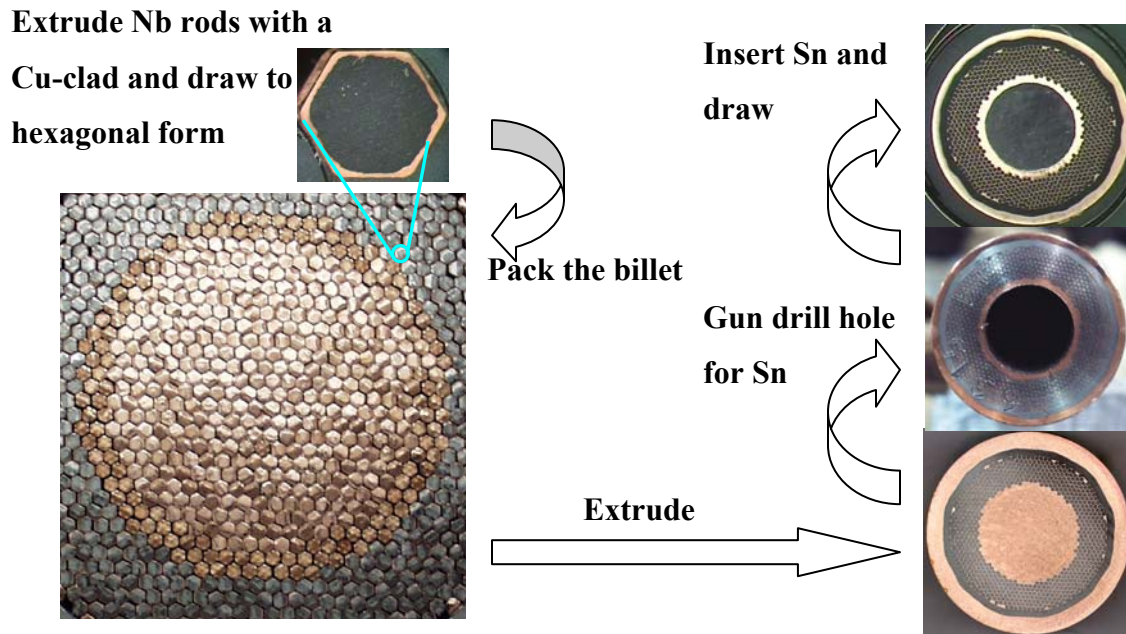


Fig. 1-10 Sub-element fabrication in the restack rod process; courtesy of OST

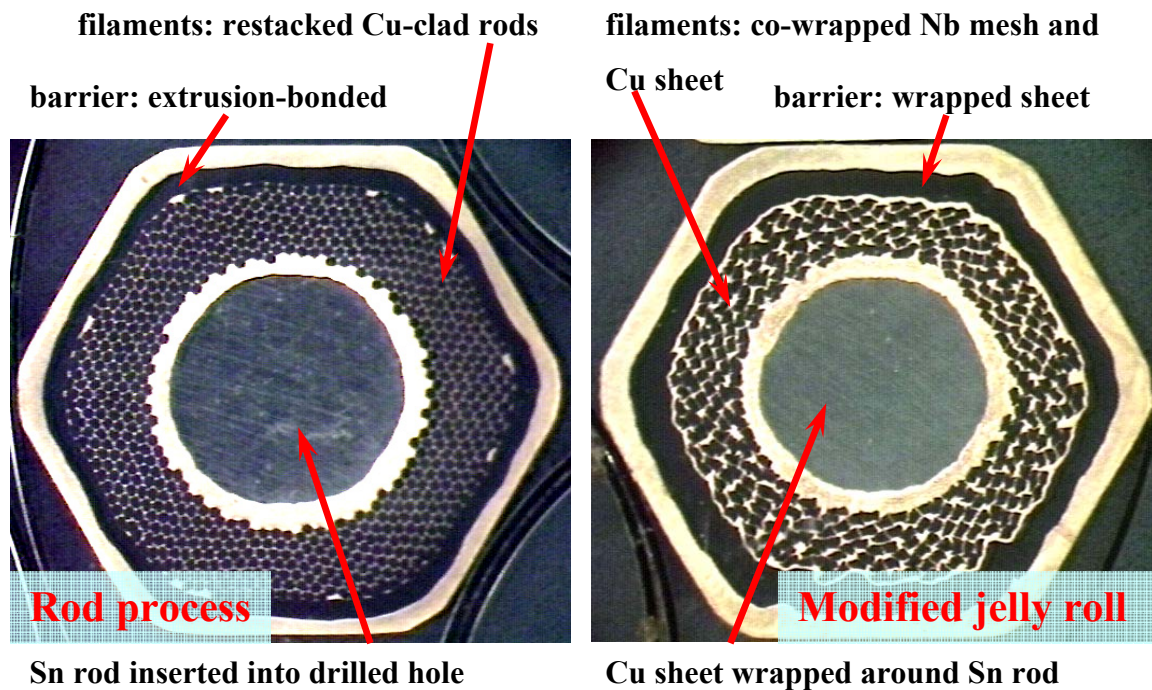


Fig. 1-11 Comparison between a RRP and a MJR sub-element before the heat treatment; courtesy of OST

## 1.6 Rutherford-type superconducting cables

Large superconducting magnets such as accelerator magnets are usually wound from multi-strand cables. The main reasons why cables are preferred to single strands are that it: 1) reduces the strand piece length requirement by a factor equal to the number of strands per cable; 2) limits the number of turns facilitating the coil winding; 3) allows strand-to-strand current redistribution in the case of a strand being locally resistive (a defective or a quenched strand); 4) decreases the coil inductance by a factor equal to the square of the strands number per cable. For a fixed current ramp rate a smaller magnet inductance reduces the voltage requirement of the power supply. Moreover the smaller the magnet inductance, the lower is the voltage to ground in the case of a magnet quench.

The main disadvantage of using cables is the need of large high current supplies and larger leads which connect the power supply to the magnet cable. In the cables, the strands are twisted together in order to prevent large current imbalance and to limit inter-strand coupling current while ramping.

Cables for accelerator magnets are generally “Rutherford-type” cables. A Rutherford cable is made up of a few tens of strands, twisted together, and shaped into a flat, two layer cable, Fig. 1-12.

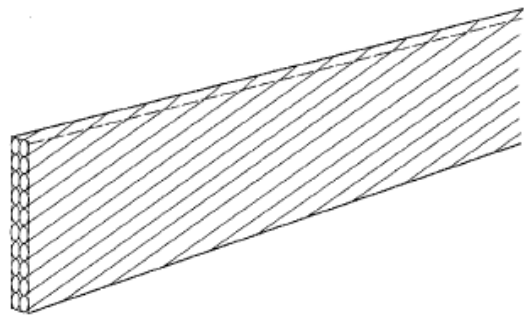


Fig. 1-12 Sketch of a Rutherford-type cable

This type of cable was developed in the early 1970s at the Rutherford Appletown

Laboratory in the UK [44] and it is used mainly in dipole and quadrupoles magnets for particle accelerator. Rutherford cables can have a rectangular or a trapezoidal cross section (keystoned cables) Fig. 1-13. This latter cross section allows the cables matching the shell shape often used in cos-theta magnets (see next section).

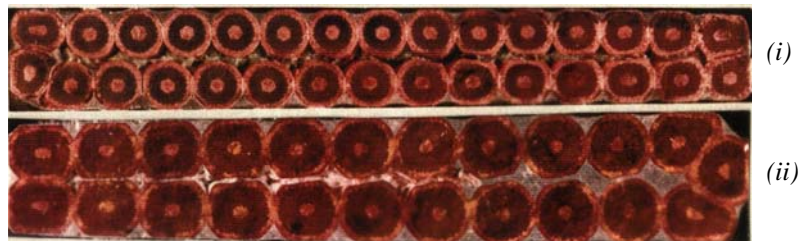


Fig. 1-13 Rutherford cable cross sections: (i) rectangular cable; (ii) key-stoned cable.

## 1.7 Typical superconducting accelerator magnets

The main dipole and quadrupole accelerator magnets (arc magnets) consist of a beam pipe surrounded by superconducting coils where the current flows parallel to the pipe axis (except at the magnet's ends). The pipe has a straight axis and a circular cross section. Actually the pipe of dipole magnets has a slight curvature to follow the beam orbit; however the deviation from a straight line is typically only few millimeters for a few meters long magnet.

The beam pipe is also referred to as the *bore* or *aperture*. In the highest energy circular machines the bore diameter is typically in the range 56-76 mm for the dipoles

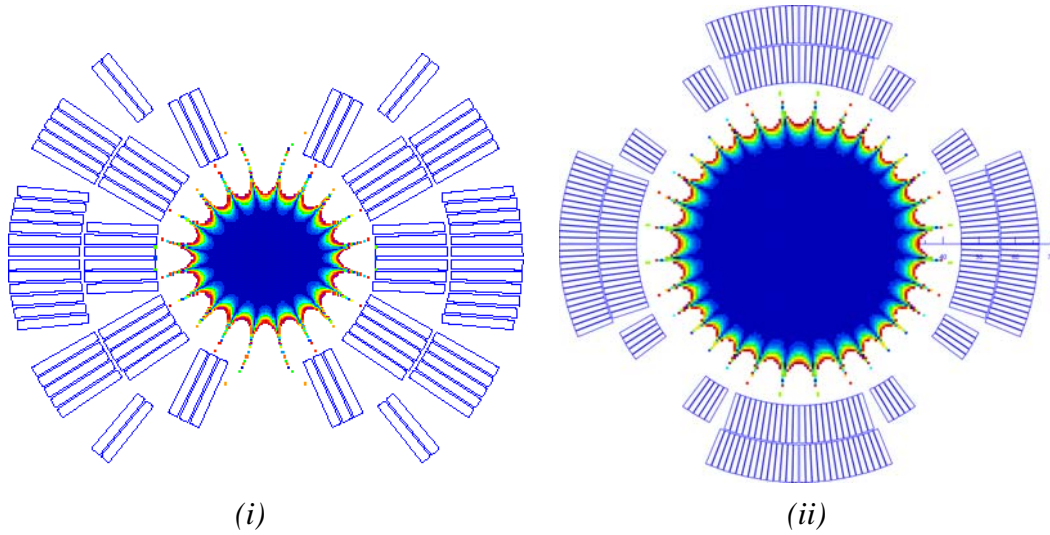
**Tab. 1-2 Design parameters of superconducting main magnets in accelerator**

	Dipoles			Quadrupoles			Operation temperature [K]
	Central field [T]	Coil aperture [mm]	Eff. Unit length [m]	Field gradient [T/m]	Coil aperture [mm]	Eff. length [m]	
<b>TEVATRON</b>	4.4	76.2	6.1	75.8	88.9	1.7	4.6
<b>HERA *</b>	4.7	75	8.8	91.2	75	1.9/1.7	4.5
<b>RHIC</b>	3.5	80	9.5	71.8	80	1.1	4.6
<b>LHC 56 mm</b>	8.4	56	14.2	223	56	3.1	1.9

\* Before upgrading in 1998 which brought the dipole field to 5.3T

and 56-89 mm for the quadrupoles. Tab. 1-2 shows the design parameters of superconducting main magnets in accelerators [45].

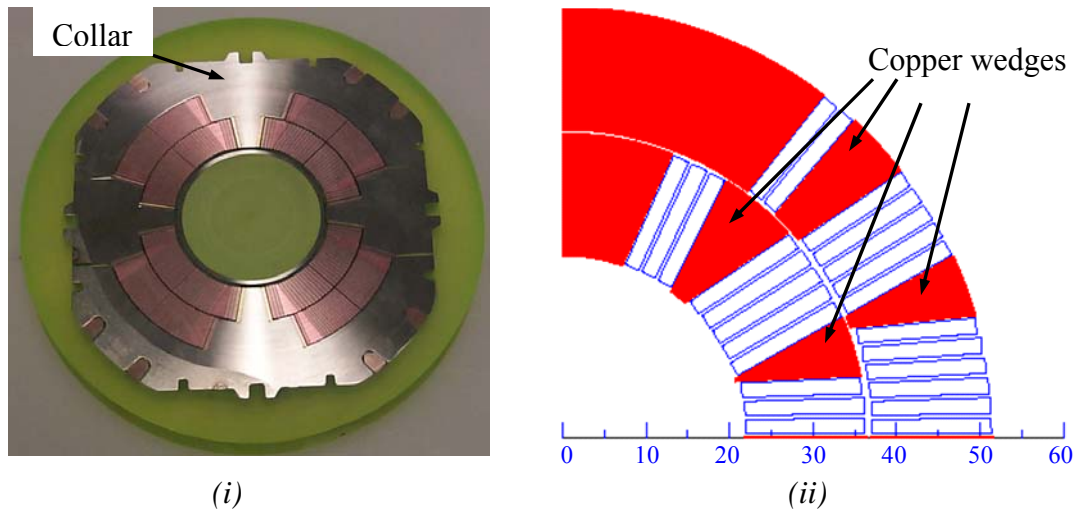
The field distribution of these magnets is dominated by the coil configuration. Generally in the central part of the magnet the Rutherford cables are parallel to the beam pipe and they are distributed such a way to approximate a  $\cos-\theta$  (dipoles) and  $\cos-2\theta$  (quadrupoles) current distributions. Magnets using these coil layouts are referred to as  $\cos-\theta$  magnets. Fig. 1-14 shows a typical cross section of the coil layout for a  $\cos-\theta$  dipole and  $\cos-2\theta$  quadrupole magnet. In this particular case each coil has two layers of cables. The plots also show how much the magnetic field deviate from a perfect uniform



**Fig. 1-14 Practical approximation with cables of a  $\cos-\theta$  (i) and a  $\cos-2\theta$  (ii) current distribution; in the bore is showed the relative field errors between  $10^{-5}$  (blue) and  $20 \cdot 10^{-5}$  (red)**

transversal field in the dipole and from a transversal field with a uniform gradient in the quadrupole.

The coils are subject to extremely high Lorentz forces; in order to support them, the coils are placed within a cavity. This cavity is generally made of stainless steel or aluminum collars. Collars have also the function of positioning precisely the coils in order to guarantee a high field quality.



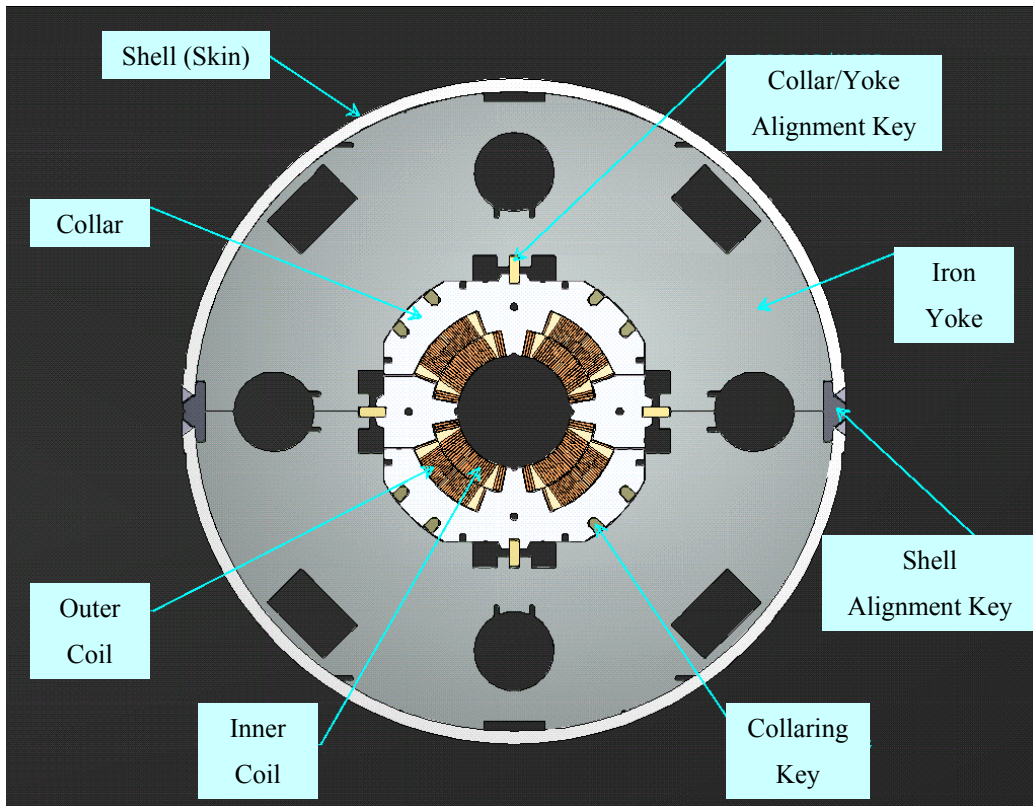
**Fig. 1-15 (i) collared coils cross section of a quadrupole; (ii) copper wedges in one quadrant of a dipole**

Fig. 1-15 (i) shows the collared coils cross section of a NbTi  $\cos-2\theta$  quadrupole built at Fermilab (MQXB).

To achieve a high field quality, copper wedges between different turns of the same coil are typically used. Moreover the wedges can correct for the non radial geometry of the cables. Fig. 1-15 (ii) illustrates the copper wedges in a  $\cos-\theta$  dipole used to optimize the current distribution.

The collars are surrounded by an iron *yoke* which has the purposes of: 1) shielding the surroundings against the high inner fields; 2) increasing the magnetic field in the magnet bore.

The magnet assembly is typically enclosed within a cylindrical shell which may or may not provide additional structural confinement, for example by welding under stress. All these components are visible in the cross section of the MQXB quadrupole magnet shown in Fig. 1-16.



**Fig. 1-16 Cross section of a MQXB quadrupole magnet**

An alternative design to  $\cos-\theta$  dipole magnets is the ‘race-track’ dipole design. It is based on two parallel flat coils shaped as racetrack, Fig. 1-17. This particular figure shows the *common coil* configuration where the same coil provides the current to the two apertures of the magnet. By inverting the polarity of one of the coils, one obtains the classical race-track design where the field is perpendicular to the coil plane and there is only one central aperture.

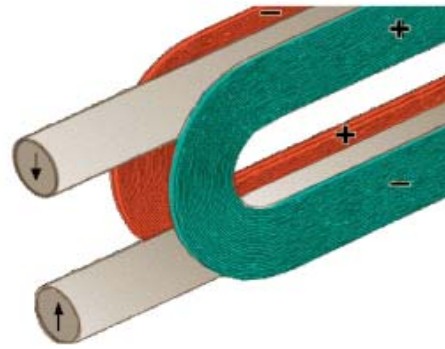


Fig. 1-17 Sketch of Common coil magnet

### **1.8 Current state of the art $Nb_3Sn$ accelerator magnets**

At present, research and development of  $Nb_3Sn$  accelerator magnets is largely carried out by three USA government laboratories [46] and by a European Joint Research Activity named NED (Next European Dipole) [47].

The USA laboratories are: Fermi National Accelerator Laboratory (FNAL), Lawrence Berkeley National Laboratory (LBNL) and Brookhaven National Laboratory (BNL); these labs beyond having a base High Field Magnet (HFM) program [48], are also collaborating within the framework of the US LHC Accelerator Research Program (LARP) on the development of  $Nb_3Sn$  quadrupoles for the LHC luminosity upgrade (foreseen in 2015) [49].

NED is supported by a collaboration of eight partners: CCLRC/RAL (UK), CEA (France; coordinator), CERN (International), CIEMAT (Spain), INFN-Genova and INFN-Milan (Italy) Twente University (Netherlands), and Wroclaw University of Technology (Poland). The main goal of NED is to build a large aperture (88 mm) high field (15 T conductor peak field) dipole magnet model in preparation for a luminosity upgrade of LHC. At present NED is not proceeding at full speed because of funding problems [47].

The efforts of the magnet R&D groups in US labs are mostly focused on the LARP project. Their goal is to demonstrate by 2009 that  $Nb_3Sn$  magnets are a viable

choice for an LHC Interaction Region upgrade. By that date a 4 m long quadrupole with a 90 mm aperture and a gradient  $> 200\text{T/m}$  it is planned to be built and tested.

### 1.9 High Field Magnet program at Fermilab

Beside LARP which is a recent project, there has been a strong HFM program ( $\text{Nb}_3\text{Sn}$ ) at FNAL since 1999 [50]. It is largely due to the experience and maturity of the FNAL base program that at present the LARP collaboration is confident that it will build successful magnets avoiding limitations due to thermo-magnetic instabilities [51, 52, 53, 54, 55, 56, 57, 58, 59].

Since 1999 at FNAL 18  $\text{Nb}_3\text{Sn}$  dipole magnets were built; these magnets belong to 5 different design configurations. Tab. 1-3 summarizes the main characteristics for each magnet configuration: the coil design (cos- $\theta$  or racetrack in the common coil configuration); if the coil was wound first and then reacted (W/R) or vice versa reacted first and then wound (R/W); the bore aperture; the number of strands in the Rutherford cable; the number of cable turns per coil; the strand diameter.

Tab. 1-4 shows the electromagnetic design parameters for the different types of magnets: the maximum current and magnetic field; the inductance and the stored energy in the magnet per length unit.

**Tab. 1-3 Types of  $\text{Nb}_3\text{Sn}$  dipole magnets built at Fermilab**

	Coil design	Technology	Bore aperture [mm]	Magnet length [m]	Strand per Cable	Number of turns	Strand Diameter [mm]
<b>HFDA</b>	Cos-theta	W/R	43.5	1	28	48	1
<b>HFDB</b>	Com. coil	R/W	none	1	41	28	0.7
<b>HFDC</b>	Com. coil	R/W	40	1	59	58	0.7
<b>HFDM 1-3</b>	Cos-theta	W/R	none	1	28	24	1
<b>HFDM 4&amp;5</b>	Cos-theta	W/R	none	1	39	37	0.7
<b>SR</b>	Com. coil	W/R	none	0.3	28	26	1

**Tab. 1-4 Electro-magnetic design parameters at 4.5 K of Fermilab magnets**

	Max Current [kA]	Max Field [T]	Inductance [mH/m]	Stored Energy [kJ/m]
<b>HFDA</b>	21	12	1.29	310
<b>HFDB</b>	14	9	0.33	34
<b>HFDC</b>	24	10	2.95	820
<b>HFDM 1-3</b>	25	11	0.47	146
<b>HFDM 4&amp;5</b>	13	11	1.1	93
<b>SR</b>	28	11	0.05	19

Four magnets, 3 race tracks (HFDB01-03) [60, 61, 62], and 1 common coil (HFDC01) [68], were built using the react and wind approach where the coils are wound after the cable has been formed.

The racetrack magnets consist of two flat racetracks coils, connected in a common coil configuration. These magnets did not have a bore and their purpose was to develop and optimize the fabrication technique and to study the conductor performance for the subsequent common coil magnet. The coils were supported by a bolted mechanical structure, Fig. 1-18. For the first racetrack an internal tin based conductor produced by IGC was used; for the other two a MJR conductor by OST.

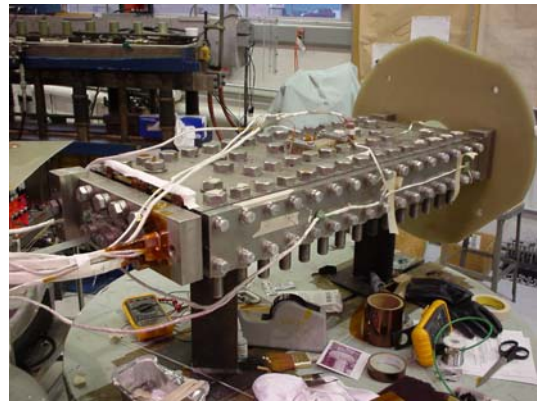
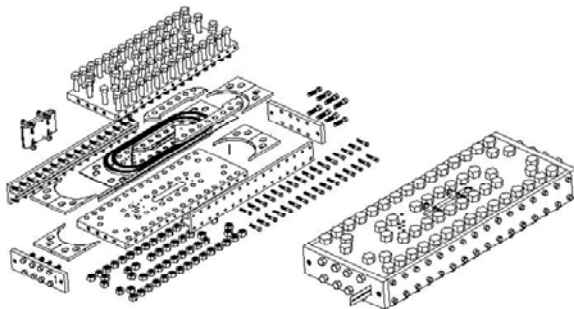


**Fig. 1-18 HFDB01 the first ‘race track’ coil design magnet**

The common coil magnet was a 1-m model designed to generate nominal field of 10 T at 4.5K in two 40 mm apertures. The coils were single layer racetrack, enclosed in a laminated collar structure and impregnated with epoxy. Fig. 1-19 shows a picture and a

drawing of common coil magnets. The wide separation of the two apertures allows for a wide bends in the ends thus making it possible to employ a conductor with the react-and-wind approach.

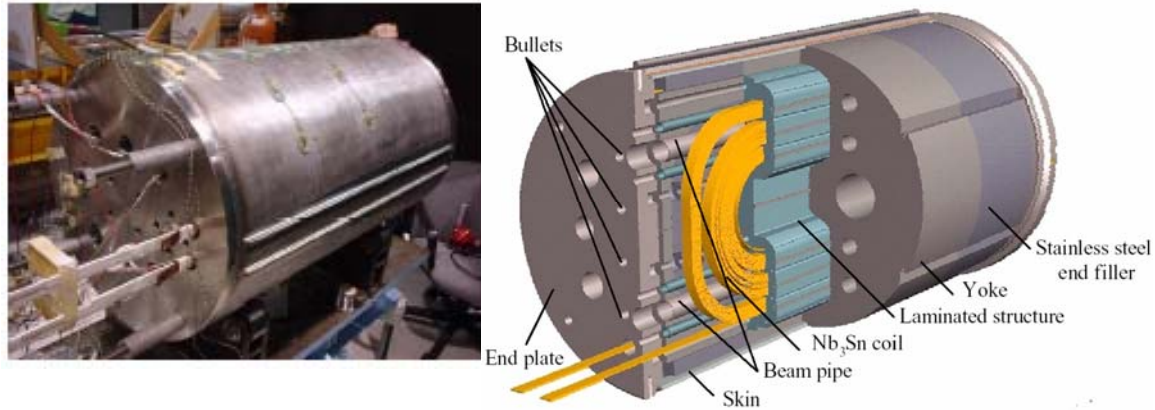


**Fig. 1-19 HFDC01 the the first double aperture race track**

All the other magnets were built using the wind and react approach; this approach will be also used for the LARP magnets.

Tab. 1-5 shows the conductor properties of the superconducting strands used for building the Fermilab magnets based on the wind and react approach: the strand type (MJR, PIT, RRP); the effective filament size; the residual resistivity ratio measured on the magnet ; and the critical current at 12 T measured on short sample strands.

**Tab. 1-5 Strand properties of Fermilab Nb<sub>3</sub>Sn magnets based on the wind and react approach**

	Strand type	D <sub>eff</sub>	RRR	<i>j<sub>c</sub></i> @ 12 T
<b>HFDA 02</b>	MJR	110	5	1700
<b>HFDA 03</b>	MJR	110	5	1880
<b>HFDA 04</b>	MJR	110	5	1730
<b>HFDA 05</b>	PIT	50	113	1620
<b>HFDA 06</b>	PIT	50	150	1310
<b>HFDA 07</b>	PIT	50	43.5	1310
<b>HFDM 01</b>	MJR	110	5	1880
<b>HFDM 02</b>	MJR	110	6	1800
<b>HFDM 03</b>	PIT	50	84	1620
<b>HFDM 04</b>	RRP	80	20	2400
<b>HFDM 05</b>	RRP	80	39	2200
<b>SR01</b>	PIT	50	129	1730
<b>SR02</b>	MJR	110	125	1700
<b>SR03</b>	RRP	80	170	2400

At Fermilab 6 cos- $\theta$  dipoles (HFDA02-07) [63, 50, 64, 65] were built and tested. The cos- $\theta$  dipoles were 1-meter models whose design is based on the two-layer shell-type coil with a 43.5 mm bore and cold vertically-split iron yoke. Fig. 1-20 and Fig. 1-21 show the full assembly and a cross section of a FNAL cos- $\theta$  dipole.

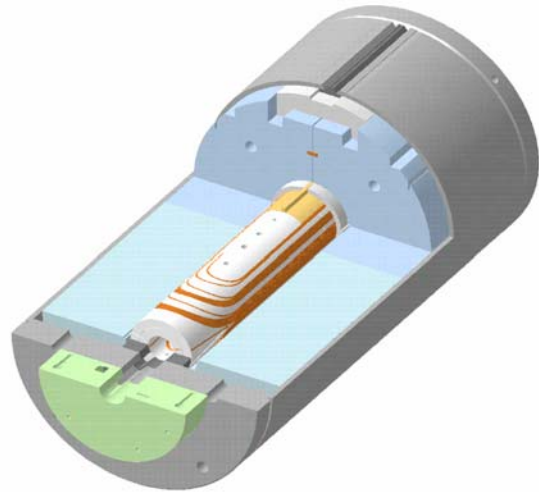
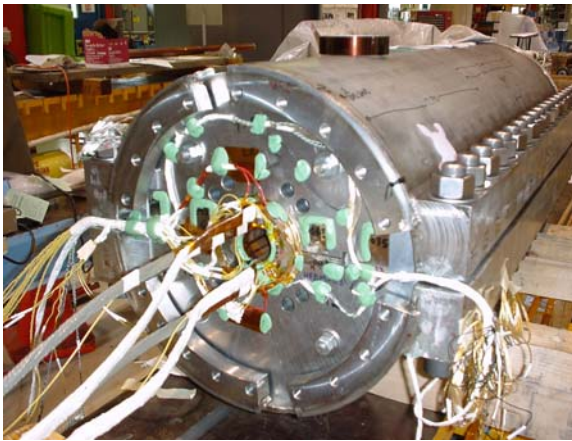


**Fig. 1-20 Full assembly of a FNAL cos-  $\theta$  dipole**

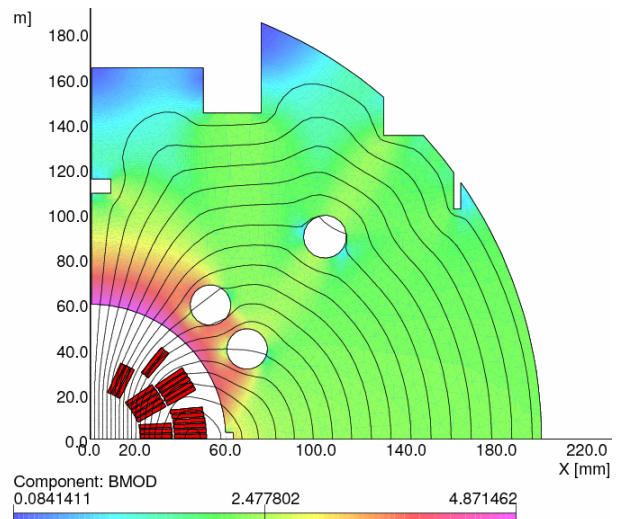
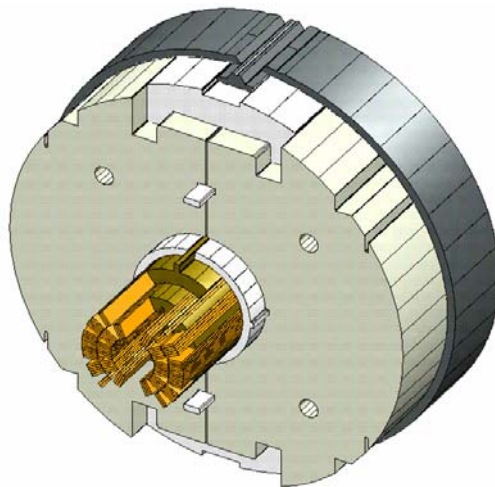


**Fig. 1-21 Cross sections of a FNAL cos-  $\theta$  dipole**

Five ‘mirror’  $\cos\theta$  dipoles [64, 65, 66, 67,] were also built and tested at Fermilab. The mirror dipoles have the same configurations as the  $\cos\theta$  dipoles. They use the same mechanical structure with either a vertically or horizontally split yoke in which one of the two half-coils is replaced with an iron half-cylinder (magnetic mirror), Fig. 1-22. The details of the magnet design and technology are described in [66]. The mirror magnet configuration was chosen because it is less expensive, and allows shorter fabrication time (allowing a more expeditious study of the cause of the poor quench performance observed in the first dipole magnets, HFDA-02 through 04).

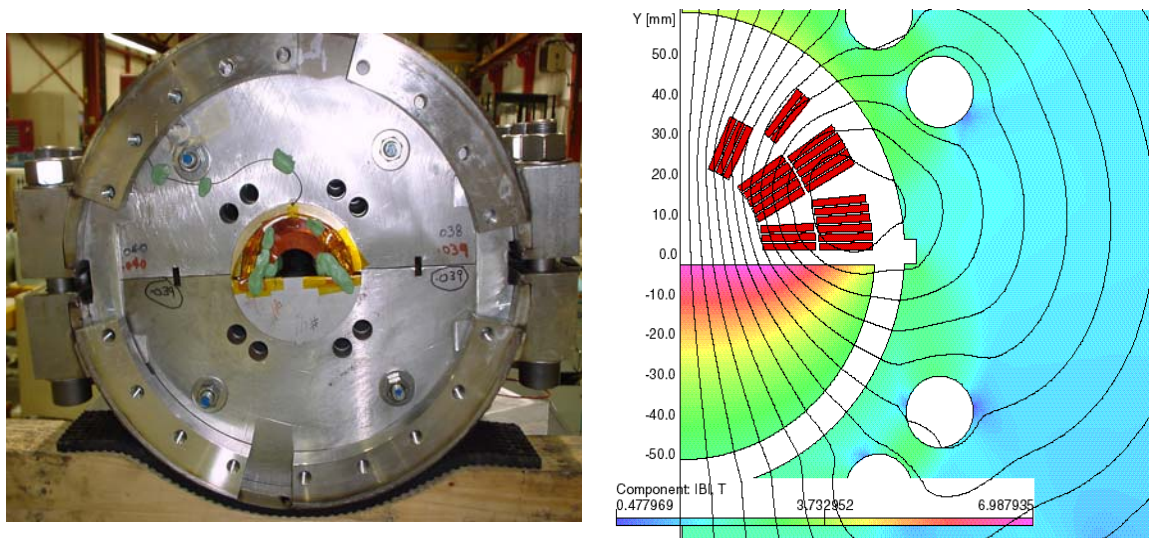


**Fig. 1-22 FNAL mirror magnet**

At Fermilab the small-race track design was developed to study cable performance. Three small racetrack coils were fabricated and tested (SR01-03) [69]. The FNAL SR is made by one double layer racetrack coil. The two layers are arranged in a common coil configuration. The support of the coil is based on the mechanical structure developed at LBNL for subscale models. A general layout, showing the internal magnet components, is shown in Fig. 1-23. The main goal of this work is to test full-size  $\text{Nb}_3\text{Sn}$  cables using compact coil systems that employ  $\text{Nb}_3\text{Sn}$  magnet technology and real cable operating conditions. Fig. 1-24 shows how the SR coil and the whole assembly looks like.

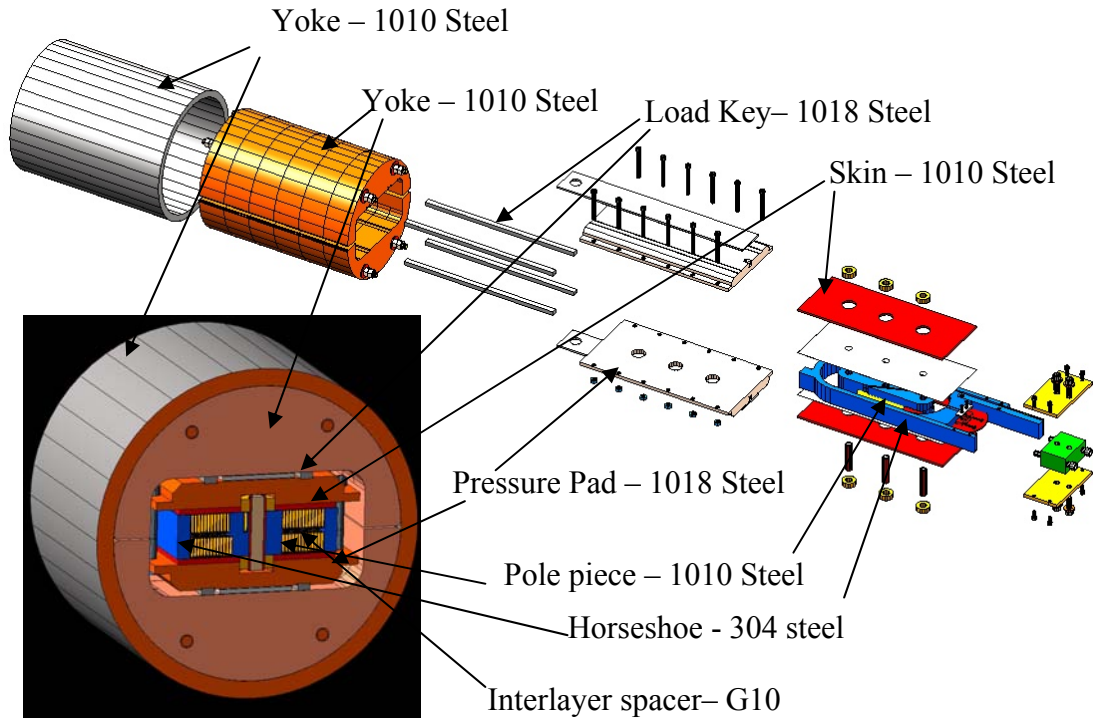


**Fig. 1-23 Small Racetrack magnet**

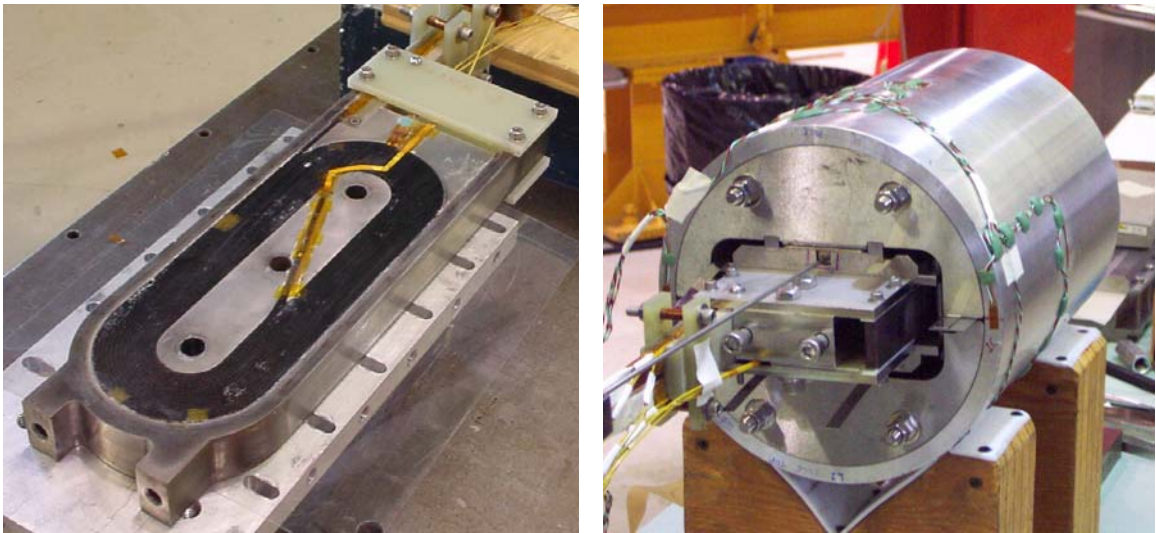


**Fig. 1-24 Small Racetrack magnet: coil and full assembly**

## 1.10 Scope of the thesis

At the time the research for this thesis started, all the high field magnets built at Fermilab exhibited limited performance. All these magnets were built using MJR strands by OST (only exception was HFDB01). In particular the  $\cos\theta$  magnets, made with 1 mm strands, quenched at a current which was ~50-60% of the nominal value.

After extensive research the principal suspect for this quench behavior was identified as conductor thermo-magnetic instabilities. Although strand measurements showed that MJR strands were unstable at low magnetic fields, the quench current value could not explain the magnets premature quenches.

The questions addressed by this research are:

- Were the magnets limited by thermo magnetic instabilities?

Magnet test results (chapter 3) show that premature quenches were due to sudden magnetic flux changes (flux jumps) in the conductor. The heat released by flux jumps were the reasons for the premature quenches.

- Were the quench currents of a  $\text{Nb}_3\text{Sn}$  strand with high- $j_c$  limited by thermo-magnetic instabilities?

Strand test results (chapter 4) shows that they were thermo-magnetically unstable and that under particular conditions the quench current values were very low. This value was comparable with quench current per strand values of low performing magnets.

- What are the mechanisms that produce flux jumps in strands?

Measuring strand voltage signals with a fast data acquisition system (chapter 4) two types of flux jumps were identified; they were produced by two different thermo-magnetic instability mechanisms ('self-field' and 'magnetization' instabilities).

- What is the minimum current at which a strand can have a premature quenches due to thermo-magnetic instabilities?

Chapter 5 shows a semi-analytical model that simulates this minimum current for different physical conditions of the strand taking into account both thermo-magnetic instability mechanisms ('self-field' and 'magnetization' instabilities).

## Chapter 2 – Superconducting magnet instabilities

A quench for a superconducting magnet is an irreversible transition from a non-resistive to a resistive state, in the sense that the magnet can not go back to its superconducting state if the current is not decreased.

Normally a magnet quenches when in the highest magnetic field region the cable current gets to its critical current value. At this point a further increase of the current produces heat dissipation; since the heat dissipation rises steeply with the current and the critical current decreases with the temperature, the high field region will soon reach the critical temperature. The normal zone will then propagate irreversibly to the rest of the magnet.

When the magnet quenches without reaching the conductor critical current it is said to have: a *premature* quench or current *degradation*.

In this chapter the following topics are described:

- current degradation due to energy releases within the coils (*disturbances*);
- type of disturbances (*local* and *distributed* disturbances);
- origins of the disturbances (*mechanical* and *thermo-magnetic instabilities*);
- conservative criteria to prevent thermo-magnetic instabilities (the *adiabatic* criteria);
- the dynamic effect on the thermo-magnetic instabilities;
- stability of a magnet made of a thermo-magnetic unstable conductor.

### 2.1 Degradation and training

At a certain operating temperature, the expected quench current of superconducting magnets is estimated by the magnet *load line* and the conductor critical current. The load line represents the relationship between the maximum transverse magnetic field in the coils and the value of the current which is flowing in the magnet.

The conductor critical current is estimated using critical current measurements of short samples and an appropriate scaling law (chapter 4). Generally, when the magnet conductor is a cable made out of strands, the short sample is a small piece (~1 m) of

strand (chapter 1 & 4). The estimate of the conductor critical current also takes into account that the cabling process reduces the strand performance.

The intersection between the magnet load line and the conductor critical current gives the estimated quench current value,  $I_{SS}$  (Short Sample). Fig. 2-1 shows the load line and the expected critical current for a  $Nb_3Sn$  small race-track magnet (chapter 1). In this

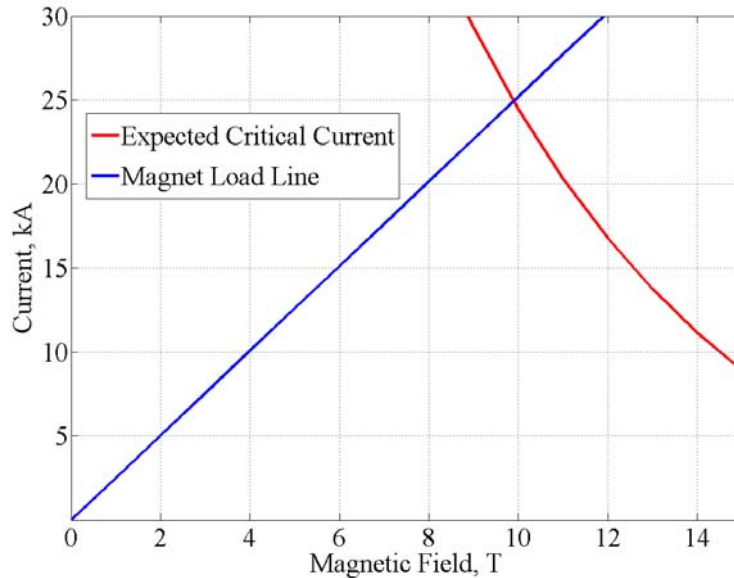


**Fig. 2-1 Expected quench current value**

case, the expected quench current was about 25 kA.

The performance of superconducting wires, when wound into magnets, can be worse than expected from results of tests on short samples of superconductor. This effect is named *coil degradation*.

A special case of degradation is observed during the first quenches of the magnet: the magnet shows a progressive improvement in performance after repeated quenching. This phenomenon, named *training*, is shown in Fig. 2-2 where the ratio between the quench current and  $I_{SS}$  is plotted as a function of the number of the quenches performed.

Degradation and training are usually caused by the release of energy within the magnet as the current and the field are increased. Temperatures are raised locally, causing the critical current of the superconductor to be reduced. If this reduced critical current is less than the current which is actually flowing, ohmic heating will ensue, probably causing a quench.

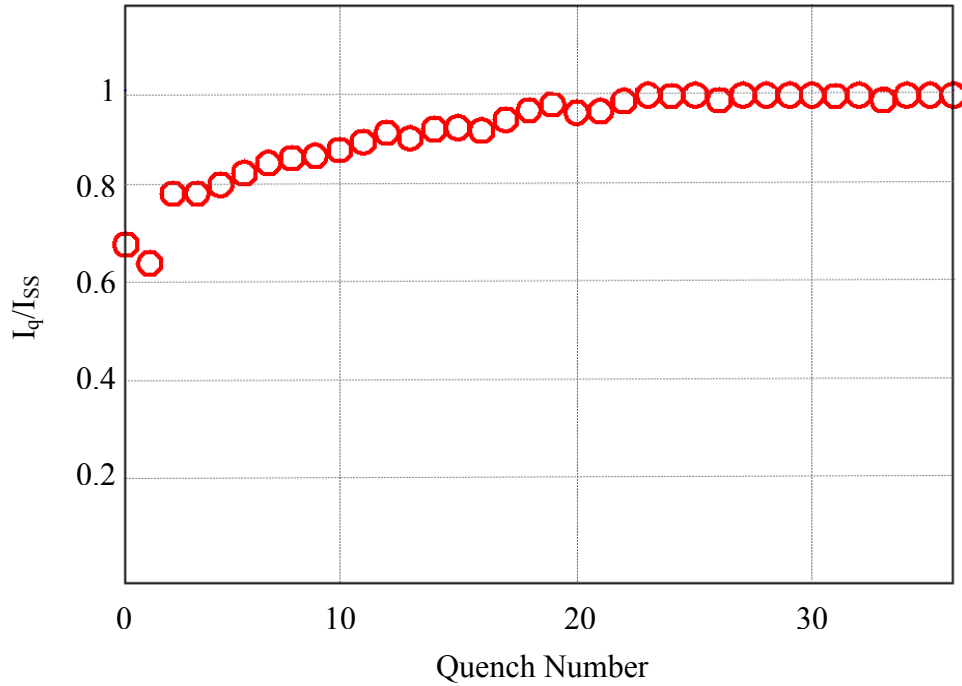


**Fig. 2-2 Training: progressing increase in quench current after repeated quenching**

These releases of energies can be divided in two categories: continuous and transient releases. Continuous disturbances are usually quite regular and reproducible; an example is excessive a.c. losses. These effects are generally well understood, and they should not provide serious problem in developing an adequate magnet design. Much more problematic are transient energy releases; the major sources of these disturbances are thermo-magnetic instabilities and conductor motion.

## **2.2 Type of disturbances**

In order to evaluate the relation between the amount of energy released and the degraded quench current value it is useful to divide the transient disturbances into distributed and local disturbances. In case of distributed disturbances the heat does not diffuse along the cable so the relevant value which determines the quench current it is not the total energy but the energy density.

In the case of an insulated composite strand, the maximum temperature,  $T_M$ , that the strand can stand without quenching after a distributed energy release, follows the relation:

$$\boxed{J_{ave} = J_e(T_M)} \quad eq. 2-1$$

where  $J_{ave}$  is the average current density which is flowing in the strand ( $=I/A$ ) and  $J_e$  is the engineering critical current density (critical current divided by the strand total cross section). Defining  $\lambda$  as the volume superconductor fraction in the strand, this implies:

$$J_e = \lambda J_c$$

Making the hypothesis that the critical current density varies linearly with the temperature from the bath temperature (4.2 K for boiling helium at 1 atm) to the critical temperature,

$$J_c(T) = J_{c0} \left( \frac{T_c - T}{T_c - T_0} \right) \quad J_e(T) = J_{e0} \left( \frac{T_c - T}{T_c - T_0} \right),$$

the  $T_M$  temperature can be calculated from eq. 2-1:

$$J_{ave} = J_{e0} \left( \frac{T_c - T_M}{T_c - T_0} \right) \Rightarrow T_M = T_c - \frac{J_{ave}}{J_{e0}} (T_c - T_0) \quad \text{eq. 2-2}$$

At 12 T for a 1 mm MJR strand with a  $J_c$  of 2000 A/mm<sup>2</sup>, the critical temperature is about 11 K. For a critical temperature,  $T_c$ , equal to 11 K and a bath temperature,  $T_0$ , equal to 4.2 K, in order to reach 90% of the critical current ( $J_{ave}/J_{e0} = 0.9$ ), according to eq. 2-2 the internal distributed disturbance should not increase the temperature above 4.88 K. This increase of temperature corresponds to an energy density of about 2140 J/m<sup>3</sup>.

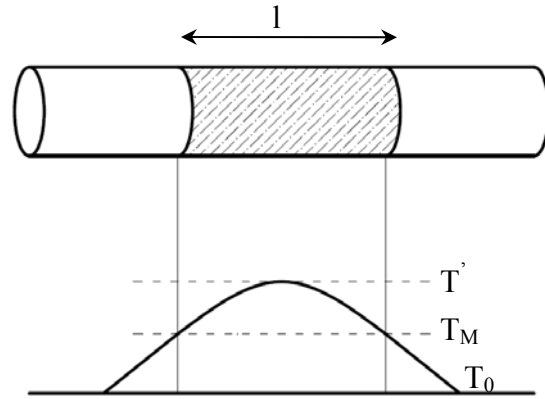


**Fig. 2-3 Temperature distribution in a strand after a disturbance**

If the amount of energy released is slightly higher than this threshold value, the strand will start to be resistive and as it is thermally insulated the temperature will increase further. An avalanche process will be established where the temperature is rising and the current will flow more and more in the strand matrix also increasing the power generation. When the temperature reaches  $T_c$ , practically all the current will flow in the strand matrix since the normal electrical resistivity of the superconductor is extremely high (for Nb<sub>3</sub>Sn  $2.7 \cdot 10^{-7}$  ohm m [23] that is more than 10 times higher than the copper resistivity at 300 K).

In order to quantify what it means to have distributed disturbance for a strand that is thermally insulated, assume that some energy is uniformly released over a finite strand length, increasing in that section the temperature above  $T_M$ . Some heat will diffuse along the strand and some other will be generated where  $T > T_M$ . After an initial transitory, the temperature profile will be characterized by a central part with an almost parabolic shape. This central part of length  $l$ , Fig. 2-3, is resistive and the temperature is maximum in the center,  $T'$ , and minimum and equal to  $T_M$  at the ends. For a specific  $l$  value,  $l_M$ , the temperature profile will not change; if the length were shorter the strand would recover while if it were longer the strand would quench.

If the disturbance covers a region which is much larger than  $l_M$  heat conduction effects will be negligible and the disturbance can be considered distributed. For this particular case, the value  $l_M$  represents the Minimum Propagating Zone (MPZ). More in general the MPZ is the smallest region where the current density in the superconductor is slightly higher than the critical current density and the Joule heating is capable of maintaining the quench propagation.

To estimate the  $l_M$  value, a condition of a thermal equilibrium between the heat generated for joule effect and the heat that will diffuse along the strand will be imposed. Assuming a uniform heat generation per unit volume,  $G$ , and that the heat will diffuse entirely along the copper because its thermal conductivity it is more than three orders of magnitude higher than  $Nb_3Sn$  thermal conductivity ( $0.04 \text{ W m}^{-1} \text{ K}^{-1}$ ), the balance equation will be:

$$\boxed{2k_{Cu}A(1-\lambda)\frac{(T' - T_M)}{l_M} = A \cdot l_M \cdot G} \quad \text{eq. 2-3}$$

where  $A$  is the strand cross section. In order to calculate  $G$ , it will be assumed that  $T \leq T_c$ .

When the current density in a superconductor is raised above its critical value, the superconductor develops a resistance and the electric field,  $E$ , rises steeply. Neglecting a small transition region around the critical current value, the current voltage characteristic can be approximated assuming  $E=0$  for current density lower than  $j_c$ , and for higher values, a differential resistivity  $dE/dJ = \rho_f$ . This differential resistivity is known as the flux-flow resistivity because it is associated with the motion of flux vortices through the superconductor. Flux-flow resistivity is a function of temperature and magnetic field; it is

always less than the resistivity of the superconductor when in normal state but it is always very much greater than the resistivity of copper.

In a composite conductor above its critical current, the current divides between copper and superconductor. As the copper resistivity is much lower than the flux-flow resistivity, even if the electric field is not zero, the current density in the superconductor will be practically equal to the critical current density. The current density associated with the electric field will generate a power per unit volume,  $G$ , equal to:

$$G = J_{ave} \cdot E \quad E = \rho_{Cu} J_{Cu} \quad J_{ave} = (1 - \lambda) J_{Cu} + \lambda J_c \rightarrow G = J_{ave} \cdot \rho_{Cu} \frac{J_{ave} - \lambda J_c}{(1 - \lambda)}$$

Assuming a linear dependence of the critical current density with the temperature gives

$$G = \frac{J_{ave} \cdot \rho_{Cu}}{(1 - \lambda)} \left\{ J_{ave} - \lambda J_{c0} \left( \frac{T_c - T}{T_c - T_0} \right) \right\}.$$

Substituting eq. 2-2

$$G = \frac{J_{ave} \cdot \rho_{Cu}}{(1 - \lambda)} \left\{ J_{ave} - \frac{J_{ave}}{\left( \frac{T_c - T_M}{T_c - T_0} \right)} \left( \frac{T_c - T}{T_c - T_0} \right) \right\}$$

$$G = \frac{J_{ave}^2 \cdot \rho_{Cu}}{(1 - \lambda)} \left\{ 1 - \left( \frac{T_c - T}{T_c - T_M} \right) \right\} \rightarrow \boxed{G = \frac{J_{ave}^2 \cdot \rho_{Cu}}{(1 - \lambda)} \left( \frac{T - T_M}{T_c - T_M} \right)} \quad eq. 2-4$$

Making the hypothesis that  $T = T'$  ( $T_M \approx T'$ ) and introducing eq.2-4 in eq. 2-3:

$$2k_{Cu}(1 - \lambda) = l_M^2 \cdot \frac{J_{ave}^2 \cdot \rho_{Cu}}{(1 - \lambda)} \left( \frac{1}{T_c - T_M} \right) \rightarrow \boxed{l_M = \left[ 2k_{Cu}(1 - \lambda)^2 \frac{(T_c - T_M)}{J_{ave}^2 \cdot \rho_{Cu}} \right]^{0.5}} \quad eq. 2-5$$

Assuming  $T_M \sim 4.2$  K,  $k_{Cu} \sim 50$  Wm<sup>-1</sup>K<sup>-1</sup>,  $\rho_{Cu} \sim 2 \cdot 10^{-9}$  Ωm (copper with RRR 10 at 4.2 K and 12 T),  $\lambda \sim 0.5$ ,  $J_{ave} \sim 900$  A mm<sup>-2</sup> ( $I/I_c = 0.9$   $J_c = 2000$  A mm<sup>-2</sup>) and  $T_c \sim 11$  K, the value of  $l_M$  is  $\sim 0.3$  mm.

In case of local energy release the important factor is the value of the total energy released and it is not relevant how this energy is spatially distributed. A disturbance is local if it affects a region that is smaller than the Minimum Propagating Zone. A local disturbance will not quench the sample if the released energy is not big enough to

develop a MPZ. The minimum amount of energy which is necessary to develop the MPZ is usually named Minimum Quench Energy (MQE).

For local disturbances, even if the superconductor gets normal, the strand can still recover if the heat can axially diffuse faster than it is generated. This is not possible for large disturbances. In order to overcome this problem Stekly with his coworkers introduced cryogenic stabilization in superconducting magnet design. It allowed building magnets capable of recovering after a distributed normalizing perturbation.

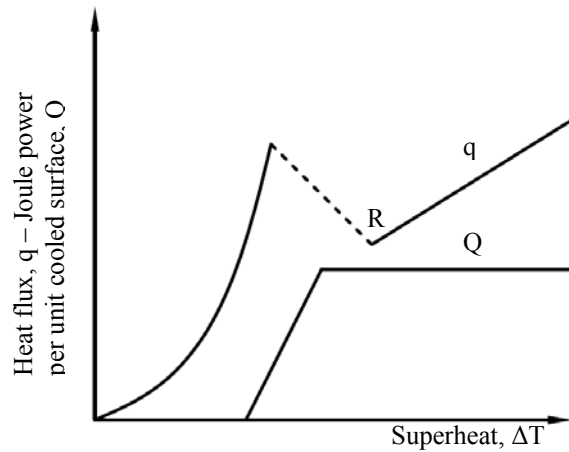


Fig. 2-4 Stekly stable configuration [70]

The general principle is that the superconductor is joined along its entire length to a conductor of low resistivity (usually copper) with a much greater cross sectional area. If for any reason the superconductor stops conducting, current switches to the copper where it generates heat. By means of cooling channels in the magnet, the copper is sufficiently well cooled that the heat dissipation into the helium is faster than the joule heat generation. In particular the Stekly criterion is based on the idea that for any increase of temperature due to a disturbance, the joule power generation is lower than the heat escaping in to the helium:

$$\alpha = \frac{\lambda^2 J_c^2 \rho_{Cu} A}{(1 - \lambda) P \cdot h (T_c - T_0)} < 1 \quad \text{eq. 2-6}$$

where  $h$  is the heat transfer coefficient to the helium and  $P$  is the conductor wet perimeter.

Fig. 2-4 shows the Joule heat generation and the heat flux to the helium as a function of the variation of the conductor temperature,  $\Delta T$ , respect to the helium bath ( $\Delta T = T - T_0$ ) in a Stekly

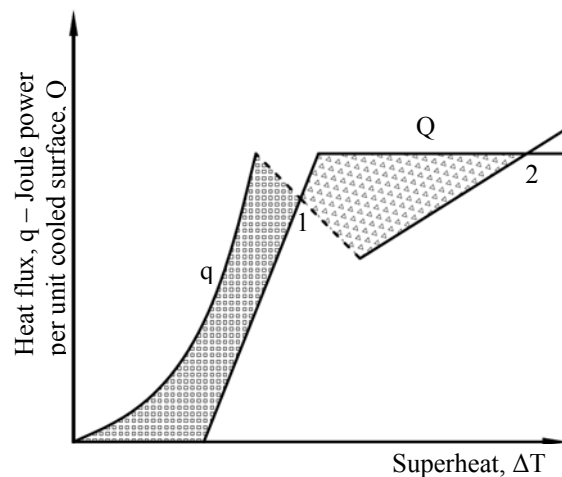


Fig. 2-5 Maddok stable configuration [70]

stable configuration. It can be noted that the heat flux curve is characterized by three regions: the nucleate boiling, the transition and the film boiling regions. The transition region is represented with a dashed line because it is an unstable region: an infinitesimal perturbation will make the system jump in the film boiling or nucleate boiling region.

The power generation increases linearly from  $T_M$  to  $T_c$  and then it gets constant because all the current it is flowing into the copper; for the Stekly criterion this curve has to be below the heat flux curve for every  $\Delta T$  generated by an external perturbation.

A less restrictive criterion which still guarantees the stability is the one based on the famous equal-areas theorem by Maddok and others. Under specific conditions the power generation curve can cross the heat flux curve and the magnet being still stable.

Taking as reference Fig. 2-5, the magnet will immediately recover if the superheat due to the perturbation is lower than  $\Delta T_1$ , while for bigger perturbation the conductor will reach the equilibrium status where the superheat is  $\Delta T_2$ . The equal-areas theorem demonstrates that the magnet is stable and it will get back to the bath temperature if the net area between the generation and cooling curves is zero, the thermal conductivity is not a function of the temperature, and the large normal zone is enclosed by cold superconductor. For the last assumption of the criterion, this stability condition is often called 'cold end' recovery condition.

The equal area theorem can be generalized to the case where the thermal conductivity is a function of the temperature; the stability will be guaranteed if:

$$\int_{T_0}^{T_2} \{q(T) - Q(T)\} \cdot k(T) dT = 0$$

Cryogenics stabilization works well and indeed has made possible all the large superconducting magnets in operation today. Its big drawback is the large amount of copper and cooling channels required to satisfy cryogenic stabilization. This is possible for detector magnets, while for accelerator magnets a way is needed to reduce degradation without diluting  $J_e$  too much.

### **2.3 Disturbances origins**

In order to stabilize superconducting magnets without using the cryogenic stabilization is to limit the energy released by disturbances. There are two disturbance

sources: mechanical and thermo-magnetic instabilities. These instabilities are sudden releases of mechanical or electromagnetic potential energy stored in the winding during magnet energization.

### **2.3.1 Mechanical instabilities**

Large stresses are present in the winding of a magnet due to Lorentz forces, magnet pre-compression, and materials with different thermal contraction coefficients. If a crack occurs, part of the energy associated with the stresses is released.

Many observers have recorded creaks, cracks, and groans while energizing the magnets. They have generally found a progressive increase in the sound amplitude and rate of incidence up to the point at which the magnet quenches. Such sounds may have large components in the ultrasonic region (Nomura and others found a peak of intensity at frequency around 800 kHz). Cracks are probably the most serious mechanical instability and the primary reason for magnet training.

Another possible source of disturbances is conductor motion. A strand, under Lorentz forces, can be held in place by frictional forces; increasing the current in the magnet causes the electromagnetic force to become larger than the restraining force. The strand then moves for a distance  $\delta$  before being stopped by friction or impact against another strand. The work done by the magnetic field is dissipated in heat; a motion of the order  $1\mu\text{m}$  is enough to induce a quench. The problem of wire movement has been solved by impregnating the coil with resins.

On the other hand, the use of organic impregnates, of which epoxy resins are the most popular choice, increases the possibility of cracks, since they are quite brittle and there is a significant difference in thermal contraction between organic materials and metals.

### **2.3.2 Thermo-magnetic instabilities in type II superconductors**

Fig. 2-6 shows the field distribution (continuous line) for a semi-infinite superconducting (type II) slab, initially not magnetized, when an external magnetic field, parallel to the slab surface is ramped up from 0 T to  $B_s$ . The  $x$  axis represents the distance from the slab surface. The magnetic field at the slab surface is equal to the external field

$B_s$ . Inside the superconductor the field decreases linearly (using the Bean's model of the critical state, for details see 1.2.5) reaching 0 T at a distance  $L$  from the slab surface.

This field distribution is due to currents which are flowing perpendicular to the plot in the layer between  $x=0$  and  $x=L$ . In this 'critical-state' layer the current flows at the critical current density.  $L$ , which is the width of the critical-state layer, is named penetration depth.

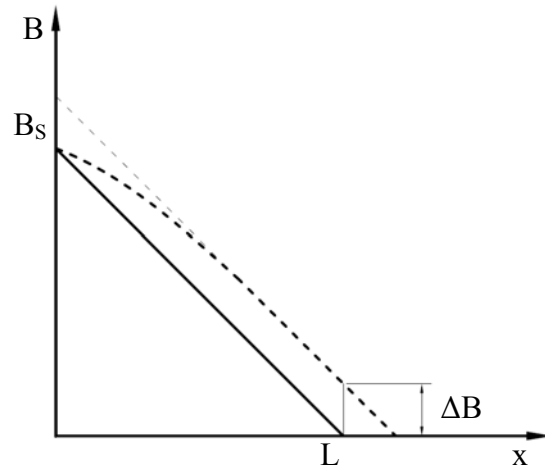


**Fig. 2-6 Magnetic field distribution in a semi-infinite slab: field parallel to the slab surface**

More generally, a long cylindrical superconductor (type II) has always in its section an external 'critical-state' layer once it has been exposed to a changing transverse external field. The magnetic field in the critical-state layer varies linearly with a slope that is proportional to the critical current density. The value of the magnetic field at the superconductor surface is equal to the external magnetic field.

The 'critical-state' layer, which screens the internal part of the superconductor from the variation of the external magnetic field, is the main source of thermo-magnetic instabilities. Indeed, a perturbation of the magnetic field inside the critical state layer that brings the field closer to the external field will produce heat. In the slab case of Fig. 2-6 the perturbation is indicated by the dashed line.

This heat will warm up the superconductor, reducing the critical current density; this current reduction will change further the magnetic field distribution in the superconductor.

If the field variation associated with the reduction of the screening current is bigger than the initial field perturbation, the superconductor is unstable; it reacts to the initial perturbation with a bigger perturbation.

In general, a superconductor is thermo-magnetically unstable if a perturbation (an infinitesimal energy deposition in the superconductor) will cause a finite change in the magnetic flux distribution in the superconductor – a flux jump.

In the thesis, the terms perturbation and disturbance will be always used to identify an infinitesimal and a finite amount of energy respectively.

## **2.4 Thermo-magnetic instabilities: the adiabatic criteria**

The distribution of the current in a ‘critical-state’ layer produces an electromagnetic energy stored in the superconductor. The most secure way to avoid quenches due to the release of this potential energy is to have a stable superconductor.

The next paragraphs illustrate the calculation of the stability criterion for the semi-infinite slab case showed in Fig. 2-6 using the most conservative approach (adiabatic model). It will also be shown how this criterion is not followed for Nb<sub>3</sub>Sn strands.

Using the Bean model of the critical state ( $j_c$  independent of local magnetic field) the penetration depth  $L$  is:

$$L = \frac{B_s}{\mu_0 j_c} \quad \text{eq.2-7}$$

An instantaneous infinitesimal field penetration,  $\Delta B$ , will cause energy dissipation per unit volume,  $\Delta Q'''$ , which can be approximated by [71]:

$$\Delta Q''' = E \cdot j_c \cdot \Delta t \approx \Delta B(L - x) \cdot j_c \quad x \leq L$$

$$\Delta Q''' = 0 \quad x > L$$

Assuming the process adiabatic the temperature variation of the superconductor is:

$$\Delta T = \frac{\Delta Q'''}{\nu} = \frac{\Delta B(L - x) \cdot j_c}{\nu} \quad x \leq L$$

where  $\nu$  is the volumetric specific heat.

Since the critical current density is temperature dependent, there will be a corresponding fall in current density:

$$\Delta j_c = \frac{dj_c}{dT} \frac{\Delta B}{\nu} (L - x) \cdot j_c$$

Associated with this fall in current density there will be an increase of the magnetic field in the superconductor, and for  $x=L$ , this increase,  $\Delta B_j$ , is [71]:

$$\Delta B_j = \mu_0 \left| \frac{dj_c}{dT} \right| \frac{\Delta B}{\nu} j_c \frac{L^2}{2}$$

The slab will be stable if:

$$\Delta B_j \leq \Delta B \rightarrow B_s \leq \sqrt{2\mu_0\nu} \frac{j_c}{\left|\frac{dj_c}{dT}\right|} \quad \text{eq. 2.8}$$

This is the famous adiabatic stability criterion by Hancox for a semi-infinite superconducting slab. The term adiabatic is not used here in the sense that the superconductor is insulated from the environment, but in the sense that the phenomenon is so fast that also the thermal diffusion inside the superconductor is negligible. The criterion provides the magnetic field at which a perturbation will cause a flux jump. Substituting eq. 2.7 in eq 2.8 the criterion can be written

$$\beta = \mu_0 \left|\frac{dj_c}{dT}\right| \frac{L^2}{\nu} j_c \leq 2 \quad \text{eq. 2.9}$$

The parameter  $\beta$  characterizes spontaneous heating of the superconductor by external perturbations.

The solution obtained by Hancox is based on an approximation for the calculation of the energy dissipation per unit volume,  $\Delta Q'''$ , ( $\Delta B(x) = \Delta B$ ). The exact solution of the adiabatic case was obtained first by Swartz and Bean [72]:

$$B_s < B_{FJ} = \frac{\pi}{2} \sqrt{\mu_0 j_c \nu / \left|\frac{dj_c}{dT}\right|} \quad \text{eq. 2.10}$$

$$\beta = \mu_0 \left|\frac{dj_c}{dT}\right| \frac{L^2}{\nu} j_c \leq \left(\frac{\pi}{2}\right)^2 \quad \text{eq. 2.11}$$

For example Nb<sub>3</sub>Sn at 4.2K has the following properties (based on a MJR strand with a non-copper  $j_c$  of 1800A/mm<sup>2</sup> at 4.2 K and 12 T):

$$j_c(12T) = 2500 \text{ A mm}^{-2} \quad j_c(1T) = 36600 \text{ A mm}^{-2}$$

$$\left|\frac{dj_c}{dT}\right|_{12T} = 450 \text{ A mm}^{-2} \text{ K}^{-1} \quad \left|\frac{dj_c}{dT}\right|_{1T} = 2310 \text{ A mm}^{-2} \text{ K}^{-1}$$

$$\nu(12T) = 4460 \text{ J K}^{-1} \text{ m}^{-3} \quad \nu(1T) = 1780 \text{ J K}^{-1} \text{ m}^{-3}$$

Substituting these values in eq. 2.10:  $B_{FJ}(12T)=0.28T$  and  $B_{FJ}(1T)=0.3T$ ; in general for any type II superconductor the value  $B_{FJ}$  is almost independent of the magnetic field. For  $Nb_3Sn$  the first flux jump may appear above  $\sim 0.3T$ .

In the case of a finite slab of width equal to  $2a$ , the eq. 2.10 is valid till  $a \geq L$ , for higher values of  $L$ , it is easy to demonstrate that eq. 2.11 it is still valid substituting  $L$  with  $a$ . Since the critical current density and its derivative with respect to the temperature are decreasing with the magnetic field, the most critical situation for a finite slab is at the total penetration field  $B_p$  when  $L=a$ . The slab will be always stable if at  $B_p$  it is stable. Hence, it can be concluded that at fixed temperature, a finite superconducting slab will be stable if:

$$\mu_0 \left| \frac{dj_c}{dT} \right| \frac{a^2}{\nu} j_c \leq \left( \frac{\pi}{2} \right)^2 \quad \text{for} \quad B = B_p = \mu_0 j_c(B_p) \cdot a$$

At 1 T and 4.2 K, for  $Nb_3Sn$  using the previous values and eq. 2-7 it comes out that a slab with  $a=22\mu m$  is fully penetrated; a slab of such half-width would have  $\beta \sim 29$  and it would not satisfy the adiabatic criterion. At 1 T, in order to respect this criterion, a  $Nb_3Sn$  slab should be smaller than  $6.5 \mu m$ . This value is much smaller than the filament size of high  $j_c$   $Nb_3Sn$  superconducting strands.

It is important to notice that the adiabatic criteria were derived by assuming the presence of perturbations; in the case of disturbances, even if the adiabatic criteria are satisfied, flux jump may still occur.

The adiabatic stability criteria for the slab were derived assuming that the external magnetic field was ramped up from 0 T. The same criteria are also valid in the case that the transport current is ramped up. Indeed, when ramping up the current, once again a critical state layer is formed at the superconductor surface carrying the transport current, and if the adiabatic stability criteria are not respected, flux-jumps may occur.

## ***2.5 Thermo-magnetic instabilities: the dynamic effect on the stability criteria.***

The adiabatic criteria give an extremely tight restriction to the conductor size needed to avoid flux jumps. This section shows a less restrictive criterion which takes into account the dynamic effect of thermal diffusion inside the conductor. These criteria

are derived by linearizing the full set of the equations which describe thermo-magnetic instabilities, including the thermal diffusion [73, 74, 75, 76, 77, 78]. Also presented will be how these criteria affect the strand design.

## 2.5.1 Thermo-magnetic instability: linearization of the equations

The linearization of the equations describing thermo-magnetic instability allows analysis of the initial development of the instability and derivation of the stability criteria not only in the adiabatic case, but also in a dynamic one.

The equations adopt the Bean's model of the critical state assuming that  $j_c(T, B) = j_c(T, B_s)$  where  $B_s$  is the magnetic field at the conductor surface. The stability of the critical-state for an arbitrary dependence of  $j_c$  on  $B$  has been analyzed elsewhere [74, 77]. The thermal balance and Maxwell equations describing thermo-magnetic instabilities in superconductors are:

$$\nu(T) \frac{\partial T}{\partial t} = \nabla \cdot [\kappa(T) \nabla T] + \vec{j} \cdot \vec{E} \quad \text{eq. 2-12}$$

$$\vec{\nabla} \times \vec{E} = -\mu_0 \frac{\partial \vec{j}}{\partial t} \quad \text{eq. 2-13}$$

The constitutive equation of the superconductor electrical properties is:

$$\vec{j} = \frac{\vec{E}}{E} [j_c(T, B_a) + j_n(T, B_a, E)] \quad \text{eq. 2-14}$$

For the linear analysis, the solutions are written in the following form:

$$T(\vec{r}, t) = T_b(\vec{r}, t) + T_c \theta \left( \frac{\vec{r}}{L} \right) \exp \left( \frac{\lambda t}{t_k} \right) \quad \text{eq. 2-15}$$

$$\vec{E}(\vec{r}, t) = \vec{E}_b(\vec{r}, t) + \frac{k(T_0) T_c}{j_c(T_0) L^2} \vec{\varepsilon} \left( \frac{\vec{r}}{L} \right) \exp \left( \frac{\lambda t}{t_k} \right) \quad \text{eq. 2-16}$$

$T_b$  and  $\vec{E}_b$  are the temperature and electric field which act as background field for small perturbations.  $\theta$  and  $\vec{\varepsilon}$  are dimensionless small perturbations of temperature and electric field;  $L$  is the characteristic length of critical state layer;  $t_k$  is the characteristic time of heat-flux diffusion:  $t_k = L^2 \nu / k$ .

The temperature and the electric field right after the perturbation will be named  $T_0$  and  $E_0$ . It will be assumed that:

$$T_0 \approx T_b = T_{coolant} \quad \frac{dT_{coolant}}{dt} = 0$$

$$\frac{d\vec{E}_b}{dt} = 0$$

The linearized form of eq. 2-14 is:

$$\vec{j} = \frac{\vec{E}}{E} \left[ j_c(T, B_a) + \left. \frac{\partial j_n}{\partial E} \right|_{T_0 E_0 B_a} dE \right] = \frac{\vec{E}}{E} [j_c(T, B_a) + \sigma dE] \quad eq. 2-17$$

$\sigma$  is the differential conductivity of the superconductor right after the perturbation. Substituting eqs. 2-15, 2-16, 2-17 in eqs. 2-12 and 2-13 the linearized form of the problem is obtained:

$$\lambda \theta = \nabla^2 \theta + \varepsilon \quad eq. 2-18$$

$$\vec{\nabla} \times \vec{\varepsilon} = \lambda \beta \theta \vec{e} - \lambda \tau \vec{\varepsilon} \quad eq. 2-19$$

$$\vec{e} = \vec{\varepsilon} / \varepsilon \quad \beta = \left( \mu_0 \frac{L^2}{\nu} j_c \left. \frac{dj_c}{dT} \right|_{T_0} \right) \quad \tau = \left. \frac{t_m}{t_k} \right|_{T_0 E_0} = \frac{L^2 \mu_0 \sigma}{L^2 \nu / k} \Big|_{T_0 E_0} = \left. \frac{\mu_0 \sigma k}{\nu} \right|_{T_0 E_0}$$

In eq. 2-18 and 2-19, the differentiation is performed with respect to the dimensionless coordinate  $r/L$  and,  $\tau$  is the ratio between the characteristic time of magnetic flux diffusion,  $t_m$ , and the characteristic time of heat flux diffusion,  $t_k$ .

In order to determine the eigenvalue  $\lambda$  of eq. 2-18 and 2-19, the thermal and electro-dynamic boundary conditions have to be imposed. Once they are introduced, a linear set of equations is obtained and the eigenvalue  $\lambda$  can be calculated by imposing that the kernel is not zero. The critical state is unstable when the real part of  $\lambda$  is bigger than zero, eq. 2-15 and 2-16.

## 2.5.2 Stability criteria and the role of $\tau$

For the slab problem presented in the previous section, assuming that the thermal diffusivity is much less than the magnetic diffusivity ( $\tau \ll 1$ ), the stability criteria derived by eq. 2-18 and 2-19 is

$$\beta \leq \beta_c = \left(\frac{\pi}{2}\right)^2 \left[1 + 2\sqrt{\tau}\right] \quad \text{eq.2-20}$$

if the slab surface is thermally insulated.

If the slab has an isothermal boundary condition the criterion is:

$$\beta \leq \beta_c = \left(\frac{\pi}{2}\right)^2 \left[1 + 3\left(\frac{4\tau}{\pi^2}\right)^{\frac{1}{3}}\right] \quad \text{eq.2-21}$$

In the case of infinite magnetic diffusivity,  $\tau$  is equal to zero and the eq. 2-20 and 2-21 become equal to the adiabatic criteria eq. 2-11. Assuming for Nb<sub>3</sub>Sn at 1 T:

$$k \sim 0.04 \text{ W m}^{-1} \text{ K}^{-1}$$

$$\sigma = \sigma_f(1T) \sim 10^8 \Omega^{-1} \text{ m}^{-1}$$

$$\nu = 1780 \text{ J K}^{-1} \text{ m}^{-3},$$

$\tau$  is  $2.8 \cdot 10^{-3}$  and the value  $\beta_c$ , according to

eq. 2-20, is about 10% higher than the value obtained by the adiabatic criteria.

The difference between  $\beta_c$  in the adiabatic, eq. 2-20, and isothermal, eq. 2-21, boundary conditions is very limited (10-25% with  $\tau \sim 10^{-4}$ - $10^{-1}$ ); this means that when  $\tau \ll 1$  the flux jumping is weakly dependent on the heat transfer conditions.

The distribution of the temperature and electric field variation ( $\delta T$ ,  $\delta E$ ) during the first stages of a flux jump in a slab with  $\tau \ll 1$  are showed in Fig. 2-7 for adiabatic boundary conditions, and in Fig. 2-8 for isothermal boundary conditions.

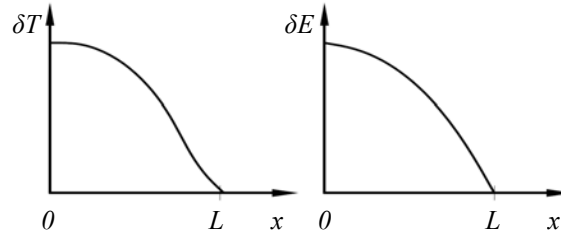


Fig. 2-7 Distribution of  $\delta T$  and  $\delta E$  during the first stages of a flux jump in a slab with  $\tau \ll 1$  and adiabatic boundary conditions [23]

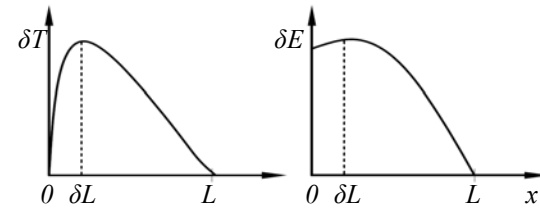


Fig. 2-8 Distribution of  $\delta T$  and  $\delta E$  during the first stages of a flux jump in a slab with  $\tau \ll 1$  and isothermal boundary conditions [23]

In general the linear analysis leads to the following conclusion:  $\beta_c \sim 1$  for  $\tau \ll 1$  and  $\beta_c \gg 1$  for  $\tau \gg 1$ . The improved stability with increasing  $\tau$  is due to the better capability of the critical state layer to diffuse away the heat produced after a perturbation.

### 2.5.3 Design of stable strand

Taking in to account this result, the practical solution to have a stable superconductor is to realize a composite strand made of twisted small superconducting filaments embedded in a metal matrix with good thermal and electrical conductivity.

The size of each filament has to satisfy the criteria for  $\tau \ll 1$ . Twisting the filaments avoids their acting as a single big filament with respect to variation of the background field Fig. 2-9.

The strand acts as a monofilament also in the case of changing fields generated by the transport current. In that case, the width of the critical-state layer has to satisfy the stability criteria for  $\tau \gg 1$ . Indeed the physical properties of this big ‘monofilament’ are a combination of the matrix and superconductor properties.

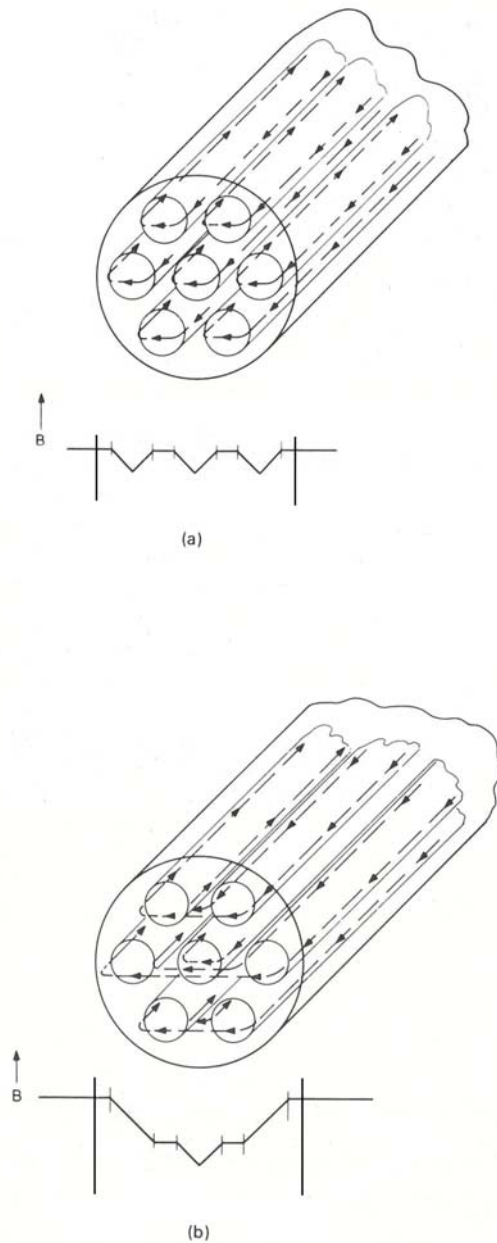


**Fig. 2-9 (a) Composite conductor in which the filaments are not coupled together by the background field; (b) the same conductor with filaments completely coupled [22]**

Choosing properly the matrix material and the strand geometry,  $\tau$  can be much larger than one and yet the stability criteria can be satisfied even for large dimension of the critical-state layer.

Fig. 2-10 shows the schematized cross section of a composite strand and the distribution of the magnetic field produced by the transport current. The hatched parts are generally made of copper while the white part is composed by superconducting filament embedded in a matrix generally made of copper. The transport current flows between  $c$  and  $R$  perpendicular to the drawing. The width of the critical-state layer in this case will be then  $R-c$ .

#### 2.5.4 Non linear electric conductivity and dynamic effect

The considerations regarding the strand design in the previous section are based on the implicit assumption that during the instability the differential electric conductivity of the superconductor is equal to that one of the flux flow regime. This assumption is the most conservative, and so is the best one for strand design. Indeed if the electric field in the superconductor right after the perturbation,  $E_0$ , were lower than  $E_f$  ( $\sim 10^4 \text{V/m}$ ), the differential electric conductivity would be much higher and the superconductor would be much more stable.

Since it is always possible having a perturbation that increases the electric field above  $E_f$  (for example a fast variation of the external magnetic field), it is not secure to base the superconductor stability on the hypothesis of high differential conductivity of the superconductor.

In this thesis a superconductor will be named stable if it is not subject to flux jumps even in the case of perturbations which lead the superconductor to be in the flux flow regime.

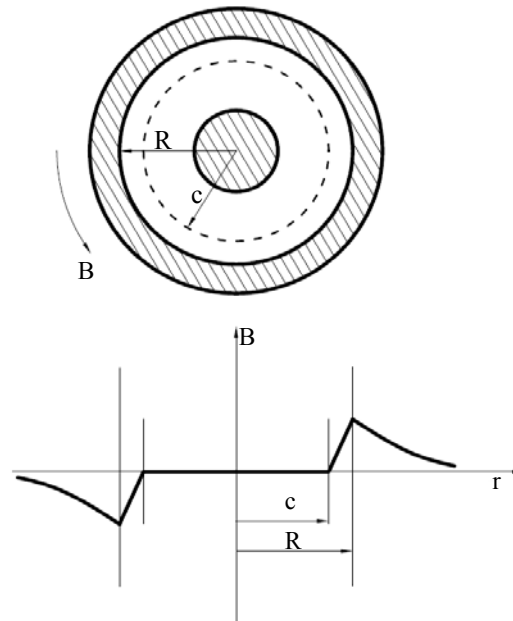


**Fig. 2-10 Distribution of the magnetic field produced by the transport current in a composite strand; the transport current flows between  $c$  and  $R$  perpendicularly to the drawing**

## 2.6 Stability of a magnet made of an unstable superconductor

At present Nb<sub>3</sub>Sn strands for high energy physics superconducting magnets can not follow the stability criteria because the  $j_c$  is extremely high and there are technological problems to make sufficient small filaments. For these reasons it has to be accepted that these strands may have flux jumps. On the other hand, it is not necessary to completely eliminate flux jumping in order to achieve stable strand performance [79].

The criteria for superconductor stability are based on a differential approach which analyzes the development of the perturbation using the assumption that the properties of the superconductor are constant. Actually these properties change significantly; the volumetric specific heat increases drastically with temperature: from 4.2 K to  $T_c$ , depending on the magnetic field, it can increase more than 2 orders of magnitude. The increase of specific heat improves the superconductor stability, thus there are some situations in which a flux jump can start at  $T_0$  but stop before  $T$  reaches  $T_c$ . These are called partial flux jumps.

A partial flux jump can take place in the strand without quenching the transport current. While superconductor stability theory became more and more sophisticated in the 70s' 80s' and 90s', the study of the maximum current that could be withstood by a superconductor affected by thermo-magnetic instabilities has not developed much since Hancox proposed his model in 1968 [79].

In this section its model will be presented. The model analyzes a slab, fully magnetized and with transport current. The distribution of the magnetic field is shown in Fig. 2-11 [79]; the slab width is equal to  $D$ .

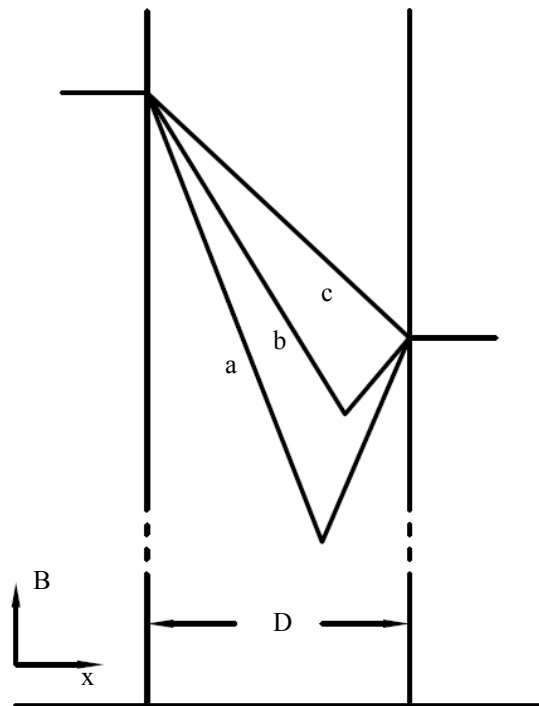


Fig. 2-11 Field distribution in a slab with transport current

The field distribution is based on Bean's model of the critical state and on the assumption that temperature is uniform in the whole slab. While the slab is stable, the superconductor will be in the critical state and there will be a field minimum as in distribution *a* in Fig. 2-11; the critical current density at the helium temperature will be referred to as  $J_1$ . If flux motion is unstable, the superconductor will be heated, and the critical current density will fall, leading to a new profile, distribution *b*. The limit case is when the temperature rises to the point at which the superconductor can only just carry the current, corresponding to distribution *c*. The critical current density in the field distribution *c* will be named  $J_2$ . The limiting condition is given by:

$$\Delta Q = \frac{\pi D^2}{6} \left\{ J_1^2 - J_2^2 + 6J_2^2 \ln \left( \frac{J_1}{J_2} \right) \right\} \leq \int_{T_1}^{T_2} \nu dT \quad \text{eq. 2.22}$$

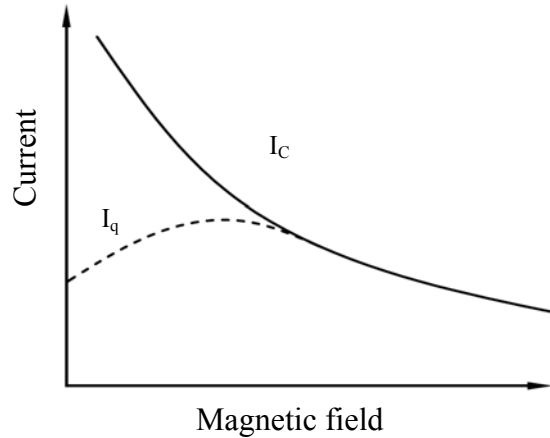


Fig. 2-12 Calculated quench

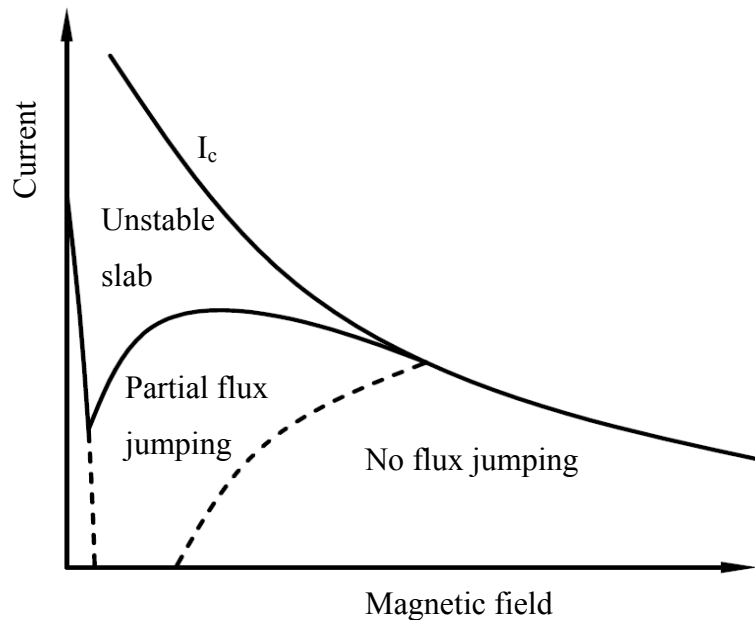


Fig. 2-13 Flux jump in semi infinite slab

where  $\Delta Q$  is the amount of heat per unit volume released by the flux motion and  $v$  is the volumetric specific heat. Fig. 2-12 shows the solution of eq. 2.22; the plot shows the critical current and the calculated degraded current [79].

The equation 2.22 does not take into account that when ramping the field up from 0 T, the field is not fully penetrated initially. Considering this phenomenon, the quench current curve assumes the shape shown by the lower continuous line in Fig. 2.13 [80]. The other continuous line represents the critical current.

In this plot the terms unstable refer to the transport current. The region where the transport current is unstable is a region where thermo-magnetic instability may lead to current quench.

The dashed line divides the region where the conductor is thermo-magnetically unstable (where may have flux jumps) from the region where it is stable.

It is interesting to note that the quench current has minimum in the low field region. If this minimum has a current value which is lower than the magnet nominal current, the magnet could be unstable and it could quench at a current that is lower than the nominal current. This is due to the fact that different parts of the magnets have different load lines. The design load line is associated to the magnet region where the magnetic field is maximum; this load line has the smaller slope. In the magnets, there will be a low field region whose load line passes through the minimum current value.



## Chapter 3 – Magnet test results

The first Nb<sub>3</sub>Sn magnets built and tested at Fermilab exhibited limited performance due to premature quenches. Quench studies excluded all other possible causes of these magnets' behavior leaving as a potential explanation conductor thermo-magnetic instabilities (flux jumps). This idea was also supported by the observation of voltage spikes while ramping up the current in the magnets [81]; voltage spikes could have been generated by partial flux jumps.

In this chapter are presented the main magnets' experiments performed to confirm this hypothesis. Using small race track magnets, cables with different sensitivities with respect to thermo-magnetic instabilities were tested and the quench performance compared with the cable critical current. During the test of the suspected thermo-magnetically unstable cable an ad hoc system built to monitor voltage spikes was also used.

Since the small race track tests supported the idea of thermo-magnetic instabilities limiting magnets performance, cos- $\theta$  Nb<sub>3</sub>Sn magnets based on a more stable conductor were built and tested. Even though the conductor was not perfectly stable (indeed voltage spikes were still collected) these magnets reached the critical current limit.

In this chapter the following topics are described:

- The set-up of the Vertical Magnet Test Facility (VMTF) where superconducting magnets up to 4 m length are tested at Fermilab
- The Voltage Spike Detection System (VSDS), a device to capture flux variations in the magnet coils;
- Quench studies of Nb<sub>3</sub>Sn Fermilab magnets;
- Flux jump observations in Fermilab magnets before the introduction of the (VSDS);
- Instabilities studies using two small race track magnets equipped with two different conductors;
- Performance of Nb<sub>3</sub>Sn cos-theta magnets made of a more stable conductor (PIT).

### **3.1 Vertical Magnet Test Facility**

At Fermilab Nb<sub>3</sub>Sn Magnets are tested in the Vertical Magnet Test Facility. This facility has three major components: a dewar capable of working between 1.8 and 4.4K with helium at 1 atm; a high current power system capable of providing 30 kA; hardware and software for controlling and monitoring the dewar, the power supply, and the magnet instrumentation.

#### **3.1.1 Vertical dewar**

The dewar is designed for magnets up to 4 m length and 620 mm diameter, Fig. 3-1. The inner vessel containing the helium (helium shell), the heat exchanger, and tubing are surrounded by an 80 K thermal shield (liquid nitrogen cooled). All these components are contained in a vacuum vessel. The vacuum vessel flange rests on the top of the concrete-lined pit and serves as the vessel support.

The helium volume is divided by an insulator plate (lambda plate) in two chambers: the upper one contains liquid and vapor helium at 4.3 K; the lower chamber, where the magnet is located, contains liquid helium at 1.8-4.4 K and 1.2 atm. The temperature of the volume below the lambda plate is controlled by a built-in heat exchanger. This heat exchanger consists of 4 m long OFHC copper tubes in direct contact with the helium in the lower chamber. The temperature of the helium in the heat exchanger is controlled by a vacuum system which is capable removing 30 W of heat at 1.8 K. There are several penetrations through the lambda plate, for instrumentation, superconducting power leads and pressure relief valves. The lambda plate also supports the weight of the magnet.

The magnet assembly (which includes instrumentation tree, top plate, current leads, lambda plate, magnet, and eventually helium displacer) is inserted as an assembled unit into the inner vessel from the top. For short magnets, the helium volume can be significantly reduced by using a closed-cell foam displacer (helium displacer) connected to the magnet assembly. More details on the dewar system can be found in [82, 83].

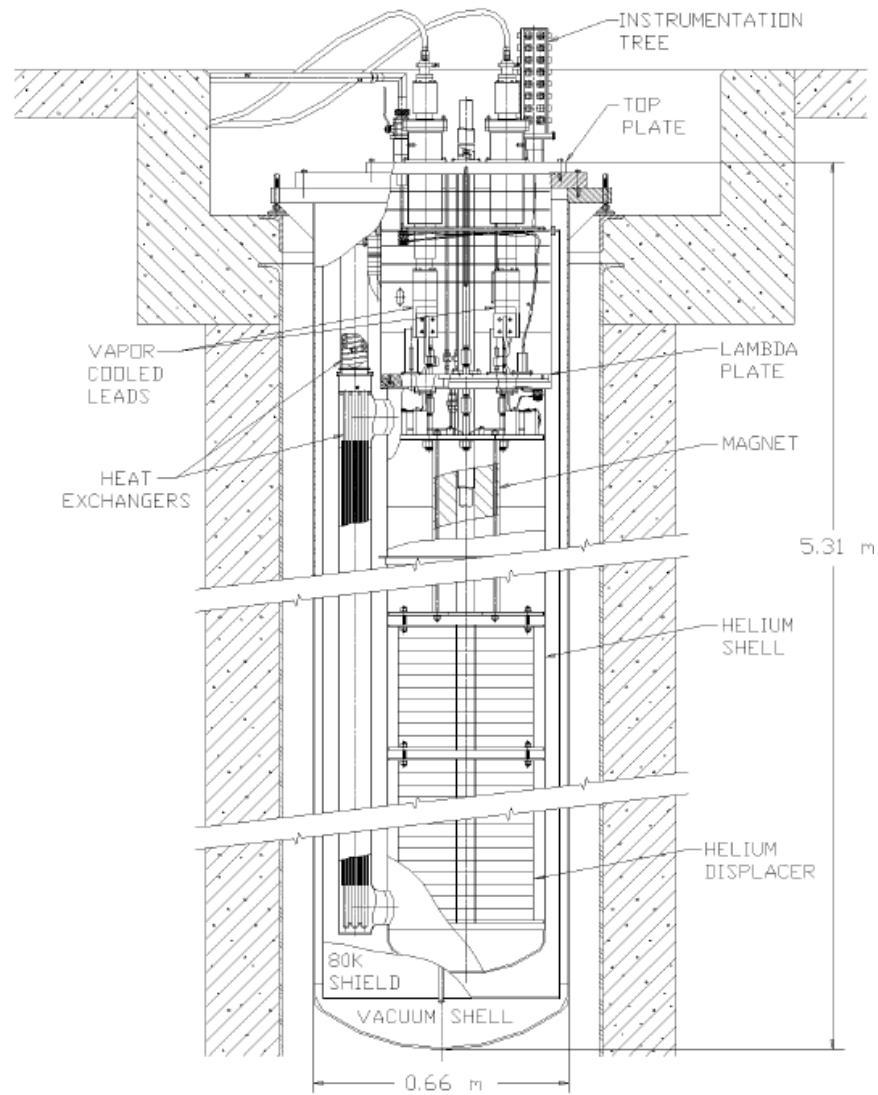


**Fig. 3-1 Sketch of the Vertical Dewar of the Vertical Magnet Test Facility at Fermilab**

### 3.1.2 30 kA power supply system

The power system as shown schematically in Fig. 3-2 consists of six power supplies, an extraction circuit (dump switches and dump resistor) and water cooled copper bus. In the figure electrical signals are shown as dashed lines [84].

The power supplies are 150 kW commercial units from Power Energy Industries (PEI); they are in a master/slave configuration. The Master Power Supply (MPS) provides the Silicon Controlled Rectifiers (SCR) firing signals for all modules. Each power supply has four firing modules with three SCRs each (one per phase), for a total of

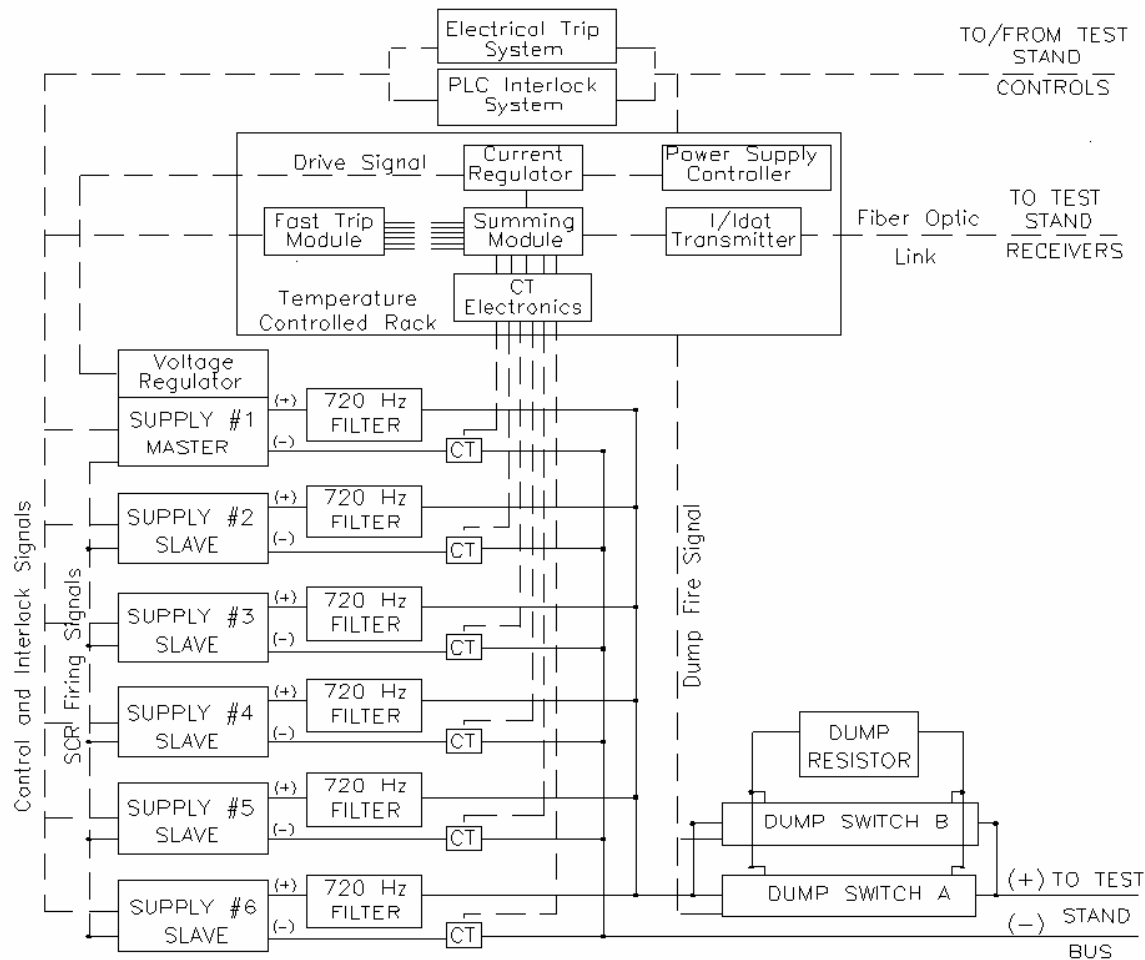


**Fig. 3-2 kA Power System Block Diagram**

12 SCRs. Current regulation is accomplished by an external precise current regulator cascaded to the MPS internal regulator set to “Voltage” mode. Each PEI supply is capable of delivering 5000 Amps dc at 30 Volts. The system is highly modular, and it can

operate with just the master supply or with the master supply plus any combination of slave supplies.

The use of SCRs to provide DC current results in a 720 Hz ripple ( $12 \times 60$  Hz) due to the twelve pulses per period. In order to reduce this ripple a Praeg style filter was designed, built, and added to each supply [84].

The extraction circuit protects the superconducting accelerator magnet after a quench. Without an extraction circuit, after a quench, practically the whole energy of the system would be dissipated in the magnet normal zones, heating the coil and generating huge turn-to-turn and coil to ground voltages. Even if the power supply stops supplying energy into the system, the energy stored in the magnet could be enough to damage the cable. Indeed, since the propagation velocity of the normal zone is usually low relative to the heating rate, the energy would be dissipated in a small region which could reach temperature values harmful to the coil materials.

At the VMTF, the stored energy extraction from a magnet is accomplished by quickly switching a load resistor in series with the bus. Fast switching is accomplished with two 15 kA 1000 V dc solid state dump switches. These switches include six SCRs mounted in water-cooled heat-sinks. The SCRs continuously carry their share of the rated current, and they are commutated off from stored energy in capacitors. Once the SCRs turn off, the bus current flows through the dump resistor connected in parallel with the dump switches. The switch opening time is approximately 25  $\mu$ s after detection of a fault or a trip command. The dump resistor, built from air-cooled stainless steel elements, is rated for a maximum current of 30 kA, a maximum energy dump of 3 MJ, and a maximum voltage across the resistor of 1000 V dc [84].

Magnets can also have protection heaters which are activated when a quench occurs in order to distribute uniformly the energy dissipated in the magnet. These heaters are activated by discharging capacitors.

### **3.2 Instrumentation and software**

Instrumentation is used to monitor cryogenics status and mechanical strain transducers detect and characterize quench propagation in the superconducting magnet, and control power supply and cryogenic operation.

Particularly important is the instrumentation for the quench detection and protection (Quench Management Hardware). For quench detection there are two systems working in parallel for redundancy: an Analog Quench Detection (AQD) system based on NIM modules [85] and a Digital Quench Detection (DQD) system [86]. These detection systems condition and compare ‘quench’ signals from the superconducting magnets under test, to user-set threshold values. When these thresholds are exceeded a quench status is set. A Fermilab built VME Quench Logic Module (QLM) [85] monitors the quench status and sets off a chain of events that controls the phase off of the power supply, the energy extraction circuit firing, and the magnet quench protection heater discharge.

The Quench Management Software manages the operation of the Quench Management Hardware and its iterations with external components such as the quench characterization hardware, which is used for capturing and characterizing magnet instrumentation data, and the quench protection heaters [85]. It also provides user settable parameters via a graphical user interface GUI. Information regarding the software monitor and controlling can be found in [87, 88, 89].

Fermilab is also using a “quench antenna” [90] to characterize quench locations in magnet models. The quench antenna is a stationary, three-section probe centered in the warm bore tube of the magnet aperture during test. The middle antenna spans much of the magnet body (coil straight section), while the two end antennas cover the magnet coil lead and return ends, respectively: antenna 1(3) is at the lead (return) end. The antenna coils are based on magnetic measurement probe winding patterns. A dipole coil on one antenna is used for alignment with the main field direction. Small gaps exist between panels for mechanical support. Each probe has four precision windings on coil forms, for detecting normal and skew quadrupole and sextapole field variations caused by current redistribution in the dipole magnet. The time and amplitude of the coil signals are used

to determine the radial and azimuthal locations of the disturbance [91]. Signals are conditioned by amplifiers with a gain of 200 and digitized by 16 bit Pentek data loggers operating at 33.3kHz sample rate when triggered; they capture data in an interval of a several hundred milliseconds around the triggering event (usually a quench, but spike study triggers have also been used to correlate antenna activity with voltage tap signals

### ***3.3 Voltage Spike Detection System***

The Voltage Spike Detection System (VSDS) is a measurement system, developed at Fermilab [90], for the detection of small magnetic flux changes in superconducting magnets, which are due to either mechanical motion of the conductor or flux jump. These flux changes are detected as small amplitude, short duration voltage spikes, which are about  $1-10^2$  mV in magnitude and lasts for few hundreds of  $\mu$ sec.

The detection system combines an analog circuit for the signal conditioning of two coil segments and a fast data acquisition system for digitizing the results, performing threshold detection, and storing the resultant data.

A superconducting magnet is generally composed by two symmetric halves and the voltage signal of interest is normally produced in the coils of one of these two halves. The VSDS monitors the two halves of the superconducting magnet. In this way the common mode signals generated outside the coil will produce similar inductive voltages across each half coil. This is important since bucking of the two half coil signals will reject common mode noise signals leaving the transient signal of interest intact. For this reason it is equally important that the two channels of the spike detection system have a matched phase and amplitude response in order to maximize common mode rejection throughout the frequency range of interest.

The detection system is able to detect transient voltages on the order of the mV in the frequency range of 0 to 30 KHz between two superconducting half coils whose inductance is from  $\sim 15$   $\mu$ H to 1 mH. The VSDS is able to measure these signals throughout the power supply range: 0 to 30 KA at 0 to 30 V and be protected up to 1 kV to ground when the magnet energy extraction resistor is enabled.

In order to prevent ground loops and protect against high common mode voltages the data acquisition system is isolated from the power system bus. In addition, the

frequency responses of the isolation amplifiers are matched in order to satisfy the bucking requirements.

The specification of the magnet voltage tap wires is also important in order to prevent both inductive and capacitive coupling with other voltage taps or the magnet. Such noise voltage is generally uncorrelated and would not be easily rejected. Therefore, the careful routing of the wires, twisting, and shielding are all specified for each magnet to be tested. The cabling of the detection system is also specified carefully to prevent ground loops, etc.

Since the half coil signals are digitally bucked the performance of the data acquisition system's analog-to-digital converters (ADC) have been chosen to have excellent gain and stability characteristics, and to sample at least twice the frequency of interest in order to satisfy the Nyquist criterion.

### 3.3.1 Hardware

The VSDS was developed using high quality components. The front-end electronics were designed and assembled in-house and the data acquisition (DAQ) system was purchased commercially. A block diagram of the spike detection circuit is shown in Fig. 3-3. Special attention was taken in selecting the passive components that determine the frequency response of both channels. This was done to assure that the two coil

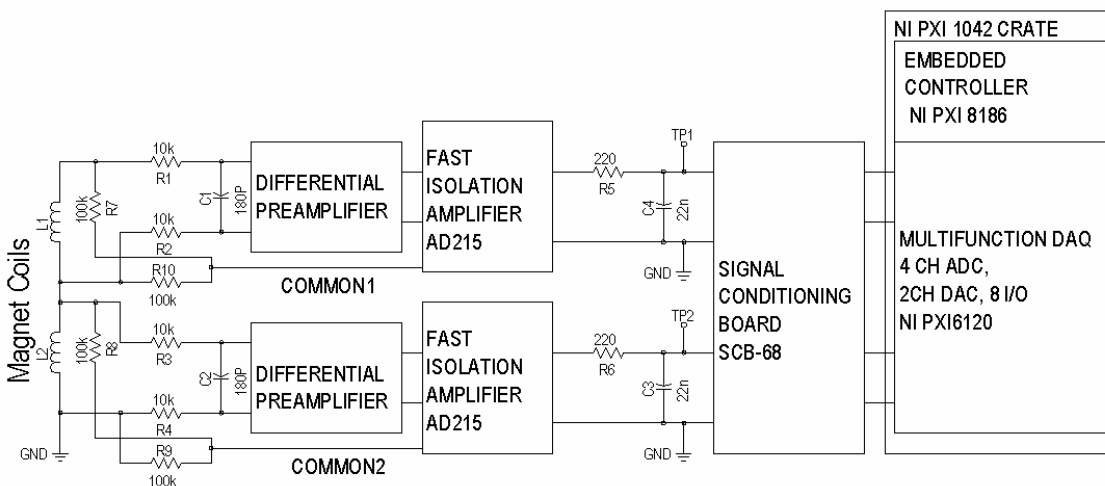


Fig. 3-3 Voltage transient "Spike" detection circuit block diagram

channels have identical temperature and time stable frequency characteristics.

The input signal is first conditioned by a low pass filter, which attenuates frequencies greater than 30 KHz and also blocks RF noise to the preamplifier preventing harmonic distortion and rectification of the signal.

The input differential pre-amplifiers provide the major amplification of the signal. The gain is jumper-selectable with the range of 5 to 100. These amplifiers were placed upstream of the fast isolation amplifiers in order to increase the signal magnitude before isolation, therefore improving the signal to noise ratio (SNR).

The isolation amplifier component chosen for this circuit is the Analog Devices AD215. It has a 1500 V isolation voltage rating, a wide bandwidth of 120 kHz, and a low harmonic distortion of -80 dB. A second filter at the output of the isolation amplifiers filters out high frequency modulation noise produced by the isolation amplifiers – typically ~2.5 mVpp (peak-to-peak voltage). Together with the input filter, this forms a 2<sup>nd</sup> order low pass filter for the input signal.

The signal-conditioning board (SCB) is commercially available from National Instruments, SCB-68, and its output is digitized by the National Instruments PXI multifunction DAQ: NI PXI-6120. This module has 4 channels of simultaneous Analog to Digital Converters (ADC), 2 channels of Digital to Analog Converters (DAC), 8 channels of input/output (I/O), and 2 counter/timers. The ADC has 16-bit resolution, built-in anti-aliasing filters, and can sample up to 800 KHz.

### **3.3.2 Software**

The software for the DAQ system is written in Labview, and runs under the National Instruments real-time environment of the PXI controller. The main purpose of this software is to perform digital bucking and triggering for data storage along with pseudo real-time visualization of the data with FFT's of the current and bucked magnet half-coil signal.

Each signal monitored by the VSIDS is recorded in a circular buffer where it is divided temporally. Each interval contains 50000 data points per signal. During the measurement the VSIDS program sequentially checks each interval, and if a voltage spike is detected the data associated with that interval are appended in a Labview binary file;

otherwise the data are removed from the circular buffer. The software saves the data if the absolute value of the bucked signal (difference of the two half coil signals) is larger than the threshold value set by the operator.

The VSDS software also allows conditioning the two half coil signals before bucking them in order to be more sensitive to voltage spikes. This signal conditioning consists of ‘balancing’ and filtering the signals. Either of these operations are optional.

The ‘balancing’ is accomplished by multiplying one of the two signals (e.g. signal 2) by an appropriate ‘gain’ factor. The gain factor is calculated to minimize the noise level of the bucked signal and it is derived using the signals of the previous temporal interval when a voltage spike was not detected. The gain is equal to the ratio of the standard deviation of signal 1 divided by the standard deviation of signal 2.

When the noise level of the bucked signal is too high with respect to the desired threshold, the operator can activate a linear phase digital band-pass filter that conditions the two half-coil signals before the bucking operation.

This filter was initially designed to reject signals below 1500 Hz and all signals beyond the bandwidth of interest, >30 kHz. It was then modified so that the low frequency threshold was 800 Hz since it was found that sometimes real spikes were not detected. Due to the high sample rate of the ADC, such a filter required 800 taps.

### 3.4 Test Results

#### 3.4.1 Quench studies of Fermilab Nb<sub>3</sub>Sn Magnets

In 2001 and 2002 Fermilab built and tested three 1m long shell-type dipole models (HFDA02, HFDA03, and HFDA04). The coils were all wound with a 28-strands Rutherford cable made of 1 mm MJR strands by OST (for more details see chapter I). A good, well understood field quality was achieved, however the quench performance of these magnets was

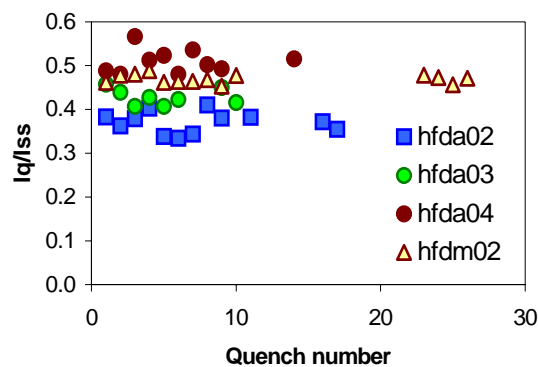


Fig. 3-4 Performances of Fermilab magnets based on 1mm MJR strands

limited: their quench currents were well below expectations. The maximum quench current was only 40-60% of expected short sample limit  $I_{ss}$  ( $B_{max} \sim 6-7$  T) [50], Fig. 3-4.

All of the quenches occurred near splices in the low field region of the coil where the Nb<sub>3</sub>Sn conductor is spliced to the NbTi cable which connects the magnet to the current leads. The quench currents were limited to 8-11 kA with no discernible training. Lowering the temperature from 4.5 K to 3.3 K did not result in any significant increase in quench current. These currents, which are far from the expected short sample limit, were suggestive of possible conductor damage in that region.

The last model, HFDA04, had an improved splice design and it was built very carefully. Developing a robust splice design and fabrication procedure was the primary purpose of building this magnet, however the quench performance of HFDA04 was still limited in the splice regions.

During the first six months of 2003, to address magnet technology and quench performance issues in an efficient way, a special half coil assembly – ‘magnetic mirror’ configuration – was used in which one of the half-coils was replaced with half-cylinder made of low carbon steel (the magnetic mirror) inside an existing magnet mechanical structure. The same type of cable and strand were used (table chapter I).

Two different mirror magnets (HFDM01, HFDM02) and a cable-and-splice assembly (HFDA03B) have been built and tested [66, 67].

Once again the quench performance was limited at the same level as the previous magnets (HFDA 02-04) but these tests demonstrated that the premature quenches were not due to joule heating in the splice region. Moreover temperature margin measurements, performed at fixed currents by using a small internal heater to increase the cable temperature until the magnet or cable quenched, showed that the cable at high temperature (above  $\sim 9$  K) quenched at the critical temperature Fig. 3-5. This meant that premature quenches at 4.5 K were not due to degradation of the cable critical current. The cable-and-splice assembly test also excluded the possibility of mechanical limitation since in the cable configuration the Lorentz forces were much smaller than the magnet configuration. The tests also showed that the current distribution between the cable’s strands was not unbalanced; hence the premature quenches were not related to the quench of a strand reaching the critical current before the other strands.

Every other possible origin for magnet premature quenches having been excluded the only remaining reasonable explanation was the conductor thermo-magnetic instability (flux-jump). Signs of partial flux jumps had actually been observed while testing some magnets.

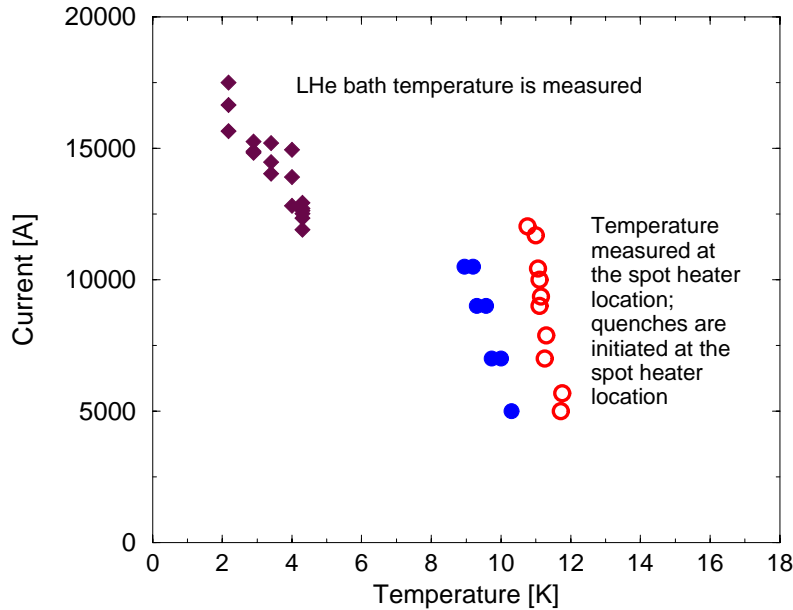


**Fig. 3-5 Temperature dependence for HFDM 01 (filled circles) and cable-and-splice assembly (open circles)**

### 3.4.2 Flux jump observations

Flux jump (thermal-electromagnetic phenomena) and mechanical motion are two primary causes of magnet instabilities. If a flux jump or mechanical motion occurs in the magnet it will generate a flux change in the coils, which can be detected either by monitoring the coil voltages or the magnetic field.

During the test of HFDB01, the first ‘race track’ coil design (for more details see chapter I), and HFDC01, the first double aperture race track magnet (for more details see chapter I), unexpected high voltage spikes were generated [92]. Although the mechanical structures of these magnets differ, all utilize Nb<sub>3</sub>Sb conductor. These spikes were so large that they occasionally tripped our quench detection circuits. At that time the VSDS had

not been developed yet and flux changes were collected with different readout systems: the Digital Quench Detection (DQD) system and the Quench Antenna.

When the voltage spikes were large enough (over 50 mV) they triggered our regular quench detection system and data were recorded. The data analyzed are from the “DQD” (digital quench detection) system, which uses a fast, multi-channel ADC to digitize quench detection signals. These data are processed in a VME-based processor where DSP algorithms are used to suppress noise. Since the data have been digitally filtered there is a group delay of 2 milliseconds and frequencies  $>300\text{Hz}$  are attenuated, changing the characteristic shape of the voltage spike signal. The DQD system records four seconds of data prior to the quench trigger. The signals used to look for spikes are the ‘bucked’ half coils where the signal from one half coil is subtracted from the other to cancel common noise.

The first attempts at ramps to quench of magnet HFDB01 were interrupted by quench detection system trips at low currents. These trips were found to be due to voltage spikes in the quench detection signals. Upon examination of these data, it was determined that the trips were not accompanied by resistive growth in the magnet and hence these events were not identified as real quenches. The quench detection thresholds were raised to avoid tripping and the test proceeded. When the first real quench was observed, however, it was found to be correlated with the presence of spikes in the voltage signals.

Many of the voltage spikes were recorded ranging from few tens of mV to few hundreds of mV. These voltage spikes were collected with quench data files. Since no special trigger was developed to capture them, consequently we were able to study only those spikes which occurred within a 4 second interval before the quench. A typical spike is shown in Fig. 3-6 for a quench when the ramp rate was 500 A/s. This spike plot displays the DQD half coil balance signal for the 4 second time interval prior to the quench trigger (defined as  $t=0$  in our system). In Fig. 3-6 it can clearly be seen that a voltage spike is associated with the onset of the quench (quench initiation region displayed as an inset).

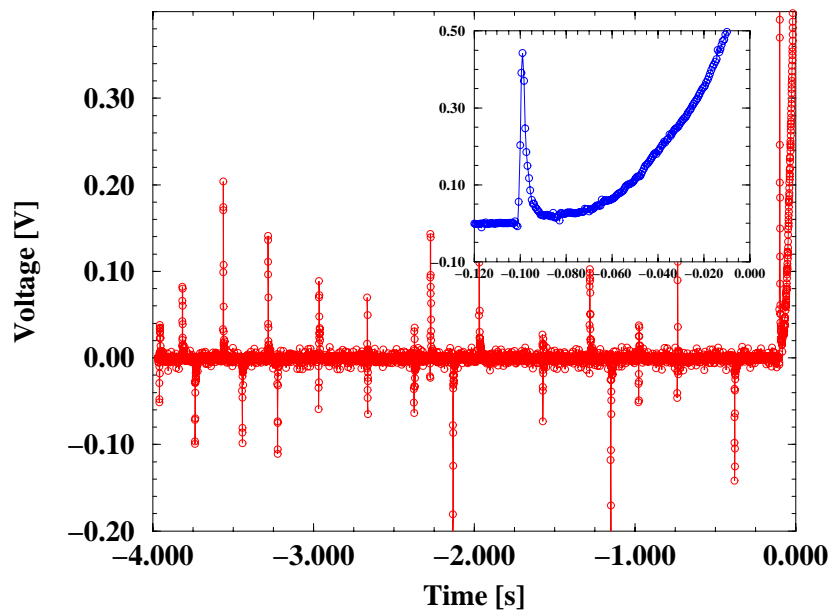


**Fig. 3-6 Typical Voltage Spike is shown in HFDB01 magnet.**

Analyzing the whole data set the following generalizations about ‘spikes’ were concluded:

- Spikes occur on every ramp
- Spikes occur in both half coils at roughly the same time, but with somewhat different amplitude and detailed time structure
- Spike frequency and amplitude increase with ramp rate
- Spikes are associated with quench initiation in all plots; in a few cases there is on the order of 20 milliseconds between the spike and quench start; in one case, a spike appears to occur after the quench has begun propagating.

The magnet current always drops (sometimes dramatically, up to 20A in  $\leq 1\text{-}2\text{msec}$ ) at the time of a spike; a current increase has not been observed.

During the test of HFDC01 a special “Snapshot” trigger was implemented. “Snapshot” events are triggered by transient excursions in the difference between half coil voltages. The half coil signals were digitized and the data were captured before and after a trigger, in which  $|H_{coil1} - H_{coil2}|$  exceeded 0.05 or 0.1 V (the quench detection threshold was 0.25V). Recall that HFDC01 was the first dual aperture race track coil magnets.

One of the magnet apertures contained a quench antenna (QA) so we were able to perform a special test. When snapshot events occurred we read out QA signals as well. On a few occasions we were able to correlate voltage spikes with the QA signal (see Fig.

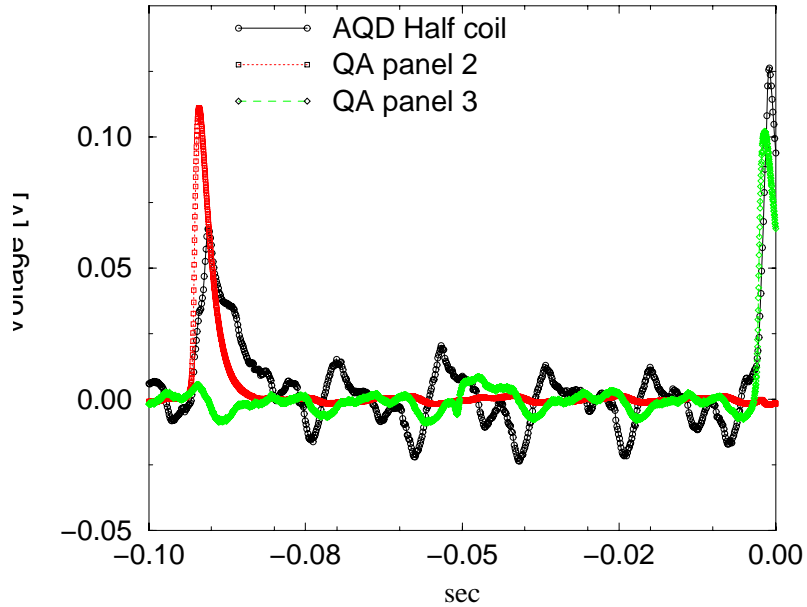


**Fig. 3-7 Two AQD voltage spikes are shown correlated with quench antenna signals in magnet HFDC01. Different QA panels picked up the flux change.**

3-7). This was an important test since it proved that these voltage spikes are “real” magnet related events, not just random noise. We also observed that these spikes are not localized, and they were distributed along the cable randomly.

### 3.4.3 Instability studies using small racetrack

In order to verify the idea that previous Nb<sub>3</sub>Sn magnets were limited by conductor thermo-magnetic instabilities, two different cables were tested: one made with the same conductor (1 mm MJR) and the other with a more stable conductor (1mm PIT). The PIT has a smaller effective filament size than the MJR (~50 μm instead of ~110 μm) and it generally guarantees a high quality of the copper stabilizer. The cable based on PIT strands was used to wind the small racetrack magnet SR01 while the MJR cable for SR02. The fabrication procedure and the mechanical structure were exactly the same for both magnets [69].

These racetracks were instrumented with a minimal number of voltage taps. Two voltage taps were soldered to the leads and one to the center of the magnet to make two half coil voltage segments for protection. Two additional voltage taps were soldered on the NbTi side of the splices. In order to be able to initiate a quench, a spot heater was installed on one of the coils. This heater was useful to check that the magnet protection circuits were functional before the magnet was fully energized.

SR01 was tested in February – March 2004 [93]. After the magnet was cooled down to 4.5 K a quench test was performed. The history of the quench test is summarized in Fig. 3-8. The first quench of the magnet occurred at relatively high current of 19292 A. This current was already much higher than any previously built Nb<sub>3</sub>Sn magnet at Fermilab. It took 14 more quenches at a ramp rate of 20 A/sec to train the magnet. The maximum current value was at 23713 A. This value is consistent with the calculated critical current value estimated by measuring critical current of strands at the Fermilab Short Sample Test Facility (SSTF) taking into account additional degradation of PIT cable due to its sensitivity to transverse pressure.

In order to expose the magnet to larger Lorentz forces the magnet was cooled down to 2.2 K and quenched several times. Both low and high ramp rate quenches exhibited erratic behavior showing no sign of any training. Although the magnet quench current was much lower than what one would expect from any reasonable temperature parameterization of the quench current, we were able to increase the Lorentz forces within the magnet. So if the magnet was not trained at 4.5 K we should have accelerated

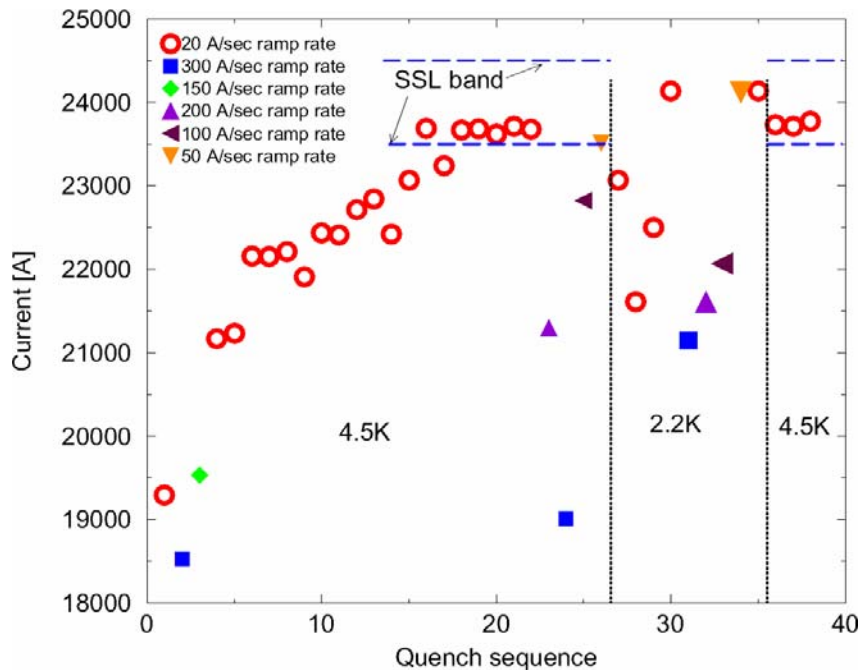


**Fig. 3-8 Quench history of SR01**

its training. On the other hand if the magnet reached its critical limit value the quench current should not show any improvement once it is warmed up again to 4.5 K. From Fig. 3-9 one can conclude that the magnet quench current remained the same consequently the magnet reached its critical current limit.

The SR01 test demonstrated that with a more stable conductor, the coil built at Fermilab can reach high current values.

SR02 was tested in June 2004 [94]. Training of this magnet was much longer than SR01. It took more than 20 quenches to reach a quench plateau (see Fig. 3-9). However, this plateau was not very smooth indicating that the magnet didn't reach its critical current limit. After ramp rate studies we cooled the magnet down to 2.2 K and quenched the magnet 11 times. The quench current was erratic and lower than what was achieved at 4.5 K. After warming up the magnet again to 4.5 K the magnet quench behavior remained erratic. Most of the quench locations were near the splices. Once again the 28 strand cable made of 1mm MJR had limited quench performance confirming that this conductor is too unstable to carry large amounts of current. It is also important to notice that for SR02 the quench current value (~20 kA at 4.5 K) is much higher than the case of the

previous magnets based on the 1 mm MJR strand (~12 kA at 4.5 K); this is due to the much higher RRR of the copper matrix.

The success of SR01 and the limited quench performance of SR02, using the same mechanical structure and fabrication procedure demonstrated that thermo-magnetic instabilities can significantly limit the maximum current of cables based on a state of the art Nb<sub>3</sub>Sn strand.

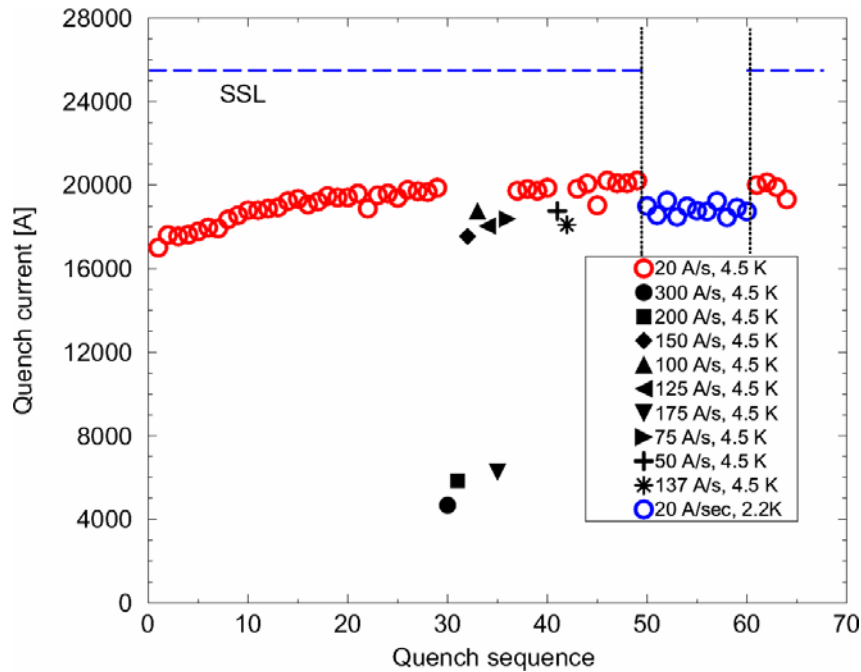


**Fig. 3-9 Quench history of SR02**

The strong instability of the MJR cable was also showed by the huge number of voltage spikes which were collected during the test of SR02. SR02 was the first magnet tested when we were able to fully utilize our new voltage spike detection system (VSDDS). The run plan of this magnet required that each time the magnet current ramped up to initiate a spontaneous quench the VSDDS was activated to capture voltage spikes. The primary goal was to capture the smallest spikes possible. The power supply regulation was not smooth so the noise magnitude and frequency spectrum was changing with current [84]. To reduce the noise level of the bucked signal a digital filter was applied. The filter cutoff was 1.5 kHz and 30 kHz.

In order to capture as many spikes as possible a variable trigger threshold was implemented. The noise of the bucked filtered signal was continuously monitored and if the voltage exceeded a 5-sigma 30- sigma value of noise then a 0.5 second time interval of data were captured. The sigma value was very low, on the order of  $10^{-1}$  mV, but every time the power supply SCRs were firing, about every msec, a noise signal one order of magnitude higher than the sigma value was produced. For this reason, in order to save only voltage spikes events, the automatic threshold had to be set 30 times larger than the sigma value. This meant that the signals were saved when the filtered bucked signal was higher than  $\sim 3$  mV from 0 to 8 kA. From 8 to 14 kA the noise level was increasing with the current and the threshold passed from 3 to 6 mV. Above 14 kA the threshold was almost constant  $\sim 6$  mV.

Over 1500 voltage spikes were collected during 44 ramp-to-quench events at 4.5K and 20 A/sec [92]. Between 0 and 8 kA the number of events above 6 mV were about 30-

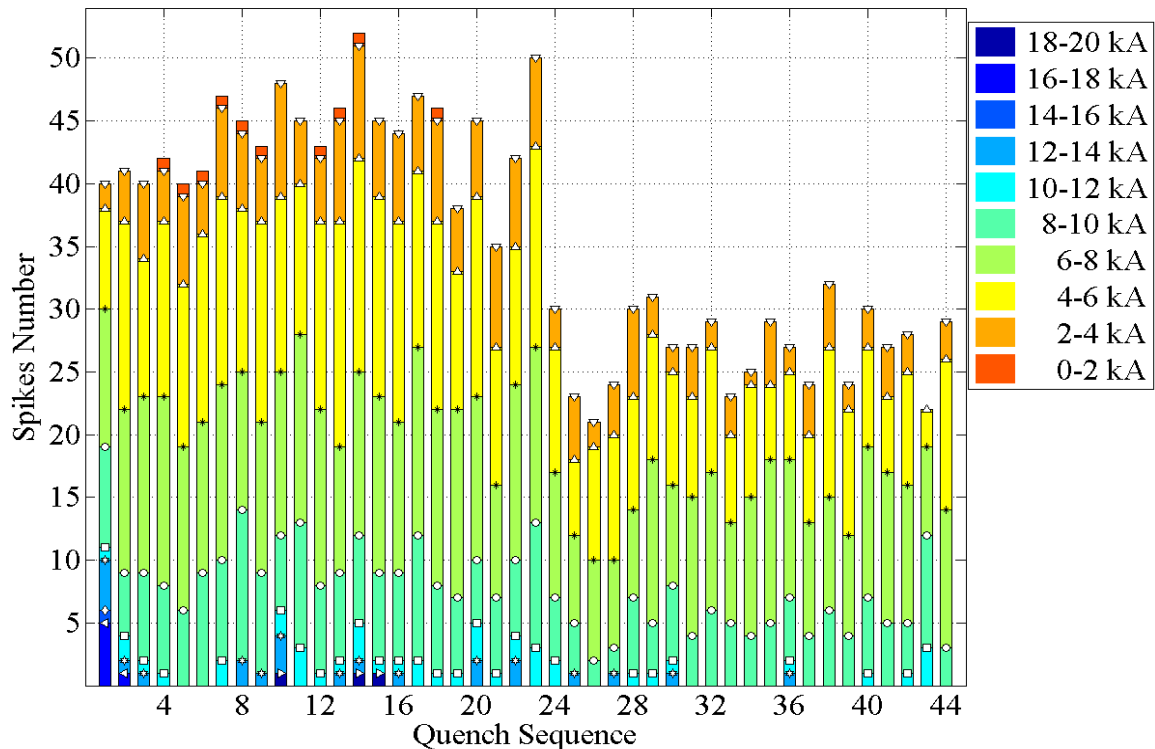


**Fig. 3-10** Voltage spike distribution is plotted binned them in 2 kA bins and as a function of ramp-to-quench sequence.

40% of the total number of spike collected in that current range. In Fig. 3-10 the number of voltage spikes for different ramp-to-quench events are plotted. After the 22<sup>nd</sup> quench the number of spikes per ramp didn't change significantly (see Fig. 3.). We also noticed that the quench current of SR02 didn't improve much after around the 22<sup>nd</sup> – 24<sup>th</sup> quench Fig. 3-9. This is an indication that some fraction of spikes can be correlated with training of the magnet.

Fig. 3-11 also shows the total number of spikes collected as a function of the applied current. This plot shows clearly that the number of spikes reduces drastically with increasing the current; after the magnet training at high current values (>14 kA) no spikes were collected.

The voltage spike signals used in this study are the bucked signals of the two half coils. Although bucking the two half coils removed most of the common mode noise the

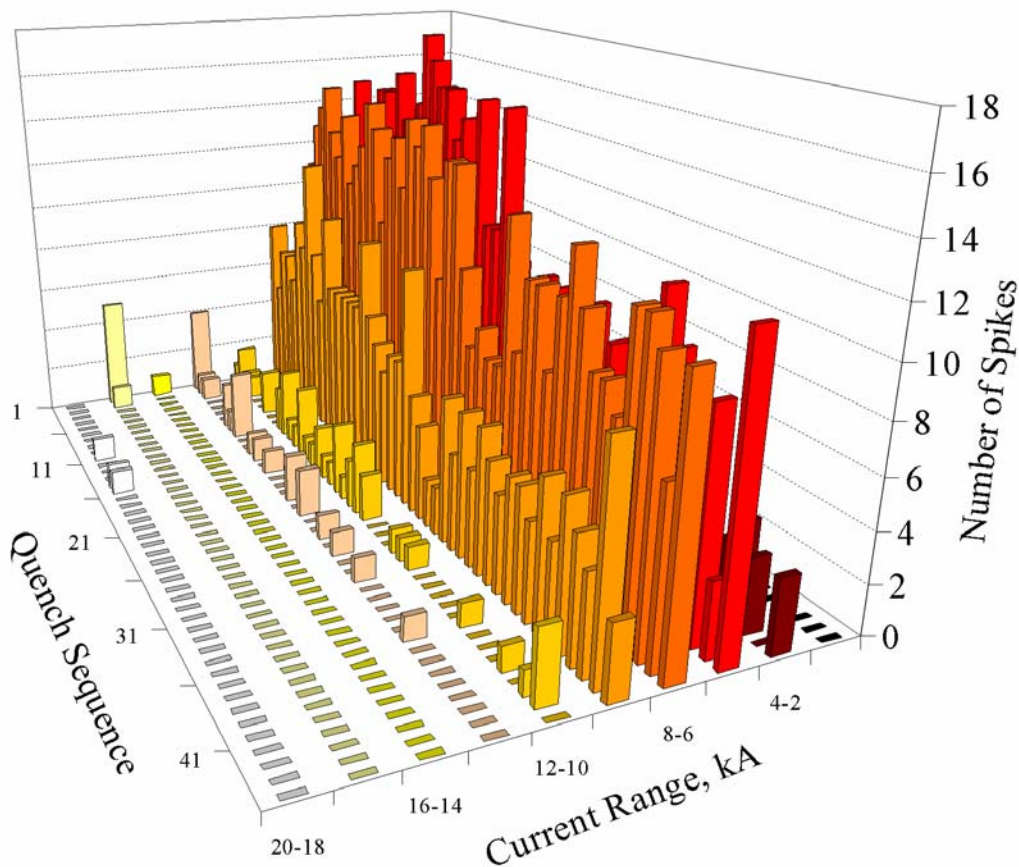


**Fig. 3-11** Voltage spike distribution is plotted binned them in 2 kA bins and as a function of ramp-to-quench sequence.

signals still contained periodic noise so we performed a matched filtering technique to further clean up the signals. A voltage spike signal after this clean up was applied is plotted in Fig. 3-12. This type of voltage spike essentially appears in the low current region (below 14 kA) and they are due to partial flux jumps in the conductor (see chapter 4). These signals could be well fitted with a curve, which has a sharp rise time ( $\sim 0.07$  msec) followed by an exponential decay with a time constant of  $\sim 0.15$  msec. Most of

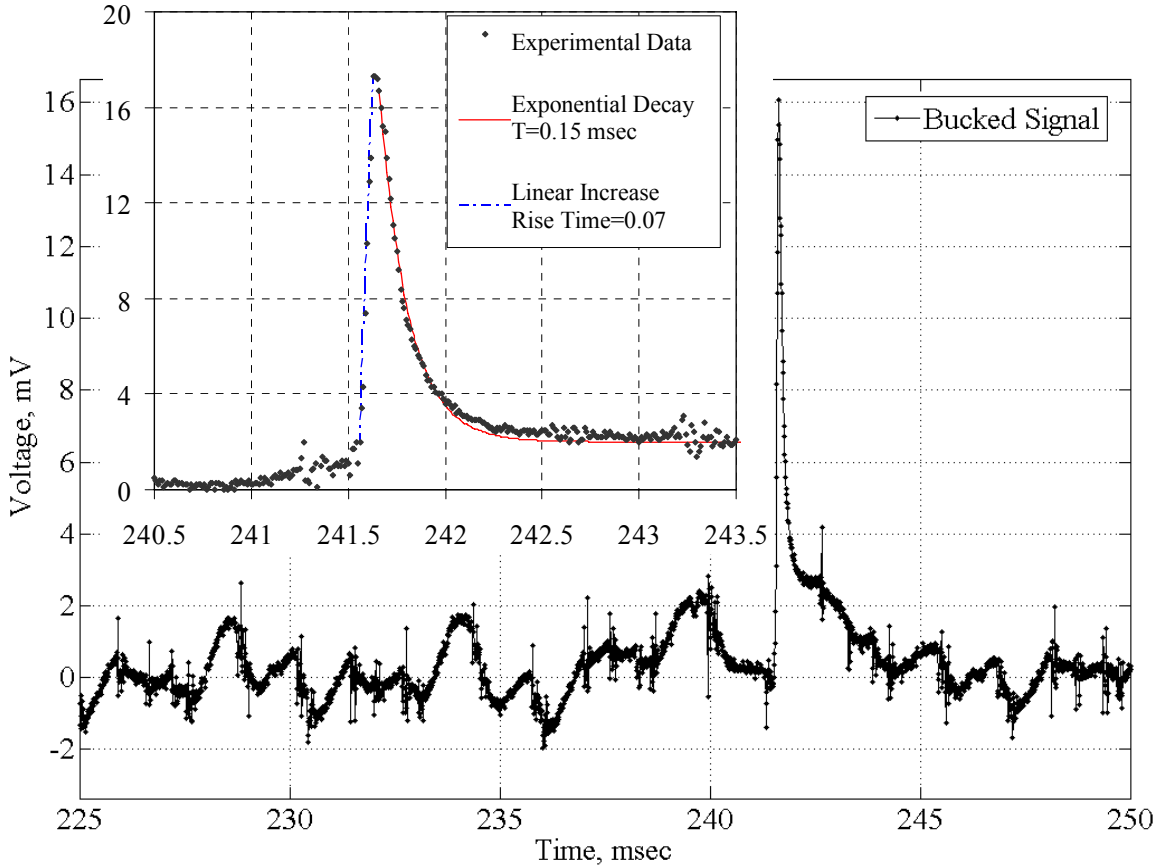


**Fig. 3-12** A simple type of ‘flux jump’ voltage spike is plotted. It can be well characterized with a curve which has a 0.07msec rise time and 0.15 msec exponential decay time.

the signals due to partial flux jumps present a much more complex shape Fig. 3-13 than the “simple” spike showed in Fig. 3-12. In Fig. 3-13 we also over-plotted a “simple” spike normalized to the height of the first ‘glitch’ of a spike signal. It seems that we could characterize the spike signal quite well as the superposition of many “simple” spikes, with different amplitude and shifted in time. Excluding the first ramp to quench, all the spikes collected below 14 kA were due to partial flux jumps.

During the first ramp to quench at 12600 A a new type of signal was observed, Fig. 3-14; this signal looked like a partial flux-jump type of spike with high frequency oscillations superimposed over it. The following spike at 13 kA was characterized mainly by high frequency oscillations with a negligible mean value, Fig. 3-15. Before quenching 7 more voltage spikes were collected: the first 6 were either pure oscillating signals or flux-jump type with high frequency oscillations; the last one, at a current value higher than 16 kA was a pure flux-jump type of spike Fig. 3-16.

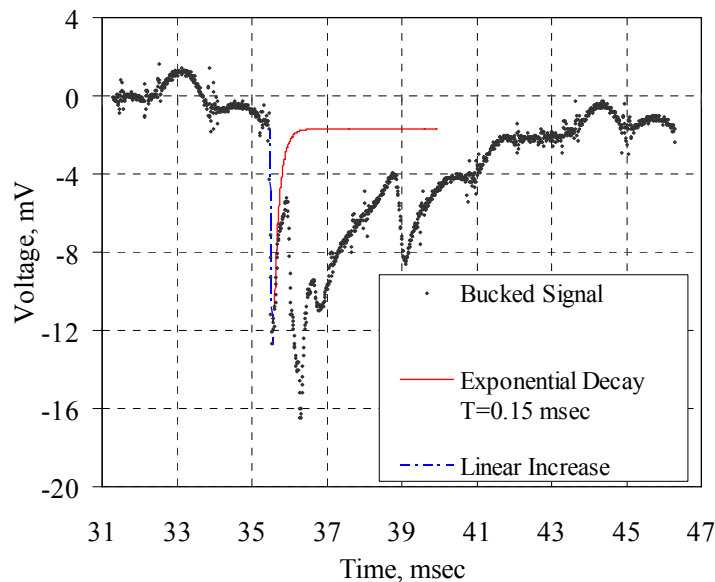


**Fig. 3-13 Typical ‘flux jump’ voltage spike. The first glitch is over-laid with a curve which has a sharp 0.07 msec rise time and an exponential decay with 0.15 msec decay time.**

During the following ramps to quench 3 more spikes presenting high frequency oscillations were collected; the last one was observed during the ramp to quench number 14. Oscillating signals occurred only when the magnet was exposed to a particular current level for the first time. The last voltage spike at high current, above 14 kA, was collected during the ramp to quench number 15; this spike was a flux jump type of spike.

Analyzing the whole data set the following generalizations can be drawn:

- After the training of the magnet all the voltage spikes were due to a flux jump and they occur in the low current region (2-14 kA);
- During magnet training flux jump type of spike may occur in the high current region (above 14 kA);

- The number of partial flux jumps decreases after magnet training;
- Signals with high frequency oscillations, different from flux jump type of spike, occurred at current values not yet reached by the magnet;
- Voltage spikes with high frequency oscillations may be either pure oscillating signals (with a negligible mean value) or flux-jump type of signals with high frequency oscillations superimposed.

This behavior can be explained by assuming that the oscillations are due to mechanical motion of the coils and the heat produced by this motion induces flux jumps in the conductor.

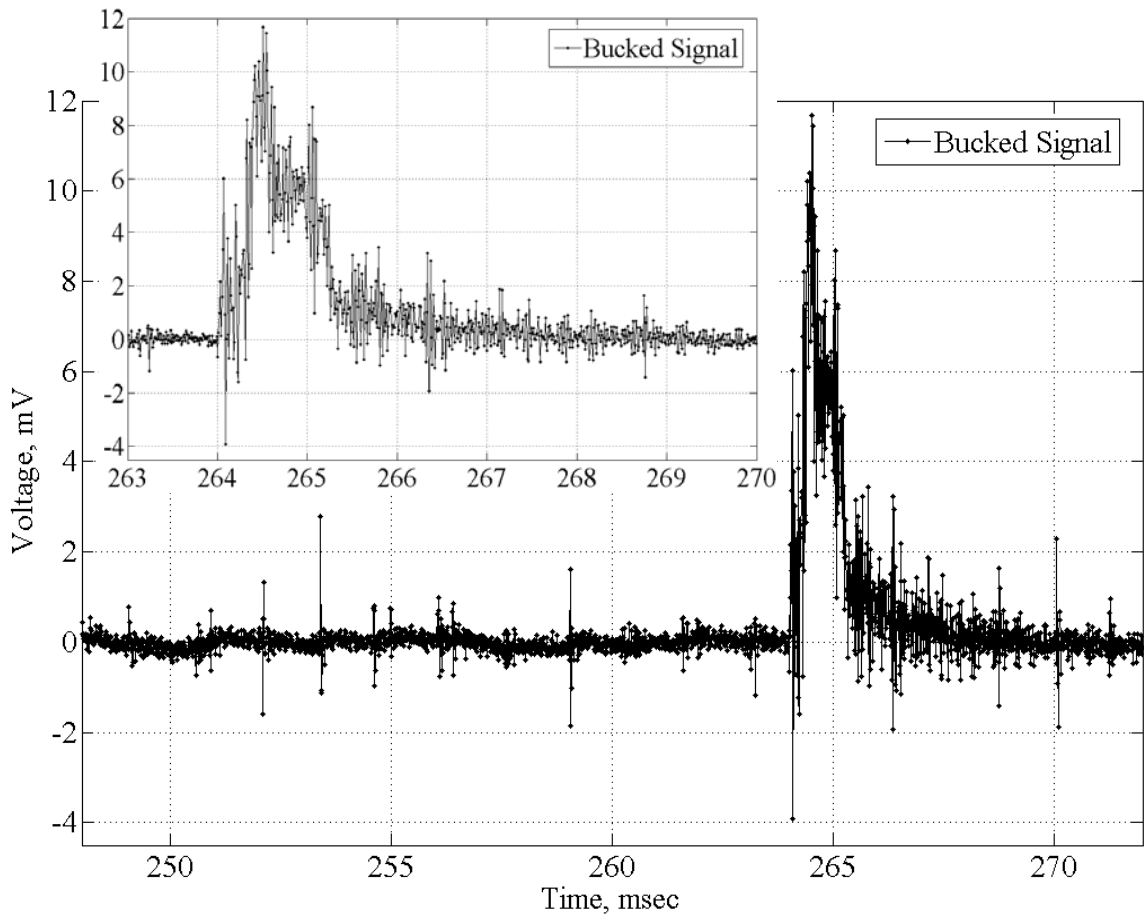


**Fig. 3-14 High frequency spike observed at high current in SR02**

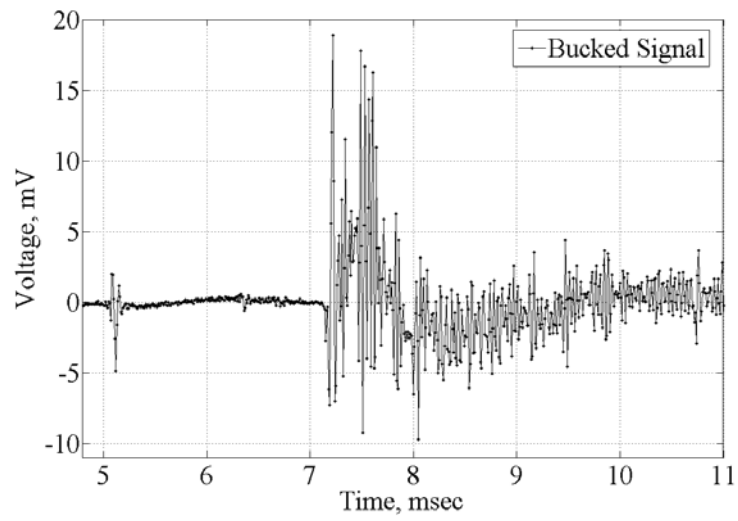


**Fig. 3-15 High frequency spike observed at high current value in SR02.**

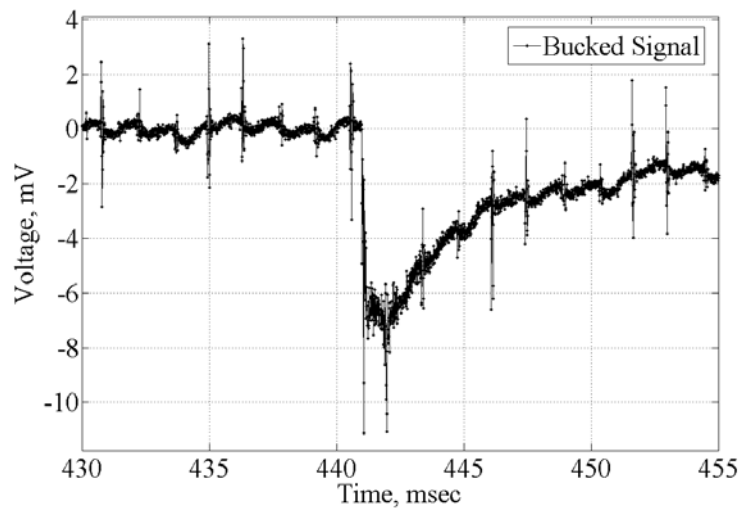


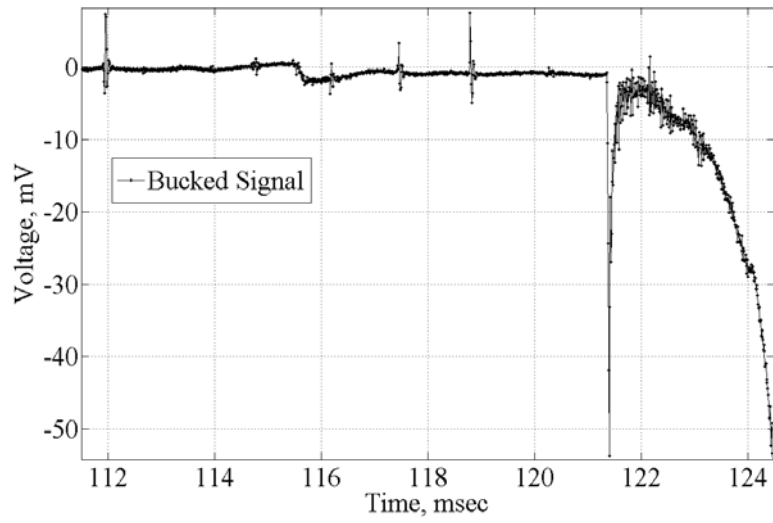
**Fig. 3-16 Flux jump type of spike observed at high current value (~16.5 kA) in SR02**

Regarding the quench signals, the first 13 show a voltage spike initiating the quench propagation, Fig. 3-17. The first two quenches had an oscillating spike; the spike signals were quite big, the peak value was about 55 mV Fig. 3-17 (a) and 15 mV respectively. In the following quenches the maximum amplitude of the oscillating spike was very small, less than  $\sim 2$  mV; nevertheless the spike signal was clear. Some of the quenches were initiated by a flux jump spike; the first case appeared during the third ramp to quench Fig. 3-17 (b). The peak value for these flux jump spikes was 8-30 mV.

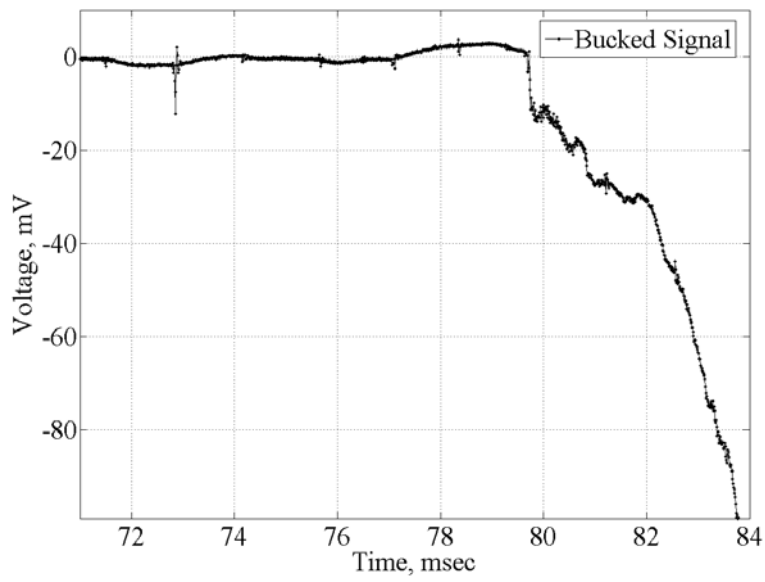
Starting from the 14<sup>th</sup> quench it was not possible to correlate the quench with a voltage spike; sometimes a voltage spike was still seen initiating a quench but most of the quenches did not show any voltage spike Fig. 3-18.

Conversely, when the magnet was cooled down to 2.2 K and tested with a current ramp rate of 20 A/sec, all the quenches were initiated by a flux jump spike Fig. 3-19. The peak value of these spikes was 2-5 mV. It is also interesting to notice that at 2.2 K almost no spikes were collected and this was most likely due to the use of the digital filter; probably, as it was observed in the PIT magnets (see next subsection), at 2.2 K the flux jump spikes are slower than at 4.5 K and the digital filter attenuated the spike signals.

From the amplitude of the voltage spikes which initiate the quench propagation it can be inferred that at  $\sim 20$  kA a small disturbance is enough to quench SR02.



(a)



(b)

**Fig. 3-17 Voltage spike initiating a quench in SR02: (a) Oscillation spike; (b) Flux Jump spike**

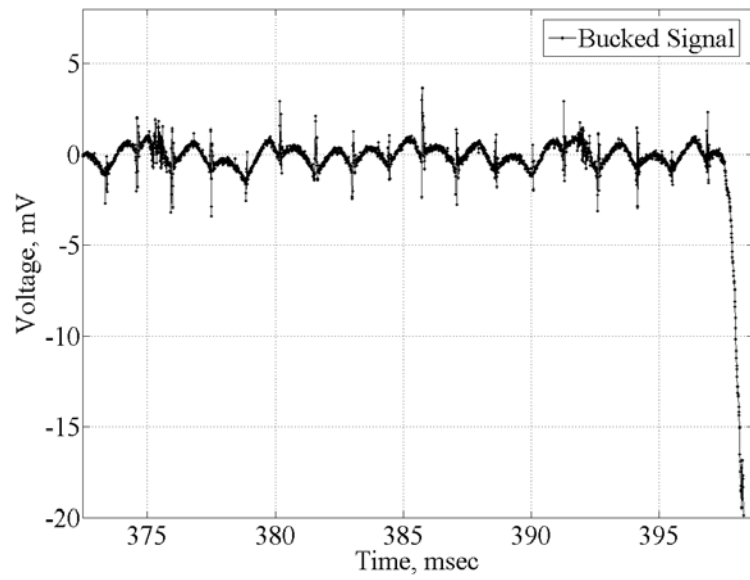


**Fig. 3-18 Quench signal in SR02 with no spike initiating the process at 4.5 K**

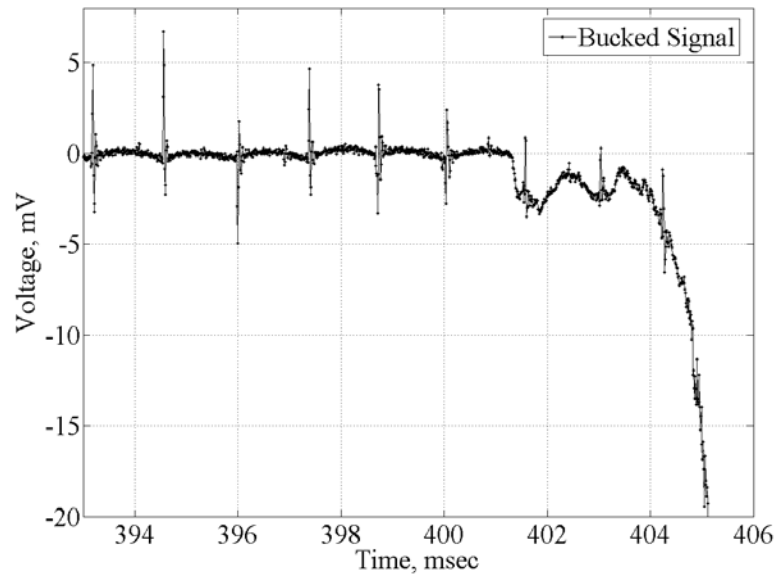


**Fig. 3-19 Flux Jump voltage spike initiating a quench in SR02 at 2.2 K**

### 3.4.4 Quench performance of FNAL dipoles based on PIT strands

The final step to demonstrate that Nb<sub>3</sub>Sn cos-theta magnets built at Fermilab were limited by thermo-magnetic instabilities was to make a successful magnet based on the same design and fabrication procedure as the previous magnets but using a more stable conductor.

For this reason two PIT cos-theta half-coils were then wound. The first one (coil #12) was first tested in a mirror configuration HFDM03 and then both coils were used in dipole model HFDA05 [64].

The quench history of mirror magnet HFDM03 is shown in Fig. 3-20. Training quenches at 4.5 K with the current ramp rate of 20 A/s were followed by ramp rate studies, magnet training at 2.2 K, and finally quenching the magnet again at 4.5 K.

The first quench in HFDM03 at 4.5 K was at 16.2 kA. The magnet exhibited slow but steady training. It took 20 quenches to reach the current plateau at 20.6 kA. In order to confirm that the magnet reached its short sample limit at 4.5 K it was cooled down to

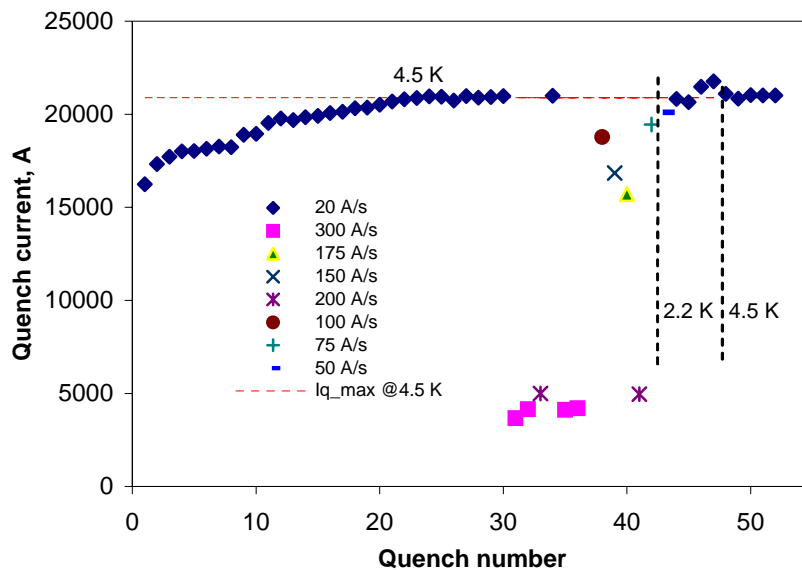


Fig. 3-20 HFDM03 quench history.

2.2 K. Although the quench behavior at 2.2 K was quite erratic, the magnet current increased to 21.8 kA, exposing the magnet to higher Lorentz forces than it was at 4.5 K. A few quenches taken again at 4.5K confirmed that the magnet had reached its short

sample limit at 4.5 K. The short sample limit calculated based on the witness strand and cable tests was within the range 17.3-20.6 kA. This range includes additional  $I_c$  degradation and present uncertainty due to PIT cable compression in the coil. The maximum field in the coil reached during the test was  $\sim 10$  T.

Based on signals from the voltage taps, all quenches occurred inside the coil body in the high field region. Some of the quenches might have started close to the transition from the first to second pole blocks of the coil inner-layer since the two segments quenched at about the same time.

The quench history of dipole model HFDA05 is shown in Fig. 3-21 [95]. The magnet training procedure was similar to the HFDM03 test procedure described above. The first quench at 4.5 K was at 14.0 kA. After 23 quenches the magnet reached a stable current plateau at 16.8 kA. After a few quenches at 2.2 K the magnet current increased to 17.9 kA. When the magnet was excited again at 4.5 K it quenched at 16.8 kA. After a thermal cycle to room temperature the magnet showed small, short re-training with the first quench only 3% below the short sample limit.

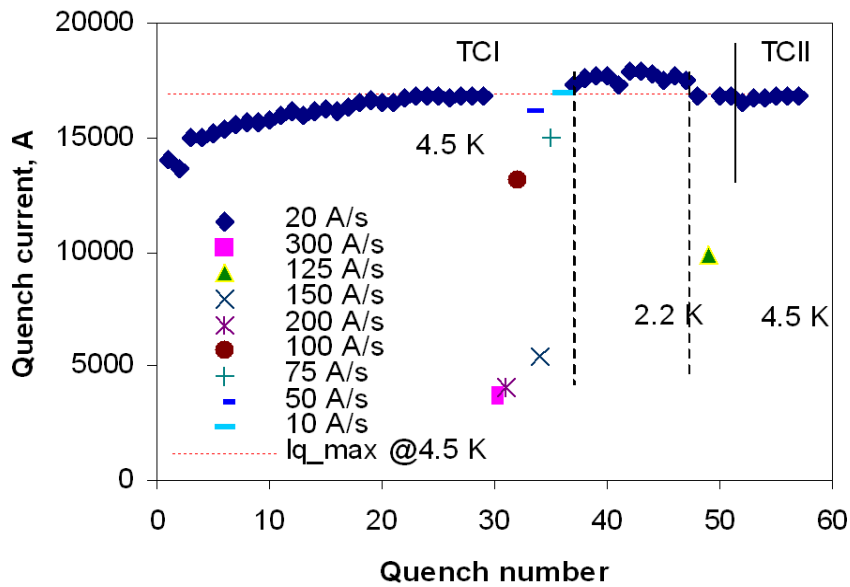


Fig. 3-21 HFDA 05 quench history.

In both thermal cycles all the training quenches occurred in the inner-layer pole block of the new half-coil at the maximum field. Training data show that the magnet has reached its short sample limit at 4.5 K. The short sample limit based on the witness strand

tests was within the range 16.2-18.7 kA. The maximum field in the bore (coil) at 4.5 K was 9.5 T (9.9 T) and at 2.2 K was 10.0 T (10.4 T). Since coil #12 never quenched in HFDA05 one could conclude that even after its re-use in HFDA05 it remembered its training. This behavior differs from the behavior of non-impregnated coils used in NbTi magnets.

The success of the HFDA05 magnet was confirmed by building and testing another cos-theta magnet HFDA06 using the PIT conductor [65]. The quench training of dipole model HFDA06 is shown in Fig. 3-22 and compared with that of HFDA05. The first training quench of HFDA06 at 4.5 K was close to 15 kA [96]. It took only 10 quenches and the magnet reached a stable current plateau at 16.4 kA. In thermal cycle II the 4.5 K magnet training was short, the third quench was already at the previous quench current plateau. To expose the magnet to higher force level the magnet was cooled down to 2.2 K. It took only four quenches to reach the quench plateau of 17.6 kA. After warming up the magnet back to 4.5 K the magnet quench current did not change relative to its previous 4.5 K quench current plateau value.

In both thermal cycles all the training quenches occurred in the inner-layer pole and middle block of half-coil #14, however, all of the quenches at the plateau were in coil #15. Training data show that the magnet has reached its short sample limit at 4.5 K. The maximum field in the bore (coil) at 4.5 K was 9.6 T (10.0 T) and at 2.2 K was 10.2 T (10.6 T).

HFDA06 quench training was shorter than that of HFDA05 and its quench behavior at 2.2 K was more stable. We also noticed that the quench current value of HFDA06 at 20A/s ramp rate was about 2% less than that of HFDA05. However, from ramp rate dependence studies (see Fig. 5.) extrapolating quench current values to 0 A/s ramp rates one can conclude that the critical current limits of the two magnets are almost identical.

Although the HFDA magnets based on the PIT conductor were stable, and they could reach their critical current and nominal magnetic field, the superconductor was still thermo-magnetically unstable. Indeed voltage spikes generated by flux-jumps were observed during the magnet energization.

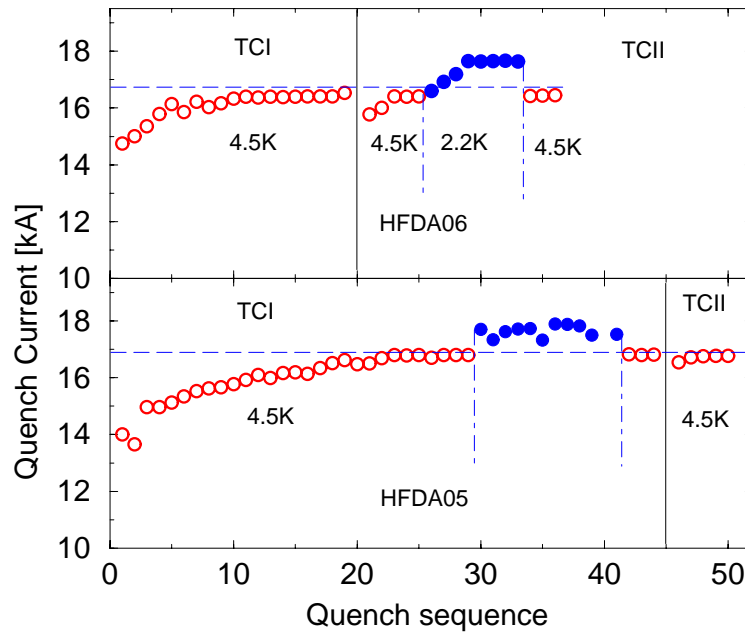
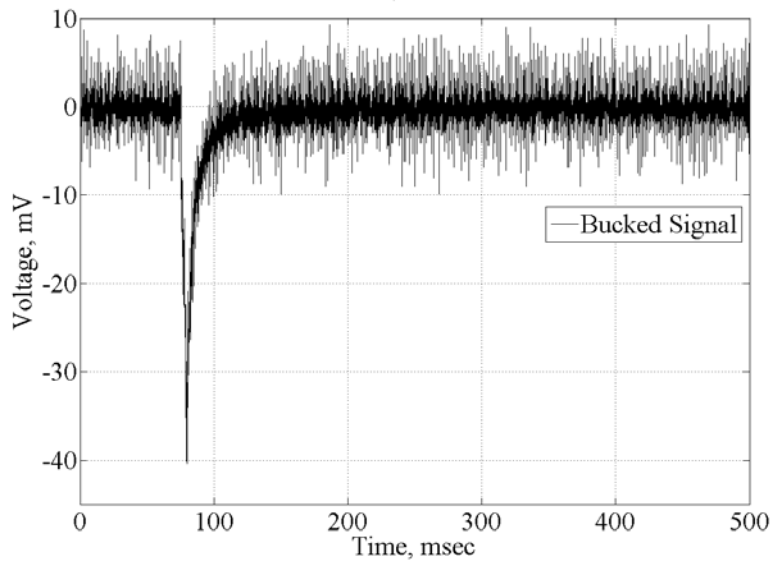


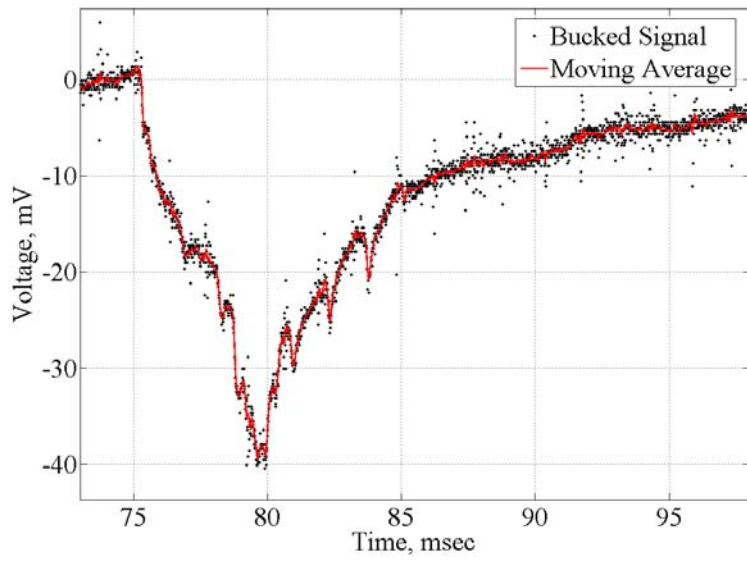
**Fig. 3-22 Quench training in HFDA05 and HFDA06**

Flux jumps in PIT magnets were observed first in the test of HFDA 06 using the VSDS without digitally filtering the signals. During this test the peak noise of the bucked signal was about 10 mV from 0 to 4800A; for currents higher than this value the noise level increased significantly. At 5000 A the peak noise was 20 mV, at 5500 it was 30 mV, and then it increased uniformly till reaching the maximum value of 40 mV at about 8500 A. For higher current values the peak noise was approximately constant. In order to capture voltage spikes the threshold was set manually at a value approximately 5 mV higher than the peak noise.

During the first thermo-cycle only few flux jumps were collected because of the use of the digital filter which was attenuating frequencies below 1500 Hz. In the second thermo-cycle the digital filter was removed and several flux jumps signals were observed. At 4.5 K and with a ramp rate of 20 A/sec, about 20 flux jumps were collected for each ramp between 800 A and 4800 A. The voltage signals were all below 20 mV but the signals were collected between 1000-1200A. In that current range spikes could reach 40 mV Fig. 3-23. For currents above 4800 A only few flux jumps were observed because of the higher noise.



(a)



(b)

Fig. 3-23 Flux Jump spike in HFDA06 at 4.5K: (a) time window 500 msec; (b) time window 6 msec

At 2.2 K with a ramp rate of 20 A/sec, flux jumps were observed as well. This time they appeared between 1800 A and 4800 A. Only 5-6 signals per ramp were collected and the peak signal was always below 20 mV.

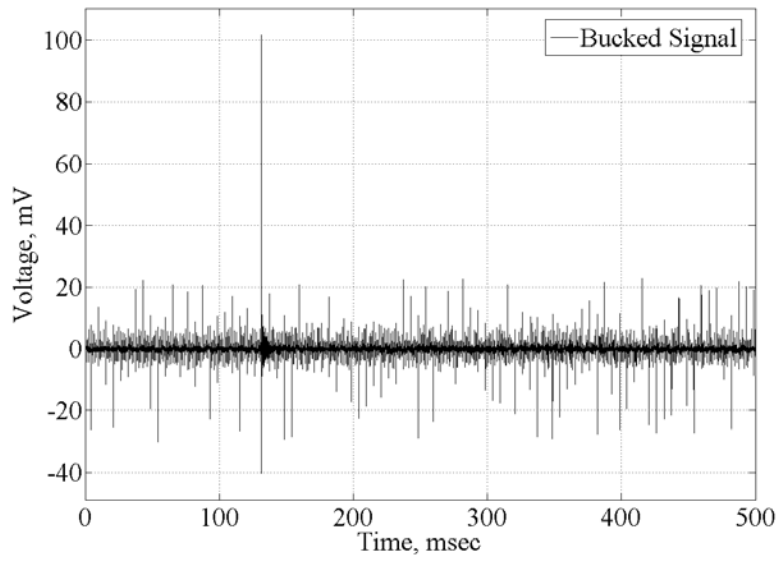
During this test motion related spikes appeared as well. These spikes, characterized by high frequency oscillations (Fig. 3-24), were observed at the beginning of the first thermo-cycle and in the second thermo-cycle when the temperature was lowered to 2.2 K. It was confirmed that motion related spikes appear when the magnet is exposed to Lorentz forces that the magnet did not see previously and, consequently, they disappear after the training of the magnet.

During the magnet training only in one case was it possible to distinguish a voltage spike preceding a magnet quench (quench number 7) Fig. 3-25. This probably means that the conductor motion which initiates the quench during the magnet training is generally too small to be detected with a noise level of several mV.

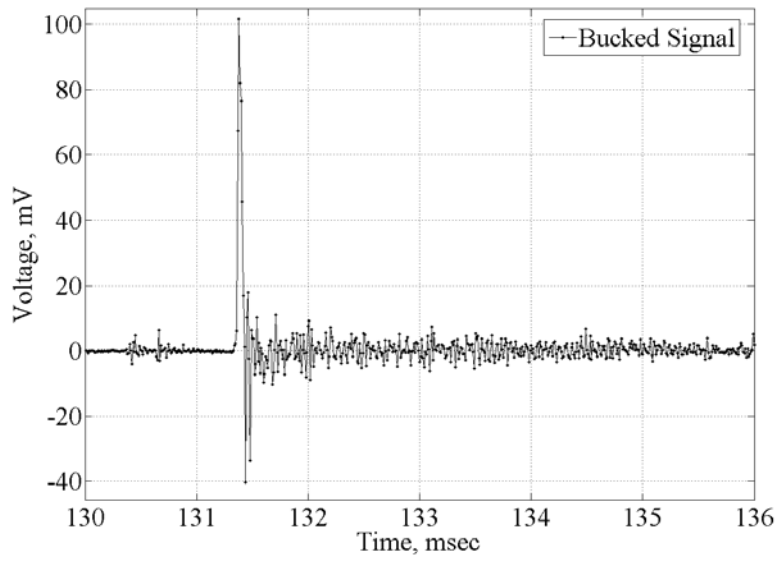
### **3.5 Conclusions**

In the low field region of superconducting accelerator magnets thermo-magnetic instabilities limit the quench current value of cables based on state of the art Nb<sub>3</sub>Sn strands. If the maximum current that the cable can carry at low field is lower than the nominal current of the magnet, the magnet will have limited quench performance. This was the case of the first Nb<sub>3</sub>Sn magnets built at Fermilab.

At present conductor instabilities can not be avoided, even magnets built using the more stable PIT strand have flux jumps; although it is still possible to build stable magnets increasing the current carrying capability of cable at low field. This can be achieved by limiting the strand magnetization (using strand with smaller effective filament size) and increasing the residual resistivity ratio of the copper matrix.

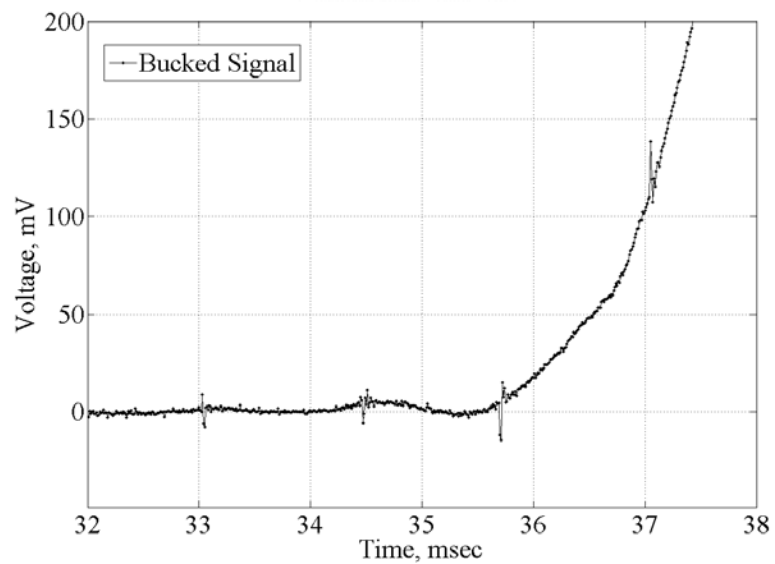


(a)

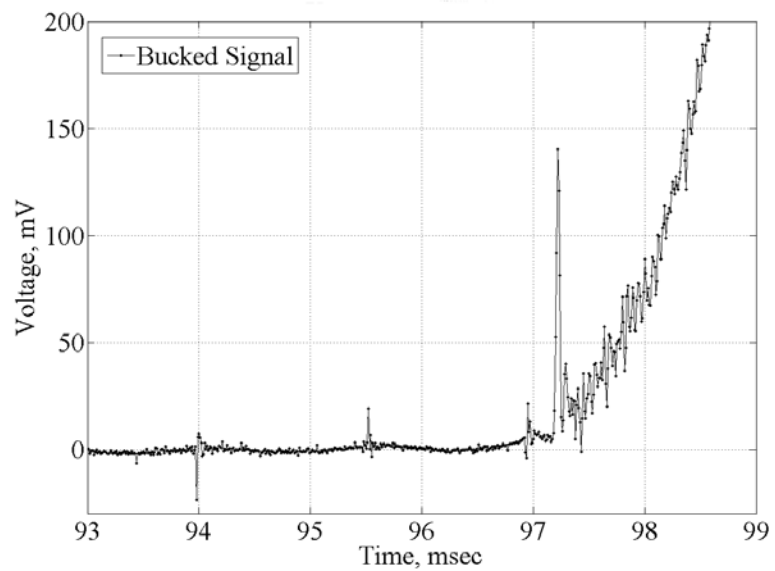


(b)

Fig. 3-24 Motion related spike in HFDA06: (a) time window 500 msec; (a) time window 6 msec



(a)



(b)

**Fig. 3-25 Quench signals in HFDA06 magnet: (a) no spike initiating the process; b) motion related spike initiating the quench**



## Chapter 4 – Strand test results

As a part of the High Field Magnet program at Fermilab, several Nb<sub>3</sub>Sn dipole models were designed and built using a Rutherford cable made of 28, 1mm Modified Jelly Roll (MJR) strands. These magnets, which were built through the end of 2003, exhibited limited performance: the quench current (around 13 kA) was only ~40-60% of the nominal value (see chapter 3 for more details). This means that the maximum current value per strand was less than 500 A.

Test results have shown that most of the quenches at low currents observed in the MJR dipole coils occurred in the low field regions. Analysis of this phenomenon, which suggests this is due to large thermo-magnetic instabilities in Nb<sub>3</sub>Sn strands with high critical current density and large effective filament size, has prompted intensive studies of multi-filamentary strand stability since early 2003. In particular, attention has shifted towards the study of strand behavior at low magnetic fields where superconducting strands are more sensitive to thermo-magnetic instabilities.

In this chapter are presented the test results of experiments performed on superconducting strands. The strand tests include: critical current ( $I_c$ ), quench current ( $I_q$ ), and voltage spike measurements. Critical current has been measured in order to characterize the strand while quench current and voltage spike measurements have been performed at different field and physical conditions in order to study strand instabilities.

The critical current measurement is performed at a constant magnetic field and temperature by ramping up the current and monitoring the voltage in between voltage taps (V-I measurement), which are usually attached to both ends of the coil (sample). The voltage is zero until the current is high enough to turn the superconductor into the normal conducting state. If the transition between the superconducting to normal state is gradual and reversible then the superconductor has reached its critical current Fig. 4-1. However, if the transition is abrupt (non-continuous) and non-reversible then it is probably due to premature quenching of the sample. These critical current measurements are performed at various external magnetic field values. Using V-I measurements, the strand  $I_c$  can be measured only at a high field (> 6-11 T) in high  $J_c$  Nb<sub>3</sub>Sn strands; indeed, for lower fields, the  $I_q$  is lower than the  $I_c$ .

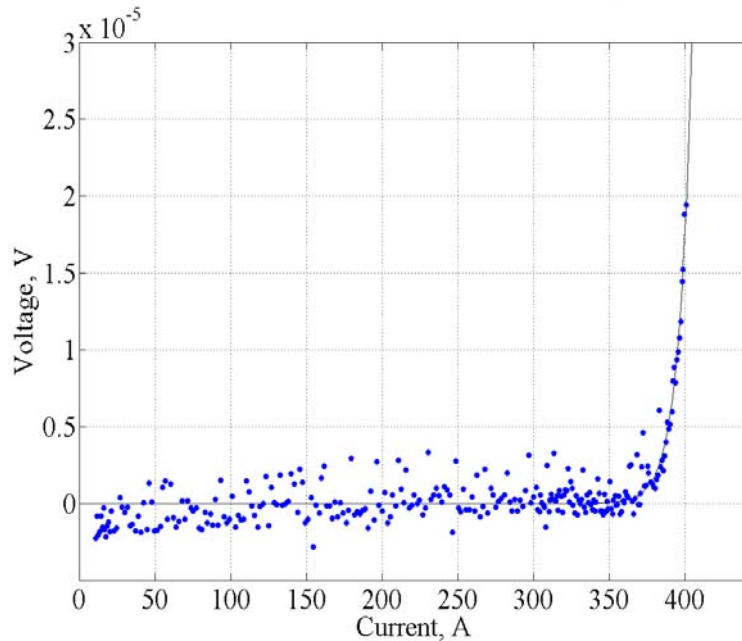


**Fig. 4-1 Critical current measurement**

The  $I_q$  is not only determined from the V-I measurement but also by ramping the magnetic field with a fixed transport current in the sample (V-H measurement).

The Voltage Spike measurement is performed during the V-I and V-H measurements. It consists of a data acquisition system, which samples at a rate of 100 kHz, and measures voltage spikes that appear between the ends of the sample. These voltage spikes are due to strand instabilities; where the voltage indicates a release of energy in the sample.

Test results will be presented in historical order. However, the most significant tests performed in the first 6 months of 2003 will initially be provided. It was during this period when, at Fermilab, the  $I_q$  measurements at low magnetic field prompted the investigation of strand instabilities. Test results from 8 samples of 1mm MJR strands will also be shown. Four of these samples had the same heat treatment used to build MJR magnets and the others used a shorter heat treatment technique. At that time only  $I_c$  and  $I_q$  were measured using the V-I technique. These strands were strongly unstable in the low field region, but the value of  $I_q$  could not explain the limited performance of the magnets. However, the  $I_q$  of the samples with a shorter heat treatment was higher than that of the

other samples. The shorter heat treatment allowed increasing the residual resistivity ratio of the copper matrix without reducing the  $I_c$ .

The following test results presented includes V-I measurements of two 0.7mm MJR strands and one 0.7mm PIT strand with high RRR (for more details on strands and RRR see chapter I). Tests of MJR strands show the spread of the measurements and the independence of  $I_q$  with the current ramp rate. The PIT sample, which has a filament size more than two times smaller than the MJR strands, is still unstable. These 3 samples were tested in the first 3 months of 2004.

The next strands presented are two 1mm MJR, the first has a high RRR while the other a low one. These strands were tested using both the V-I and the V-H technique. The V-H measurements were introduced in order to understand if changing the physical conditions of the strand does the  $I_q$  get smaller and reach the level of the  $I_q$  per strand that was in MJR magnets ( $\sim 500A$ ).

The results of the sample with high RRR is an example of a series of V-H measurements performed between March and June 2004. It was thought that the mechanism, which would have quenched the sample during the V-H measurement, was almost adiabatic and independent from the matrix quality. These tests showed that the V-H measurements reduced the  $I_q$  with respect to the V-I measurements although the  $I_q$  value was still not low enough to explain magnet performances.

The MJR with low RRR was the first sample tested at Fermilab, which had a quench  $I_q$  consistent with the magnets results. This test demonstrated that magnet limitations were related to strand problems and that these problems were due to a combination of copper quality and magnetization of the filaments.

Voltage spike measurements of the last set of samples are also presented. This set includes two 1 mm MJR, one with low RRR and one with high RRR, one 0.7 mm MJR with high RRR, one 1 mm PIT, one 0.5 mm NbTi strand with a resistive matrix (CuNi), and one NbTi monofilament. Voltage spike measurements allow the investigation of the development of strand instabilities, where the following samples were chosen in order to study the different aspect of these instabilities. These samples were tested between March 2005 and January 2006. The analysis of the voltage spike signal shapes provides an

opportunity for drawing important conclusions regarding the mechanisms of strand instabilities.

The main sections of these chapters describe: the Short Sample Test Facility (SSTF) where the strand tests were performed; the set-up for voltage spike measurements of strands; the test procedure; tools used to analyze  $I_c$  and voltage spike measurements;  $I_q$  results of samples in which only V-I measurements were performed;  $I_q$  results of samples that had both V-I and V-H measurements; and results of voltage spikes measurements.

#### 4.1 Short Sample Test Facility

Critical current measurements of superconducting strands are performed at the Short Sample Test Facility (SSTF) at Fermilab. Development of this facility started in 1998 in the Technical Division within the High Field Magnet Project (HFM) to perform critical current measurements of binary and ternary NbTi, and Nb<sub>3</sub>Sn strands.

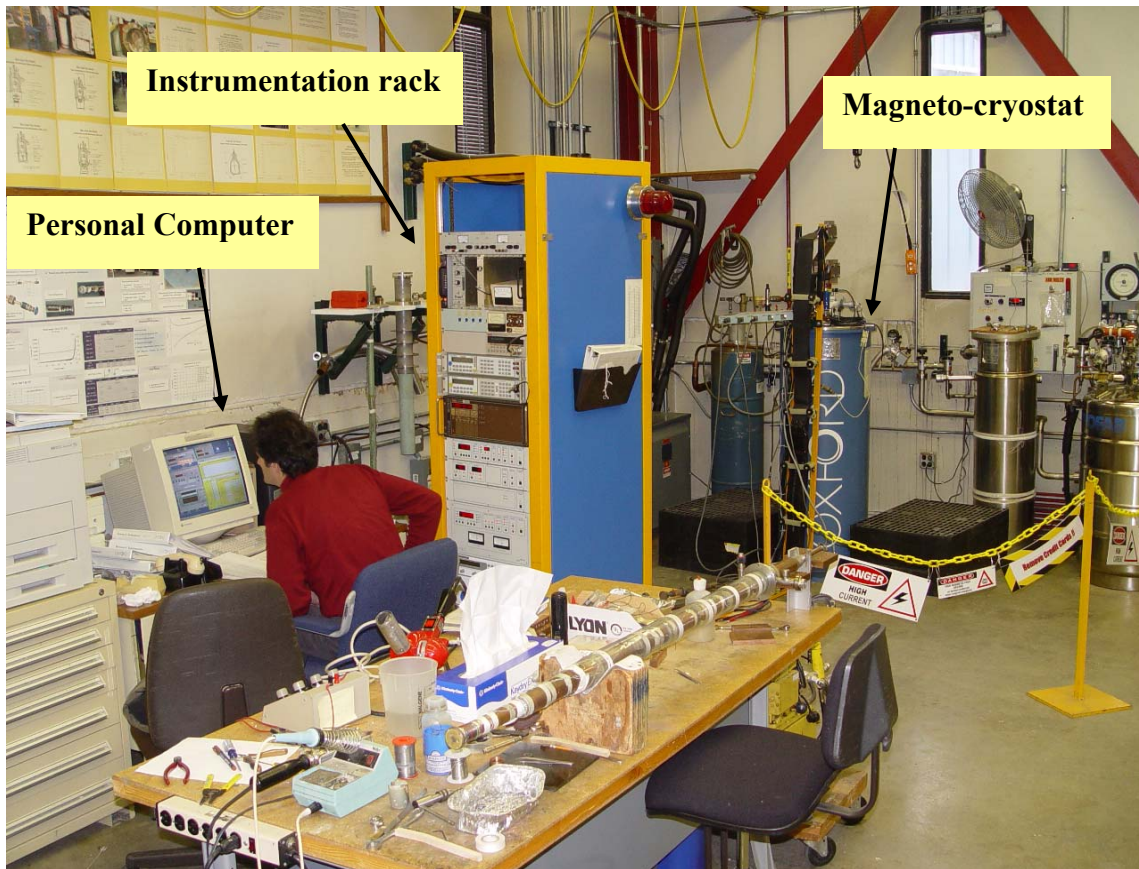
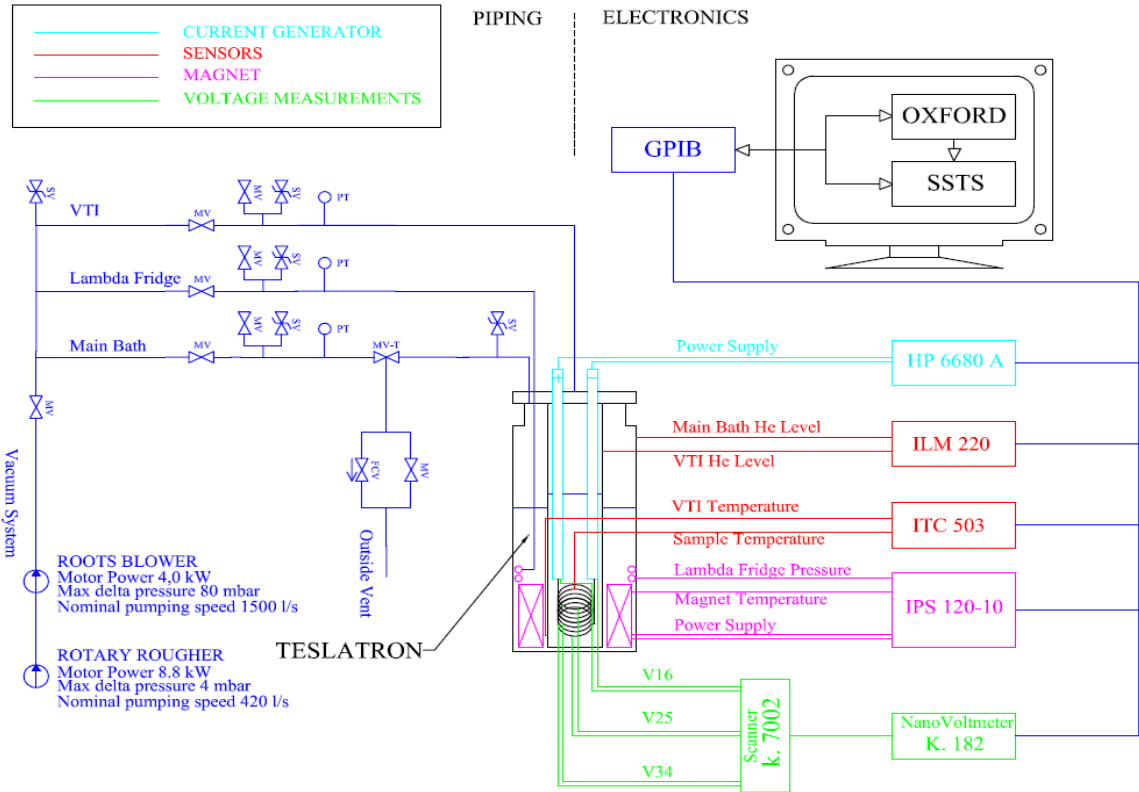


Fig. 4-2 Picture of the SSTF



**Fig. 4-3 Scheme of the SSTF**

In Fig. 4-2 a picture is shown of the SSTF. The following components can be seen: The Oxford magneto-cryostat, the rack with the electronic instrumentation and power supplies, and the PC that controls the system and where the measurements are saved. A block diagram of the SSTF is showed in Fig. 4-3.

The 15/17 T magneto cryostat (Teslatron) consists primarily of a vacuum insulated helium dewar for the main bath, which contains a superconducting solenoid at the bottom. To allow measuring at different temperatures, the main cryostat feeds a second smaller helium cryostat, called Variable Temperature Insert (VTI), which is inserted inside the main dewar, down into the solenoid bore. According to Oxford specifications, the VTI allows experiments in a temperature range between 1.5 K and 200 K at atmospheric pressure. The normal temperature of the system is 4.2K: the helium evaporation temperature at atmospheric pressure.

To operate at temperatures higher or lower than 4.2 K, a PID control is used. Oxford software written in LabView automatically controls a heater placed at the bottom of the VTI that can be operated to increase the temperature. Alternatively, the aperture of

a needle valve located between the Main Bath and the VTI can be regulated to increase coolant flow and force the temperature to drop. This temperature control system is made more effective by connecting the VTI to a vacuum system. Cernox sensors monitor the temperature in the VTI and in the magnet.

The helium level in the main bath is measured by a sensor consisting of a superconducting wire that extends from the top of the dewar to the bottom. The portion of wire below the liquid surface at 4.2 K is in a superconducting state, whereas a small heater on the wire ensures that the upper part be kept above its critical temperature. A current is made to flow in the wire at fixed intervals in order to measure the value of its total resistivity. This allows determination of the percentage of helium in the bath. The usable helium volume in the main bath is 42 liters. The helium level in the main bath is measured every few minutes. The VTI helium level is also measured every few seconds by a similar superconducting sensor placed on the probe used for the measurements.

A probe, Fig. 4-4, locates the sample at the center of the solenoid magnet in the VTI. It also provides the current to the sample through two copper lugs welded on the probe leads. A pressure contact guarantees electrical continuity between the copper lugs

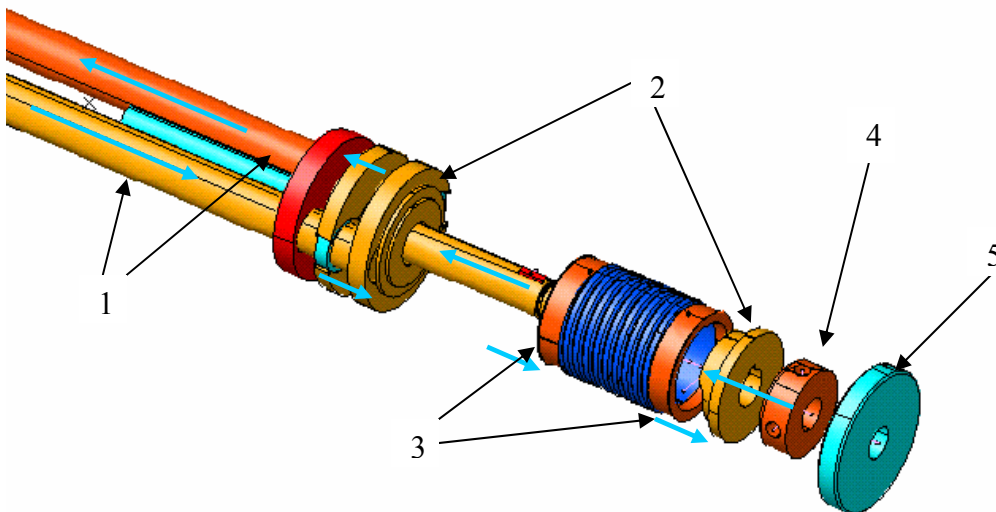


**Fig. 4-4 Probe for strand measurements: 1) copper leads; 2) copper lugs; 3) copper rings; 4) brass nut to regulate the pressure contact;5) G-10 discs for centering the probe within the magnet bore. Azure arrows indicate the current path**

and the copper rings where the sample is soldered. A thin layer of Indium is used to improve the electrical contact between the lugs and rings.

The sample is wound on a grooved cylindrical Ti-alloy barrel [97] Fig. 4-5. This sample holder is used for both the heat treatment and the measurement to minimize the risk of overstressing the sample during the preparation steps. The

Ti-alloy is chosen because it is inexpensive, nonmagnetic, has a low thermal expansion, and a high electrical resistivity ( $147 \mu\Omega\text{-cm}$  at 4 K).

Initially the sample is wound on the barrel and held in place by two removable end rings. After the heat treatment, the Ti-alloy end rings are disassembled and replaced by the Cu rings. The sample is then ready to be mounted on a probe to perform the critical current measurements. The Ti-alloy barrel is mounted at the end of the probe. The orientation is such that the magnetic field direction is perpendicular to the strand.

There are a maximum of six channels for measuring the voltages so the probe has 6 pairs of twisted wires (permanently attached to the probe). These voltage tap wires are connected to a 12 pin connector located at the top of the probe. Generally, for critical

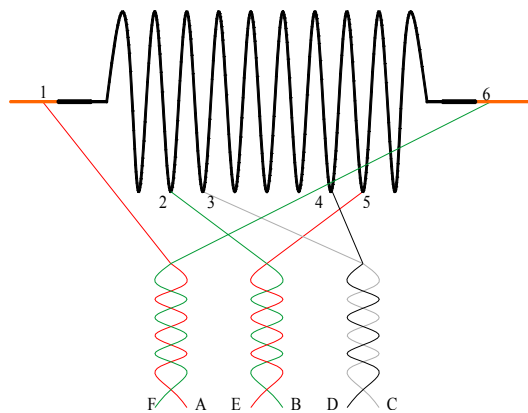


**Fig. 4-6 Sketch of the taps and wiring configuration for standard V-I, V-H measurement**

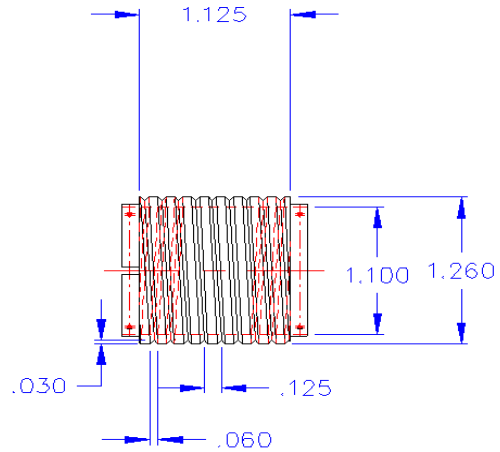


**Fig. 4-5 Barrel; dimensions are in inches**

current measurements, only three out of the six available channels are used: four voltage taps (two channels) are soldered to the sample and two taps (one channel) to the current leads in order to acquire voltages during measurement.

The sample is about 1m long (not considering the parts soldered to the copper rings), and the taps are placed in its central part to monitor the voltage; the strand's length between taps 3 and 4 is 50

cm, whereas between taps 2 and 5 the length is 75cm, Fig. 4-6. The voltage signals are named  $V_{1-6}$ ,  $V_{2-5}$  and  $V_{3-4}$ ; the subscripts indicate the voltage taps where the voltage is measured.

In the following paragraphs the electric and electronic instrumentation will be described. The solenoid is controlled by an Oxford Intelligent Magnet Power Supply (IPS 120-10) with a GPIB interface. It provides a bipolar current and allows the magnetic field to be swept smoothly through zero in either direction, usually with a ramp rate of 1 T/min.

Two power supplies – Hewlett Packard 6680As – are connected in parallel in a master slave configuration to provide current to the sample. The slave power supply follows the current that is provided by the master. The maximum programmable values of the HP 6680As are 895A and 5.125 V.

The helium level meter is an ILM220 model by Oxford. It is able to control two channels of helium level in the VTI and the Main Bath. The temperature controller is an ITC503 model by Oxford. It is a three-channel temperature controller with temperature auto ranging and automatic PID setting.

The nanovoltmeter, to measure the voltage between taps, is a 182 model by Keithley. It is a fully programmable instrument with 1nV sensitivity. The scanner, which is used to switch the signal between the taps, is a Keithley switching mainframe model 7008. It can control 10 DAQ cards with up to 40 channels per card.

All these instruments can be controlled both from the front panel and from LabView or other standard data acquisition software through a GPIB bus. National Instruments' software LabView is used for the data acquisition and hardware control. All data coming from Teslatron's sensors and instrument control parameters are processed on a PC through a GPIB bus. Specifically for the SSTF, a LabView application was written to monitor the process of the measurement and store the data. More recently, a parallel DAQ system was implemented using a NI DAQ card with a maximum sample rate of 200 kHz. This system is being used as a fast protection system by implementing a shut down of the sample current above a limit voltage value. This device is called SSTF fast DAQ system.

## 4.2 Voltage Spike Detection System at the SSTF

In order to measure the voltage spikes of the strands the VSDS [chapter II] is used in parallel to the SSTF critical current readout system [98]. For strand measurement the VSDS isolation amplifier will be bypassed because in these experiments there are no risks of over-voltage and this also improves the signal-noise-ratio.

Three signals are provided to the VSDS: the current signal and the two voltage signals between the two half coils. The two half coil signals must be inductively balanced in order to be able to remove the common noise by bucking the two signals.

The SSTF power supply provides a signal that is linearly proportional to the current value: at 0A and 895A the signal is equal to -0.125V and 5V respectively. Since the difference in current between the two power supplies is negligible, the only signal coming from the master is sent to the VSDS.

The voltage taps were installed in a configuration that allows performing voltage spike measurements and standard current voltage measurements at the same time. Three taps were added to the regular configuration: a central tap and two more taps at the end of the sample, Fig. 4-7, Fig. 4-8. Two spare twisted wire pairs, permanently attached

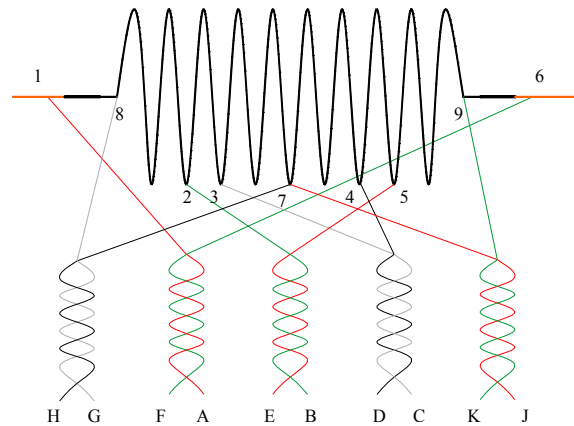


Fig. 4-7 Sketch of the taps and wiring configuration for spike studies in strands

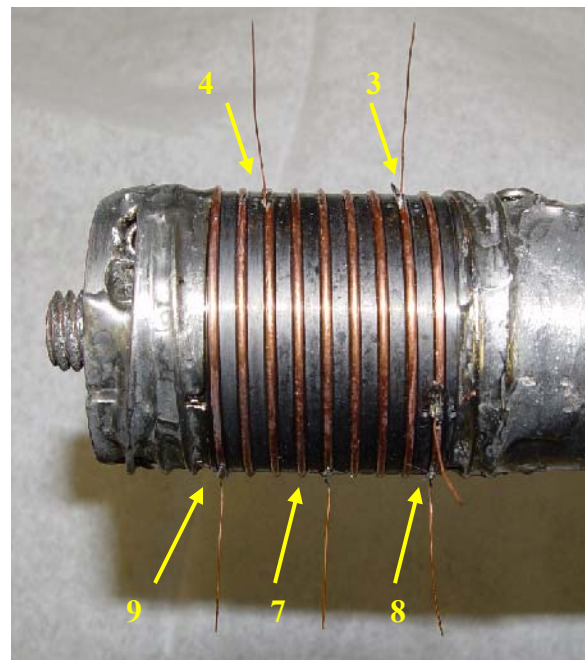
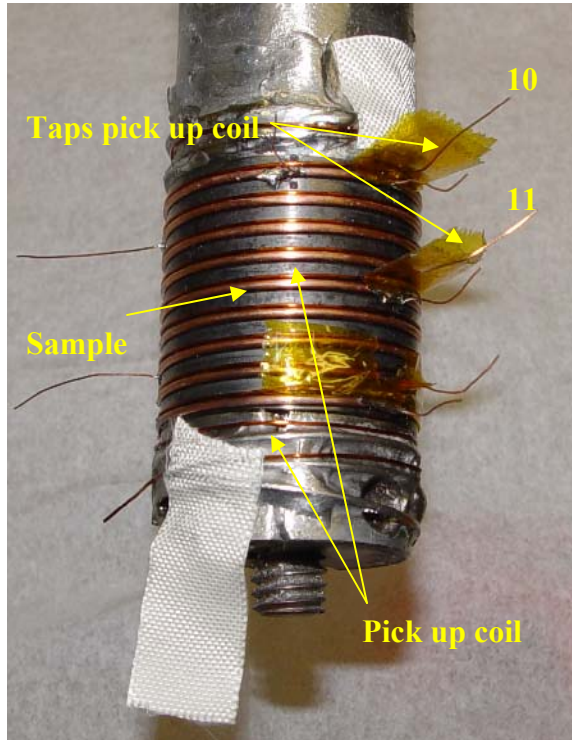


Fig. 4-8 Taps configuration for spike studies in strands

to the probe and generally not used for critical current measurements, were connected to these additional taps in order to get the two half-coil signals.

To access the V-tap signals a break-out box was made, the signals were split in the box and then each signal was connected to several different connectors. All 6 signals pairs have been duplicated for being sent to the standard critical current readout system (slow DAQ) and to the SSTF fast DAQ system; moreover the two voltage signals coming from the two half coils have been hooked up to separate 8-pin connectors to be compatible with the VSDS system.



**Fig. 4-9 Taps configuration of the pick up coil for spike studies in strands**

For some tests an additional coil was also included on the top of the sample with the same geometry Fig. 4-9. The idea was to capture the same magnetic flux variation that the sample was experiencing during a voltage spike event. This allowed understanding if the sample signal was an inductive signal, a resistive signal or a combination of the two.

This pick up coil was made up from a copper wire electrically insulated with respect to the sample. The last spare pair of twisted wires was connected to half of the copper coil placing the voltage taps as close as possible to the taps of one half of the sample. In order to guarantee the pick-up coil position respect to the sample, they were glued together using sty cast Fig. 4-10. To connect the pick up coil to the VSDS the signal provided by the connector for the SSTF fast DAQ system was used.

During critical current measurements of the SSTF the current ramp is not continuous: It is close to a step function. Frequency of the steps is  $\sim 1.5$  seconds, which generates a fast  $\sim 10^{-2}$  sec sudden increase of the current. These current steps generate

inductive voltages in the coil that would interfere with spike measurements. With steps of 20 A the inductive voltage peak in the coil is about 2 mV. This value is unacceptable since we expect to measure voltage spikes of the order of 1 mV. Moreover this fast change in current is defeating the purpose of these measurements: studying the strands in conditions as similar as possible to those of magnets. For this reason a faster current control system was used that allows updating the current value every 2 ms instead of  $\sim 1.5$  seconds; achieving a significant reduction in the amplitude of the current steps.

For voltage spike measurements the LabView program used for voltage spike detection in magnets was slightly modified: a timer was introduced along with the capability to record another signal for the pick-up coil. In addition, the voltage resolution was increased since the voltage spike signals were smaller and the gain was unity since the isolation amplifier was not implemented.

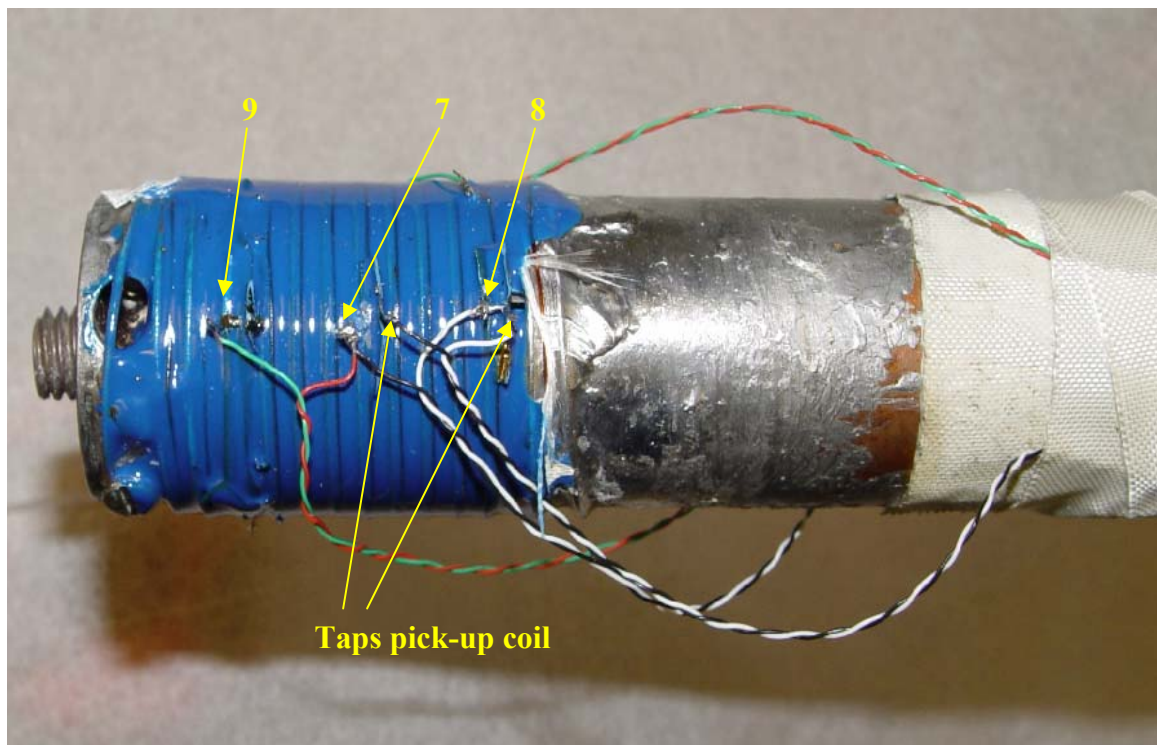


**Fig. 4-10 Taps and wiring configuration for spike studies in strands**

Since the polarity of the voltage signals depends on the direction of the sample's magnetization and the direction of the applied transport current it is important to show how the setup was made. Fig. 4-11 shows the schematic of the coil sample, the direction of the external magnetic field, the direction of the transport current, and the location of the voltage taps.

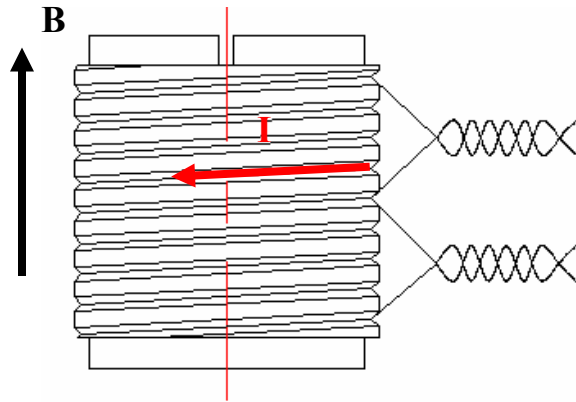


**Fig. 4-11 Magnetic field and current direction**

Voltage taps were connected to the DVM such away to obtain positive voltage signals if the sample is resistive and transport current is present. Fig. 4-11 we can also conclude that sudden flux increase will generate negative voltage signals.

### **4.3 Sample preparation and test procedure**

The strand samples were wound on grooved cylindrical Ti-alloy (Ti-6Al-4V) barrels for heat treatment in argon atmosphere. To provide adequate mechanical stability to 0.7 mm strands, Ti-alloy barrels with a smaller groove were procured and used. After reaction, the samples were either tested on the same barrel for regular tests or transferred to thicker G-10 barrels that would provide inner insulation for studies of the cooling effect. In such a case, the sample was first tested on the G-10 barrel, and then wrapped in fiberglass cloth, which was impregnated using a room-temperature epoxy to insulate it on its outer surface before being tested again. Sometimes the samples were impregnated at room temperature using sty-cast; this procedure was also used to study the cooling effect and to guarantee the mechanical stability of the sample. The mechanical stability was also favored by the relative directions of external magnetic field and transport current: They are oriented so as to generate an inward Lorentz force.

When only V-I measurements were performed, the general test procedure was to ramp up the solenoid to high field (~12-15 T), make the measurement at a constant field, and then reduce the field to 1 T for the next measurement. The magnetic field was then increased up to 12 T at a ramp rate of 1 T/min. In order to reach a higher field without quenching the solenoid the ramp rate was reduced to 0.5T/min. When decreasing the field a ramp rate of 1T/min was always employed.

For the V-I measurements two different current ramp rates were often used: a fast one at the beginning (~20A/sec) and a slower one (~1A/sec) until the sample quenched. The faster ramp rate was used to save time; however, at a certain field more than one measurement could be performed – one after the other without changing the field – to see if the quench current was different with smaller strand magnetization. Indeed, after each quench, and as long as the background magnetic field is unchanged, the strand magnetization gets smaller.

Initially when V-H measurements were introduced the general procedure was to make V-I measurements at a high field to measure the  $I_c$ , and then as soon as the  $I_q$  was smaller than  $I_c$  the solenoid field was ramped down to 0 T. At this point the V-H measurements were started. The current was raised to a certain value then the magnetic

field was ramped up, generally, to 4 T at 1 T/min. The measurement was stopped at 4 T because at higher magnetic field the difference in the quench current between V-I and V-H measurements was generally negligible. If the sample quenched before reaching 4 T, the field was brought back to 0 T and the measurement repeated at a different current value; otherwise, the V-H measurement was performed ramping down the field from 4 T to 0 T, generally at 1 T/min. The main goal of the V-H measurements was to find the minimum quench current at low field,  $I_{qm}$ .

After V-H measurements were finished, the V-I measurements repeated to measure the  $I_q$  at those magnetic fields that were not investigated. For these measurements a current ramp rate of  $\sim 1 - 20$  A/sec were used. It is important to notice that before voltage spikes measurements were introduced the current was increased by step; hence, the actual ramp rate was much higher during the current steps.

When voltage spike measurements were started the test procedure was modified slightly. The differences with the procedure described in the previous paragraphs were as follows: before making  $I_q$  measurements, using either the V-I or the V-H technique, the sample was quenched a few times in order to remove magnetization; the V-H measurements were performed by only ramping-up the background magnetic field. These measurements, which start with the sample not magnetized, are called E-2 (V-I) and E-3 (V-H). The VSIDS was activated each time the current or the magnetic field was ramped.

Before starting with the measurements the VSIDS system was checked in order to verify that everything was working properly. The first check was to inject a known signal into the system and verify that the right value was read correctly by all the channels of the VSIDS. The background noise of the bucked signal was then checked. If everything works properly the peak noise is normally less than 0.1 mV. If there is a noise problem that can not be solved a digital filter, which cuts frequencies lower than 800 Hz, can be activated. The voltage threshold generally used to detect volt spikes was 0.3 mV.

## 4.4 Data analysis steps and tools

### 4.4.1 Critical current measurements

The strands  $I_c$  is obtained through a V-I measurement (see chapter I for more details). The critical current measurement system acquires data about every 1.5 seconds. This time is not a constant value because it depends on the hardware latency in processing all the tasks. The three voltage signals,  $V_{1-6}$ ,  $V_{2-5}$  and  $V_{3-4}$ , Fig. 4-6, and the current values are saved in a text file.

For critical current measurements, generally two different current ramp rates are used. Initially the current is ramped up very fast to save time ( $\sim 20\text{A/sec}$ ). In the last part of the measurement the current ramp rate is reduced reasonably ( $\sim 1\text{A/sec}$ ) in order to record a sufficient amount of data points during the transition of the superconductor to normal state.

In order to evaluate the  $I_c$  generally only the signal  $V_{2-5}$  is used. The signal  $V_{1-6}$  is used for monitoring the resistance of the splice between the sample and the copper leads. This resistance has to be sufficiently low to guarantee that the sample does not warm up for a joule effect. If the splice's resistance is too high the signal  $V_{1-6}$  starts increasing exponentially with the current while the signals  $V_{2-5}$  and  $V_{3-4}$  are still zero. The signal  $V_{3-4}$  has two main purposes: 1) to estimate the strand homogeneity by comparing the  $I_c$  measured in different strand pieces; and 2) to be a backup signal in the case there is some problem with  $V_{2-5}$ .

Due to the inductive voltage, the signal offset is different depending on the current ramp rate. As we want to be sure to have a constant offset, in order to analyze the signals, only the voltage data associated with the lower current ramp rate is taken into account. In order to calculate the critical current – the  $n$ -value and the statistical errors associated with the voltage measurements – the experimental data have to be fitted. The parameterization that was used is the following (for detail appendix A):

$$V = V_{offset} + \frac{l}{A} \cdot \rho_c \cdot I_c \cdot e^{\frac{l-I_c}{I_c} \cdot (n+1)} \quad eq. 4-1$$

Where:

- $V$  is the measured voltage (in volts) between the two voltage taps;
- $V_{offset}$  is the measurement offset;
- $l$  is the length (in meters) of the strand between the two voltage taps;
- $A$  is the strand cross section (in square meters);
- $\rho_c = 10^{-14} \Omega m$
- $I_c$  and  $n$  are the free parameter of the fitting law.

Using eq. 4-1 as a fitting law, the signals  $V_{2-5}$  and  $V_{3-4}$  were fitted with the Matlab curve fitting toolbox. Between the different solving algorithms, the *trust region* algorithm, which represents an improvement over the popular *Levenberg-Marquardt* algorithm [99], was used. By the fitting procedure the  $I_c$ , the  $n$ -value, and the errors associated with the uncertainty of the voltage measurements were calculated. The estimation is based on the hypothesis that the uncertainty of the voltage measurement is independent of the voltage and current values.

The statistical errors on  $I_c$  and  $n$  have been calculated with a 95% ( $1.96\sigma$ )

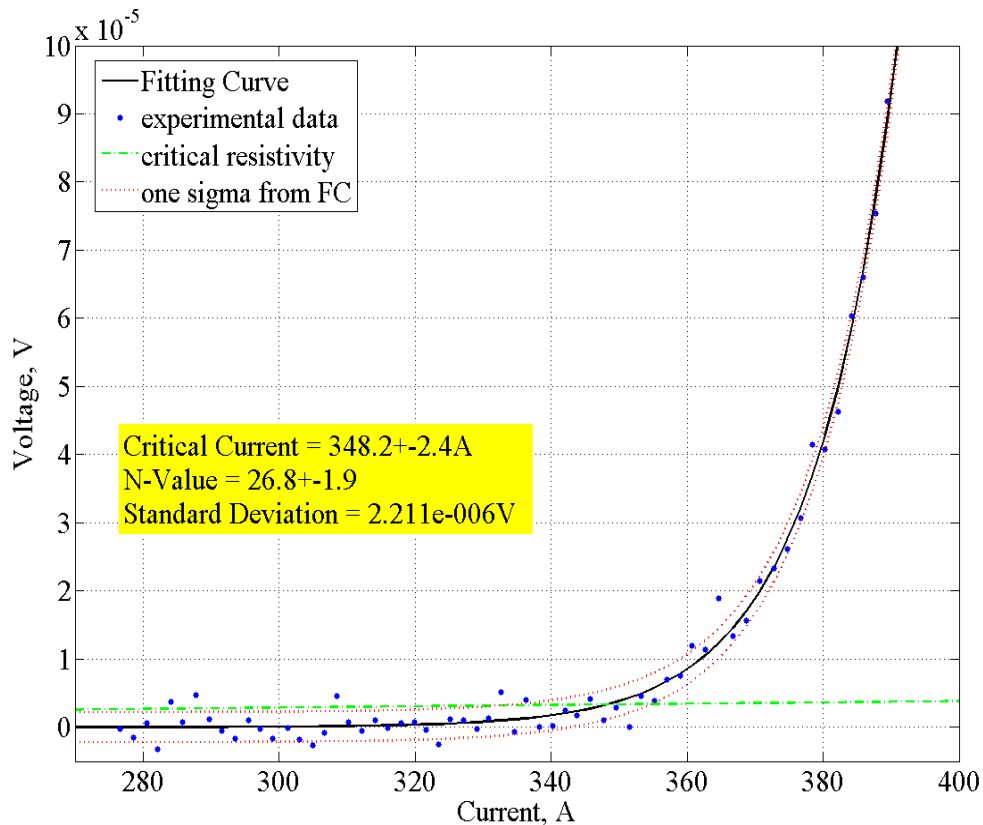


Fig. 4-12 Analysis of the critical current measurement

confidence level [100]. In Fig. 4-12 an example is shown of the results obtained using the fitting procedure: the blue dots represent the experimental data, the black line is the fitted curve, and the red lines represent the spread of the voltage measurements. In this specific case the uncertainty ( $1\sigma$ ) of the voltage measurements was  $2.211 \mu\text{V}$  and it caused a statistical error ( $1.96\sigma$ ) on  $I_c$  and  $n$  equal to 2.4 A and 1.9 respectively.

#### 4.4.2 Critical current estimate at low field using a scaling law

Using the V-I technique, the  $I_c$  can be measured only at high field ( $\sim \geq 9$  T for a Nb<sub>3</sub>Sn 1 mm MJR). In the low field region the measurement can be limited by the maximum current that the power supply can provide ( $\sim 1790$  A at the SSTF) or the quench current may be lower than the critical current value due to instabilities.

At the SSTF the  $I_c$  measurements are generally performed at high field and at 4.2 K. The values for lower fields and different temperature are then estimated using appropriate scaling laws. The goal of these estimations is to compare different data samples.

In a typical Short Sample Test Facility measurement we can assume that the temperature and strain are constant (the effect due to Lorentz forces can be neglected). Thus from eq. B-1 and B-2 (see appendix B) the following scaling law for a Nb<sub>3</sub>Sn strand perpendicular to the magnetic field can be derived:

$$I_c = \frac{A_{no\_cu} \cdot C \cdot b^p \cdot (1-b)^q}{B} = \frac{A_{no\_cu} \cdot C \cdot B^p \cdot B_{C2}^{-p} \cdot (1 - B \cdot B_{C2}^{-1})^q}{B} = C' \cdot B^{p-1} \cdot (1 - B \cdot B_{C2}^{-1})^q$$

Where:

$A_{no\_cu}$  → area of the superconductor contained in the composite strand

$$C' = A_{no\_cu} \cdot C \cdot B_{C2}^{-p}$$

Assuming for Nb<sub>3</sub>Sn the coefficients  $p$  and  $q$  are equal to 0.5 and 2 [101,102]:

$$\boxed{I_c = C' \cdot B^{-0.5} \cdot (1 - B \cdot B_{C2}^{-1})^2} \quad \text{eq. 4-2}$$

In this case the scaling law for the critical current is a function of the magnetic field with two parameters: a scaling factor and  $B_{C2}$ . In order to get these parameters from our measured data a weighted least-square fit has to be applied. The weights are the inverse of the variance of the data measurements.

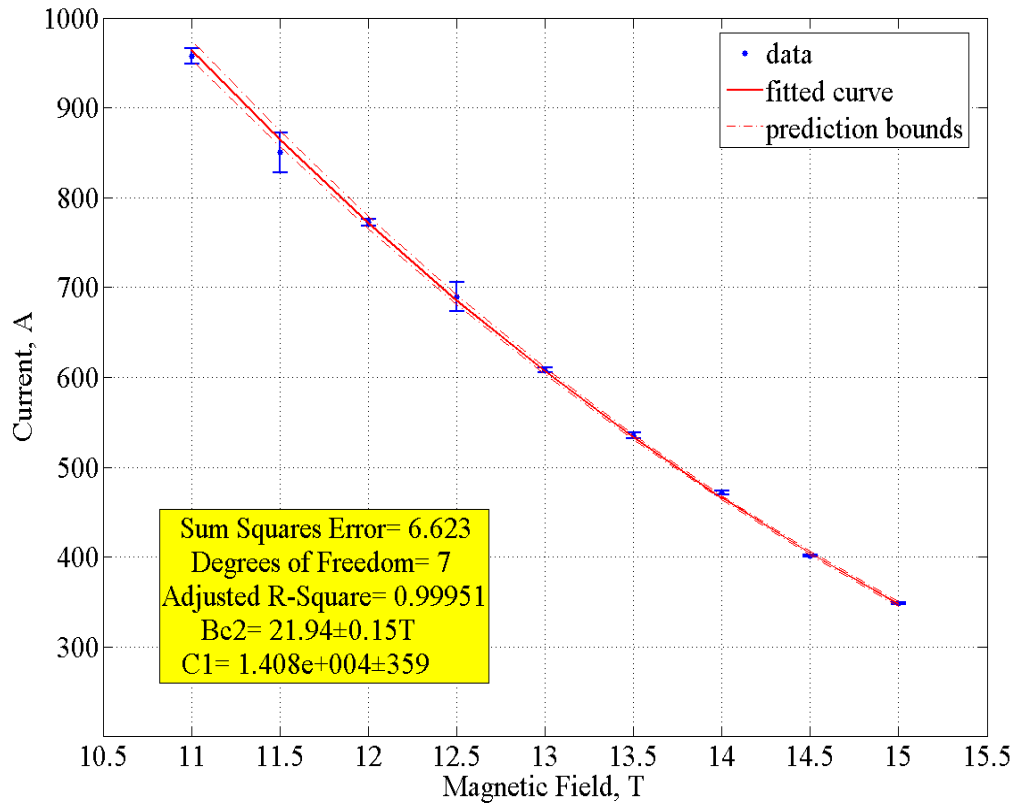


**Fig. 4-13 Fit of the critical current measurements for a 1 mm MJR strand**

To obtain the correct result the measured  $I_c(B)$  data must be corrected for self field effects. Since the self field and the current density are changing within the strand it is not obvious what field value should be taken to characterize a strand at a given  $I_c$  value.  $I_c$  itself is obtained by integrating different critical current densities along the cross section of the strand. Although naturally one would pick the average field value of the strand, it has been shown [103] that the relevant field value to apply, which works for the parameterization described in the previous paragraph, is the peak field value.

At the SSTF the background field  $B_{bg}$  is constant and oriented along the axis of the solenoid sample. This means that the peak field will be on the internal or external surface of the coil. Using a straight strand self-field approximation, the peak field at the strand surface is equal to [104]:

$$B_p = B_{bg} + \frac{\mu_0}{\pi \cdot D} I$$

For a 1mm MJR strand the diameter of the superconductor is 0.8 mm:

$$B_p = B_{bg} + \frac{4\pi \cdot 10^{-7}}{\pi \cdot 0.8 \cdot 10^{-3}} I = B_{bg} + 0.5 \cdot 10^{-3} \cdot I$$

According to a two dimensional finite element analysis the peak self-field for a current of 1000 A is anti-parallel to the background field and equal to 0.648 T while the peak field in the parallel direction is 0.413T. This means that the peak field in our coil is:

$$B_p = \max(B_{bg} + 0.413 \cdot 10^{-3} \cdot I, 0.648 \cdot 10^{-3} \cdot I - B_{bg}) \quad eq. 4-3$$

Fig. 4-13 shows the result of the fitting procedure taking into account the self-

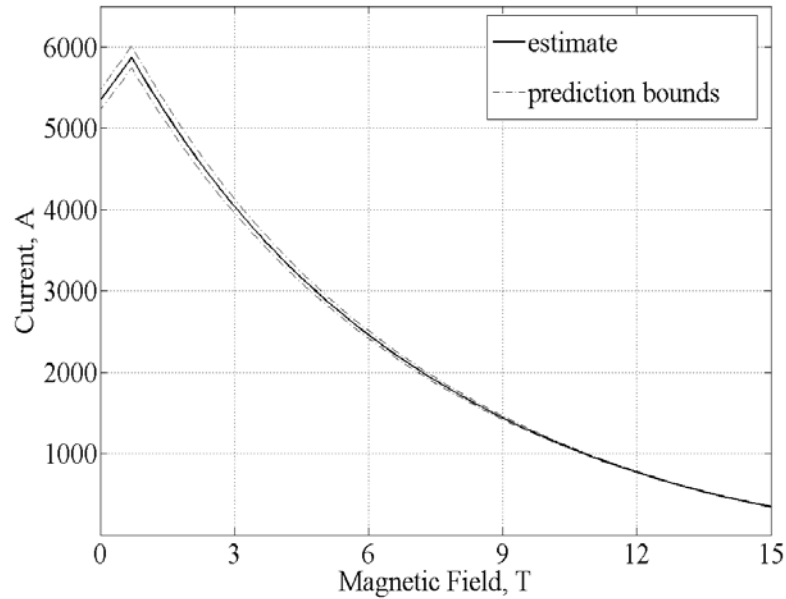


**Fig. 4-14 Critical current estimate of a 1 mm MJR strand including the self field effect.**

field correction for a 1mm MJR strand measured at the SSTF. The errors bars [100] on the measured data have been calculated with a 95% (1.96 $\sigma$ ) confidence level. For the prediction bounds as well, the confidence level is 95%. As it can be seen from the plot, the goodness of fit is excellent, 0.99951.

Fig. 4-14 shows the estimate value of the  $I_c$  at low field and 4.2K for the same strand of Fig. 4-13 . The decrease in critical current, for background field values lower than 0.7 T, is due to the increase of the peak field (*eq. 4-3*).

$$B_p = 0.648 \cdot 10^{-3} \cdot I - B_{bg}$$

### 4.4.3 Analysis of voltage spikes measurements

The first analysis was to verify the polarity of the signal by checking the signal shape during a quench. The coil section, where the quench starts, should have a positive resistive signal. If that was not the case the polarity was changed by multiplying all the signals by minus one. In Fig. 4-15 a ‘typical’ quench signal recorded by the VSIDS is shown. The voltage of the section that is quenching grows positive while the voltage of the other section grows negative. This negative signal is inductive and it is due to the decrease in current provided by the power supply.

As these voltage spikes are a phenomena not covered much in literature, the type of analysis performed was extremely simple but time consuming. Each signal was plotted and analyzed one by one by studying the polarity, shape, peak voltage, and the elapsed time of the signal. The following signal characteristics were then correlated with the physical conditions of the sample during the measurement: Magnetic field value, transport current value, and strand magnetization. Through this process the signals have been regrouped in different types.

A Matlab routine was used to generate the plots. For each time window saved by the VSIDS (0.5 ms for a sampling rate of 100 kHz), the routine identified the number of

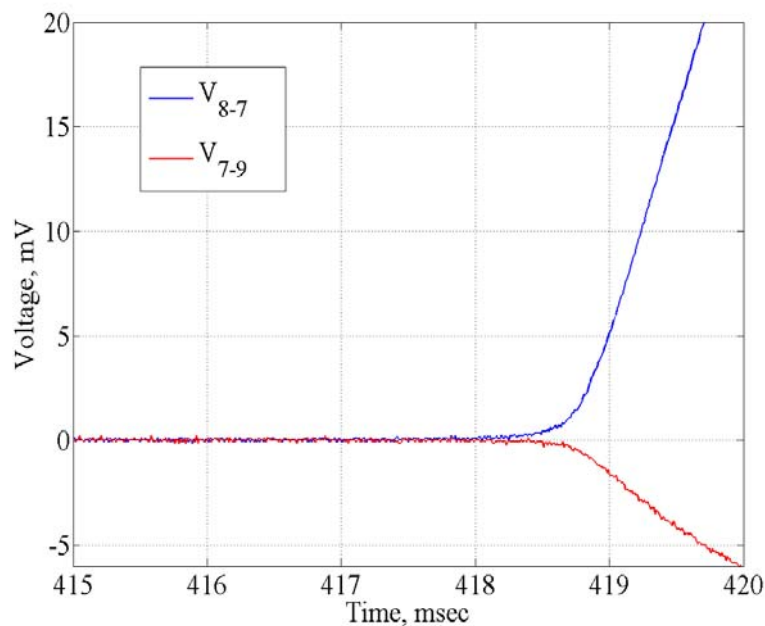
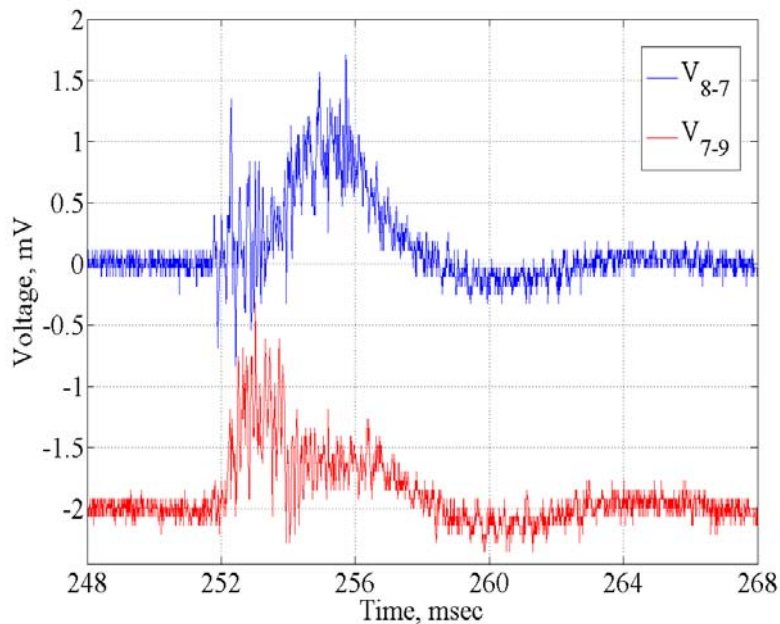


Fig. 4-15 Typical quench signal

spikes (generally one in 0.5 s) and a time frame (generally 0.1 ms) when the signals were buried in the noise floor.

Next, the program reprocessed the signals using the noise part to remove the offset and, if necessary, to improve the noise level using a matched filtering technique.

As final step, for each voltage spike, the program made two plots in a time window of 20 ms. One plot, Fig. 4-16, contained the signals  $V_{8-7}$ ,  $V_{7-9}$  and in case there was the pick up coil  $V_{10-11}$ ; the other plot, Fig. 4-17, the sum and the difference of  $V_{8-7}$  and  $V_{7-9}$ . To be able to compare the signals easily, some signals have been offset. Sometimes a third plot, Fig. 4-18, was done to show the moving averages of the signals  $V_{8-7}$ ,  $V_{7-9}$  in order to remove the high frequency components. Generally the signals were averaged over a millisecond or less. All of the quench signals were then analyzed to verify if the quench development was preceded by a voltage spike.



**Fig. 4-16 Voltage spike: 2 half coil signals**

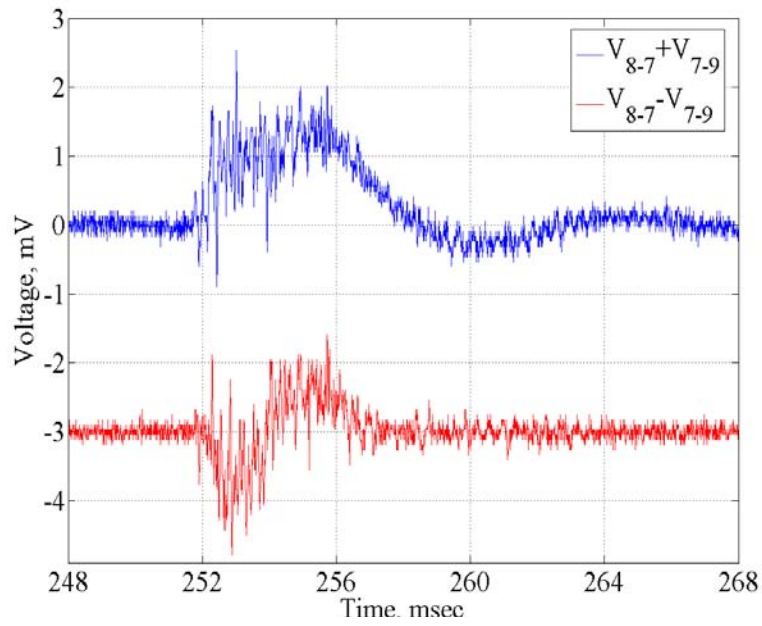


**Fig. 4-17 Voltage spike: 2 half coil signals**

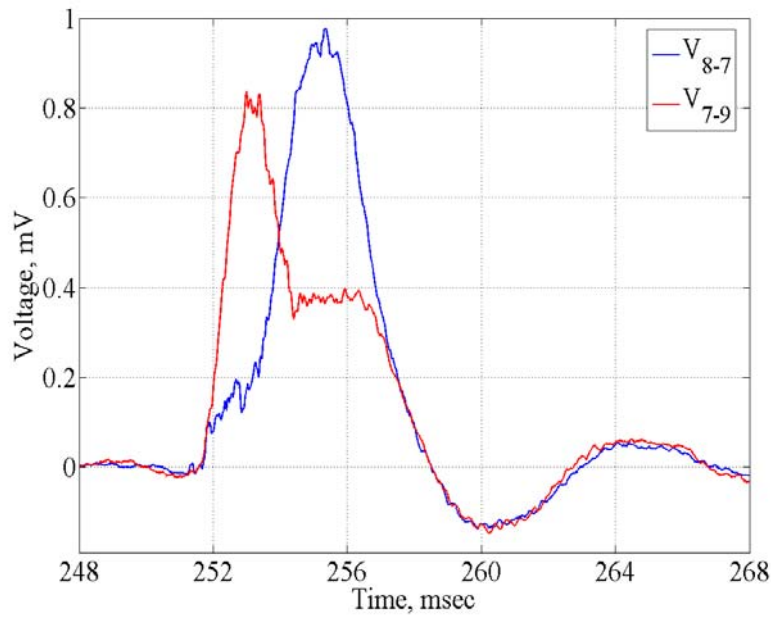


**Fig. 4-18 Voltage spike: moving average of the 2 half coil signals**

The background of voltage spike measurements was measured using the same setup but substituting the superconducting strand with a copper strand. It was found that two sources of noise can trigger the VSDS: the first one is a fast variation of the magnetic field when decreasing the solenoid field below  $\sim 0.6$ T and the other is due to a mechanical vibration of the sample holder.

Fortunately the signals generated by these two phenomena are very characteristic and they can be easily distinguished by the voltage spike signals that have been identified in this research. The signals due to the solenoid are shown in Fig. 4-19; their time constant is much higher than those of voltage spikes. The signals related to the mechanical motion, Fig. 4-20, are characterized by high frequency oscillations with a mean value equal to zero.

While sweeping up and down the magnetic field between 0 and 15 T, with the sample surrounded by air (the needle valve was closed), no signal was recorded. These ramp cycles, 0-15-0 T, were repeated three times. Once the sample was surrounded by liquid helium at 4.2 K about three oscillating signals per ramp were recorded. The experiment was repeated several times. Most of these oscillating spikes were at field and higher than 9 T; however, a signal at 4.8 T was collected. These signals could also be produced by pattering the steam of the needle valve. These results suggested that the oscillating signals are due to vibration of the sample holder probably induced by liquid helium flow.

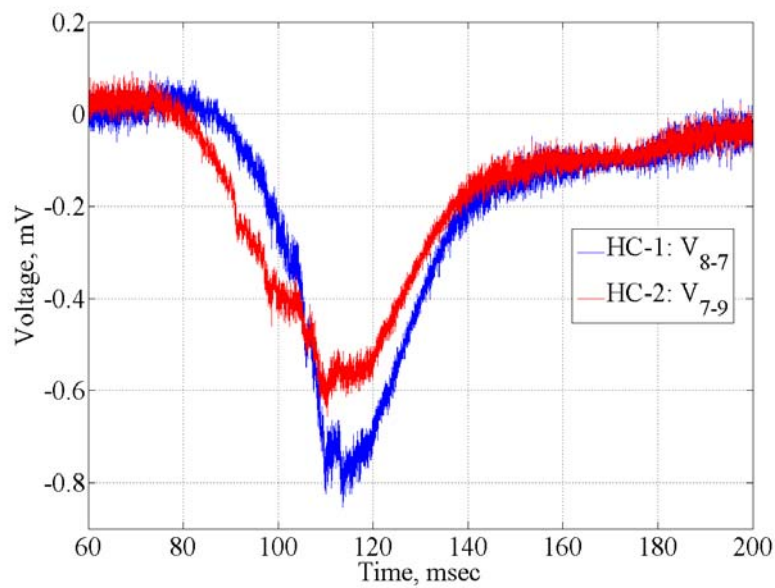


**Fig. 4-19 Voltage signals induced by the solenoid while ramping down the field below 0.6 T**

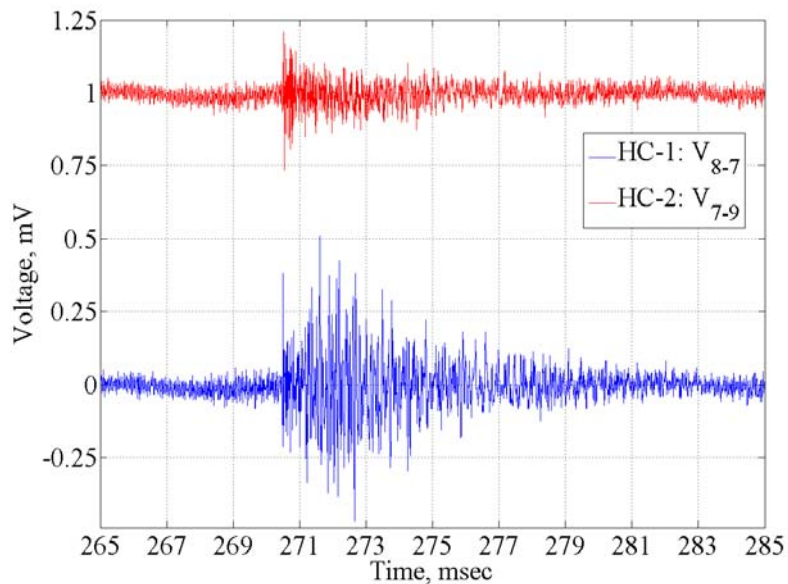


**Fig. 4-20 Voltage signals due to the sample motion**

## 4.5 Test results

### 4.5.1 Quench current of Nb<sub>3</sub>Sn strand during V-I measurements

Before this research began at the SSTF, in the first six months of 2003, some MJR strands were tested at low field using the V-I technique [105]. The scope of these measurements was to observe if the MJR strand performance was limited by thermo-magnetic instabilities and above all if the minimum quench current value in the low field region (~0–6 T) for a 1 mm strand was in a current range (~500A), which could explain the magnet's performance.

In the next pages the most meaningful measurements will be shown. These measurements have been divided into two groups according to the time length of the last phase, at 650 °C, of the heat treatment: 180 hrs or 120 hrs. The longer heat treatment was the nominal OST heat treatment and it was the same one used for the magnets.

Three types of strands are generally tested at SSTF: ‘extracted’, ‘rolled’ and ‘round’ strands. The ‘extracted’ strands are extracted from a cable; the ‘round’ strands are cut from the billet and directly wound around the barrel; the ‘rolled’ strands are ‘round’ strands, which are plastically deformed before winding them around the barrel. This last type is tested to study the effect of a controlled plastic deformation of the strand.

**Tab. 4-1 Properties and test set-up of 1mm MJR strands heat treated for 180 hrs at 650 °C**

Sample name	Filament size [μm]	Number of filaments	Cu %	Status of deformation	Barrel material	Bonding
6b	110	54	47.8 ± 0.3	Round	Ti-6Al-4V	None
14	110	60	46.7 ± 0.3	Round	Ti-6Al-4V	None
18b	110	54	47.8 ± 0.3	Rolled	Ti-6Al-4V	Sty-cast
25	110	54	47.8 ± 0.3	Extracted	Ti-6Al-4V	None

All the relevant information regarding the strand properties and the test setup are summarized in Tab. 4-1 and Tab. 4-2: name to identify the sample [105]; diameter of the sub-elements; number of the sub-elements; percentage of the copper area in the strand section; status of the strand mechanical deformation; barrel material; and the material for insulating the sample and for bonding it to the barrel. Regarding the name to identify the

sample, the same number and a different letter indicate the same sample that was tested with and without a bonding agent.

In Fig. 4-21 the normalized quench current is shown as a function of the magnetic field peak value for the samples that had the nominal OST heat treatment. Analyzing this plot, despite the fact that the sample conditions are quite different, it can be observed that the quench behavior is quite similar. There is a stable region at high magnetic field, above 10 T, where the MJR strands reach their critical current; there is also a strongly unstable region below 6 T where the normalized quench current is very low and is almost linearly decreasing with the magnetic field. The spread in the normalized quench current values is limited at the ‘transition’ region, 10-6 T, where the strands are unstable and where a quite big spread in the normalized quench current values occurs.

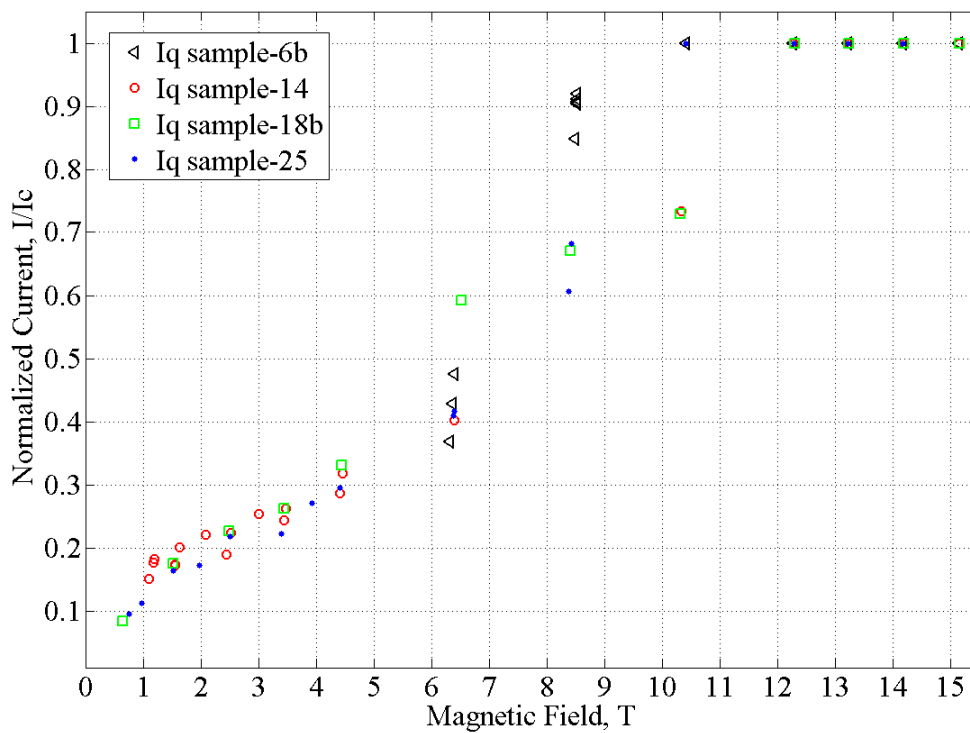


Fig. 4-21 Normalized quench current of 1mm MJR strands, HT 180h at 650K

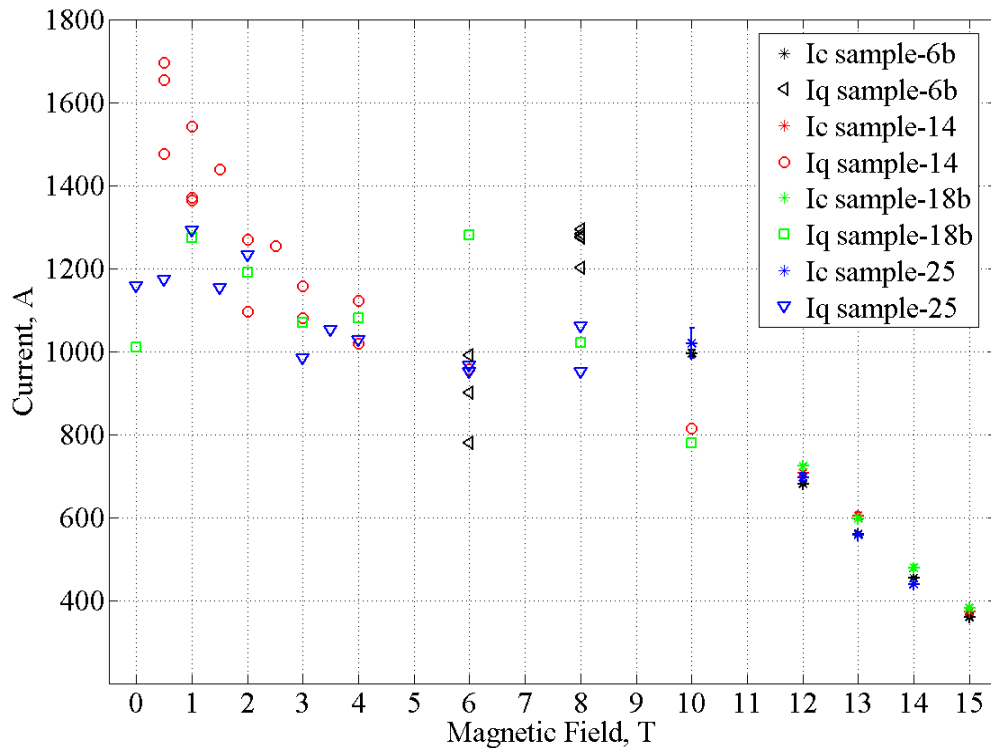


Fig. 4-22 Quench current of 1mm MJR strands, HT 180h at 650K

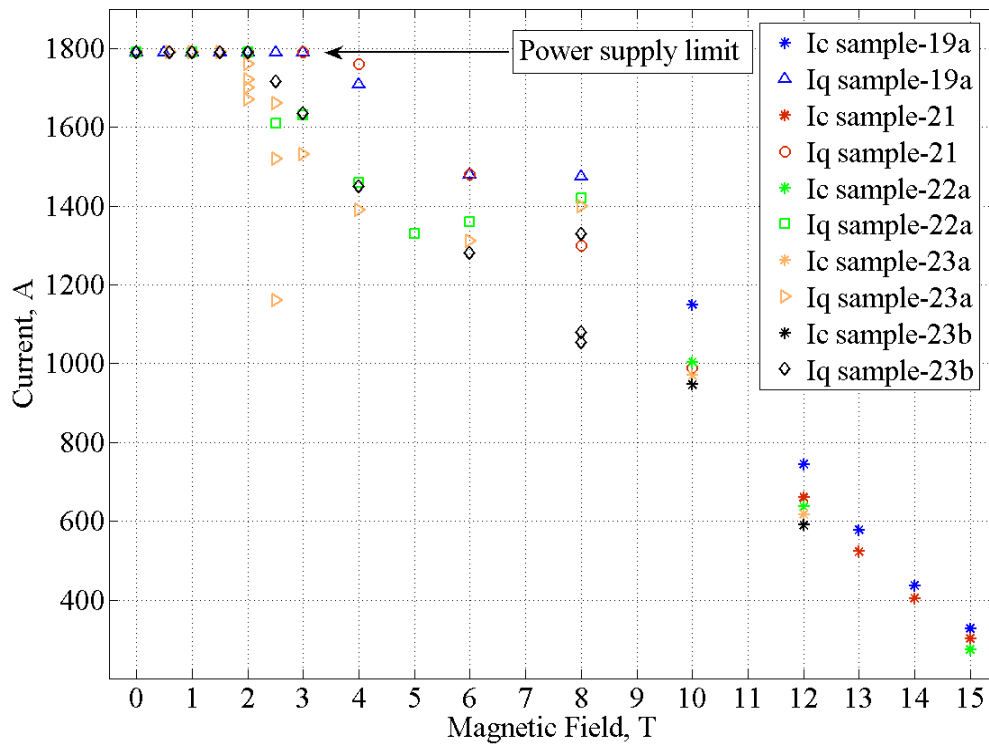
The same measurements are also showed in Fig. 4-21 where the quench current values are plotted as a function of the background magnetic field. From this plot it can be noticed that when the magnetic field is decreased the quench current increases down to 8T then it starts decreasing where it reaches a minimum around 6 T. At that point it increases again. It can also be observed that the quench current variation below 8T is limited to only few hundreds Amperes. The most relevant information, which can be drawn from this plot, is that even if the strands are strongly unstable the minimum quench current value in the low field region can not justify the magnets' limited performance.

Fig. 4-23 shows the quench current, as a function of the background magnetic field, for the strands that had a shorter heat treatment. In the high field region, the critical current is reached down to 10 T and the quench current keeps increasing down to 8 T. This behavior was similar to what was observed for the strands with a longer heat treatment. The only relevant difference was at lower magnetic fields, although the quench currents were still much lower than the critical currents, in this case  $I_q$  values were a few

hundred amps higher. Note that for a magnetic field lower than 2-3 T the power supply limit was reached.

**Tab. 4-2 Properties and test set-up of 1mm MJR strands heat treated for 120 hrs at 650 °C**

Sample name	Filament size [ $\mu\text{m}$ ]	Number of filaments	Cu %	Status of deformation	Barrel material	Bonding
19a	110	54	$47.8 \pm 0.3$	Round	Ti-6Al-4V	None
21	110	54	$47.8 \pm 0.3$	Round	Ti-6Al-4V	Sty-cast
22a	110	54	$47.8 \pm 0.3$	Round	G-10	Sty-cast
23a	110	54	$47.8 \pm 0.3$	Round	G-10	None
23b	110	54	$47.8 \pm 0.3$	Round	G-10	Sty-cast



**Fig. 4-23 Quench current of a 1mm MJR strands, HT 120h at 650K**

The increase in the quench current at low field is due to the higher thermal and electrical resistivity of the copper stabilizer. The smaller quantity of tin in the copper allows increasing significantly its RRR. In this case, the tin diffusion process into the

copper was limited because the barriers around the sub-elements were not damaged by mechanical deformation and because the duration of the heat treatment was shorter.

**Tab. 4-3 Properties and test set-up of 0.7mm MJR strands heat treated for 60 hrs at 650 °C**

Sample name	Filament size [ $\mu\text{m}$ ]	Number of filaments	Cu %	Status of deformation	Barrel material	Bonding
39ab	80	54	$47.4 \pm 0.2$	Round	Ti-6Al-4V	None
40a	80	54	$47.4 \pm 0.2$	Round	G-10	None
40b	80	54	$47.4 \pm 0.2$	Round	G-10	Glass

In order to study the details of thermo-magnetic instabilities in MJR strands with high RRR copper stabilizer during V-I measurements, it was decided to test strands with a smaller diameter, 0.7 mm, so the results are not limited by the power supply. The last step of the heat treatment at 650 °C lasted 60 hrs; this short heat treatment allowed to keep quite high (220) the copper RRR. In Tab. 4-3 additional information for these strands are summarized.

The same three field regions observed for low RRR 1 mm MJR strands, can be identified from the normalized quench current as a function of the magnetic peak field, Fig. 4-24. The main difference is that in the ‘transition’ region, between 6 T and 10 T of the background magnetic field (6.7 -10.3 T of the peak field), the drop of the normalized quench current is much more limited. For the 1 mm strands, which had a long heat treatment, the value of the normalized quench current with a background field of 6 T was between 0.4 and 0.6 while it was between 0.8 and 0.9 in this case.

It is also interesting to note that, with a background field of 0 T, the normalized quench current value is more than two times higher than for the former case. This significant improvement in the strands' stability is not only due to the better copper stabilizer but also to the fact the self-field instability is stronger in the strand with the larger diameter.

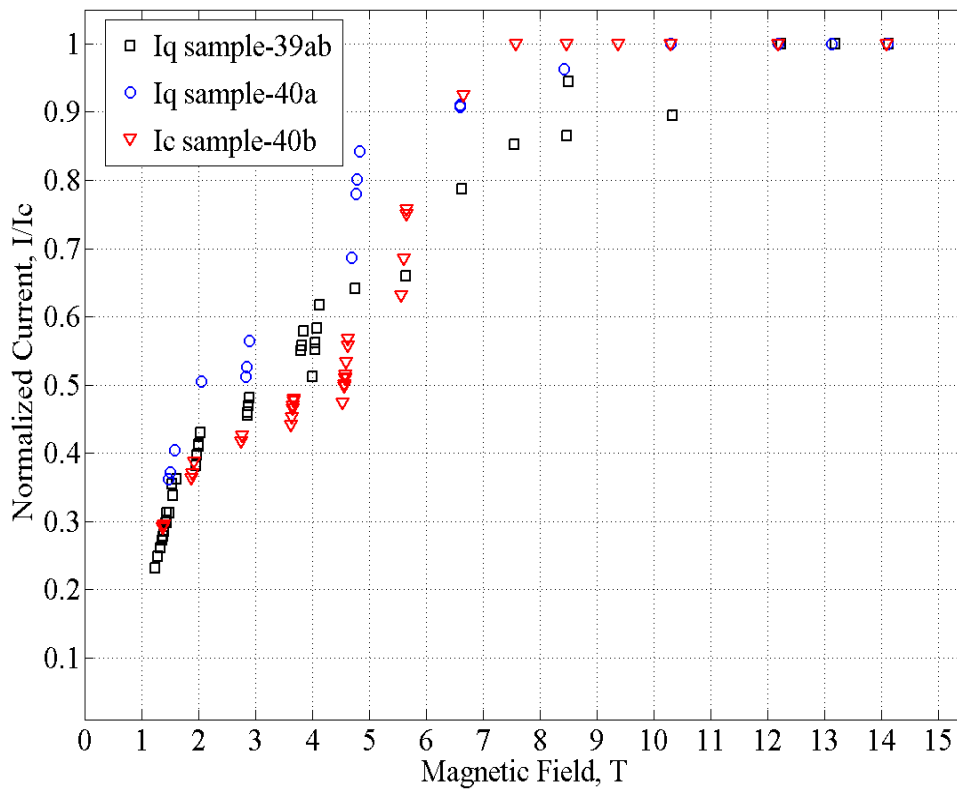
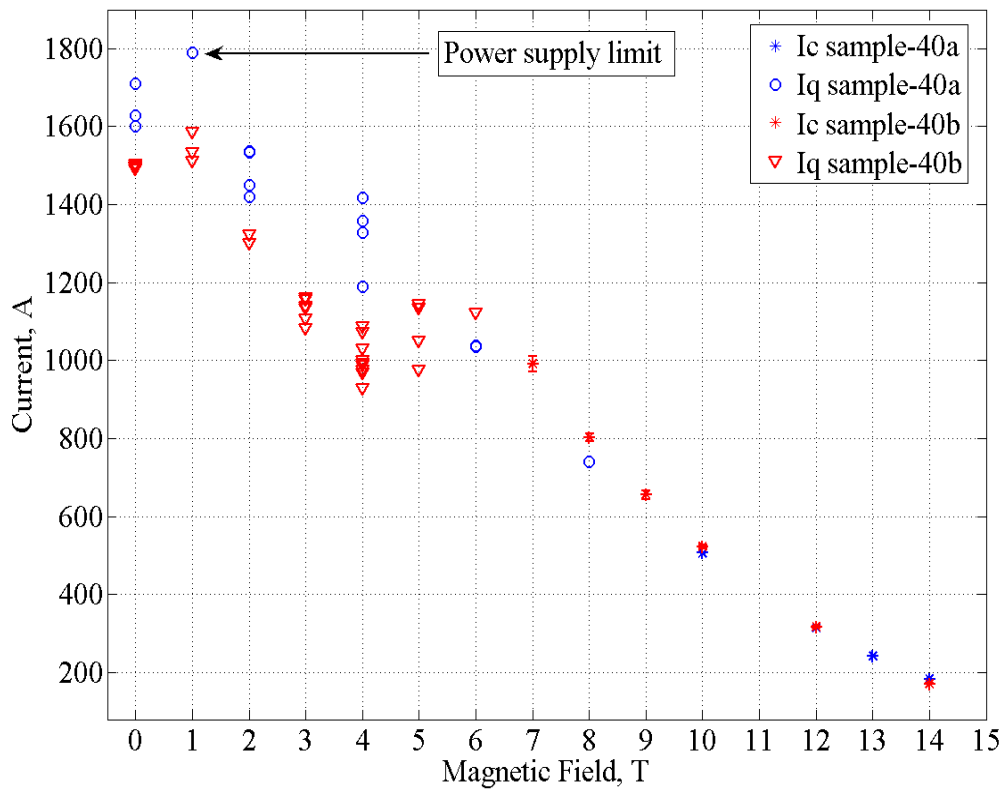


Fig. 4-24 Normalized quench current of a 0.7mm MJR strands, HT 60h at 650K

In Fig. 4-25 the quench current for the same strand with high RRR is compared with and without a bonding agent. Despite the fact that the critical current value is almost identical, it can be observed that the quench current of the sample without the bonding agent is about 20% higher at low field; this is most likely due to the cooling effect. When the copper RRR is sufficiently high to slow down the instability process, part of the heat generated can diffuse in the liquid helium.

These measurements show also that the bonding agent allows measuring the critical current at a lower magnetic field. In this case it was possible to measure the critical current down to 7 T while without the bonding agent the critical current could not be measured below 10 T. This phenomenon has been observed frequently and it is most likely due to a reduction of the perturbation spectrum (the bonding agent reduces the micro-motion of the conductor).



**Fig. 4-25 Quench current of a 0.7mm MJR strand, HT 60h**

In Fig. 4-26 the quench current of a 0.7mm MJR strand is shown for a different current ramp rate. In all the experiments shown, the current is changed by a step; the time of the variation is of the order of  $10^{-2}$  sec. In this test, using different current steps, no significant dependence of the quench current with the ramp rate could be observed.

During V-I measurement the same type of instabilities are also present in strand with much smaller filament size. In Fig. 4-27 it is shown that the quench current of a 0.7 mm PIT strand with a critical current comparable to that of the previous 0.7 mm MJR strands. Despite the fact that for this case the filament size of the strand is only 35  $\mu\text{m}$ ; the quench behavior is very similar to what observed for the 0.7 mm MJR strand with high RRR.

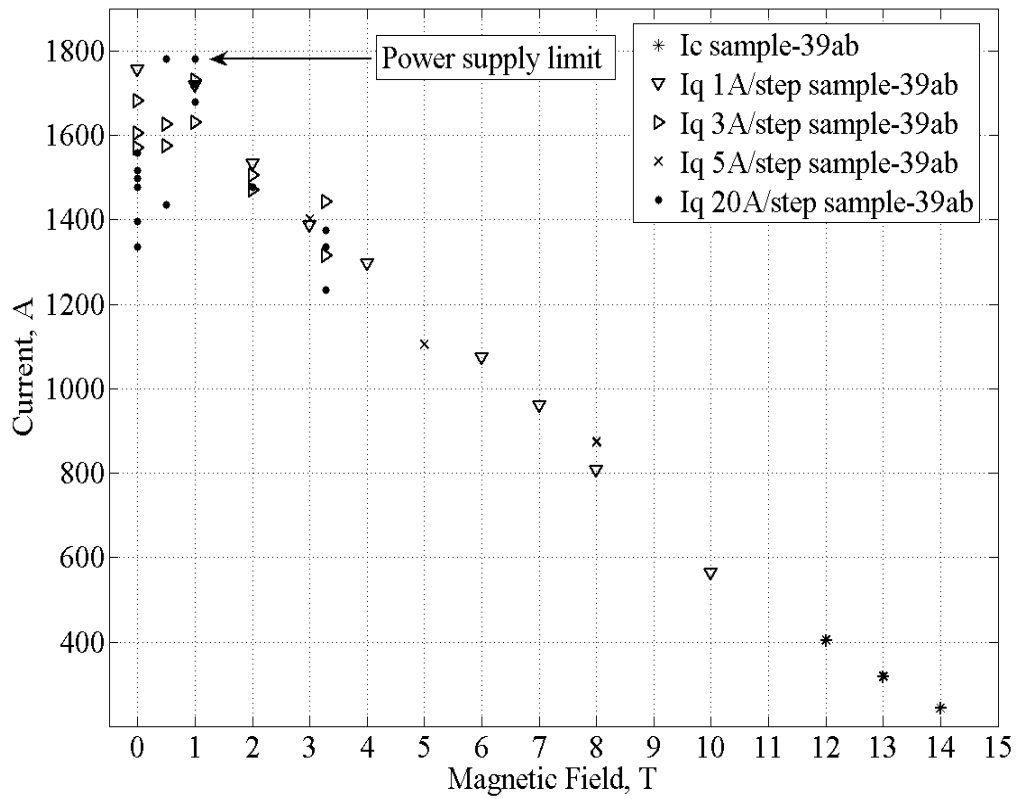


Fig. 4-26 Quench current of a 0.7mm MJR strand, HT 60h at 650K

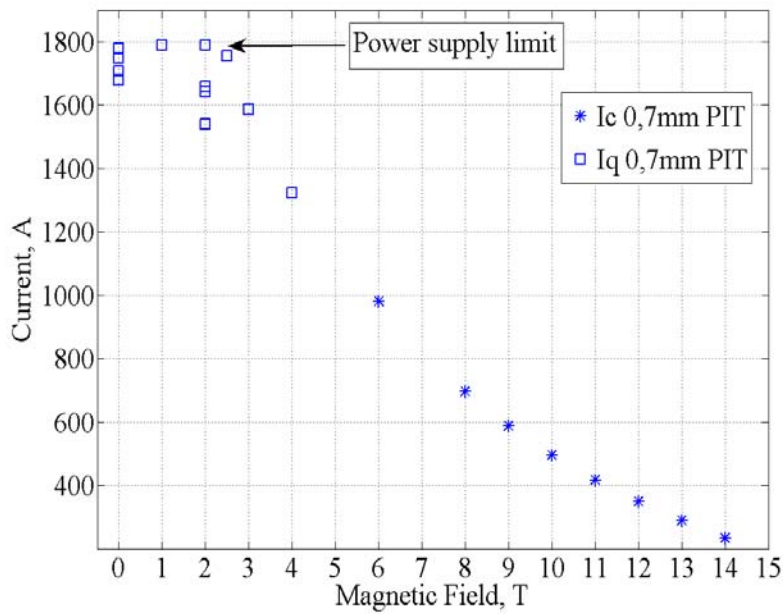


Fig. 4-27 Quench current of a 0.7mm PIT tested on a Ti-alloy barrel

#### 4.5.2 Quench current of Nb<sub>3</sub>Sn strand during V-H measurements

The V-I measurements showed that at low fields Nb<sub>3</sub>Sn MJR and PIT strands had premature quenches due to thermo-magnetic instabilities. Nevertheless the values of the quench current during these measurements were too high to explain the limited quench performance of magnets built at Fermilab and based on 1 mm MJR strands.

During V-I measurements, the strand physical conditions are much different from those of a strand in a magnet where the current is increasing. The main difference is that during the magnet energization not only the transport current increases in the strand but also the background magnetic field. A variable magnetic field magnetizes the strands, and for strands with high  $j_c$  and big filament size this means a significant amount of magnetization energy stored in the strand. The magnetization energy can be suddenly released and this can further reduce the value of the quench current.

At Fermilab, sudden releases of magnetization energy were observed in MJR and PIT strands during magnetization measurements. The magnetization of strand samples was measured while ramping the magnetic field, which is perpendicular to the strand, up and down between 0 T and 3 T.

In Fig. 4-28 a typical magnetization measurement is shown. The sample is a 1 mm

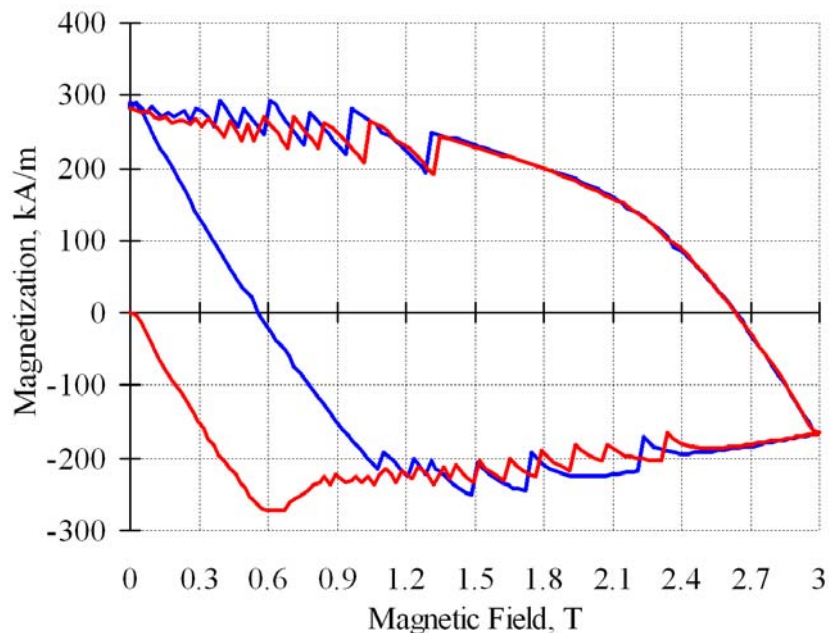
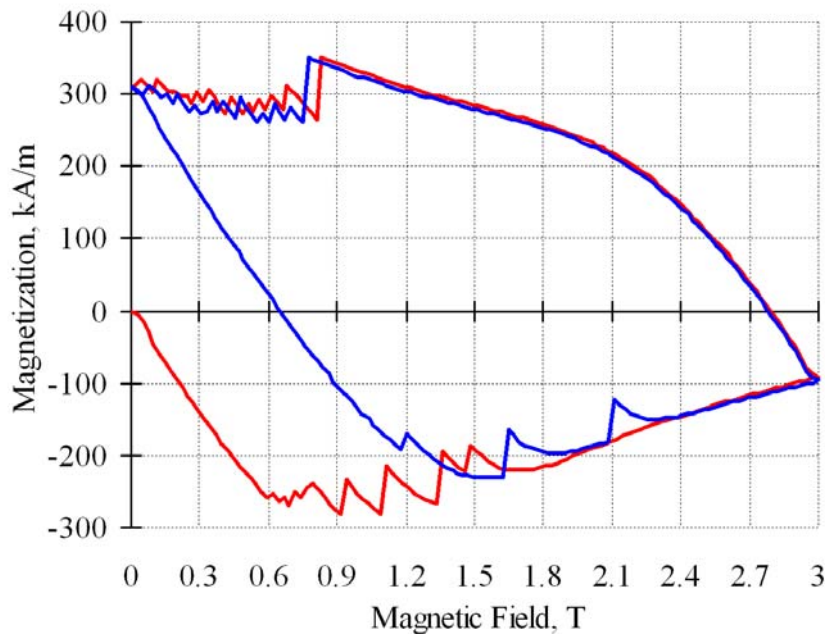


Fig. 4-28 Magnetization loop: 1mm MJR; HT 180hrs at 650 °C

MJR strand with the same characteristics and heat treatment as the sample 6b presented in Tab. 4-1. The red line represents the curve of first magnetization: the magnetic field is ramped up starting with a sample not magnetized. The blue line is the magnetization loop once the hysteretic effect is developed. In these curves the collapse of the magnetization are represented by the sharp variations of the magnetization value.

Fig. 4-29 shows the magnetization loop for a 1 mm MJR strand with the same geometrical characteristics as sample 14 (Tab. 4-1) but with a different heat treatment: the sample was at 650 °C for only 72 hrs. In this case, the flux jumps appear in a smaller field range than for the previous case.



**Fig. 4-29 Magnetization loop: 1mm MJR; HT 72hrs at 650 °C**

In order to simulate the physical condition of a strand in a magnet it was decided to perform V-H measurements. This technique was already used in the 1970's to study thermo-magnetic instability in NbTi multifilament strands [80].

Initially these measurements were performed on 1 mm MJR strands which had a short heat treatment (high RRR). The magnetic field was swept up from 0 to 5 T with a ramp rate of 1 T/min. In Fig. 4-30 V-H measurements of a 1 mm MJR with a high RRR are presented. The strand properties and the test set-up are summarized in Tab. 4-4.

**Tab. 4-4 Properties and test set-up of first 1mm MJR strands measured with the V-H technique**

Sample name	Filament size [ $\mu\text{m}$ ]	Number of filaments	Cu %	Cu RRR	Status of deformation	Barrel material	Bonding
38a	110	60	$46.7 \pm 0.3$	146	Round	G-10	None
38b	110	60	$46.7 \pm 0.3$	146	Round	G-10	Sty-cast
41abcd	110	60	$46.7 \pm 0.3$	7.4	Round	G-10	None

Note that the quench current was lower using the V-H technique than for the V-I in the very low field region ( $\sim 0\text{-}3$  T). The minimum value of the quench current in this field range will be called *minimum quench current*,  $I_{qm}$ .

In July 2004 it was then decided to perform V-H measurements on a 1 mm MJR strand with low RRR. The test results are shown in Fig. 4-31 and the strand properties are summarized in Tab. 4-4. The minimum quench current was 550 A at about 1.4 T; this

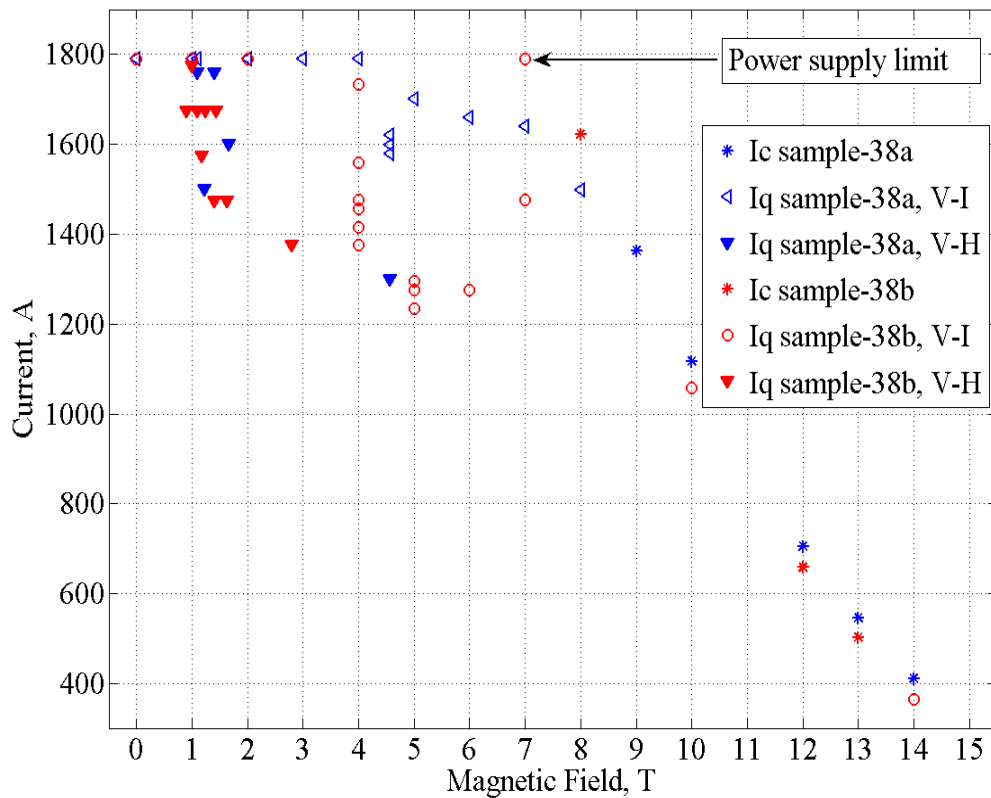


**Fig. 4-30 Quench current of a 1 mm MJR strand, RRR=146**

current value was consistent with the limited quench performance of the MJR magnets built at Fermilab. This was the first experiment at Fermilab demonstrating that premature quench currents in magnets due to thermo-magnetic instabilities can be foreseen by strand's measurements. Since then, V-H measurements of strands have become a standard procedure at Fermilab to evaluate if a strand is suitable to build a magnet not limited by thermo-magnetic instabilities (52). Similar results were also obtained by other researchers (53, 54).

In Fig. 4-31 it is interesting that the most critical region is between 1 T and 2 T and this region exactly corresponds to the field range where big flux jumps were observed in magnetization measurements, Fig. 4-28.

Analyzing Fig. 4-31 further two more relevant conclusions can be drawn regarding V-I measurements: 1) at very low field ( $\sim 0-3T$ ) the quench current is lower if the measurement starts with the sample magnetized, (solid red square); 2) the quench current values at a certain field have a big spread (300-400A), even if the measurements started with the sample not magnetized.

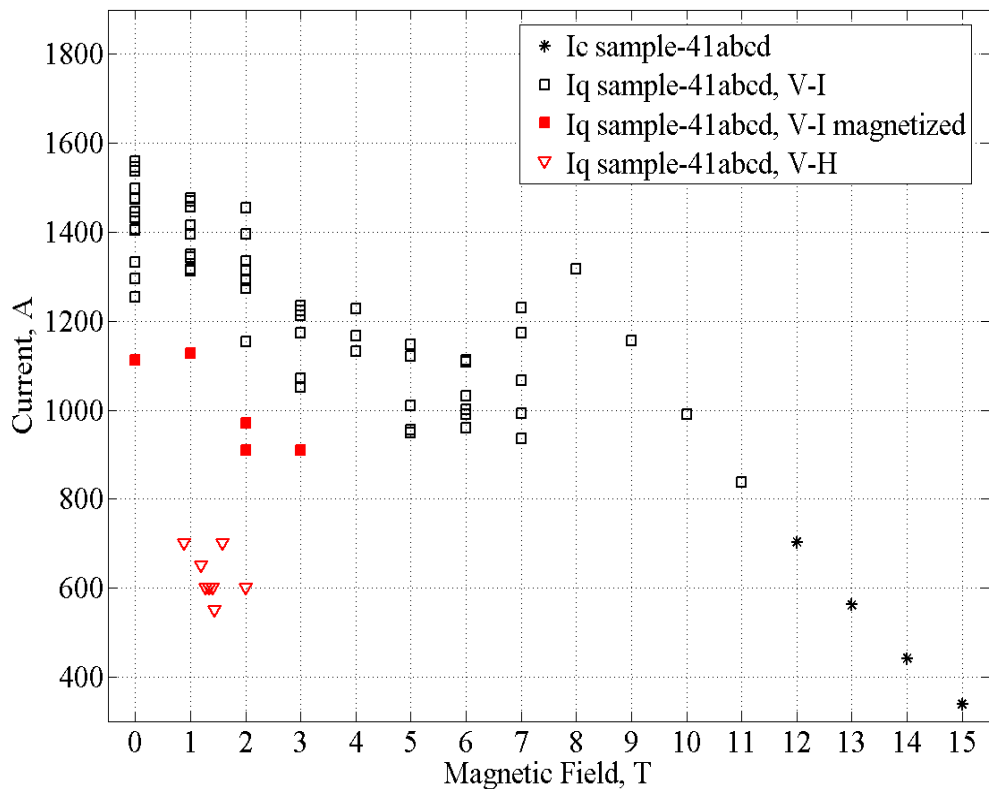


Fig. 4-31 Quench current of a 1 mm MJR strand, RRR=7

In order to understand the mechanisms that govern thermo-magnetic instabilities it was decided to test systematically different types of strand while also monitoring the voltage spike signals during each measurement [106, 107]. The spike results will be discussed in the next section, while here the quench current values are analyzed. All of these strands were tested in Ti-alloy barrels and unlikely previous experiments, the current was increased continuously and not in steps.

The strand properties are summarized in Tab. 4-5. Each sample was exposed to all three different measurement conditions (E1, E2, E3) described in section 4.3. Each point in the following figures is labeled with a symbol corresponding to the type of experiment performed (E1, E2, E3).

The first two samples were identical 1 mm MJR strands that were heat treated differently in order to have: 1) a low RRR (=7) sample A, and 2) a high RRR (=130) sample B.

For sample A, Fig. 4-32, we observed reversible transitions down to 11 T. Further decreasing the field from 10 T to 8 T and performing E2 type measurements, the  $I_q$  was below  $I_c$  but was still increasing. When decreasing the field further to 7 T,  $I_q$  started to decrease. The ratio  $I_q/I_c$  at 3 T was about 0.6. In the low field region between 0-3 T,  $I_q$  was significantly lower than  $I_c$ .

For sample B, Fig. 4-32, the transition was measured down to 11 T. With further decrease in the field,  $I_q$  increased until the power supply limit (PSL) was reached. Despite

**Tab. 4-5 Properties and test set-up of 0.7mm MJR strands heat treated for 60 hrs at 650 °C**

Sample name	SC	Strand type	Diam. [mm]	Filament size [μm]	Number of filam.	Heat Treat.	Matrix
A	Nb <sub>3</sub> Sn	OST-MJR	1	110	54	180 hrs 650 °C	Cu
B	Nb <sub>3</sub> Sn	OST-MJR	1	110	54	72 hrs 650 °C	Cu
C	Nb <sub>3</sub> Sn	OST-MJR	0.7	80	54	72 hrs 650 °C	Cu
D	Nb <sub>3</sub> Sn	SMI-PIT	1	50	192	170 hrs 655 °C	Cu
E	NbTi	OST	0.5	46	54	—	CuNi
F	NbTi	Supercon	0.3	185	1	—	Cu
G	Nb <sub>3</sub> Sn	OST-MJR	1	110	54	180 hrs 650 °C	Cu

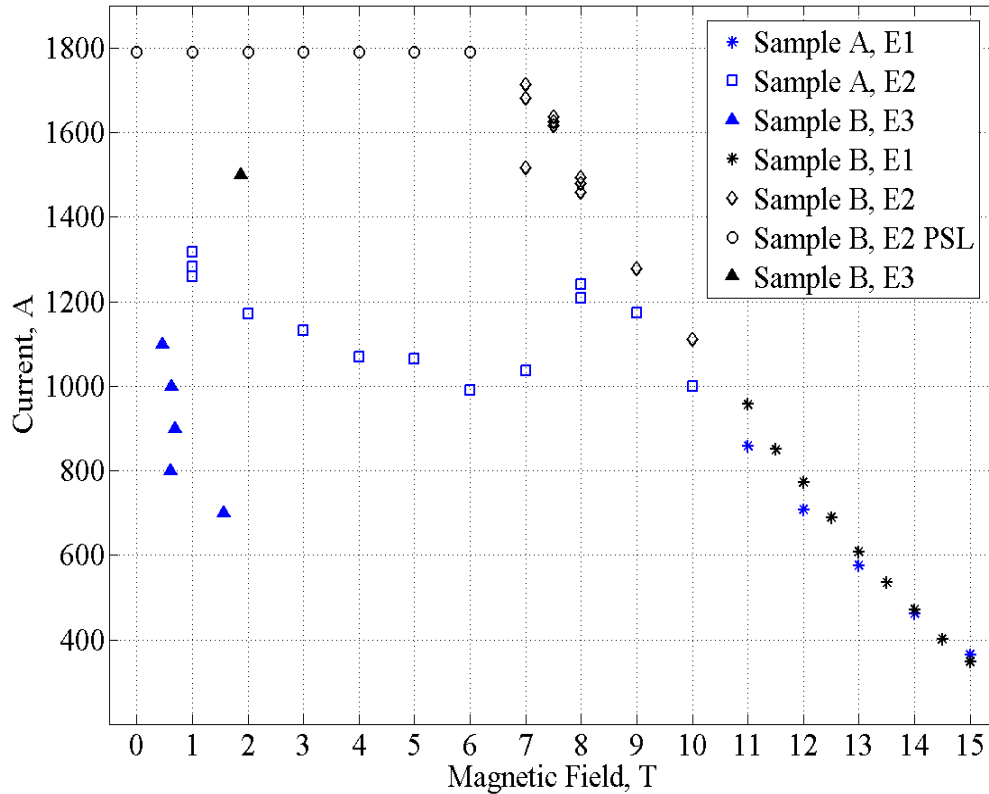


Fig. 4-32 Quench current of 1mm MJR samples with low and high RRR

the different heat treatment the critical current of the two samples was very similar. These results were completely consistent with what was already observed in the previous section 4.5.1.

In E3 (strong magnetization) measurements, for both samples the magnetic field was swept up between 0 T and 4 T at 1 T/min. During this test, sample A had a minimum quench current ( $I_{qm}$ ) of 700 A at 1.57 T;  $I_{qm}$  was about 1.8 times smaller than the  $I_q$  obtained at the same field during the E2 experiment. Sample B had a  $I_{qm} = 1500$  A at  $\sim 2$  T.

Sample C was a 0.7 mm MJR strand which had the same heat treatment as sample B. For this sample the RRR was not measured but it is expected to be lower than for sample B, since the strand dimensions are smaller and a higher quantity of tin can diffuse into the copper. Sample C, Fig. 4-33, had a reversible transition down to 9 T; decreasing the field from 8 T to 6 T, and performing E2 type measurements,  $I_q$  was below  $I_c$  but it

was still increasing. At 5 T the quench current dropped, and for lower fields  $I_q$  started to deviate significantly from  $I_c$ . During E3 experiments the minimum quench current was 650 A at 0.8 T; this current value was about 1.7 times smaller than the  $I_q$  obtained at the same field value during E2 experiment. For sample C  $I_{qm}$  occurred at a lower magnetic field than for samples A and B; this was most likely due to the smaller effective filament size of sample C. Moreover sample C  $I_{qm}$  was more than 2 times smaller than sample B  $I_{qm}$ . Since the area ratio between the two strands was 2, it can be concluded that sample C was more unstable than sample B during E3 measurements. This was an indirect confirmation that the sample C copper RRR was not as good as in sample B.

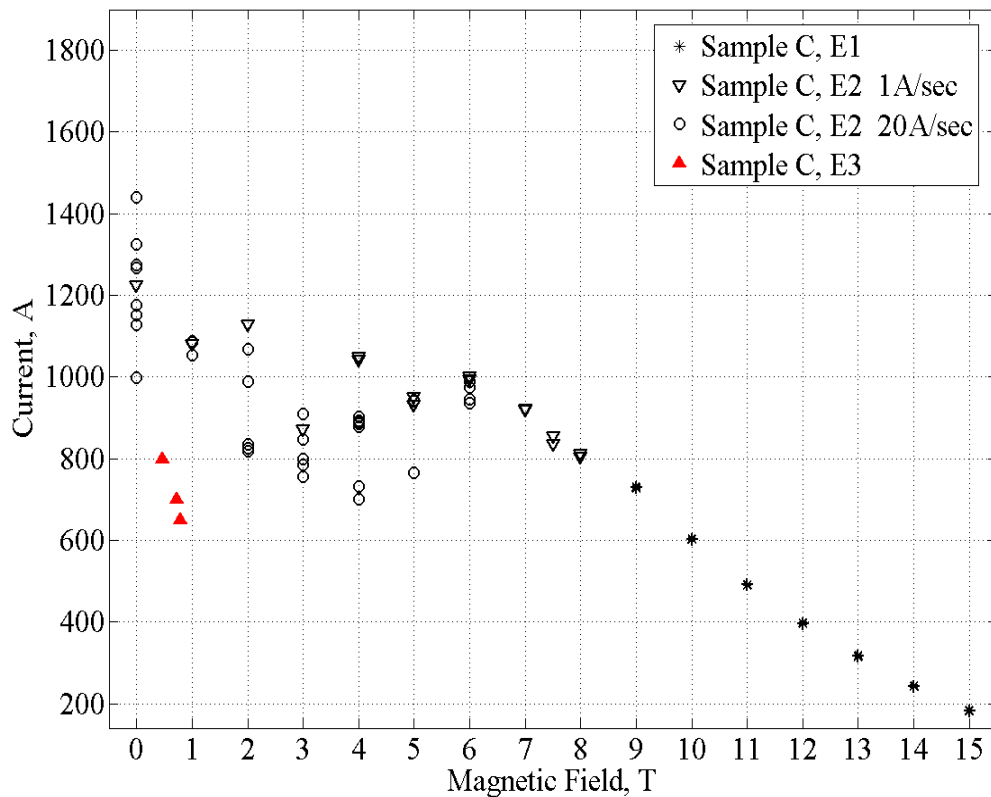
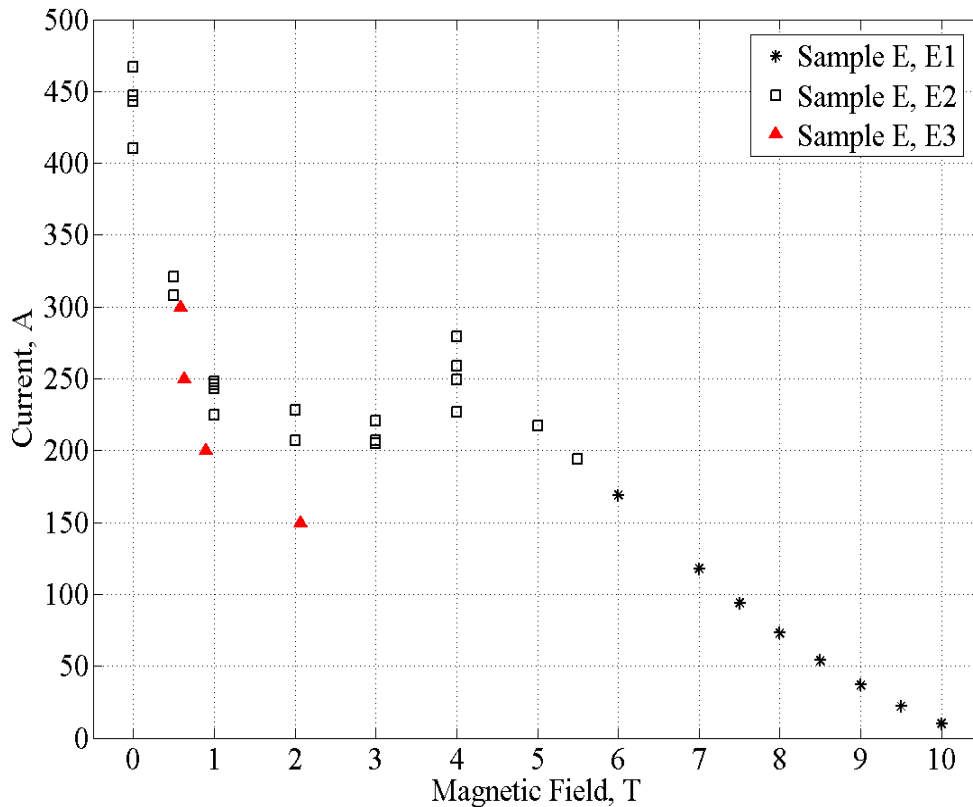


Fig. 4-33 Quench current of a 0.7mm MJR strand, HT 72h at 650K

From this test we also conclude that the current ramp rate does not play a significant role in limiting the quench current during E2 experiments. This observation was discussed

earlier, but now is much more significant since this time the current was ramped up continuously.

Sample D was a 1 mm PIT strand. The copper RRR was not measured because as long as this strand is not mechanically deformed it is quite high, >100 [52]. The superconductor reversible transition was observed down to 8 T. The  $I_c$  at a background field of 12 T was about 700 A. Decreasing the field in E2 experiment,



**Fig. 4-34 Quench current of a 0.5mm NbTi strand with CuNi matrix**

at 7 T, the  $I_q$  was below  $I_c$  but it was still increasing. For fields lower than 6 T the power supply limit was reached (1790 A). In the E3 experiment between 0 T and 4 T the strand did not quench even at the maximum current that the power supply can provide.

Sample E was a superconducting strand made of 54 NbTi filaments embedded in a CuNi matrix. The reversible transitions, Fig. 4-34, were observed down to 6 T. Further decreasing the field from 5.5 T to 4 T and performing E2 type measurements, the  $I_q$  was below  $I_c$ , but was still increasing. When decreasing the field further to 3 T,  $I_q$  started to

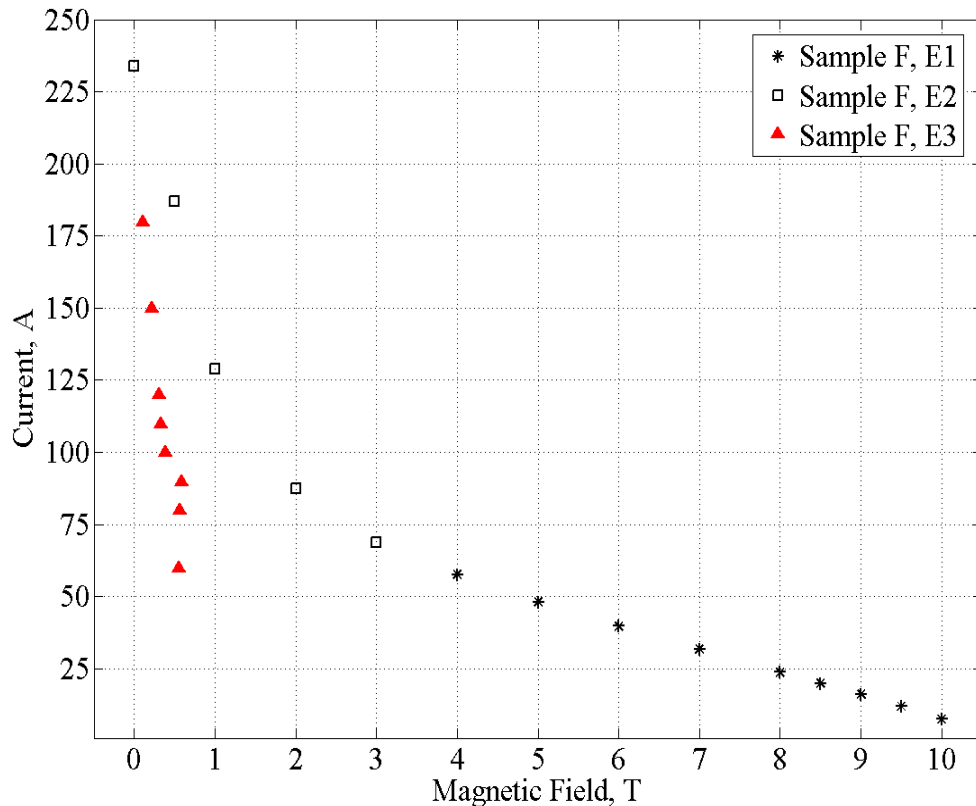


**Fig. 4-35 Quench current of a NbTi monofilament surrounded by a copper shell**

decrease. The ratio  $I_q/I_c$  at 3 T was about 0.6. In the low field region between 0-3 T,  $I_q$  was significantly lower than  $I_c$ . In E-3 measurements, the  $I_{qm}$  of sample E was 150 A at ~2 T, respect to E2 experiment the quench current was a reduced by a factor of ~1.4.

Sample F was a big NbTi monofilament (185 $\mu$ m) surrounded by a copper shell. This sample, Fig. 4-35, exhibited stable behavior under conditions E1 and E2. It showed reversible transitions down to 4 T and none below 4 T.  $I_q$  had to be very close to  $I_c$  since the derivative of quench current was monotonically increasing with decreasing magnetic field, as one would expect if the sample is at (or close to) its critical value. In E3 measurements, the sample F  $I_{qm}$  of was 60 A at 0.5 T. The  $I_{qm}$  was about 3 times smaller than the  $I_q$  obtained at the same field during E2 measurements.

Sample G was heat treated with sample A, and was from the same billet as sample A; the only difference was that a bonding agent (stycast) was used on sample G.

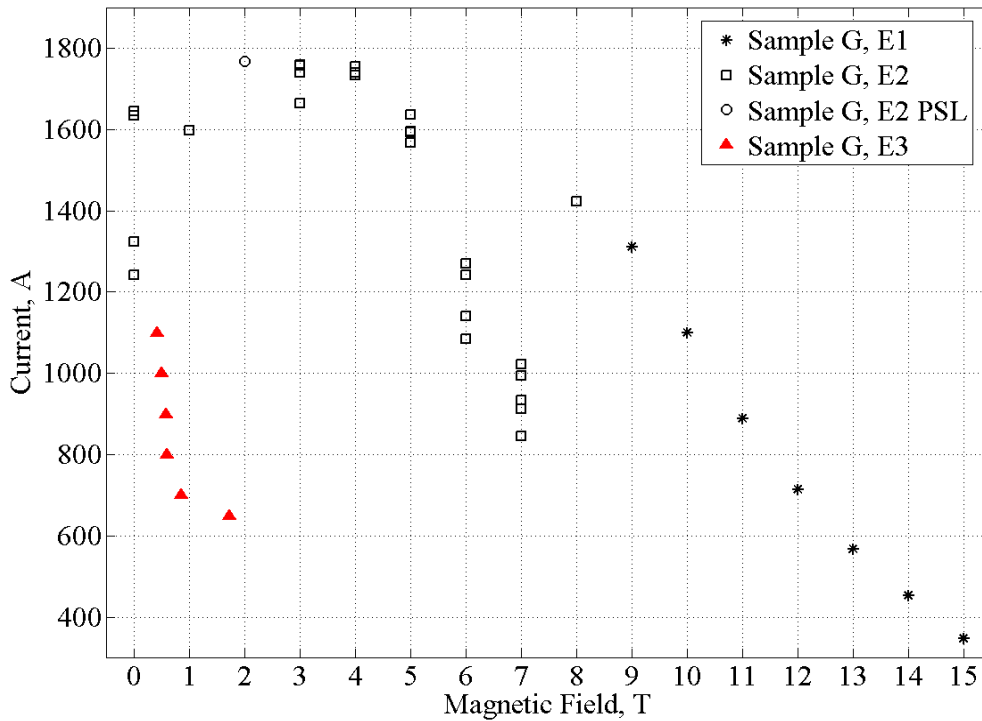


Fig. 4-36 Quench current of a 1mm MJR with low RRR tested with a bonding agent (stycast)

For sample G, Fig. 4-36, it was possible to measure  $I_c$  down to 9 T. Further decreasing the field to 8 T and performing E2 type measurements,  $I_q$  was below  $I_c$ , but was still increasing. When decreasing the field further to 7 T,  $I_q$  started to decrease. Below 7 T, during E2 measurements,  $I_q$  was much smaller than  $I_c$ .

In E3 measurements, the magnetic field was swept up between 0 T and 10 T at 1 T/min. During this test sample G had  $I_{qm} = 650$  A at 1.7 T.

### 4.5.3 Voltage spikes in superconducting strands

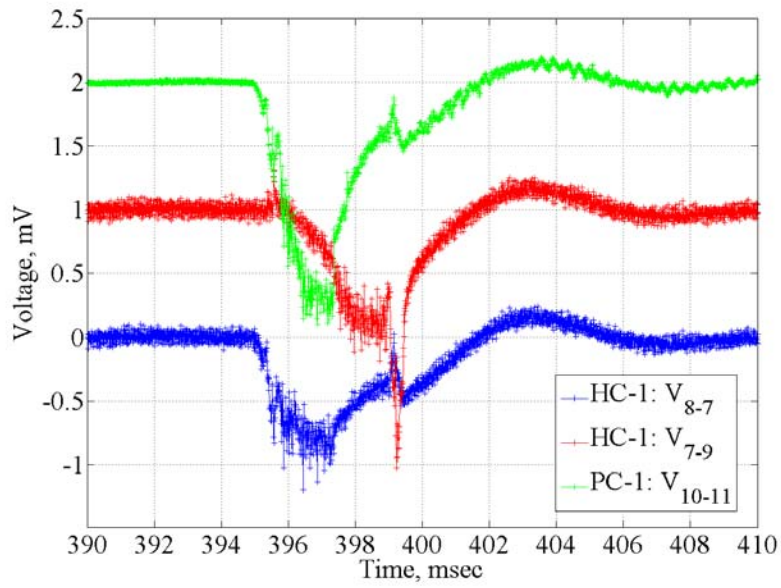
The signal shape exhibited strong correlation with physical conditions of the sample: presence of filament magnetization and/or transport current. We were able to distinguish three different type of spikes based on the physical condition of the sample. All these signals were produced by flux jumps in the superconducting strand.

A general characteristic feature of the signals was that a fast spike in one half of the sample induced an opposite polarity smaller signal in the other half of the sample, even if the transport current was zero.

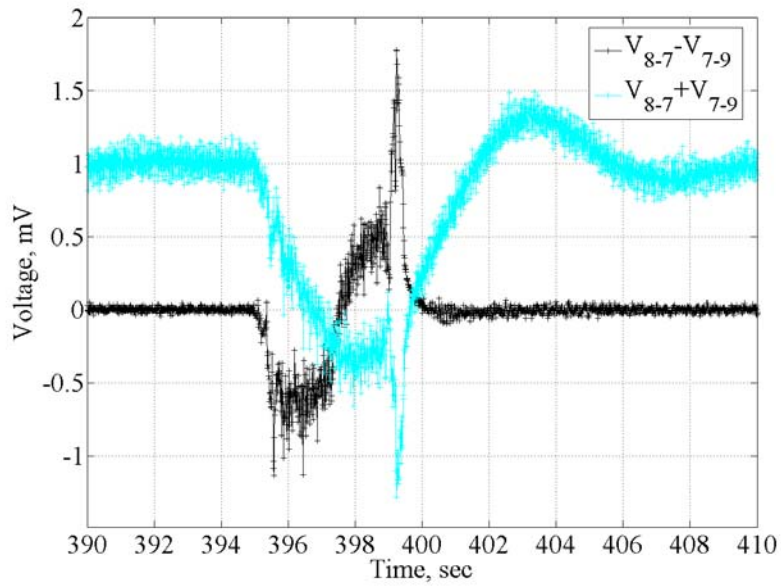
The first group of spikes can be associated with demagnetization of the strand's filaments, the second group with the transport current in the strand; hence they have been named 'magnetization' spikes and 'transport current' spikes. The third group consists of spikes whose signal shape is the result from a combination of the previous two mechanisms; for this reason they have been named 'mixed' spikes.

During V-H measurements with no transport current in the strand all the spikes were 'magnetization' spikes. Increasing the magnetic field, starting with a non-magnetized sample, the filaments get negatively magnetized; however ramping down the magnetic field the filaments get positively magnetized. In our test configuration the 'magnetization' spike polarity was the same as the magnetization polarity.

Fig. 4-37 shows an example of a 'magnetization' spike while ramping up the magnetic field with no transport current in the sample. In Fig. 4-37 (a) the blue and red lines represent respectively the two half coil signals (HC-1 and HC-2) while the green line the pick up coil signal (PC-1). This pick up coil has been set up to have the same magnetic flux as HC-1. To be able to compare the signals easily, two signals have been offset. In this case the demagnetization started in HC-1; at the same time the pick up coil PC-1 recorded a negative signal. This signal was due to the sudden penetration of the flux in the superconductor filaments: the flux penetration produces an increase of the flux in HC-1 and PC-1. The filament demagnetization then propagated longitudinally into HC-2 and it ended at  $\sim 400$  ms, Fig. 4-37 (a). At this time all three signals (HC-1, HC-2, PC-1) were the same following a slow damped sinusoid. This second part of the signal is



(a)



(b)

Fig. 4-37 Magnetization spike in sample G: negative magnetization

probably due to slow oscillations of the background magnetic field. Fig. 4-37 (b) shows the sum and the difference of the two half coil signals.

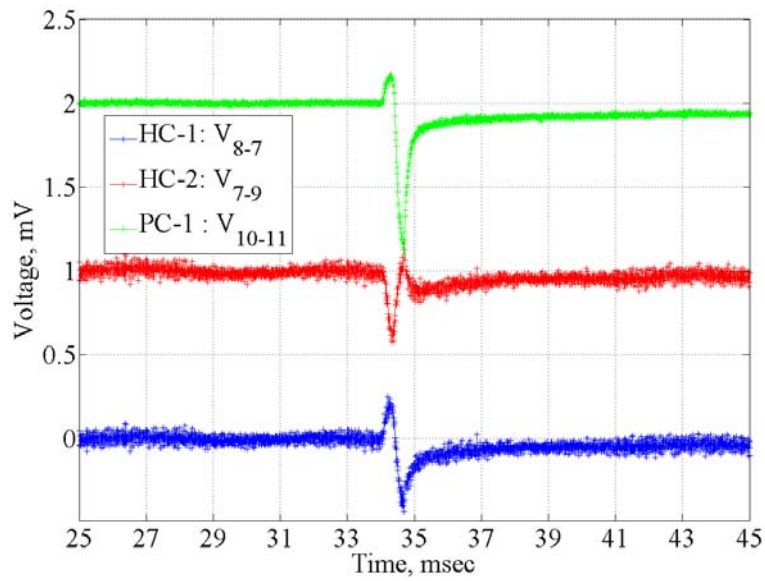
The polarity change of the signal is a characteristic feature of ‘magnetization’ spikes. Fig. 4-38 shows two magnetization spikes in sample D while ramping the magnetic field up (a) and down (b) without transport current in the sample. In the first case (a) the demagnetization started in HC-2 and then it propagated to HC-1. As always a flux-jump in one half coil induced an opposite flux variation in the other half coil. In the second case (b) the flux-jump started in HC-2 and then propagated to HC-1.

During E3 measurements with no transport current, not all the flux jumps propagated from one to the other half of the coil. For example in 1 mm MJR strands between 0 T and ~0.9 T most of the flux-jumps did not propagate. For these samples (MJR) even above 0.9 T, magnetization spikes were observed in only one half-coil when the magnetic field ramp was not stopped after a quench during an E3 experiment (so after the current supply was shut off), Fig. 4-39. In sample F all the voltage spikes observed did not propagate.

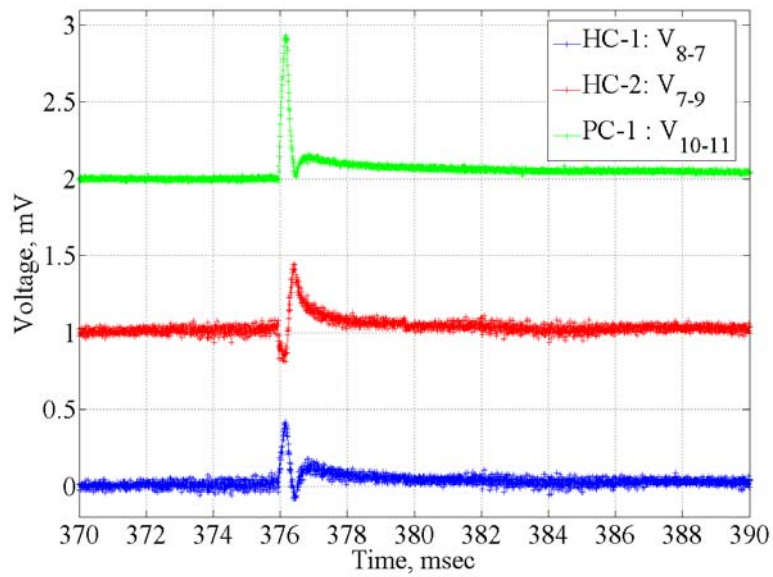
Fig. 4-40 shows an example of magnetization spike with no transport current in sample F; since the flux-jump occurred only in HC-1 the bucked signal is representative of the signal development in HC-1. It is interesting to notice that the signal shape was complex even if the sample was a monofilament. Hence the complexity of the signals due to flux jumps is not only due to having many filaments in a strand. This signal shape also suggests that the filament demagnetization process is not a continuous process.

Unlike from all other samples, in sample A, during ‘magnetization’ spikes with no transport current, high frequency oscillations (few kHz) were observed, Fig. 4-41 (a). When these oscillations are smoothed out by applying a moving average over 1 msec, the signals show the typical shape of a magnetization spike Fig. 4-41 (b).

The origin of these oscillations is not clear; the only differences between sample A and sample G were the use of a bonding agent (sty-cast) and better wiring (twisting) in sample G. A possible explanation could be mechanical motion that initiates strand demagnetization.



(a)



(b)

**Fig. 4-38 Magnetization spike in sample D: (a) negative magnetization; (b) positive magnetization**

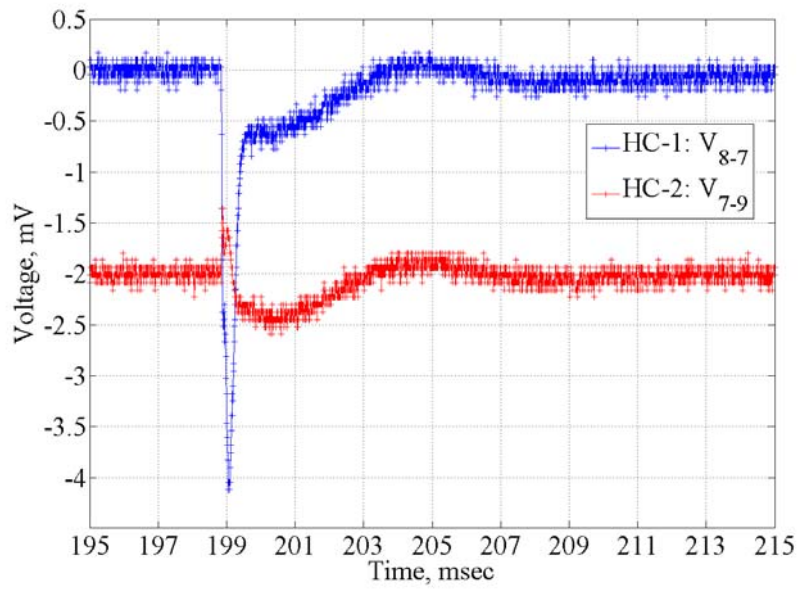


**Fig. 4-39 Magnetization spike in sample A: negative magnetization**

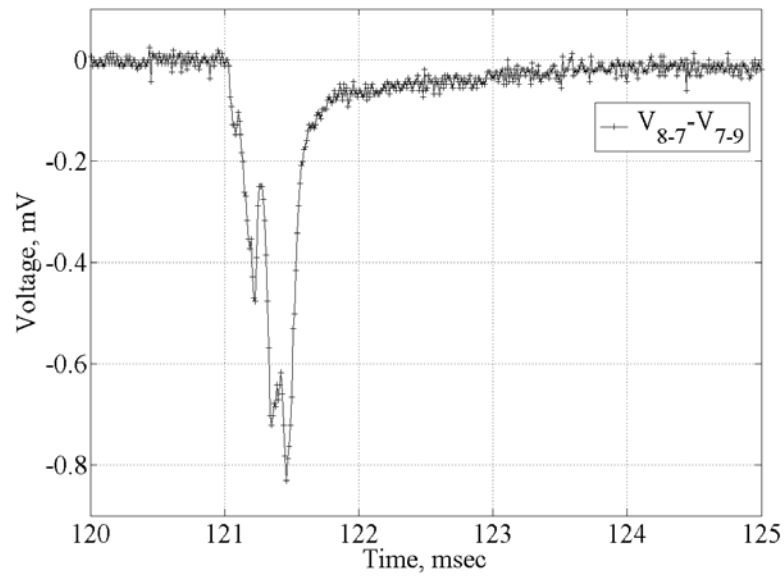
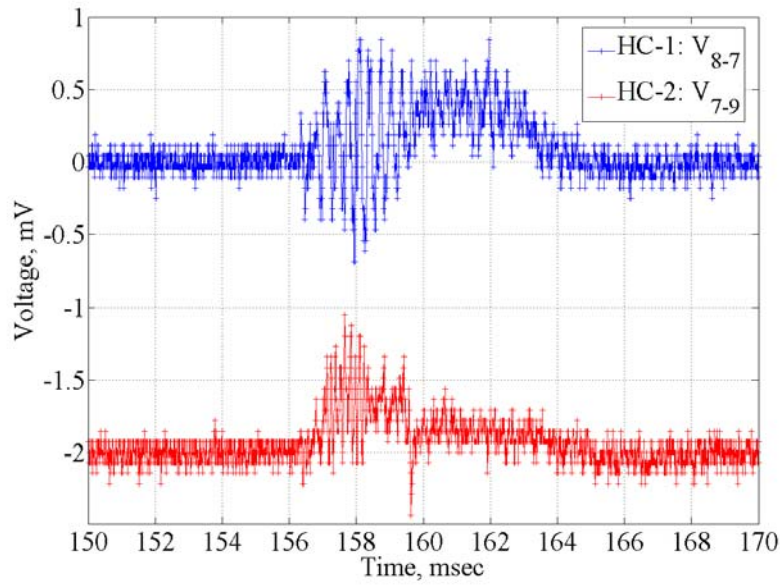
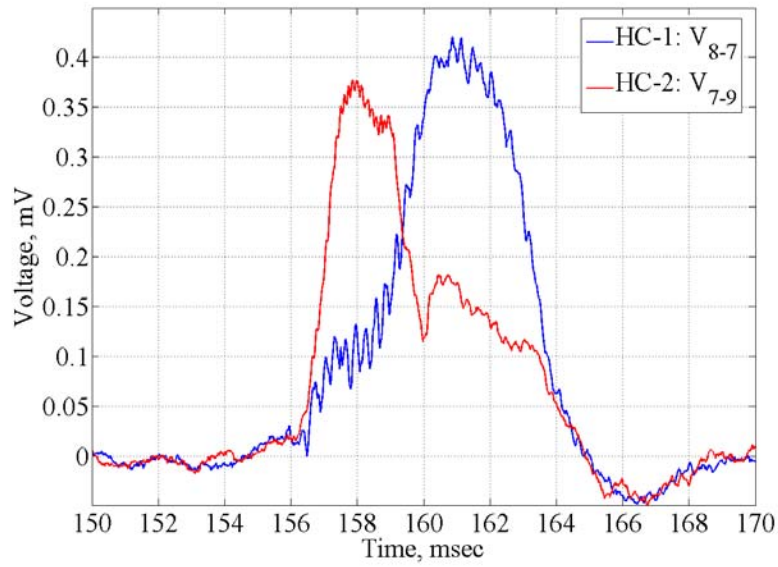


**Fig. 4-40 Magnetization spike in sample F**



(a)



(b)

**Fig. 4-41 Magnetization spike in sample A (positive magnetization): (a) raw signals; (b) moving average signals**

Further information regarding ‘magnetization’ spike signals during E3 experiments with not transport current are summarized in Tab. 4-5. The first four samples (A, B, C, E) were tested using the isolation amplifier of the VSDS with gain = 21; it also used a digital filter that cut out frequencies below 1.5 kHz and above 30 kHz. For the other three samples (D, F, G) the isolation amplifier was bypassed, this allowed decreasing the noise level; in this case a digital filter that cut out frequencies below 0.8 kHz was used. The table shows: the maximum duration of the longitudinal propagation of the flux jump (e.g., 8 msec for Fig. 4-42); the magnetic field range where these spikes occurred; the threshold value for the filtered bucked signal; the number of events recorded per field ramp; and the number of events whose the filtered bucked signal was above 1 mV.

**Tab. 4-6 Magnetization spike in E3 experiments with no transport current**

Sample name	Max width [ms]	Field range [T]	Threshold [mV]	Events	Events above 1 mV
A	8	~0.8-4	1	8	8
B	2	~0.8-1.8	0.5	10	4
C	1.5	0.6-2.4	0.5	6	2
E	-	-	0.5	0	0
D	1	0.64-0.74	0.3*	2	
F	0.5	0.08-0.4	0.3*	~100	
G	8	0.3-4.6	0.3*	60	

\*isolation amplifier bypassed

During E3 experiments with transport current not only ‘magnetization’ spikes but also ‘transport’ current spikes were observed. Their feature is that the signals were positive even if the sample was negatively magnetized; hence these signals can not be associated with filament demagnetization.

‘Transport current’ spikes are most likely related to the redistribution of the transport current within the strand. In composite superconducting strands the transport current flows into the outermost filament layers at the critical current density while in the internal filaments no transport current flows; if a perturbation occurs the transport current

may suddenly redistribute in the internal filaments, producing a jump of the self field inside the strand. The flux jump of the self-field produces an electric field inside the strand and hence the positive signal of the 'transport' current spike.

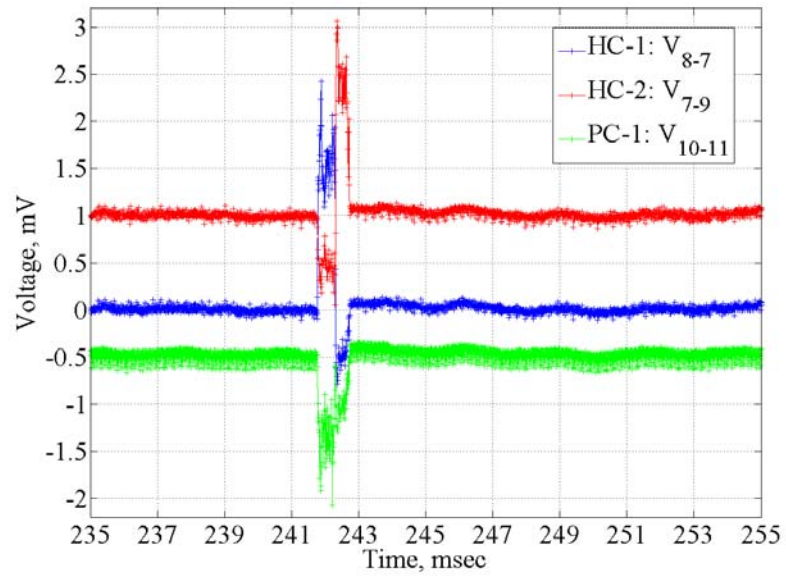
Fig. 4-42 displays a 'transport current' voltage spike: the transport current redistribution started in HC-1 and then propagated longitudinally in HC-2. Also for this type of spike the flux jump in one half coil induces a smaller opposite signal in the other half. Unlike the case of 'magnetization' spikes where PC-1 recorded a signal similar to HC-1, here PC-1 always recorded a negative signal. It is important to say that the pick up coil signal was negative even in the case where the sample was positively magnetized; this means that during transport current spikes the coils always experienced an increase of the magnetic flux.

The shape of these voltage spike signals is characterized by fast rise and fall times. Although transport current spikes were generally recorded with maximum amplitude of the order of one mV, sometimes a very large spike occurred, Fig. 4-43.

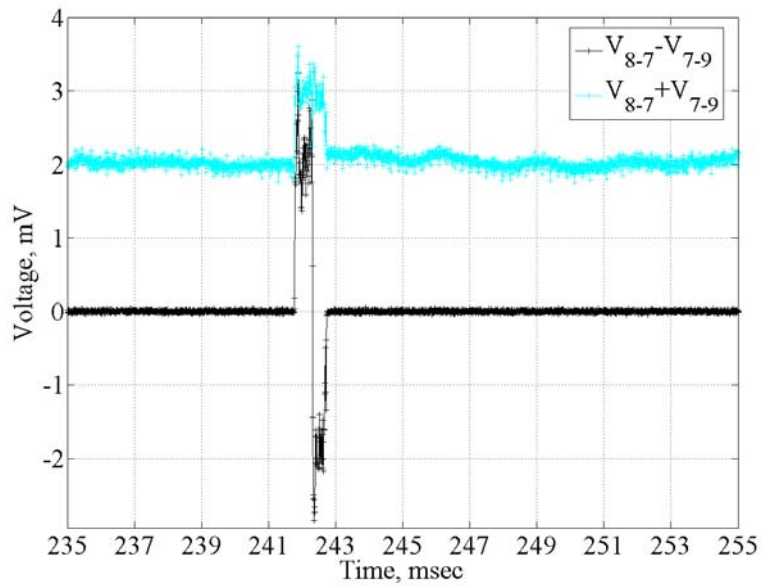
If the sample is magnetized spikes can appear in V-I measurements at 0-2 T, while they did not appear if the sample was not magnetized (E2 measurements). This probably means that these events are initiated by the collapse of the persistent current (magnetization). Hence 'transport current' spikes are a superposition of the demagnetization signal and the current redistribution signal where the latter signal, prevails over the former.

Superposition of the 'transport current' and the 'magnetization' spikes has been observed frequently during E3 experiments, as shown in Fig. 4-44 (*b*). The first part of the signal was positive due to the 'transport current' redistribution; the second part was negative due to the demagnetization process in the filaments.

In the case of sample E transport current spikes were not observed, and only one was collected for sample F. In these cases the signal associated with the current redistribution was not large enough. The electric field generated during current redistribution is proportional to the strand diameter and the critical current density; in the case of samples E and F, these values were much lower than those of the Nb<sub>3</sub>Sn samples.



(a)



(b)

**Fig. 4-42 Magnetization spike in sample A (positive magnetization): (a) raw signals; (b) moving average signals**

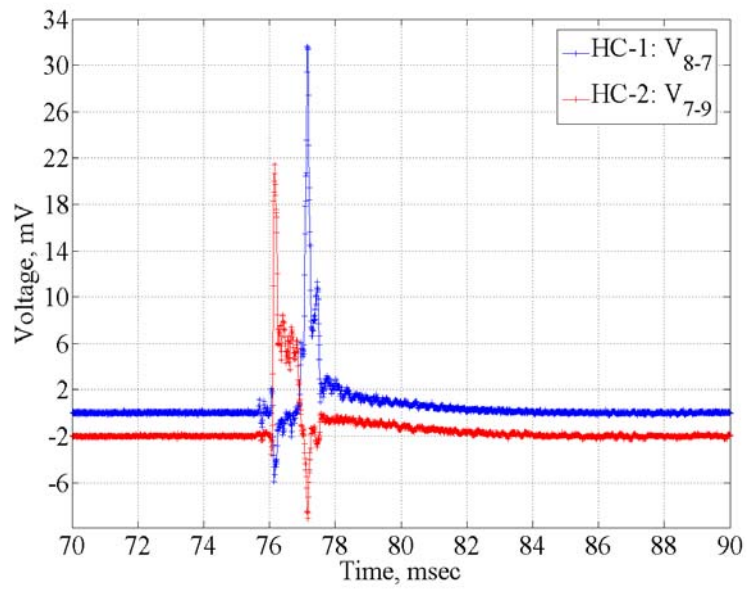
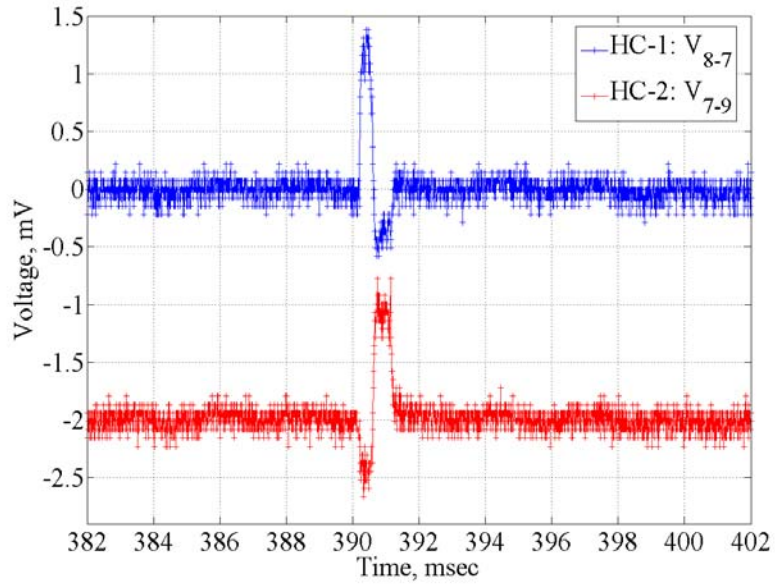
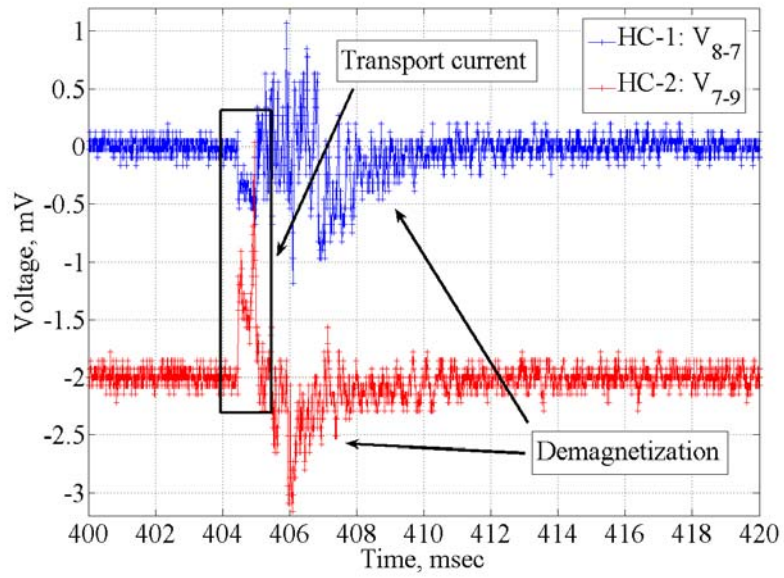


**Fig. 4-43** Transport current spike in sample A



(a)



(b)

Fig. 4-44 Comparison between a 'Transport current' spike (a) and a Mixed spike (b) in sample A

The frequency of voltage spikes had a strong variation with the magnitude of the strand magnetization and the value of the transport current. The number of spikes scales with the magnitude of the magnetization. In the E2 experiments, when the sample was not magnetized, no spikes were observed even if the sample was unstable. In the E3 experiments, where the sample was always magnetized, many spikes were collected and the number of spikes increased with the transport current: sample E had no spikes without transport current; with 150A, thirty spikes were collected between 1.9 and 2.07 T (at this field the strand quenched). For sample D, the number of spikes as a function of the transport current is shown in Fig. 4-45.

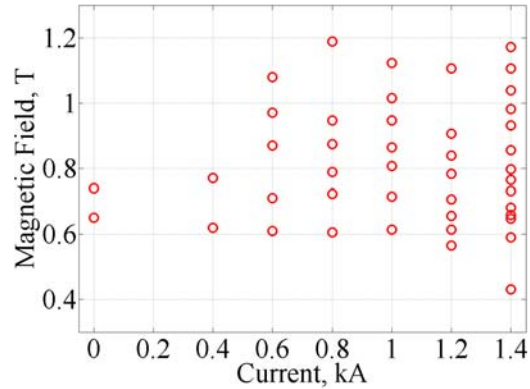
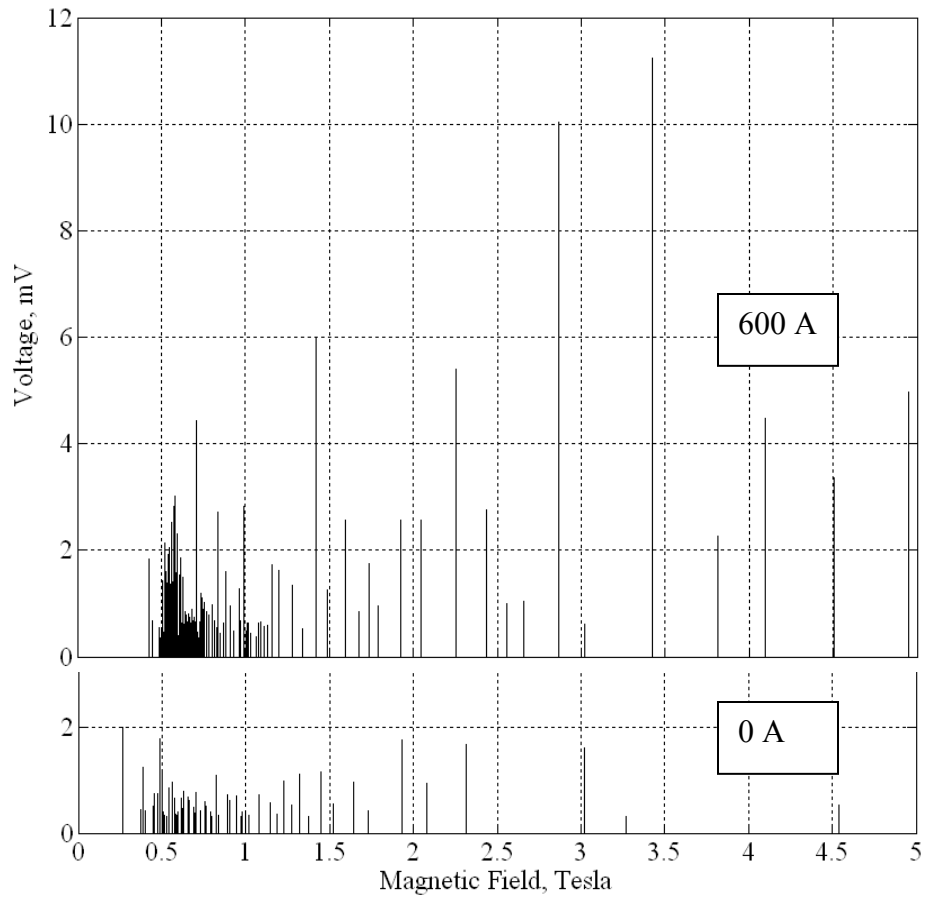


Fig. 4-45 Sample D: Spikes in E3 experiment

The field range where spikes occurred did not change significantly with the value of the transport current for all samples except E. For this sample, decreasing the transport current from 150 A to 100 A, the spike start moved from 1.9 T to 2.7 T.

For the Nb<sub>3</sub>Sn samples, the maximum number of spikes occurred in the low field region where the magnetization, during E3 experiments, is expected to have a maximum. Fig. 4-46 shows the amplitude of the spikes (bucked signal) as a function of the background magnetic field during E3 experiments in sample G. The plot is divided in two parts: the lower part shows the spikes collected with no transport current while the upper part shows those collected with 600 A. It can be seen that the number of flux jumps and the voltage signal amplitude increases significantly with current (from 60 to 140). It is also interesting to see that the field range where flux jumps occurred did not change significantly with current, and all of them were recorded below 5 T.

It was also discovered that when the strands were strongly magnetized the quenches always had a spike initiating the quench, fig. 4-43. It is interesting that in strongly magnetized samples, when the  $I_q$  was close to the  $I_{qm}$ , many spikes were observed immediately prior to the quench.



**Fig. 4-46 Spikes collected in sample F during E3 experiments with 0 A and 600 A**

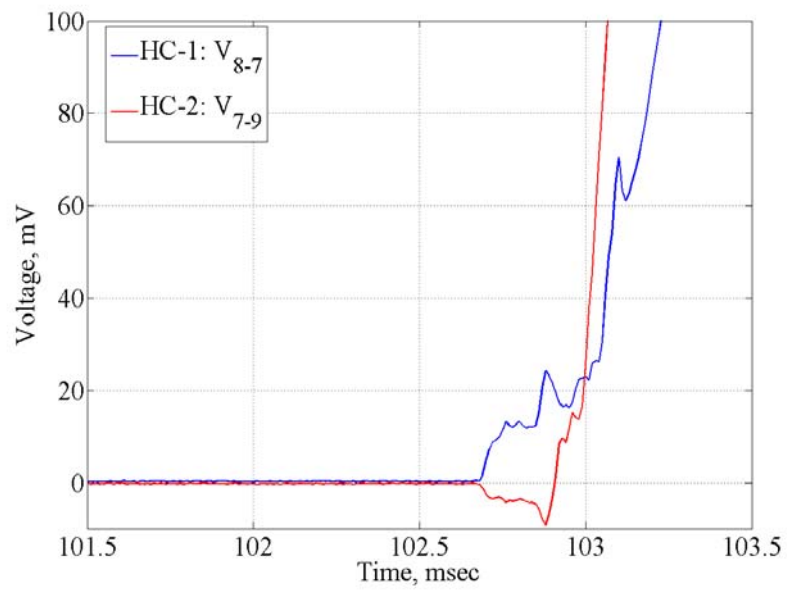


**Fig. 4-47 Quench of sample a during E3 experiment with 700A**

#### 4.5.4 Discussion

In this section test results will be discussed, analyzing separately the three different measurements: V-I, V-H, and spike measurements.

A conductor will be defined to be unstable if it may have premature quenches; it will be defined thermo-magnetically unstable if it may have flux jumps. Similarly conductor instability/conductor thermo-magnetic instability will indicate the process which leads the conductor to have premature quenches/flux-jumps.

V-I measurements of 1 mm MJR strands which had a long heat treatment, showed that these strands had premature quenches at low magnetic field due to thermo-magnetic instabilities. At 6 T the ratio between the  $I_q$  and the  $I_c$  was about 0.5 and this value decreased almost linearly with decreasing the magnetic field. In particular these premature quenches were due to the release of energy associated to with the transport current redistribution (self-field instability).

This strand instability was not directly due to the strand motion under Lorentz forces. Indeed for background fields lower than 6 T the quench current did not change much, while the Lorentz forces reduced significantly, vanishing at 0 T. Also the release of the magnetization energy could not be the primary cause of this strand instability, because at 6 T the maximum magnetization energy stored in the strand filaments is very limited, and the  $I_q$  value does not change reducing the strand magnetization (repeating the test several times without changing the background magnetic field).

Test results of NbTi samples (E, F) confirm that premature quenches during V-I measurements were not due to the strand magnetization (and the filament size). The multifilament sample (E) was strongly unstable at low fields and the ratio  $I_q/I_c$  was much lower than one. Instead, the monofilament (F) almost reached its  $I_c$  at every magnetic field, even if its filament size was more than three times bigger than that of the multifilament strand (E). The low quench currents of the multifilament (E) were due to the high resistive matrix, which does not allow the heat to diffuse during the transport current redistribution. The monofilament was stable because the superconducting strand diameter was very small (185  $\mu\text{m}$ ) and hence the energy associated with the transport current redistribution was also small.

**Tab. 4-7  $I_q$  at 6 T during V-I measurements of 1.0 mm MJR strands**

Sample name	Final step heat treatment	Quench current
6b, 14, 18b, 25	180 hr.	~800-1300A
19a, 21, 22a, 23a, 23b	120 hr	~1300-1500A
B	72 hr	> PSL (~1800A)

In order to improve the stability of a strand limited by self-field instability, without decreasing the  $j_c$ , it is necessary to reduce the strand diameter or to increase the heat diffusion capability. This strand property can be enhanced by increasing the thermal conductivity of the strand matrix. Reducing the duration of the last step of the heat treatment, it was possible to improve the matrix quality of 1 mm MJR strands without reducing significantly the  $j_c$ . The matrix improvement increased significantly the  $I_q$  at low field; Tab. 4-7 shows a comparison of the  $I_q$  at 6 T for the three different heat treatments used.

The matrix's thermal conductivity is generally higher than the superconductor's. In this case the strand's heat diffusion capability can be also enhanced by decreasing the filament size. Indeed, the smaller the filament size the more homogeneous is the strand cross-section. For a homogenous section the strand thermal conductivity is the average of the superconductor and the matrix thermal conductivities weighted over the area of each component. In the case of big filaments, the heat diffusivity is essentially determined by the superconductor thermal conductivity. For this reason, the smaller the filament size the higher the strand's heat diffusion capability.

Another relevant result is that the quench currents were not strongly dependent on the current ramp rate. For example, in testing sample C no significant difference was observed using a ramp rate of 1 A/sec and a ramp rate of 20 A/sec.

This result is important because it shows that the theory of the thermo-magnetic instability-based on the hypothesis that the superconductor is in the flux creep regime in the initial stage of the instability-development can not explain the quench current value. Indeed this theory predicts that the current at which the superconductor thermo-magnetic instability may appear is dependent on the current ramp rate. Hence if the strand

quenched when it gets thermo-magnetically unstable, the quench current value should be dependent on the current ramp/rate.

As already discussed in chapter 2, the models that describe when thermo-magnetic instability may occur in the conductor can not predict the quench current, because after the thermo-magnetic instability the conductor can recover without quenching the sample.

During V-I measurements the quench current is significantly reduced if the sample is strongly magnetized. In 1 mm MJR strands this effect was observed for magnetic fields between 0 and 3 T.

The main results obtained during V-H measurements will be discussed in the next chapters.

The effect of the magnetization is more evident in V-H measurements. During this measurement the background field is swept up and the strand can be strongly magnetized. At very low fields ( $\sim 0-3$  T) the quench current was never higher than the value obtained at the same field during E2 experiments, and for MJR strands and the NbTi monofilament (sample F) the quench current was always much lower.

A quench due to thermo-magnetic instabilities may occur if the potential energy associated with the current distribution (transport and on magnetization) is high enough to warm up the strand sufficiently so that the conductor gets thermo-magnetically unstable.

Thus, the lower quench current during V-H measurements is due to a twofold effect produced by the strand magnetization: the conductor gets more thermo-magnetically unstable and the energy stored in the strand is higher than the case of E2 experiments.

The increased thermo-magnetic instability of the conductor is experimentally demonstrated by the presence of voltage spikes (partial flux jumps) preceding these quenches and by their absence during E2 experiments. In the E2 experiments the superconductor gets thermo-magnetically unstable when the strand quenches; this means that in the very low field region, during V-H measurements conductor thermo-magnetic instabilities occur at smaller current values.

For the NbTi multifilament strand (F) some quench current values (300, 250 and 200 A) at very low fields (0.59, 0.63, 0.9T) were not significantly different from those obtained during E2 experiments at the same field. It is interesting to notice that these were the only quenches during V-H measurements at very low fields which were not preceded by voltage spikes. This quench behavior was probably due to the fact that for those magnetic fields the superconductor gets unstable at the same current value for both E2 and E3 experiments. With a lower transport current (150 A) the sample F quenched at 2.07 T and the quench was preceded by 31 voltage spikes which started at 1.9 T.

For sample A, F, and G the quench current during E3 experiments decreased with increasing the magnetic field until it reached a minimum value,  $I_{qm}$  at  $B_{qm}$ . Sweeping the magnetic field with a current smaller than  $I_{qm}$ , the sample quenched at much higher magnetic field and the results of V-H and V-I measurements were the same. These three samples were characterized by a small thermal conductivity (the MJR strand has a copper matrix with a low RRR, the NbTi strand is a monofilament) and big filament size.

This quench behavior between 0 T and  $B_{qm}$  was due to the strong thermo-magnetic instability in this field range and to the low thermal conductivity of the strands. Since the conductor was thermo-magnetically unstable, when the strand potential energy was high enough the strand quenched. Due to the low thermal conductivity the quench development was almost adiabatic. Hence, since the conductor was thermo-magnetically unstable, the quench current depended only on the amount of strand potential energy. A model describing the quench development in case of strands with low thermal conductivity and big filaments is presented in chapter 5.

For currents smaller than  $I_{qm}$ , the strands were still thermo-magnetically unstable (indeed voltage spikes were still observed for fields higher than  $B_{qm}$ ) but the stored energy was not high enough to quench the sample.

In superconducting strands with low thermal conductivity and big filaments, the  $I_{qm}$  can be lower than the critical current at high magnetic field - which is a reference design parameters for light field magnets. This was the case for the first magnets built at Fermilab. Due to the very low  $I_{qm}$  of the strands, these magnets had limited performance.

It is important to notice that the V-H measurements showed in this chapter were performed on round strands. In the case of strands mechanically deformed by cabling, the

RRR of the copper matrix can be even lower and the filament size bigger by merging those of round strands which had the same heat treatment. Hence the cabling process can further reduce the  $I_{qm}$ .

The other main results obtained by voltage spikes measurements will be discussed next.

Partial flux jumps were present only in the case of strands strongly magnetized and they were observed only at low fields (1 mm MJR  $\sim 0-5T$ ). The number of partial flux jumps increased with the current. Quenches of strands strongly magnetized were initiated and preceded by partial flux jumps.

The voltage signal associated with these partial flux jumps is the superimposition of two signals: one due to the demagnetization of the filaments and the other due to the transport current redistribution. This means that during the development of these partial flux jumps, the energies associated with the transport current redistribution and filament demagnetization are released at the same time.

Partial flux jumps are local phenomena which propagate longitudinally. It means that the flux jump does not happen at the same time for the whole length of the strand even if the strand conditions are practically uniform everywhere. This implies that the development of thermo-magnetic instability is actually a 3 dimensional process. In the literature, thermo-magnetic instability is generally described as a two-dimensional process taking in to account the strand section. The two dimensional approach can still be considered valid to evaluate if a thermo-magnetic instability starts in a strand, but it is not sufficient to predict the evolution of the instability if dynamic effect play a relevant role. In the adiabatic case the development of the instability can be studied with a 2 dimensional model.

## **4.6 Conclusions**

V-H measurements on extracted strands can predict if a magnet will be limited by strand thermo-magnetic instabilities at low fields.

A practical solution to avoid these magnet limitations is to increase the copper matrix RRR by reducing the heat treatment time and carefully controlling the mechanical

deformation of the strands during cabling. For 1 mm MJR strands it was possible to improve significantly the matrix properties without changing the critical current density. Another solution is to adopt a magnet design which guarantees that the nominal field is reached when the current that flows through each strand is lower than the minimum quench current ( $I_{qm}$ ) of the strand.

These solutions were applied and worked, although in order to eliminate this problem at the root it is necessary to have sufficiently small strand sub-elements and a strand design which guarantees a high quality of the strand matrix. At present superconducting strand manufacturers are working towards this direction.



## **Chapter 5 Thermo-magnetic instabilities in strands: calculation of the minimum quench current**

Two different types of thermo-magnetic instability mechanisms were observed depending on the experimental conditioning of the sample as seen in chapter 4. Starting the current ramp when the sample was not magnetized we obtained different quench current values as a function of the external magnetic field and a different voltage spike behavior compare to the case when the sample was strongly magnetized by ramping up the magnetic field at fixed current values until the sample has quenched.

In order to model this quench behavior of the strand two instability mechanisms were considered: self field instability and magnetization instability. Modeling both instability mechanisms have the following assumptions: 1) the energy associated with the redistribution of the self field/transport current and the energy associated to the demagnetization of the filaments are released instantaneously (adiabatic approach); 2) once the flux jump mechanism starts it will continue until the total energy has been released (complete flux jump).

The released energy will warm up the superconductor (no escape of heat will be assumed) and if the temperature is high enough that the superconductor can not carry (with a negligible electrical resistivity) the transport current it will quench. The model has been applied to sample A (see chapter 4).

The aim of this model is to calculate the minimum current at which a strand can quench due to thermo-magnetic instabilities.

In this chapter the following topics are described:

- the strand geometrical dimensions and detailed material properties used in the model;
- the calculation of the energy released during a complete flux jump in the case the sample is magnetized with no transport current;
- the calculation of the energy released during a complete flux jump in the case the sample is not magnetized with transport current;
- the calculation of the strand enthalpy and the way how the model calculates the quench current value;

- the quench current results obtained by the model;
- the effect of the magnetization produced by the self-field;
- the comparison between the model results and the experimental data.

### 5.1 Geometry of the 1 mm MJR strand

The MJR strand cross section, Fig. 5-1, is composed by three regions: a central copper rod, a composite zone and an external copper shell. The composite region is made

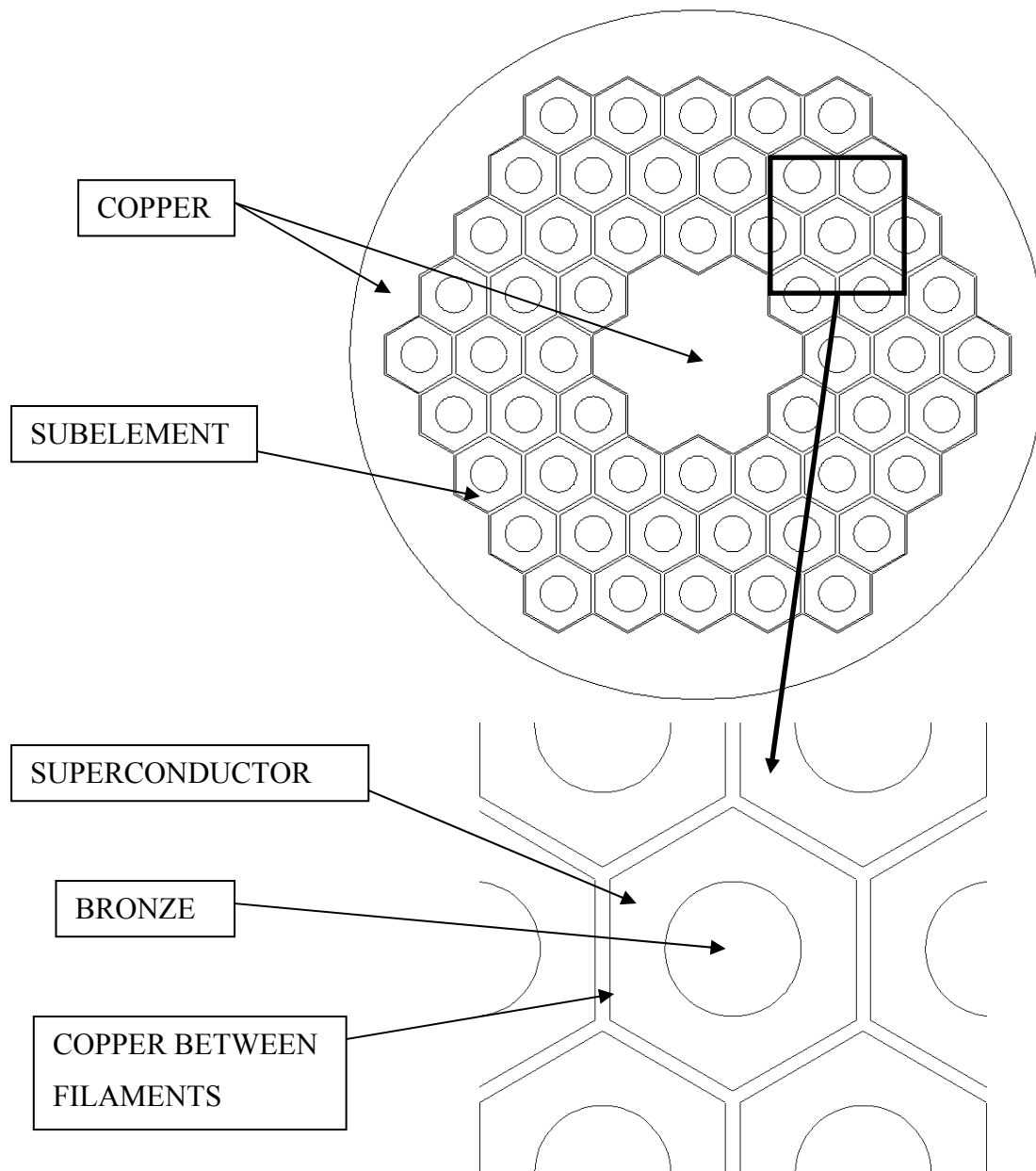


Fig. 5-1 Geometry of a 1 mm MJR strand

of hexagonal sub-elements; in our case the number of sub-elements is 54 (12 in the first, 18 in the second and 24 in the third layer).

After the heat treatment of the strand, each sub-element has a central part made of bronze surrounded by Nb<sub>3</sub>Sn. This part of the sub-element will be named ‘filament’; the filament area is generally named ‘non-copper area’. The external part of the sub-element is a thin copper layer which separates the filaments from each other. The area values for the different parts in the strand cross section are shown in Tab. 5-1.

**Tab. 5-1 Areas in mm<sup>2</sup>**

Non-Cu	Sub-elements	Nb <sub>3</sub> Sn	bronze	Cu sub-elements	Cu rod	Cu shell
0.422	0.474	0.305	0.117	0.052	0.0615	0.250

The model, presented latter in this chapter takes into account only the composite region. This region is approximated with an area within two circles (external and internal radius named to  $R$  and  $R_f$  respectively), Fig. 5-2. These values have been established using the following criteria:

$$\pi R_f^2 = Cu\_Rod\_Area \quad \rightarrow \quad R_f = 0.14[mm]$$

$$\pi(R^2 - R_f^2) = Sub-elements\_Area \quad \rightarrow \quad R = 0.413[mm]$$

Another relevant parameter for the model is the ratio,  $\lambda$ , between the non copper area and the total area of the composite. For our geometry:

$$\lambda = \frac{Non-Cu\_area}{Sub-elements\_area} = 0.89$$

The filaments themselves will be approximated as circles with radius  $F$ . For the radius the following relation is assumed:

$$\pi F^2 = \frac{Non-Cu\_area}{Number\_of\_filaments} \quad \rightarrow \quad F = 49.9[\mu m]$$

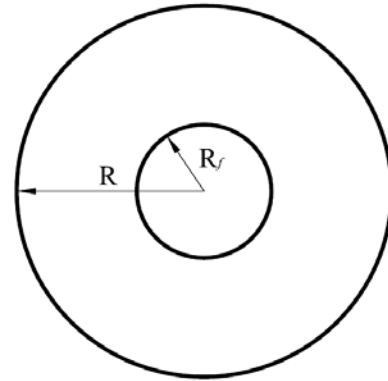


**Fig. 5-2 Schematization of a 1mm MJR**

## 5.2 Volumetric specific heat of Nb<sub>3</sub>Sn $T < T_c$

For high fields and temperature below  $T_c$  the specific heat of the Nb<sub>3</sub>Sn follows the relation [108]:

$$C_{Nb_3Sn} = \beta \cdot T^3 + \alpha \cdot T$$

Where  $\alpha$  and  $\beta$  are functions of the magnetic field only. At lower fields this relation is valid only for temperatures between  $\sim 1.9$  and 4.5 K; in this temperature range  $\alpha$  and  $\beta$  have been parameterized fitting the experimental data by Bouquet [109]:

$$\alpha = (4.48 \cdot 10^{-3} B^2 + 4.08 \cdot 10^{-1} B + 9.34 \cdot 10^{-1}) \cdot [mJ \cdot K^{-2} \cdot gat^{-1}]$$

$$\beta = (6.08 \cdot 10^{-2} \cdot \log(11.22 \cdot B + 17)) \cdot [mJ \cdot K^{-4} \cdot gat^{-1}]$$

The experimental data and the values obtained using the above relations are shown in Fig. 5-3 and Fig. 5-4 respectively.

For temperatures higher than 4.5 K and fields lower than 10 T, this parameterization is not sufficiently accurate.

At 0 T and 4 T magnetic field values for temperatures higher than 4.5 K, we will use the following parameterizations calculated by fitting experimental data between 4.5 K and  $T_c$  [108]:

$$C_{Nb_3Sn}(0T) = \{3.36 \cdot 10^{-1} \cdot T^3 - 1.06 \cdot T^2 + 2.42 \cdot T\} \cdot [mJ \cdot K^{-1} \cdot gat^{-1}]$$

$$C_{Nb_3Sn}(4T) = \{2.92 \cdot 10^{-1} \cdot T^3 - 1.87 \cdot 10^{-1} \cdot T^2 + 2.83 \cdot T\} \cdot [mJ \cdot K^{-1} \cdot gat^{-1}]$$

For field values between 0-4T and 4-10T we will use a weighted average:

$$C_{Nb_3Sn}(B) = C_{Nb_3Sn}(4T) \cdot \frac{B}{4} + C_{Nb_3Sn}(0T) \cdot \left(1 - \frac{B}{4}\right) \quad 0 \text{ T} < B < 4 \text{ T}$$

$$C_{Nb_3Sn}(B) = C_{Nb_3Sn}(10T) \cdot \frac{B-4}{6} + C_{Nb_3Sn}(4T) \cdot \left(1 - \frac{B-4}{6}\right) \quad 4 \text{ T} < B < 10 \text{ T}$$

This parameterization allowed fitting very accurately the experimental data [108] for temperature above 4.5 K. In Fig. 5-5 and Fig. 5-6 the experimental data [108] and the values calculated for temperatures higher than 4.5 K are shown.

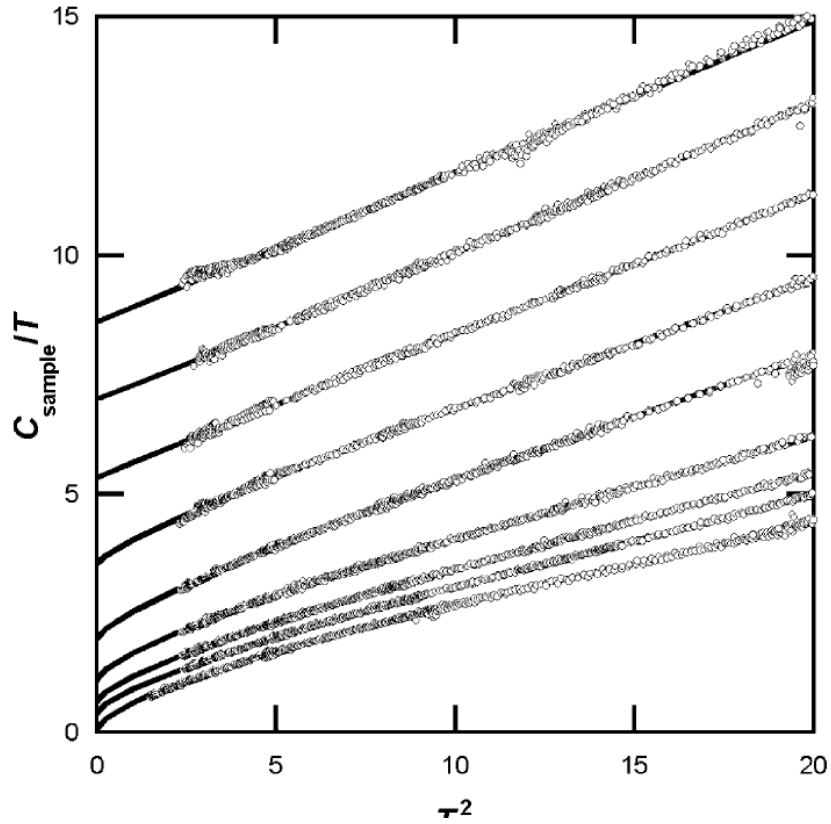


Fig. 5-3 Heat Capacity of Nb<sub>3</sub>Sn at 0, 0.5, 1, 2, 4, 7, 10, 13, 16 T; experimental data [109]; the heat capacity increases with the magnetic field

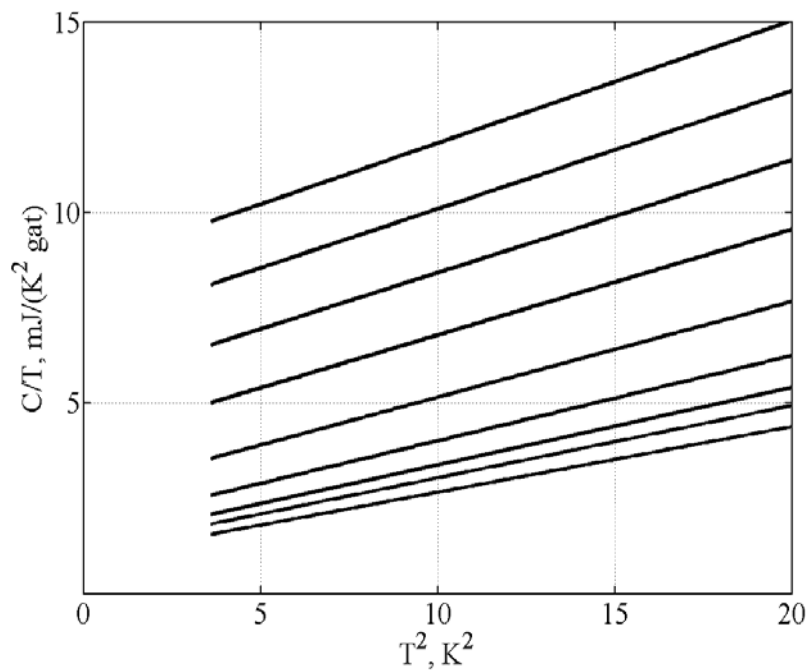


Fig. 5-4 Calculated Heat Capacity of Nb<sub>3</sub>Sn at 0, 0.5, 1, 2, 4, 7, 10, 13, 16 T; the heat capacity increases with the magnetic field

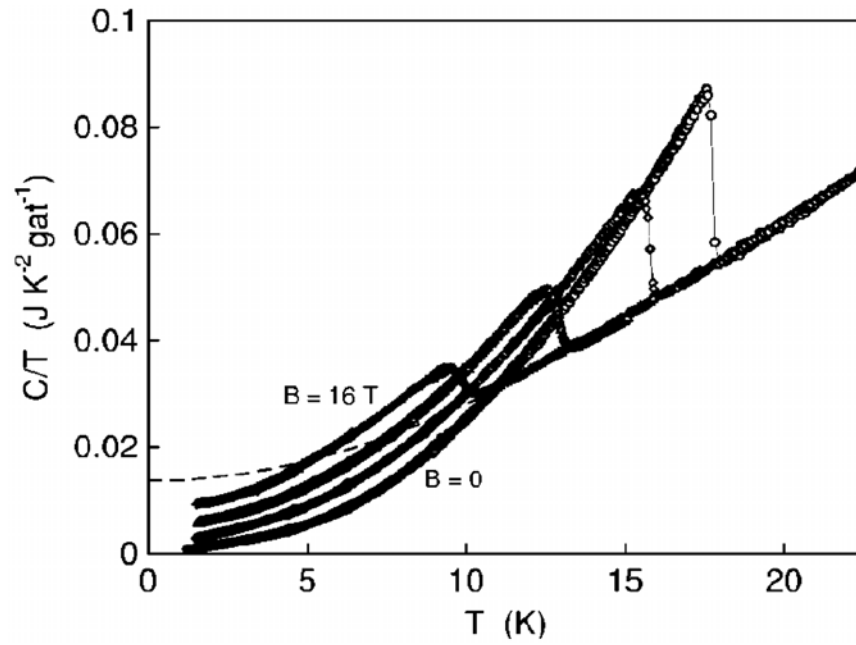


Fig. 5-5 Heat Capacity of  $\text{Nb}_3\text{Sn}$  at 0,4,10 and 16 T; experimental data [108]; the heat capacity increases with the magnetic field

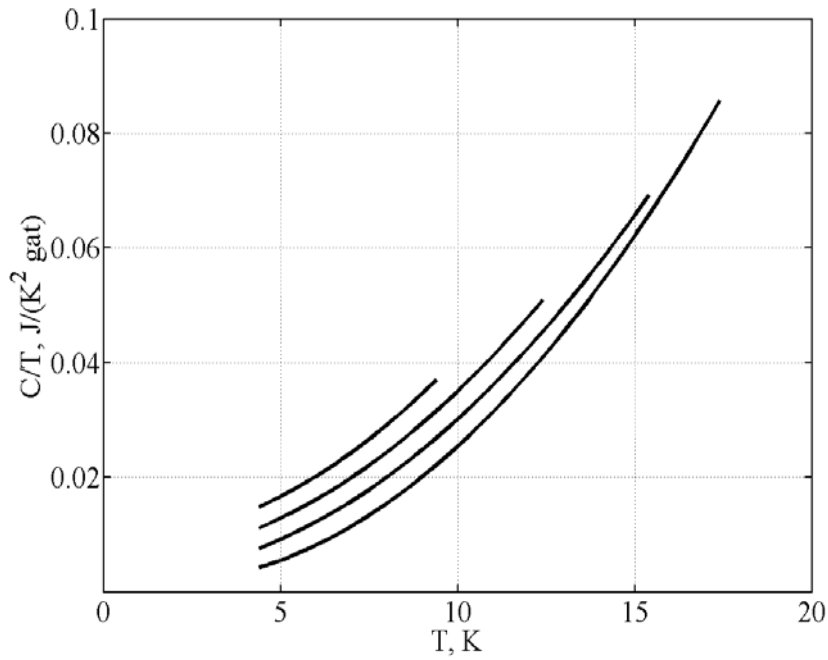


Fig. 5-6 Calculated Heat Capacity of  $\text{Nb}_3\text{Sn}$  at 0,4,10 and 16 T; the heat capacity increases with the magnetic field

Taking into account that:

$$1\text{gat} = 0.25[\text{mole}] \quad 1\text{gat}_{\text{NbSn}} = 99.5[\text{g}] \quad \rho_{\text{NbSn}} = 8910[\text{kg} \cdot \text{m}^{-3}]$$

to convert the specific heat value into S.I. units, Fig. 5-7, we have to introduce for the following multiplication factor:

$$\frac{1\text{mJ}}{\text{K} \cdot \text{Gat}} = \frac{10^{-3}\text{J}}{\text{K} \cdot 99.5 \cdot 10^{-3}\text{kg}} \cdot 8910\text{kg} \cdot \text{m}^{-3} = 89.55 \cdot \text{J} \cdot \text{K}^{-1} \cdot \text{m}^{-3}$$

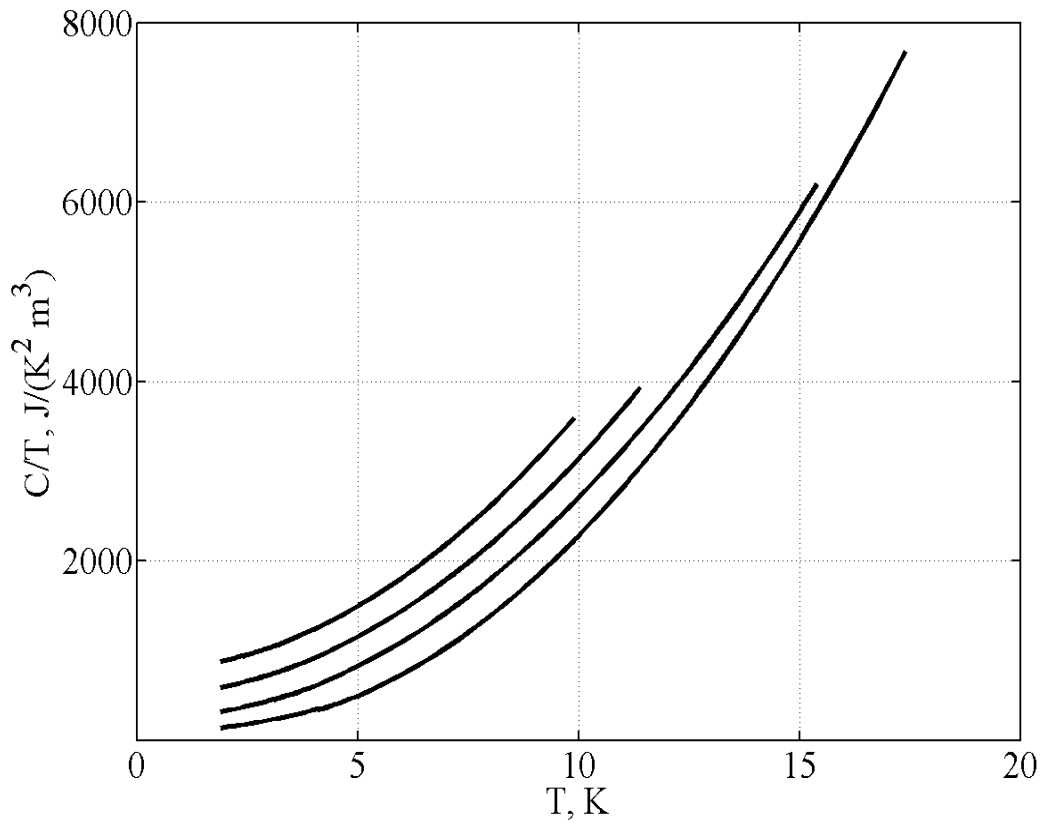


**Fig. 5-7 Calculated Heat Capacity of  $\text{Nb}_3\text{Sn}$  at 0,4,10 and 16 T; the heat capacity increases with the magnetic field**

### 5.3 Volumetric specific heat of the MJR composite $T < T_c$

As seen in the geometry section, the composite is made of Nb<sub>3</sub>Sn, copper and bronze. For the volumetric specific heat of copper, the following parameterization will be used:

$$C_{Cu} = 6.8 \cdot T^3 + 97.4 \cdot T \quad [110]$$

The same equation will be also used to calculate the volumetric specific heat of the bronze, considering negligible difference between copper and bronze.

The volumetric specific heat of the composite will be calculated as the average, weighted over the areas, of the volumetric specific heat of each component, from Tab. 5-1:

$$C_{comp} = \frac{305}{474} C_{NbSn} + \frac{52}{474} C_{Cu} + \frac{117}{474} C_{Bronze} \approx \frac{305}{474} C_{NbSn} + \frac{52}{474} C_{Cu} + \frac{117}{474} C_{Cu}$$

### 5.4 Critical current of the 1 mm MJR strand

At a fixed temperature the critical current of a MJR strand follows the following parameterization (see chapter 4):

$$I_c = C' \cdot B_{pk}^{-0.5} \cdot (1 - B_{pk} \cdot B_{C2}^{-1})^2$$

where the peak field,  $B_{pk}$ , in a 1mm MJR strand is (see chapter 4):

$$B_{pk} = \max(B_{bg} + 0.413 \cdot 10^{-3} \cdot I, 0.648 \cdot 10^{-3} \cdot I - B_{bg})$$

The measured strand (sample A chapter 4), at 4.2 K, has:

$$C' = 12232.49 \cdot [T^{0.5} A] \quad B_{C2} = 22.32 \cdot [T]$$

For a background field of 12 T the critical current was about 705 A and the peak field about 12.3 T. Regarding the critical current density:

$$J_c = \frac{I_c}{non\_cu\_area} = \frac{C'}{non\_cu\_area} \cdot B_{pk}^{-0.5} \cdot (1 - B_{pk} \cdot B_{C2}^{-1})^2$$

For the 1 mm MJR geometry presented in section 5.1:

$$\frac{C'}{non\_cu\_area} = \frac{12232.49}{0.422} = 28987 \cdot [T^{0.5} A \cdot mm^{-2}]$$

This means that the  $J_c$  at 12.3 T is about 1670 A/mm<sup>2</sup>.

In order to calculate the temperature dependence we will use the following relations  
[104]:

$$T_c(0) = 18[K] \quad [102]$$

$$I_c(T, \bar{\varepsilon}) = C'' \left( 1 - \left( \frac{T}{T_c(\bar{\varepsilon})} \right)^2 \right)^2 \cdot B_{pk}^{-0.5} \cdot \left( 1 - \frac{B_{pk}}{B_{c2}(T, \bar{\varepsilon})} \right)^2$$

where:

$$B_{c2}(4.2, \bar{\varepsilon}) = B_{c2}$$

$$B_{c2}(4.2, 0) = 28.1 \left( 1 - \left( \frac{4.2}{18} \right)^{1.374} \right) = 24.3[T]$$

$$T_c(\bar{\varepsilon}) = T_c(0) \cdot \left[ \frac{B_{c2}(4.2, \bar{\varepsilon})}{B_{c2}(4.2, 0)} \right]^{\frac{1}{3}}$$

$$C'' = C' \cdot \left( 1 - \left( \frac{4.2}{T_c(\bar{\varepsilon})} \right)^2 \right)^{-2}$$

$$B_{c2}(0, \bar{\varepsilon}) = B_{c2}(4.2, \bar{\varepsilon}) \left( 1 - \left( \frac{4.2}{T_c(\bar{\varepsilon})} \right)^{1.374} \right)^{-1}$$

$$B_{c2}(T, \bar{\varepsilon}) = B_{c2}(0, \bar{\varepsilon}) \left( 1 - \left( \frac{T}{T_c(\bar{\varepsilon})} \right)^{1.374} \right)$$

## 5.5 Energy dissipated in a magnetized sub-element during a complete flux jump: the 'magnetization' energy

We will consider the magnetic field distribution generated in a superconductor where no current is flowing when the external magnetic field is ramped up starting from 0 T.

According to Wilson [22] the energy dissipated per unit volume ( $dq$ ) due to an infinitesimal reduction of the critical current density ( $dJ_c$ ) for a slab when the field was fully penetrated, can be obtained by the following formula:

$$dq = \mu_0 J_c (-dJ_c) \frac{a^2}{3} \quad \text{eq. 5-1}$$

where  $2a$  is the slab thickness.

Using a slab approximation, the energy dissipated per unit length ( $dQ$ ) in a circular shaped filament fully penetrated (Fig. 5-8) can be estimated integrating eq. 5-1 over the entire cross section. In order to do the integration (of eq. 5-1) for a circular section,  $a$  (slab thickness) was introduced as a function of  $y$ . The energy dissipated per unit length in a slice  $2a$  wide and  $dy$  thick is:

$$dQ(y, J_c) = 2a(y)dy \cdot \mu_0 J_c (-dJ_c) \frac{a(y)^2}{3}$$

The next few equations help to follow how the analytical solution for calculating the energy dissipated was obtained in a case when the field was fully penetrated.

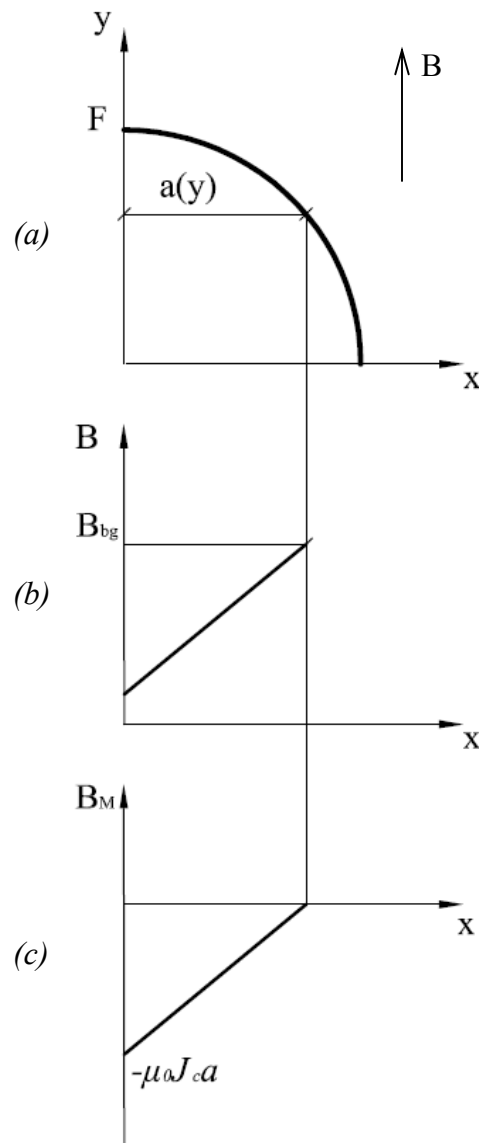


**Fig. 5-8 Magnetic field distribution of a fully penetrated circular filament in an external field  $B_{bg}$  (slab approximation): (a) filament geometry and magnetic field orientation; (b) distribution of the total field; (c) distribution of the field  $B_M$  generated by the magnetization currents ( $B_M = B - B_{bg}$ )**

$$a = \sqrt{F^2 - y^2} = F \sqrt{1 - \frac{y^2}{F^2}}$$

$$dQ(J_c) = 2 \cdot \int_0^F \left[ 2a(y) \mu_0 J_c (-dJ_c) \frac{a(y)^2}{3} \right] dy$$

$$dQ(J_c) = 4 \cdot \frac{\mu_0 J_c (-dJ_c)}{3} \int_0^F a(y)^3 dy$$

$$\int_0^F a(y)^3 dy = F^4 \int_{\frac{\pi}{2}}^0 \cos^4(\alpha) d\alpha = F^4 \frac{3}{16} \pi$$

$$dQ(J_c) = 4 \cdot \frac{\mu_0 J_c (-dJ_c)}{3} F^4 \frac{3}{16} \pi = F^4 \pi \frac{\mu_0 J_c (-dJ_c)}{4}$$

Hence the total magnetization energy per unit length ( $Q$ ) can be calculated assuming that the  $J_c$  gets zero.

$$Q = \int_{J_c}^0 F^4 \pi \frac{\mu_0 J_c (-dJ_c)}{4} = \frac{\pi \cdot \mu_0}{4} F^4 \frac{J_c^2}{2}$$

$$Q = \frac{\pi^2 \cdot 10^{-7}}{2} F^4 J_c^2 \quad \text{eq. 5-2}$$

For example assuming (1 mm MJR at 3 T):

- $J_c = 1.3 \cdot 10^{10} \text{ A/m}^2$
- $F = 50 \mu\text{m}$  (1 mm MJR)

$$Q = \frac{\pi^2 \cdot 10^{-7}}{2} R^4 J_c^2 = 5.21 \cdot 10^{-4} \text{ Joule/m}$$

Since we need to calculate the stored energy even if the field was not fully penetrated another approach was used. It is easy to demonstrate that the dissipated energy per unit length released during a complete 'flux jump' in a magnetized slab with no transport current is:

$$Q = \frac{1}{2 \cdot \mu_0} \int_V B_M^2 \cdot dV$$

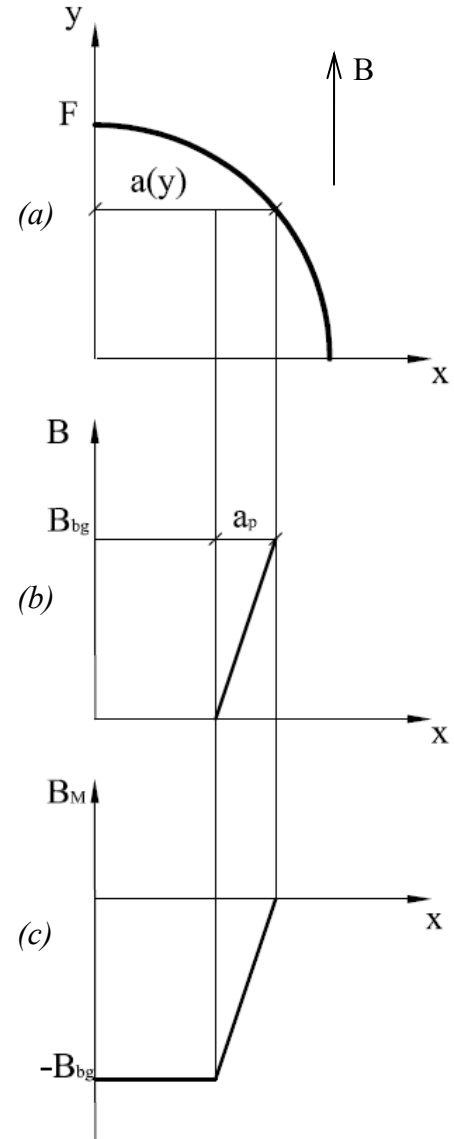


**Fig. 5-9 Magnetic field distribution of a not fully penetrated circular filament in an external field  $B_{bg}$  (slab approximation): (a) filament geometry and magnetic field orientation; (b) distribution of the total field; (c) distribution of the field  $B_M$  generated by the magnetization currents ( $B_M = B - B_{bg}$ )**

where  $B_M$  is the field generated by the magnetization currents:  $B_M = B - B_{bg}$ . We will call this energy as ‘magnetization’ energy.

For a circular shaped filament using the slab approximation and introducing the following definitions  $B_p(y) = \mu_0 J_c a(y)$  and  $a_p = \frac{B_{bg}}{\mu_0 J_c}$  we can write:

$$B_{bg} \leq B_p \text{ (Fig. 5-9 c)} \rightarrow \begin{cases} B_M = -B_{bg} & x \leq a - a_p \\ B_M = -\{B_{bg} - \mu_0 J_c \cdot [x - (a - a_p)]\} = \mu_0 J_c (x - a) & x > a - a_p \end{cases}$$

$$B_{bg} > B_p \text{ (Fig. 5-8 c)} \rightarrow B_M = \mu_0 J_c (x - a)$$

$$Q = \frac{1}{2 \cdot \mu_0} 4 \cdot \int_0^R \left\{ \int_0^a B_M^2 \cdot dx \right\} \cdot dy$$

To verify that this approach will give the same result as what we obtained in eq. 5.2 let us calculate the energy for a filament when the magnetic field is fully penetrated:

$$B_M = \mu_0 J_c (x - a)$$

$$Q = \frac{1}{2 \cdot \mu_0} 4 \cdot \int_0^F \left\{ \int_0^a \mu_0^2 J_c^2 (x - a)^2 \cdot dx \right\} \cdot dy$$

$$Q = \frac{\pi^2 \cdot 10^{-7}}{2} F^4 J_c^2$$

Indeed we obtained the same result.

It is important to point out that this model is not exact since the finite cylindrical shape conductor can not be estimated as a slab so neither the current distribution neither the field distribution is exactly correct. Better value can be obtained by using finite element modeling.

## 5.6 Energy dissipated in a not magnetized strand with transport current during a complete flux jump: the ‘Self field’ energy

Due to the self field the transport current flows in the outermost filaments as close as possible to the composite surface. The current flows at the critical current density of the conductor and it penetrates only as deep as it is necessary to carry the transport current shielding the interior of the conductor from the self-field.

Taking as a reference a superconducting strand which has an annular section with an internal radius equal to  $R_f$  and an external radius equal to  $R$ , Fig. 5-10, the transport current will flow in the external shell between  $R$  and  $c$ , where  $c$  has to satisfy the following equation:

$$I = \pi(R^2 - c^2)$$

During self field instability the current redistributes in the superconductor section producing heat.

We will assume: not to have an external copper shell around the composite; the heat does not escape from the composite; the temperature is uniform in the section of the superconductor where the current flows and  $J_c = f(T, B_{peak})$ . Using this approximation we will be able to calculate analytically the energy dissipated by a complete redistribution of the transport current when the strand is not magnetized (we will call this energy as ‘self field’ energy).

With our assumptions the energy dissipated for unit length due to an infinitesimal reduction of the critical current density is [22]:

$$dQ = \mu_0 \lambda^2 J_c (-dJ_c) R^4 \pi \left\{ -\frac{1}{2} \ln \varepsilon - \frac{3}{8} + \frac{\varepsilon^2}{2} - \frac{\varepsilon^4}{8} \right\} \quad \text{eq. 5-3}$$

where  $\varepsilon = c/R$

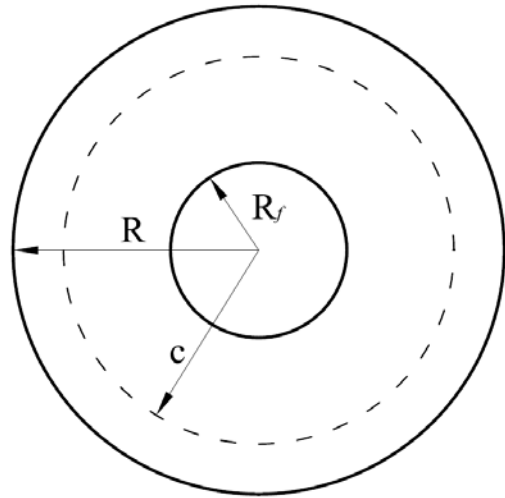


Fig. 5-10 Transport current distribution in a superconducting strand

In order to calculate the total self field energy per unit length, eq. 5-3 has to be integrated from the beginning of the instability to the time ( $t$ ) when the transport current is uniformly distributed over the whole cross section of the superconductor.

As a function of time eq. 5-3 has the following form:

$$dQ(t) = \mu_0 \lambda^2 J_c(t) (-dJ_c(t)) R^4 \pi \left\{ -\frac{1}{2} \ln \varepsilon(t) - \frac{3}{8} + \frac{\varepsilon^2(t)}{2} - \frac{\varepsilon^4(t)}{8} \right\} \quad \text{eq. 5-4}$$

Since the current is constant:

$$\pi(R^2 - c^2(t)) \lambda J_c(t) = \pi(R^2 - c^2(0)) \lambda J_c(0) = I$$

$$J_c(t) = \frac{I}{\pi \lambda (R^2 - c^2(t))} \quad dJ_c(t) = \frac{I}{\pi} \cdot \frac{2c(t)}{\lambda (R^2 - c^2(t))^2} dc(t)$$

Substituting the expressions of  $J_c(T)$  and  $dJ_c(T)$  in eq. 5-4:

$$dQ(t) = -\mu_0 \lambda^2 \frac{I}{\lambda \pi (R^2 - c^2(t))} \frac{I}{\pi} \cdot \frac{2c(t)}{(R^2 - c^2(t))^2} dc(t) R^4 \pi \left\{ -\frac{1}{2} \ln \varepsilon(t) - \frac{3}{8} + \frac{\varepsilon^2(t)}{2} - \frac{\varepsilon^4(t)}{8} \right\}$$

$$\text{Since: } d\varepsilon(t) = \frac{dc(t)}{R}$$

$$dQ(t) = -\mu_0 \lambda \frac{I^2}{\pi} \cdot \frac{2\varepsilon(t)}{(1 - \varepsilon^2(t))^3} d\varepsilon(t) \left\{ -\frac{1}{2} \ln \varepsilon(t) - \frac{3}{8} + \frac{\varepsilon^2(t)}{2} - \frac{\varepsilon^4(t)}{8} \right\}$$

Hence the total self field energy per unit length is:

$$Q = -\mu_0 \lambda \frac{I^2}{\pi} \cdot \int_{\varepsilon_0}^{\varepsilon_f} \left[ \frac{2\varepsilon}{(1 - \varepsilon^2)^3} \left\{ -\frac{1}{2} \ln \varepsilon - \frac{3}{8} + \frac{\varepsilon^2}{2} - \frac{\varepsilon^4}{8} \right\} \right] d\varepsilon$$

where:

$$\varepsilon_0 = \frac{c_0}{R} \quad \varepsilon_f = \frac{R_f}{R}$$

## 5.7 Enthalpy calculation and quench criterion

If the quench current is lower than  $I_c$ , the first part of the quench development is characterized by redistribution of the transport current in the composite section. This part of the quench development will end at the time  $t_f$ , when the transport current is completely distributed in the whole composite section. At  $t_f$ , according to the Bean's model and making the hypothesis that the temperature in the strand section is equal everywhere (same approximation used in section 5.6), the final current density,  $J_f$ , has to be:

$$J_f = J_c(T_f) = \frac{I}{\pi(R^2 - R_f^2)}$$

Using this relation and the parameterization of the critical current density, we can calculate the temperature,  $T_f$ , that the composite must have for a complete redistribution of the transport current.

Once we have this temperature, we can calculate the enthalpy variation per unit length of the composite:

$$\Delta H = \pi(R^2 - R_f^2) \int_{4.2}^{T_f} C_{comp} dT$$

To find out at what transport current value will occur a quench we had to calculate both the enthalpy change value and the released energy (magnetization and self field) value as a function of the transport current. If the two value equal with each other we assume that the sample has quenched. This is obviously an adiabatic model since we assume that during the current redistribution process no heat escapes the conductor.

## 5.8 Minimum quench current based on Self field energy

During V-I measurements of the 1 mm MJR strands we observed premature quenches in the low field region (~0-8 T). The quench currents were lower than the  $I_c$  even if the measurement started with a strand not magnetized. In these conditions the magnetization energy stored in the filaments at the moment of the quench was negligible as we will show in sections 5.10 and 5.11. The cause of the instability, during these measurements, is mostly due the self field energy.

In this section we will show and discuss the quench current calculated by the adiabatic model considering only the amount of energy released during the current redistribution equal to the self field energy neglecting the contribution of the magnetization energy.

The results of the calculations are summarized in Fig. 5-11; at low magnetic fields the quench current estimated by the model is much lower than the critical current, this difference gets smaller by increasing the magnetic field.

In Fig. 5-12 the self field energy and the enthalpy margin are shown as a function of the current for different magnetic fields. At the current level where the two curves cross each other, the sample may quench due to self field instability.

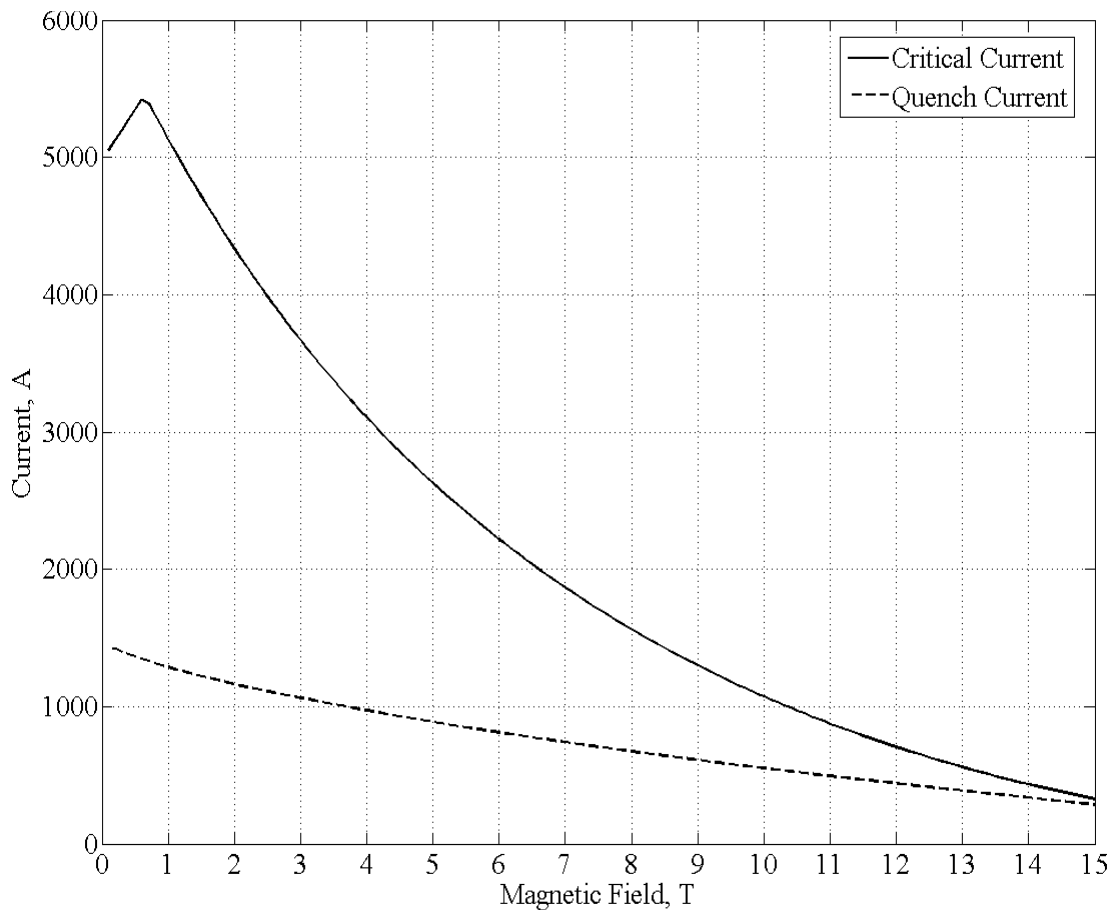


**Fig. 5-11 Quench current estimate based on self field effect for a 1 mm MJR strand**

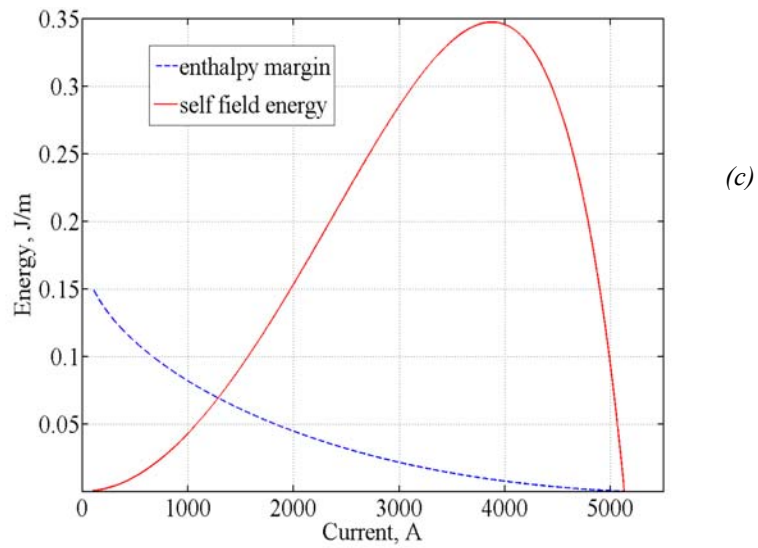
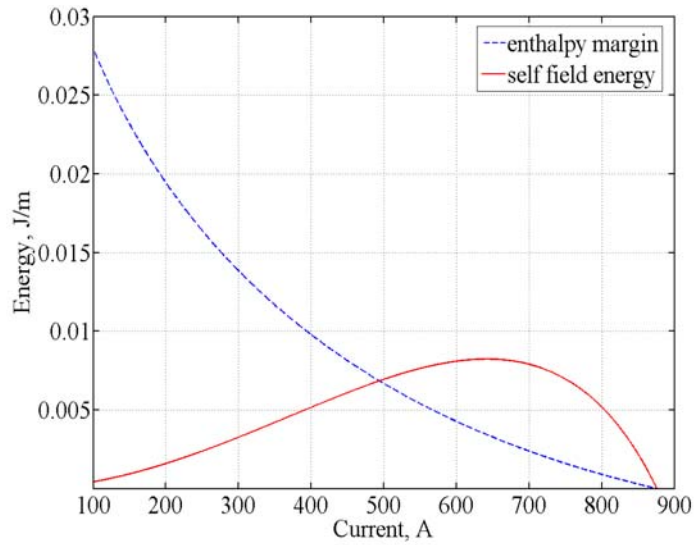
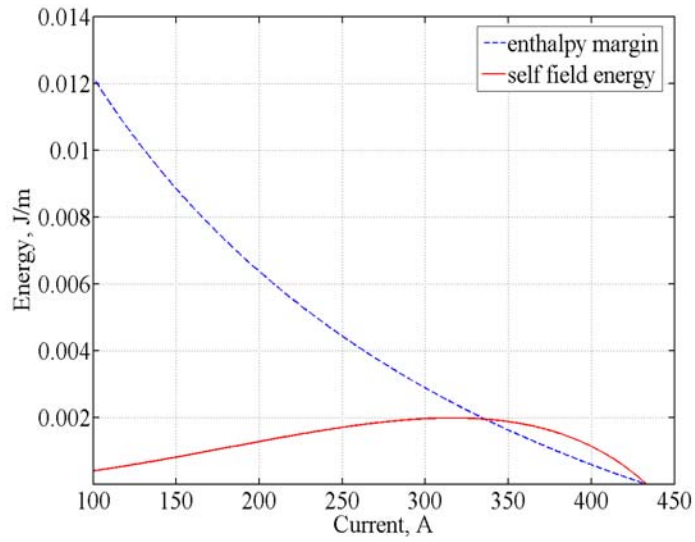


Fig. 5-12 Self-field energy and enthalpy margin for a 1mm MJR: (a) 14 T; (b) 11 T; (c) 1 T

## 5.9 Minimum quench current based on Self field and Magnetization energy

During V-H measurement the strand is strongly magnetized at low magnetic fields and the magnetization energy can not be neglected in calculating the quench current. In this section we present the quench current values obtained by the model taking in to account that during the current redistribution, both the self field and magnetization energy are released.

The model is based on the assumptions that: 1) the transport current flows in the outermost filaments while the inner filaments get magnetized; 2) the energy dissipated during a complete flux jump is the arithmetic sum of the self field energy, as calculated in section 5.6, with the magnetization energy. The magnetization energy is calculated for the case where the background magnetic field is ramped up from 0 T starting with a strand not magnetized. In these conditions the magnetization energy in a filament can be

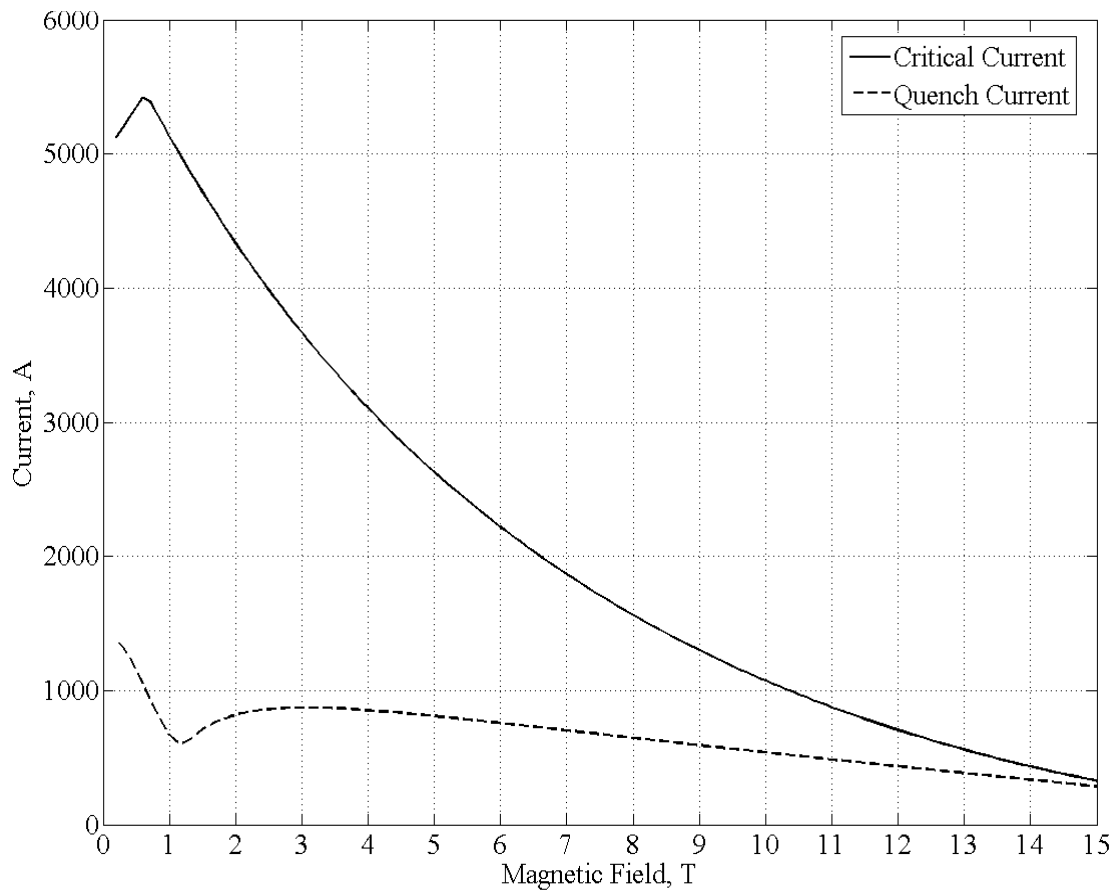


Fig. 5-13 Quench current estimate based on self field and magnetization effect for a 1mm MJR

calculated using the equations presented in section 5.5. The total amount of magnetization energy is calculated by multiplying the magnetization of a single filament by the total number of filaments and by the fraction of the composite area not occupied by transport current.

These results are summarized in Fig. 5-13. At high field values the quench current is almost the same as what was obtained by taking into account in the calculation the self field energy only (for field higher than 4 T the difference is less than 15%). However, at lower field values there is a significant difference. In particular around 1.2 T the calculated quench current has a local minimum that is almost by factor of two less than what was calculated at the same field taking in to account the self field energy only, Fig. 5-11.

### 5.10 Self Field in the strand sample

Up to now, in the calculation of the magnetization energy, the contribution due to the variation in time of the self-field was neglected; in this section, in order to calculate how much this contributes we estimate the value of the self field within the strand cross section of the sample that we use for strand V-I and V-H measurements (see chapter 4). In particular we are interested in the value of the self field in the inner filaments where the transport current is not flowing,  $B_{coil}$ .

The strand cross section is the intersection between the sample and the plane passing through the axis of the sample, Fig. 5-14.

In order to calculate the magnetic field distribution with a finite element model, the sample geometry has been drawn using the sample holder parameters presented in chapter 4 and the simplified strand geometry described in section 5.6. In agreement with the calculation presented in section 5.1 the strand radius  $R$  was set equal to 0.413 mm;

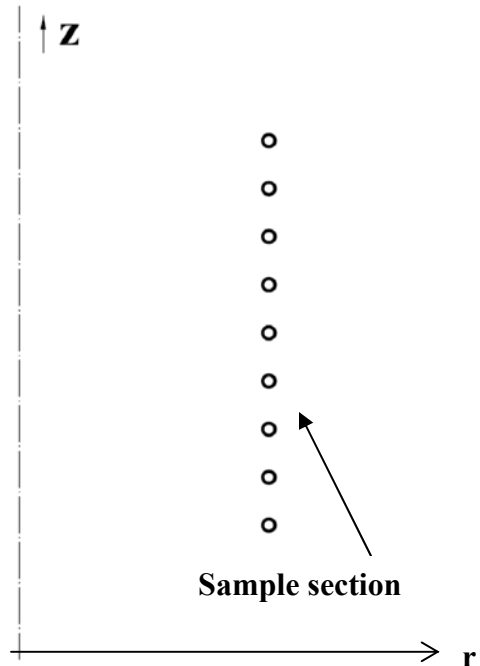


**Fig. 5-14 Half view ( $r>0$ ) of the sample's cross section in the coil like configuration**

moreover it was assumed that a transport current of 1000 A was flowing with a constant current density in an external shell characterized by a normalized skin depth  $\varepsilon$  (for the definition of  $\varepsilon$  see section 5.6).

Fig. 5-15 shows the magnetic flux distribution due to the self field in the case where  $\varepsilon$  is equal to 0.85. The self field,  $B_{sf}$ , has mainly a z component and in the inner part of the coil it is anti-parallel to the background field generated by the external solenoid magnet, Fig. 5-15 a. The self field,  $B_{coil}$ , in the central part of the strand where there is no transport current is almost uniform and anti-parallel to the background field, Fig. 5-15 b. For different values of  $\varepsilon$  the maximum and minimum values of  $B_{coil}$  do not change significantly, Fig. 5-16, and for all three cases ( $\varepsilon=0.85$ ,  $\varepsilon=0.73$ ,  $\varepsilon=0.48$ ) presented in the figure, the arithmetic average  $\hat{B}_{Coil}$  of the minimum and the maximum is 0.11 T.

Therefore, as a first approximation in the next sections we will assume that  $B_{coil}$  is uniform and equal to  $\hat{B}_{Coil}$  where:

$$\hat{B}_{Coil} = -0.11 \cdot 10^{-3} \cdot I$$

In formula the minus sign indicates that  $B_{coil}$  is anti-parallel to the background field.

### **5.11 Magnetization in the strand sample due to self field**

The self-field  $B_{coil}$  described in the previous section should be treated as a background field consequently it modifies the calculated value of the strand magnetization.

In V-I measurements (starting with the sample not magnetized), by ramping up the current the strand gets slightly magnetized due the increase of  $B_{coil}$ .

To take into account this effect in the model, the magnetization energy produced by the variation of the self field from 0 to  $B_{coil}$  in the inner filaments has to be added to the self-field energy.

The self-field plays a role in V-H measurements as well since any current change will induce a magnetization as it was described above. Because of the self field, when we start to ramp up the field from 0 T with transport current, the sample it is slightly magnetized even if it was not magnetized before ramping up the current.

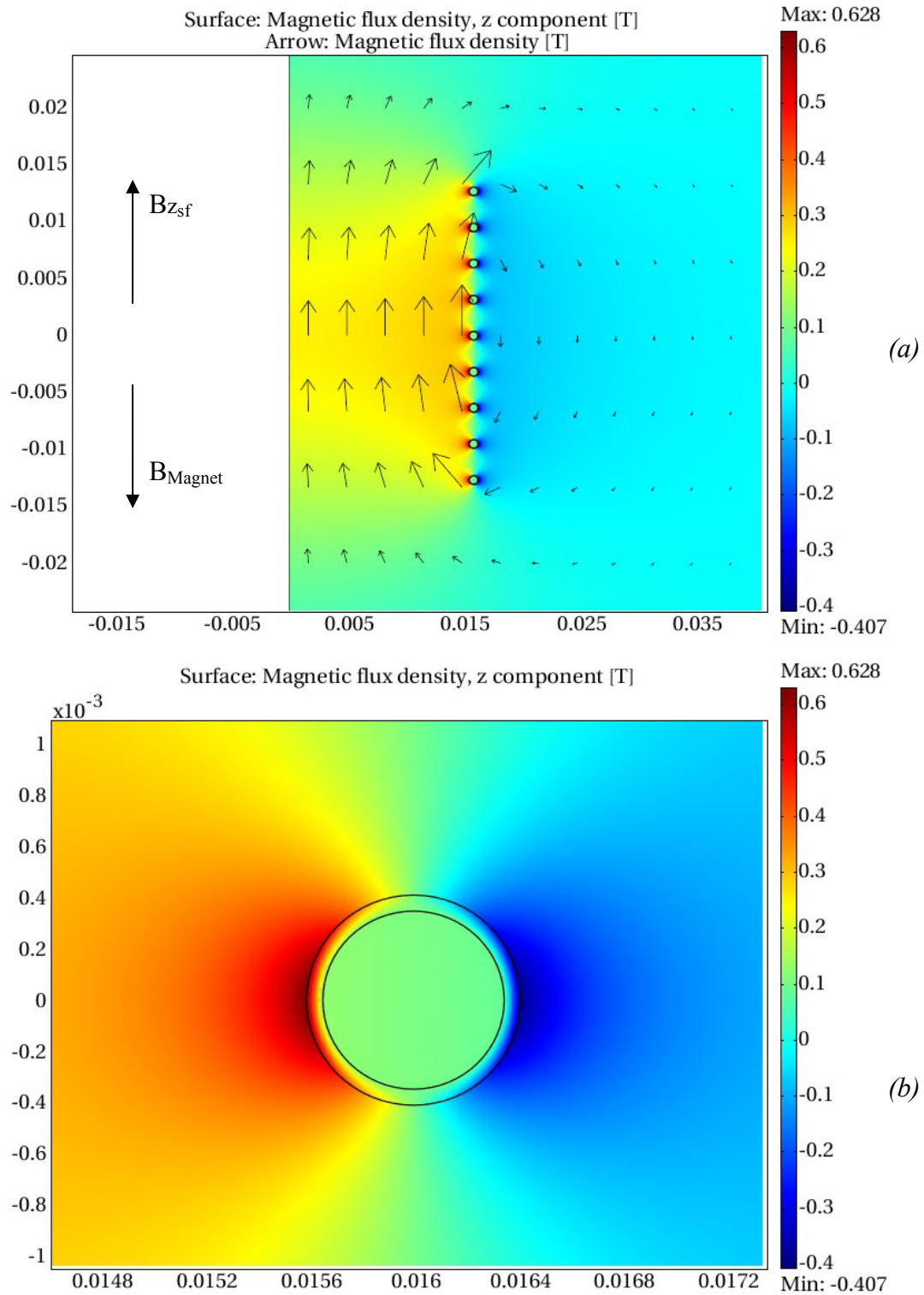


**Fig. 5-15** Magnetic flux distribution in a cross section of the coil like sample due to the self field generated by a current equal to 1000A flowing in the composite external shell which has  $R=0.413$  mm and  $\epsilon=0.85$ : (a) half coil sample; (b) central turn. In the abscissa and ordinate axes there are respectively the distance in meters from the coil axis and the magnetic flux in Tesla

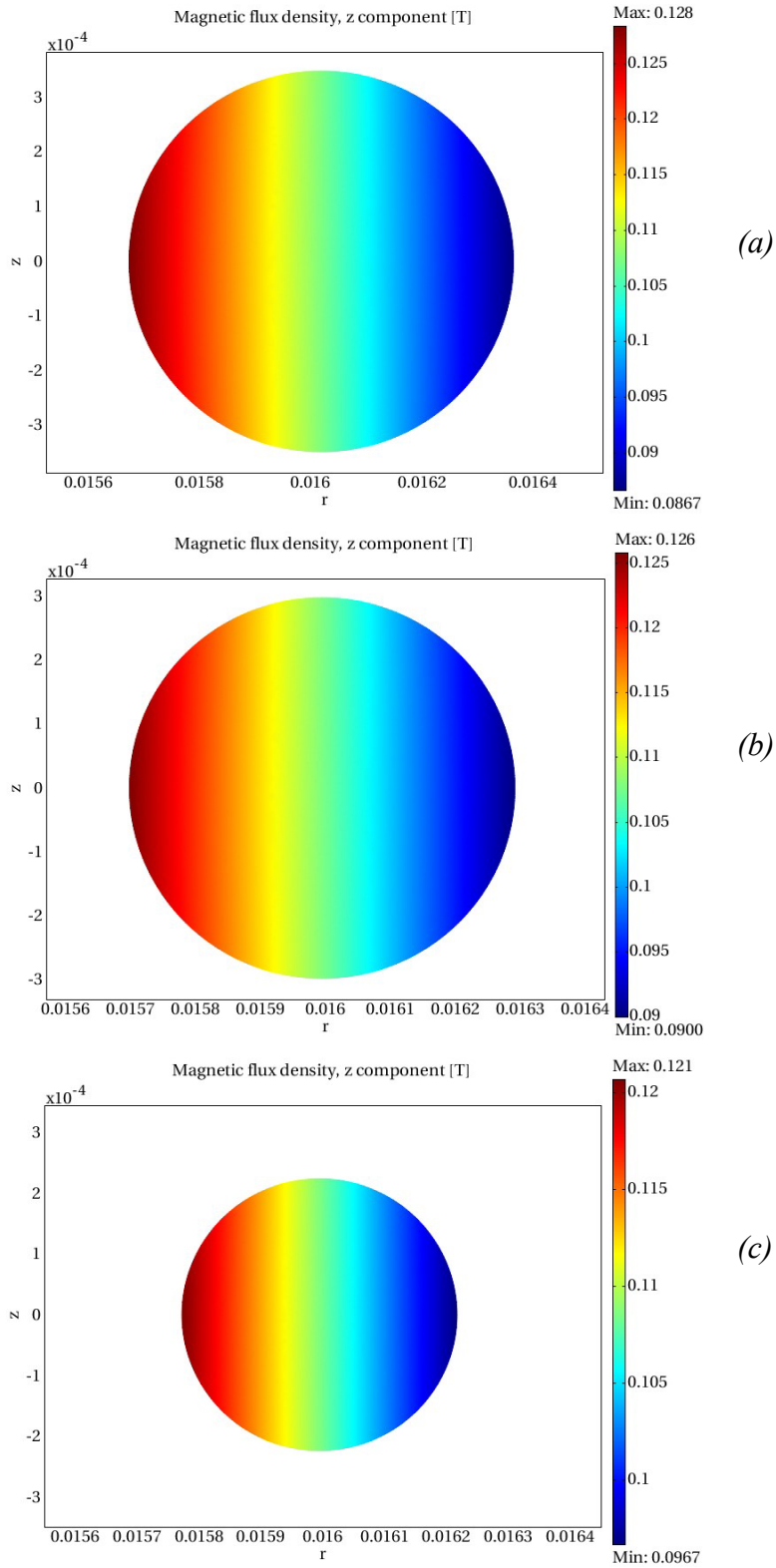


**Fig. 5-16 Magnetic flux distribution in the central part of the strand (where there is not transport current) of the coil like sample due to the self field generated by a current equal to 1000A flowing in the composite external shell which has  $R=0.413$  mm and: (a)  $\epsilon=0.85$ ; (b)  $\epsilon=0.73$ ; (c)  $\epsilon=0.48$ .**

If we ramp up the magnetic field from 0 T under a transport current the magnetization direction due to self field has opposite sign relative to the magnetization due to the background field up ramp. This means that initially, the background field will reduce the magnetization due to self field. When the field generated by the magnet is bigger than two times of  $B_{coil}$ , the distribution of the persistent current is practically the same as if the strand had been subjected to an external field increasing from 0 T to  $B_{Magnet}-B_{Coil}$ . In this case the magnetization energy can be calculated by using the same formulation as it was used previously by substituting  $B_{bg}$  with  $B_{Magnet}-B_{Coil}$ . The magnetization energy for  $B_{Magnet}=0$  is due to self-field.

Since for  $0 \text{ T} < B_{Magnet} < 2 B_{coil}$ , the calculation of the magnetization energy is a little more complicated and since the  $B_{coil}$  value is quite small, we decided not to calculate  $I_q$  in this range.

In Fig. 5-17 the quench current estimate is shown with and without taking into account the contribution of the magnetization energy due to self field effect in the strand sample. From the plot it can be clearly seen that the effect of magnetization due to the self-field on the quench currents is minimum.

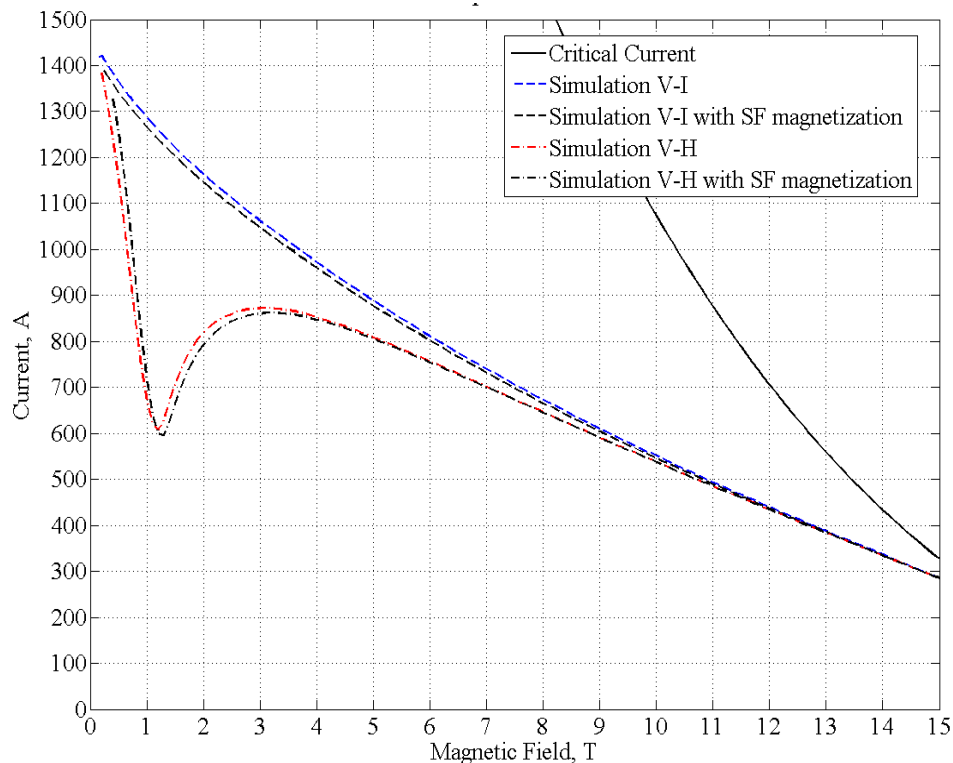


**Fig. 5-17 Effect of the magnetization produced by the self-field for a 1mm MJR**

## **5.12 Comparison with experimental results**

In this section we will show a comparison between the quench current estimated by the model and the results that we had obtained measuring 1 mm MJR strands with a low RRR copper matrix (7). This type of sample is a good candidate for this adiabatic approach because of the low thermal and electrical conductivity of the copper matrix which does not allow large amount of energy to diffuse outside of the composite.

The calculations presented in section 5.8 simulates the minimum quench currents during V-I measurements starting with a sample not magnetized, while the calculations in section 5.9 are the simulation of V-H measurements starting from 0 T with the sample not magnetized. The experimental data in these physical conditions are showed in Fig. 5-18 and compared with analytical simulations.

The adiabatic model fits quite well the experimental data collected during V-I measurements at fields lower than 6 T, while it underestimates significantly the quench current at higher field values. This discrepancy at high field is partially due to having neglected the strand's external copper shell in the calculation of the electric field during a flux jump. Indeed during the flux jump the external copper shell shares part of the transport current reducing the electric field and the heat produced by joule effect in the superconductor [111]. This effect is particularly important at high field where the energy associated with the instability is very low, for example during V-I measurements at 11 T the calculated maximum energy released by a complete flux jump is less than 10 mJ/m, Fig. 5-12. This means that an energy reduction of even a few mJ/m can prevent a premature quench of the strand. On the other hand, looking at Fig. 5-12, we can see that the same amount of energy will not have any significant effect in the quench current value during V-I measurement at 1 T.

Besides the approximations that have been made to calculate the energy released during a complete flux jump, the model results can be different from the experimental quench data for another reason: the model calculates the minimum current at which a strand can quench, rather than the expected quench current. For currents higher than the value calculated by this model, the energy that a complete flux jump would release is sufficient to quench the strand, although the strand still may not quench because the flux jump could need some 'activation' energy to be initiated (the strand is stable). That is, the

model establishes a necessary condition that has to be fulfilled for having a premature quench (the current has to be higher than the value calculated by the model), but this condition is not automatically sufficient. This model is a stability criterion that establishes for each field the current value below which we are sure not to quench.

Regarding the V-H measurements starting at 0 T with the sample not magnetized (E3 experiment), the model fits the experimental data very well. This good agreement between the model and the data is due to the fact that the sample is already unstable for fields values that are lower than the quench field (indeed many partial flux jumps were observed preceding the quench - see chapter 4); in these conditions the quench may occur when the energy released by a complete flux jump is sufficiently high.

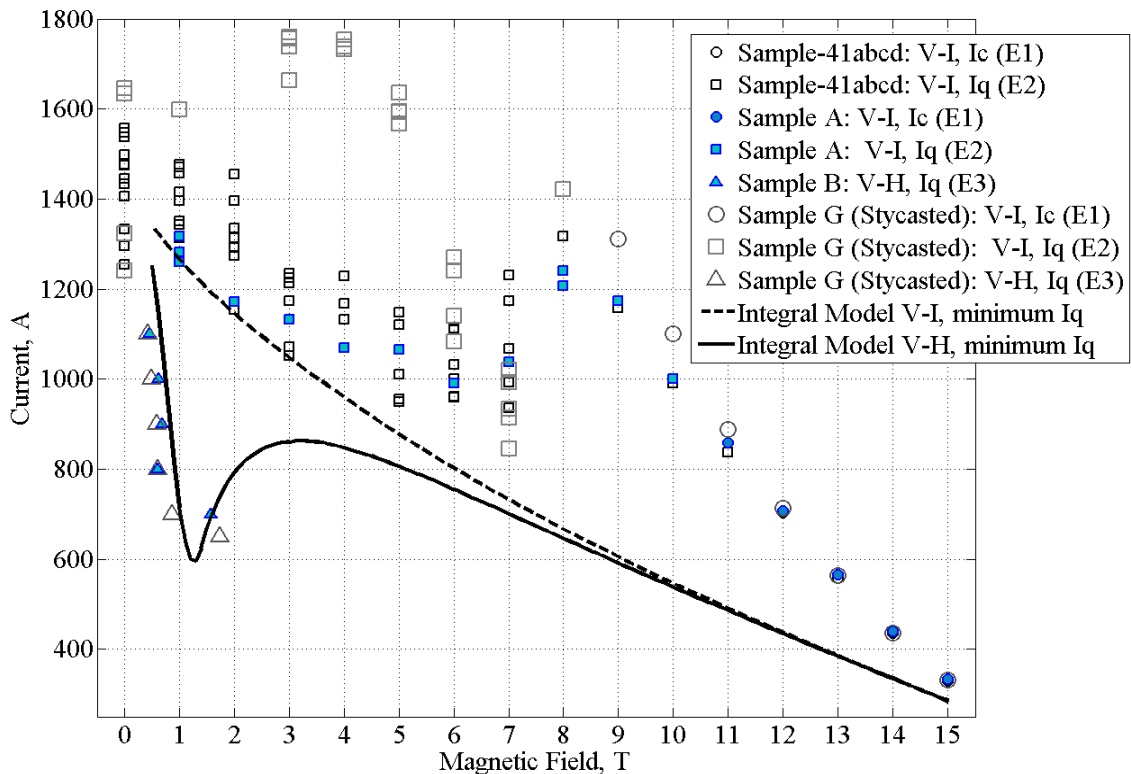


Fig. 5-18 Comparison between model and experimental data for 1mm MJR with low RRR (~7)

### **5.13 Conclusions**

A stability criterion for the transport current of superconducting strands affected by thermo-magnetic instabilities was developed. The criterion establishes the current range where superconducting strands with a low RRR of the copper stabilizer do not show premature quenches during V-I and V-H measurements. Although this model is based on simplifying approximations its results are strongly consistent with the experimental data at low fields (0-6 T). The two most relevant points that can be drawn from this model are: 1) when the electric conductivity of the strand matrix is low an integral energy balance can estimate the quench current at low field; 2) when starting with the sample not magnetized during V-I measurements the filament size does not play a strong role because the magnetization of the strand is negligible; the quench current value is essentially determined by the flux jump of the self field.

## Chapter 6 – Conclusions

This thesis work focused on superconducting accelerator magnet and superconductor instability studies. The work was performed in the Technical Division of Fermi National Accelerator Laboratory within the High Field Magnet program (HFM). Several Nb<sub>3</sub>Sn high field dipoles and several different Nb<sub>3</sub>Sn strands were tested and analyzed.

Early in the HFM program it was recognized that the observation of voltage spikes due to sudden flux changes is a good indicator of both mechanical and thermo-magnetic instabilities. These instabilities are the primary cause of superconducting magnet quench current limitations. A special Voltage Spike Detection System (VSDS) was developed and used to test the magnets.

Nb<sub>3</sub>Sn strands are intrinsically unstable due to their high  $j_c$  and large effective filament diameter. In order to understand the instability mechanisms and their influence on quench current performance, voltage spikes studies were extended to strand measurements.

Systematic studies of voltage spikes and their relationship to magnet and conductor instability are essential part of the thesis.

The following bullets summarize the main conclusions of the thesis:

- High field magnets (HFDA, SR) were built and tested at Fermilab using two different strands: the 1 mm MJR conductor and the more thermo-magnetically stable 1 mm PIT conductor. All the MJR magnets had limited quench performance while all the PIT magnets reached their design current.
- Systematic observation of voltage spikes due to sudden flux changes in Nb<sub>3</sub>Sn magnets using the newly developed VSDS showed that tens of partial flux jumps occur at low currents whenever the magnet was energized. Another type of voltage spike signal was also observed; it appeared only at high currents and was characterized by high frequency oscillations. This signal was due to the mechanical motion of the coil and always disappeared after the magnet quench training had been completed.

- Partial flux jumps were observed in PIT magnets, meaning that they were thermo-magnetically unstable. Nevertheless, the lower electro-magnetic potential energy stored in these PIT strands (with respect to the MJR conductor) and the high RRR of its copper matrix prevented premature quenches.
- V-I measurements of high- $j_c$  Nb<sub>3</sub>Sn strands starting with the sample not magnetized (E2) showed that these conductors always have premature quenches due to thermo-magnetic instabilities for magnetic fields lower than  $\sim 8$  T. These strands were limited by self-field instability. Monitoring the tests with the VSDS showed that the quenches were not preceded by voltage spikes (partial flux jumps). Therefore, when the sample became thermo-magnetically unstable during V-I measurements, the stored electro-magnetic potential energy in the strand was high enough to quench it.
- Strands in magnets can be strongly magnetized. In order to reproduce this condition in strands, V-H measurements were introduced. Using this procedure the quench current was further reduced in the very low field region ( $\sim 0-3$ T) with respect to that obtained during V-I measurements. This measurement performed on extracted strands allows one to predict whether or not the magnet will be limited by thermo magnetic instabilities. The positive influence of the high RRR of the copper matrix on quench performance was also observed.
- During V-H measurements at very low fields, premature strand quenches were always preceded by voltage spikes (partial flux jumps). Analyzing the voltage signals captured by the VSDS made it possible to distinguish two different types of flux jumps: ‘transport current’ (self field) and ‘magnetization’ flux jumps. The former were due to the redistribution of the transport current in the strand section, and the latter to the collapse of the magnetization currents. In ‘transport current’ spikes, even if the voltage signal was dominated by the current redistribution the event was initiated by a collapse of the magnetization currents. Many voltage signals appeared to be a combination of ‘transport current’ (self field) and ‘magnetization’ flux jumps.
- It was also found that flux jumps are local phenomena that propagate longitudinally. This means that in order to simulate premature quenches due to

thermo magnetic instabilities in the dynamic case it is necessary to adopt a three dimensional model.

- During V-H measurements at very low field, the lower quench current with respect to V-I measurements is due to a twofold effect produced by the strand magnetization: the conductor becomes more thermo-magnetically unstable and the electro-magnetic stored energy in the strand is higher than in the case of the E2 experiments. The potential energy is higher because the ‘magnetization’ energy is present in addition to the ‘self field’ energy.
- When the magnetic field is increased, the sample becomes strongly unstable and starts to generate partial flux jumps. When the potential electro-magnetic energy is high enough the sample quenches.
- A semi-analytical adiabatic model was developed to simulate the quench current value for V-I and V-H measurements which started with the sample not magnetized (E2 and E3). The model is based on two hypotheses: 1) a quench occurs when the electromagnetic potential energy is sufficient to quench the sample; 2) the release of energy is instantaneous (adiabatic approach). Comparing the results of the model with the experimental data of a 1 mm MJR strand that has low RRR (a good candidate to use an adiabatic approach) a good correlation was found, especially for the most interesting case, the V-H measurements.
- To improve the quench performance of superconducting strand, it is necessary to decrease the strand magnetization (reduce the effective filament size and/or the critical current density at low field) and to improve the strand capability to diffuse heat. A practical solution without changing the strand design is to increase the copper matrix RRR by reducing the heat treatment time and carefully controlling the mechanical deformation of the strands during cabling.



## Appendix A – V-I characteristic of type II superconductor

The current-voltage characteristics of type II superconductors can be described by the following formula [23]:

$$\boxed{j(E) = j_c + j_1 \ln\left(\frac{E}{E_0}\right)} \quad \text{for } E < E_f \quad \text{eq. A-1}$$

Where:

- $E_f$  is the electric field at which the superconductor enters into the flux flow regime;
- $E_0$  is the electric field developed in the superconductor at  $j = j_c$ ;
- $j_1$  is a constant that describes the current density increase as a function of the electric field.

In order to determine  $j_c$  and  $n$ -value based on the resistivity criteria the power law parameterization eq.4.3-2 has to be re-arranged:

$$E_0 = \rho_c \cdot \frac{I_c}{A}; \quad j_1 = f(n)$$

where  $A$  is the average area of the strand cross-section. From eq. A-1:

$$e^{j(E)-j_c} = \left(\frac{E}{E_0}\right)^{j_1} \quad E = E_0 e^{\frac{j(E)-j_c}{j_1}} \quad \boxed{E = \rho_c \frac{I_c}{A} e^{\frac{j(E)-j_c}{j_1}}} \quad \text{eq. A-2}$$

Differentiating eq. A-2 in  $j$ :

$$\frac{dE}{dj} = \rho_c j_c \frac{1}{j_1} e^{\frac{j(E)-j_c}{j_1}} \quad \boxed{\frac{dE}{dj} \Big|_{j_c} = \rho_c \frac{I_c}{A \cdot j_1}} \quad \text{eq. A-3}$$

From the power law parametrization, assuming that the current flows only in the superconductor:

$$E = \frac{I}{A} \cdot \rho_c \left(\frac{I}{I_c}\right)^n \quad E = \frac{j \cdot A_{n\_cu}}{A} \cdot \rho_c \left(\frac{j}{j_c}\right)^n$$

Differentiating the above equation in  $j$  we obtain:

$$\frac{dE}{dj} = \frac{\rho_c}{j_c^n} (n+1) j^n \quad \boxed{\frac{dE}{dj} \Big|_{j_c} = \frac{A_{n\_cu}}{A} \rho_c (n+1)} \quad \text{eq. A-4}$$

Equalizing eq. A-3 and A-4:

$$\rho_c \frac{I_c}{A \cdot j_1} = \frac{A_{n-cu}}{A} \rho_c (n+1) \quad \boxed{j_1 = \frac{j_c}{(n+1)}} \quad eq. A-5$$

Eq. A-2 can then be written as:

$$\boxed{E = \rho_c \frac{I_c}{A} e^{\frac{j(E)-j_c}{j_c}(n+1)}} \quad eq. A-6$$

The voltage signal during critical current measurement can then be parameterized as:

$$V = \frac{l}{A} \cdot \rho_c \cdot I_c \cdot e^{\frac{I-I_c}{I_c}(n+1)}$$

Where:

- $V$  is the measured voltage (in volts) between the two voltage taps
- $l$  is the length of the strand between the two voltage taps

Considering that the voltage measurements can have an offset, the right parameterization is the following:

$$\boxed{V = V_{offset} + \frac{l}{A} \cdot \rho_c \cdot I_c \cdot e^{\frac{I-I_c}{I_c}(n+1)}} \quad eq. A-7$$

## Appendix B – Critical current parameterization

The Critical State Model assumes that the current flows in the superconductor always at the conductor's critical current value. If there is a magnetic field present, a Lorentz force will act on the vortices:

$$\boxed{|\vec{J}_c(B) \times \vec{B}| = F_p(B)} \quad \text{eq. B-1}$$

where  $F_p$  is the maximum pinning force,  $J_c$  is the critical current density and  $B$  is the total magnetic field.

There is a variety of pinning models [112, 113] however most of them derive the same relationship for the pinning force as the function of the magnetic field:

$$\boxed{F_p(B) = C \cdot b^p \cdot (1-b)^q} \quad \text{eq. B-2}$$

where  $b=B/B_{C2}$ ,  $C$  is a scaling constant and  $p$  and  $q$  are two parameters depending on the material. For  $\text{Nb}_3\text{Sn}$   $p \approx 0.5$  and  $q \approx 2$ . Eq. B-2 has been experimentally confirmed by magnetic measurement down to 1 T [114].

Eq. B-1 and eq. B-2 describe the scaling law for the critical current as a function of the magnetic field. To introduce in eq. B-2 the temperature,  $T$ , and strain,  $\varepsilon$ , dependence, the scaling constant  $C$  and  $B_{C2}$  should be expressed as a function of the temperature and strain.  $C$  is directly proportional to  $B_{c2}(T,\varepsilon)$  and inversely proportional to the Ginzburg-Landau parameter  $k(T,\varepsilon)$  [102]. However, to fit the experimental results with the scaling law described in the previous paragraph, an additional term  $A(\varepsilon)$ , which is a function of strain only, has to be introduced into  $C$  [102].

$$C = A(\varepsilon) \frac{[B_{c2}(T,\varepsilon)]^n}{(2\pi \Phi_0)^{1/2} \mu_0 [k(T,\varepsilon)]^m}$$

Where:

$$\Phi_0 \equiv \frac{h}{2e} \approx 2.0678 \cdot 10^{-15} \text{ Wb} \quad \text{magnetic flux quantum;}$$

$$\mu_0 \equiv 4\pi \cdot 10^{-7} \text{ H} \cdot \text{m}^{-1} \quad \text{vacuum magnetic permeability}$$

The maximum pinning force can be then parameterized as:

$$\boxed{F_p(B) = A(\varepsilon) \frac{[B_{c2}(T,\varepsilon)]^n}{(2\pi \Phi_0)^{1/2} \mu_0 [k(T,\varepsilon)]^m} \cdot b^p \cdot (1-b)^q} \quad \text{eq. B-3}$$

Eq. B-3 can be written using only single variable functions.

The Ginzburg-Landau relation for the upper critical field is:

$$\boxed{k(T, \varepsilon) = \frac{B_{c2}(T, \varepsilon)}{\sqrt{2}B_c(T, \varepsilon)}} \quad \text{eq. B-4}$$

Using the two fluid model for the temperature dependence [102]:

$$\boxed{B_c(T, \varepsilon) = B_c(0, \varepsilon)(1-t^2)} \quad \text{eq. B-5}$$

where: 
$$t = \frac{T}{T_c(\varepsilon)}$$

From a linear approximation of the generalized BCS relations [102] one obtains:

$$\boxed{B_c(0, \varepsilon) \propto T_c(\varepsilon)} \quad \text{eq. B-6}$$

Substituting eq. B-5 and eq. B-6 in eq. B-4:

$$\boxed{k(T, \varepsilon) \propto \frac{B_{c2}(T, \varepsilon)}{T_c(\varepsilon)(1-t^2)}} \quad \text{eq. B-7}$$

Substituting Eq. B-7 in eq. B-3 one finally obtains:

$$\boxed{F_p(B) = \alpha(\varepsilon)[T_c(\varepsilon) \cdot (1-t^2)]^m \frac{[B_{c2}(T, \varepsilon)]^{n-m}}{(2\pi \Phi_0)^{1/2} \mu_0} \cdot b^p \cdot (1-b)^q} \quad \text{eq. B-8}$$

where  $\alpha(\varepsilon) \propto A(\varepsilon)$ .

For low-temperature A15 conductors, the upper critical field data can be parameterized using the empirical equation [102]:

$$\boxed{B_{c2}(T, \varepsilon) = B_{c2}(0, \varepsilon)(1-t^v)} \quad \text{eq. B-9}$$

Eq. B-8 and eq. B-9 are obtained via a parameterization of the maximum pinning force using only single variable functions. In this parameterization formula, the effects of the magnetic field, temperature and strain are decoupled from each other.

After applying this scaling law to experimental data, the authors [102] proposed eliminating  $m$  as a free parameter by setting  $m=2$  and parameterizing the data using:

$$\boxed{F_p(B) = \alpha(\varepsilon)[T_c(\varepsilon) \cdot (1-t^2)]^2 \frac{[B_{c2}(T, \varepsilon)]^{n-2}}{(2\pi \Phi_0)^{1/2} \mu_0} \cdot b^p \cdot (1-b)^q} \quad \text{eq. B-10}$$

This parameterization differs from that proposed by Summer *et al* by a factor  $T_c^2(\varepsilon)$ .

Eq. B-10 was compared to comprehensive experimental  $J_c(B, T, \varepsilon)$  data for a Modified Jelly Roll Nb<sub>3</sub>Sn sample and the results of the fits were excellent [102]. The fit values of the free parameters for this case were:

$$n \approx 2.5 \quad p = 1/2 \quad q = 2 \quad \nu = 1.374$$

Substituting these values in eq. B-10 and dividing by  $B$ , the scaling law for the critical current density becomes:

$$J_c = \alpha(\varepsilon) [T_c(\varepsilon) \cdot (1 - t^2)]^2 \frac{[B_{c2}(T, \varepsilon)]^{0.5}}{(2\pi \Phi_0)^{1/2} \mu_0} \cdot \frac{b^{0.5} \cdot (1 - b)^2}{B}$$

and finally considering  $\frac{1}{B} = (b \cdot B_{c2})^{-1}$ , one obtains:

$$J_c = \alpha(\varepsilon) [T_c(\varepsilon) \cdot (1 - t^2)]^2 \frac{[B_{c2}(T, \varepsilon)]^{-0.5}}{(2\pi \Phi_0)^{1/2} \mu_0} \cdot b^{-0.5} \cdot (1 - b)^2$$

eq. B-11



## References

- 1) L.R. Evans – ‘The Large Hadron Collider project.’ – In T. Haruyama, T. Mitsui and K. Yamafuji (eds.), Proceedings of the 16<sup>th</sup> International Cryogenic Engineering Conference/International Cryogenic Materials Conference, London: Elsevier, 1997.
- 2) V.V. Kashikhin, A.V. Zlobin – ‘Magnetic instabilities in Nb<sub>3</sub>Sn strands’ – FNAL Technical Note TD-03-032
- 3) D.A. Edwards and M.J. Syphers – ‘An Introduction to the Physics of High Energy Particle Accelerators’ – New York: John Wiley & Sons, 1993.
- 4) K. H. Mess, P. Schmuser, S. Wolff – ‘Superconducting Accelerator Magnets’ – World Scientific, London, 1996
- 5) H.T. Edwards – ‘The Tevatron energy doubler: a superconducting accelerator’ – Ann. Rev. Nucl. Part. Sci., 35: 605-660, 1985.
- 6) L. Rossi – ‘Very high field magnets’ – Proc. of CERN Accelerator School on Superconductivity and Cryogenics for Accelerators and Detectors, CERN Yellow Report -2004-008, Geneva, Switzerland, 2004
- 7) E. Gragory – ‘Conventional Wire and Cable Technology’ – AIP Conf. Proc. of The Physics of Particle Accelerator, Vol. 249 No.2, pp. 1198-1229, 1992
- 8) P. J. Lee *et. al.* – ‘Composite Superconductors, chapter 5: Fabrication Methods’ – Marcel Dekker, inc., pp.237-321, 1994
- 9) M.N. Wilson – ‘Superconducting materials for magnets’ – Proc. of CERN Accelerator School on Superconductivity in Particle Accelerators, CERN Yellow Report -1996-03, Geneva, Switzerland, 1996
- 10) R. Simon and A. Smith – ‘Superconductors: Conquering Technology’s New Frontiers’ – New York, Plenum Press, p.61, 1988
- 11) W. Meissner and R. Oschenfeld, Naturwiss. 21, pp. 787, 1933
- 12) J. Bardeen, L.N. Cooper and J.R. Schrieffer – ‘Theory of superconductivity’ - Phys. Rev., Vol. 108 No.5, pp. 1175-1204, 1957
- 13) A.A. Abrikosov – ‘On the magnetic properties of superconductors of the second group’ – Soviet Phys. JETP, Vol. 5 No. 6, pp. 1174-1182, 1957
- 14) J. K. Hulm and R.D. Blaugher – ‘Superconducting solid solution alloys of the transition elements’ - Phys. Rev., Vol. 123 No.5, pp. 1569-1580, 1961

- 15) B.T. Matthias, T.H. Geballe, S. Geller and E. Corenzwit – ‘Superconductivity of  $\text{Nb}_3\text{Sn}$ ’ – Phys. Rev., Vol. 95 No. 6, pp. 1435, 1954
- 16) B.T. Matthias, M. Marezio, E. Corenzwit, A.S. Cooper and H.E. Berz – ‘High temperature superconductors, the first ternary system’ – Science, Vol. 175, pp. 1465-1466, 1972
- 17) J.G. Berdoz and K.A. Muller – ‘Possible high  $T_c$  superconductivity in the Ba-La-Cu-O system’ – Z. Phys. B, Condensed Matter, Vol. 64, pp. 189-193, 1986
- 18) M. K. Wu *et. al.* – ‘Superconductivity at 93 K in a new mixed-phase Y-Ba-Cu-O compound system at ambient pressure’ – Phys. Rev. Lett., Vol. 58 No. 9, pp. 908-910, 1987
- 19) H. Maeda, Y. Tanaka, M. Fukutomi, and T. Asano – ‘A new high  $T_c$  oxide superconductor without a rare earth element’ – Jpn. J. Appl. Phys., Vol. 27, N. 2, pp. L209-L-210, 1988.
- 20) J. Nagamatsu, N. Nakagawa, T. Muranaka, Y. Zenitani, and J. Akimitsu – ‘Superconductivity at 39 K in magnesium diborite’ – Nature, Vol. 410, pp.63-64, 2001
- 21) A. Gurevich *et. al.* – ‘Very high upper critical fields in  $\text{MgB}_2$  produced by selective tuning of impurity scattering’ – Supercon. Sci. Technol., Vol. 17, pp. 278-286, 2004
- 22) M. N. Wilson – ‘Superconducting Magnets’ – Clarendon Press, Oxford, 1983
- 23) A. V. Gurevich, R. G. Mints, A. L. Rakhmanov – ‘The Physics of Composite Superconductors’ – begell house, inc., New York, 1997
- 24) C. P. Bean – ‘Magnetization of hard superconductors’ – Phys. Rev. Lett., vol. 8, num. 6, pp. 250, 1962
- 25) C. P. Bean – ‘Magnetization of High-Field Superconductors’ – Rev. Mod. Phys., vol. 36, pp. 31, 1964
- 26) H. London – ‘Alternating current losses in superconductors of the second kind’ – Phys. Lett., vol. 6, pp. 162, 1963
- 27) Y. B. Kim, C. F. Hempstead, A. R. Strnad – ‘Critical Persistent Currents in Hard Superconductors’ – Phys. Rev. Lett., vol. 9, num. 7, pp. 306-309, 1962
- 28) A. Devred – ‘Practical Low-Temperature Superconductors for Electromagnets’ – CERN Yellow Report -2004-006, Geneva, Switzerland, 2004

- 29) M.N. Wilson – ‘Practical Superconductors for Accelerators-Filamentary Conductors’ – Proc. of CERN Accelerator School on Superconductivity and Cryogenics for Accelerators and Detectors, CERN Yellow Report -2004-008, Geneva, Switzerland, 2004
- 30) E.U. Haebel and F. Wittgenstein – ‘Big European Bubble chamber (BEBC) magnet progress report’ – Proc. of 3<sup>rd</sup> International Conference on Magnet Technology (MT 3), Hamburg, Germany, pp.874-895, 1970
- 31) M.A. Green – ‘Residual field in superconducting dipole and quadrupole magnets’ – IEEE Trans. Nucl. Sci., Vol. NS-18 No. 3, pp.664-668, 1971
- 32) B. C. Brown, H.E. Fisk and R. Hanft – ‘Persistent current fields in Fermilab Tevatron magnets’ – IEEE Trans. on Magn. , Volume 21 No. 2, pp. 979-982, 1985
- 33) H. Bruck, R. Meinke, F. Muller and P. Schmuser – ‘Field distortions from persistent magnetization currents in HERA magnets’ – Z. Phys. C, Particles and Fields, Vol. 44, pp.385-392, 1989
- 34) L. F. Goodrich, F. R. Fickett – ‘Critical current measurements: a compendium of experimental results’ – Cryogenics, vol. 22, pp.225-241, May 1982
- 35) A. den Ouden *et al.* – ‘An Experimental 11.5 T Nb<sub>3</sub>Sn LHC Type of Dipole Magnet’ – IEEE Trans. Magn., Volume 30, Issue 4, July 1994 Page(s):2320 - 2323
- 36) E. Gregory – ‘Practical Fabrication Method for Nb<sub>3</sub>Sn’ – IEEE, Vol. 77 No. 8, 1989.
- 37) S. Foner and B. B. Schwartz – ‘Superconductor Material Science’ – Plenum Press, New York, 1981
- 38) C.A.M. van Beijnen and J. D. Elen – ‘Potential fabrication method of superconducting multifilament wires of the A-15-type’ – IEEE Trans. Magn., Volume 11, Issue 2, May 1975 Page(s):243 – 246
- 39) J.D. Elen, C.A.M. van Beijnen, C.A.M. van der Klein – ‘Multifilament V<sub>3</sub>Ga and Nb<sub>3</sub>Sn superconductors produced by the ECN-technique’ – IEEE Trans. Magn., Volume 13, Issue 1, May 1977 Page(s):470 – 473
- 40) J. H. Lindenhovius *et. al.* – ‘Progress in the Development of Nb<sub>3</sub>Sn Conductors based on “Powder in Tube” Method with Finer Filaments’ – IEEE Trans. Appl. Supercond. Volume 9, Issue 2, Part 2, June 1999 Page(s):1451 – 1454
- 41) W. K. McDonald – ‘Composite construction process and superconductor produced thereby’ – US patent No. 4262412, filed May 29, 1979, awarded April 21, 1981

- 42) M. Field *et al.* – ‘Progress with Nb<sub>3</sub>Sn Conductors at Oxford Instruments, Superconducting Technology’ – IEEE Trans. Appl. Supercond. Volume 11, Issue 1, March 2001 Page(s):3692 – 3695
- 43) J.A. Parrell *et al.* – ‘High field Nb<sub>3</sub>Sn conductor development at Oxford Superconducting Technology’ – IEEE Trans. Appl. Supercond. Volume 13, Issue 2, June 2003 Page(s):3470 – 3673
- 44) D.B. Thomas, M.N. Wilson – ‘Filamentary Superconductor for Pulsed Application’ – Proc. of 4th International Conference on Magnet Technology (MT 4), Brookhaven National Laboratory, USA , pp. 493-497, 1972
- 45) Romeo Perin – ‘Field, Forces and Mechanics of Superconducting Magnets’ – Proc. of CERN Accelerator School on Superconductivity in Particle Accelerators, CERN Yellow Report -1996-03, Geneva, Switzerland, 1996
- 46) S. A. Gourlay – ‘High Field Magnet R&D in the USA’ – IEEE Trans. Appl. Supercond. Volume 14, Issue 2, Part 2, June 2004 Page(s):333 – 338
- 47) A. Devred *et al.* – ‘Status of the Next European Dipole (NED) activity of the Collaborated Accelerator Research in Europe (CARE) project’ – IEEE Trans. Appl. Supercond. Volume 15, Issue 2, Part 2, June 2005 Page(s):1106 - 1112
- 48) M.J. Lamm – ‘Nb<sub>3</sub>Sn accelerator magnet development around the world’ – IEEE Trans. Appl. Supercond. Volume 13, Issue 2, Part 2, June 2003 Page(s):1278 – 1283
- 49) J. Straight *et al.* – ‘Toward a new LHC interaction region design for a luminosity upgrade’ – Proc. 2003 Particle Accelerator Conference
- 50) A.V. Zlobin *et al.* – ‘R&D of Nb<sub>3</sub>Sn accelerator magnets at Fermilab’ – IEEE Trans. Appl. Supercond. Volume 15, Issue 2, Part 2, June 2005 Page(s):1113 – 1118
- 51) V.V. Kashikhin, A.V. Zlobin – ‘Magnetic instabilities in Nb<sub>3</sub>Sn strands and cables’ – IEEE Trans. Appl. Supercond. Volume 15, Issue 2, Part 2, June 2005 Page(s):1621 – 1624
- 52) E. Barzi *et al.* – ‘Instabilities in transport current measurements of Nb<sub>3</sub>Sn strands’ – IEEE Trans. on Appl. Supercond., Volume 15, Issue 2, Part 3, June 2005 Page(s): 3364 – 3367
- 53) A. Ghosh *et al.* – ‘Investigation of instability in high J<sub>c</sub> Nb<sub>3</sub>Sn strands’ – IEEE Trans. on Appl. Supercond., Volume 15, Issue 2, Part 3, June 2005 Page(s): 3360 – 3363

- 54) D.R Dietderich *et al.* – ‘Correlation between strand stability and magnet performance’ – IEEE Trans. on Appl. Supercond., Volume 15, Issue 2, Part 2, June 2005 Page(s):1524 – 1528
- 55) B. Bordini *et al.* – ‘Voltage Spikes in Nb<sub>3</sub>Sn and NbTi Strands’ – IEEE Trans. Appl. Superconduct., Vol. 16, Issue 2, June 2006 Page(s): 366 - 369
- 56) G. Ambrosio, N. Andreev, S.E. Bartlett, E. Barzi, C. H. Denarie, D. Dietderich, A.K. Ghosh, A.P. Verweij, A.V.Zlobin – ‘Critical current and instability threshold measurement of Nb<sub>3</sub>Sn cables for high field accelerator magnets’ Volume 15, Issue 2, Part 2, June 2005 Page(s):1545 - 1549
- 57) E. Barzi, N. Andreev, V.V. Kashikhin, D. Turrioni, A.V. Zlobin – ‘Study of Nb<sub>3</sub>Sn cable stability at self-field using a SC transformer’ – IEEE Trans. Appl. Supercond. Volume 15, Issue 2, Part 2, June 2005 Page(s):1537 - 1540
- 58) A.V. Zlobin, V.V. Kashikhin, E. Barzi, – ‘Effect of Flux Jumps in Superconductor on Nb<sub>3</sub>Sn Accelerator Magnet Performance’ – IEEE Trans. Appl. Supercond. Volume 16, Issue 2, June 2006 Page(s):1308 – 1311
- 59) G. Ambrosio, N. Andreev, E. Barzi, B. Bordini, C. H. Denarie, S. Feher, V. Kashikhin, A.P. Verweij, A.V. Zlobin – ‘Measurement of Critical Current and Instability Threshold of Rutherford-Type Nb<sub>3</sub>Sn Cables’ – IEEE Trans. Appl. Supercond. Volume 16, Issue 2, June 2006 Page(s):1160 – 1163
- 60) G. Ambrosio *et al.* – ‘Development and test of a Nb<sub>3</sub>Sn racetrack magnet using the react and wind technology’ – AIP Conference Proceedings, May 2002, Volume 613, Issue 1, pp. 329-336
- 61) G. Ambrosio *et al.* – ‘Fabrication and test of a racetrack magnet using pre-reacted Nb<sub>3</sub>Sn cable’ – IEEE Trans. Appl. Supercond. Volume 13, Issue 2, Part 2, June 2003 Page(s):1284 – 1287
- 62) G. Ambrosio *et al.* – ‘Design Modifications, Fabrication and Test of HFDB-03 Racetrack Magnet Wound with Pre-Reacted Nb<sub>3</sub>Sn Rutherford Cable’ – AIP Conference Proceedings, June 2004, Volume 710, Issue 1, pp. 767-774
- 63) N. Andreev *et al.* – ‘Development and test of single-bore Cos-theta Nb<sub>3</sub>Sn dipole models with cold iron yoke’ – IEEE Trans. Appl. Supercond. Volume 12, Issue 1, March 2002 Page(s):332 – 336

- 64) A.V. Zlobin *et al.* – ‘Development and test of Nb<sub>3</sub>Sn Cos-Theta dipoles based on PIT strands’ – IEEE Trans. Appl. Supercond. Volume 15, Issue 2, Part 2, June 2005  
Page(s):1160 – 1163
- 65) S. Feher *et al.* – ‘Development and Test of Nb<sub>3</sub>Sn Cos-theta Magnets Based on RRP and PIT Strands’ – IEEE Trans. Appl. Supercond. Volume 16, Issue 2, June 2006  
Page(s):315 – 318
- 66) D.R. Chichili *et al.* – ‘Design, fabrication and testing of Nb<sub>3</sub>Sn shell type coils in mirror magnet configuration’ – AIP Conf.Proc.710:775-782, 2004
- 67) S. Feher *et al.*– ‘Test results of shell-type Nb<sub>3</sub>Sn dipole coils’ – IEEE Trans. Appl. Supercond. Volume 14, Issue 2, June 2004 Page(s):349 – 352
- 68) V.S. Kashikhin *et al.* – ‘Development and test of single-layer Common Coil dipole wound with reacted Nb<sub>3</sub>Sn cable’ – IEEE Trans. Appl. Supercond. Volume 14, Issue 2, June 2004 Page(s):353 – 356
- 69) S. Feher *et al.* – ‘Cable testing for Fermilab's high field magnets using small racetrack coils’ – IEEE Trans. Appl. Supercond. Volume 15, Issue 2, Part 2, June 2005  
Page(s):1550 – 1553
- 70) L. Dresner – ‘Stability of Superconductors’ – Plenum Press, New York 1995
- 71) R. Hancox – ‘Stability against flux jumping in sintered Nb<sub>3</sub>Sn’ – Phys. Lett.,vol. 16, pp. 208 (1965)
- 72) P. S. Swartz and C. P. Bean – ‘A Model for Magnetic Instabilities in Hard Superconductors: The Adiabatic Critical State’ – J. Appl. Phys., vol. 19, pp. 4991 (1968)
- 73) J. J. Duchateau and B. Turk – ‘Dynamic stability and quenching currents of superconducting multifilamentary composites under usual cooling conditions’ – J. Appl. Phys.,vol. 45, pp. 4989 (1975)
- 74) R. G. Mints and A. L. Rakhmanov – ‘Critical state stability in type-II superconductors and superconducting-normal metal composites’ – Rev. Mod. Phys – vol. 53, pp. 551 (1981)
- 75) H. R. Hart – Proc. 1968 Summer Study on Supercond. Dev. And Acc. – BNL, New York, 1969, pp. 571

- 76) J. J. Duchateau and B. Turck – ‘Theoretical and experimental study of magnetic instabilities in multifilamentary NbTi superconducting composites’ – IEEE Trans. on Magn., Volume 11, Issue 2, Mar 1975 Page(s):350 – 353
- 77) M. G. Kremlev R. G. Mints and A. L. Rakhmanov – ‘On the flux jumps in hard superconductors’ – J. Phys. D, vol. 9, No. 2, pp. 279 (1976)
- 78) M. G. Kremlev – ‘Damping of flux jumping by flux-flow resistance’ – Cryogenics, vol. 14, pp. 132 (1974)
- 79) R. Hancox – ‘Enthalpy stabilized superconducting magnets’ – IEEE Transactions on Magnetics, Volume 4, Issue 3, Sep 1968 Page(s):486 – 488
- 80) Superconducting Applications Group – ‘Experimental and theoretical studies of filamentary superconducting composites’ – J. Phys. D: Appl. Phys. 3, pp. 1517-1585, 1970
- 81) A. F. Lietske *et al.* – ‘Test results of RD3c, a Nb<sub>3</sub>Sn common-coil racetrack dipole magnet’ – IEEE Trans. Appl. Supercond. Volume 13, Issue 2, Part 2, June 2003 Page(s):1292 – 1296
- 82) T.J. Peterson *et al* – ‘A 1400-liter 1.8-K Test Facility’ – FERMILAB-CONF-97-268, Aug 1997; published in Adv.Cryog.Eng.43A:541-548, 1998
- 83) T.J. Peterson *et al* – ‘Large Superfluid helium system at Fermilab’ – FERMILAB-PUB-99-285, Jan 2000
- 84) Carcagno, R. *et al* – ‘New 30 kA power system at Fermilab and its use for measuring the effects of ripple current on the performance of superconducting high field magnets’ – IEEE Transactions on Applied Superconductivity, Volume 15, Issue 2, Part 2, June 2005 Page(s):1520 – 1523
- 85) D.F. Orris *et al.* – ‘A Quench Management System for Testing Superconducting Magnets’ – IEEE Transactions on Applied Superconductivity, Volume 13, Issue 2, Part 2, June 2003 Page(s):1700 – 1703
- 86) D.F. Orris, *et al.* – ‘Digital Quench Detection System for Superconducting Magnets’ – Proceedings of the PAC’99, New York, 1999
- 87) J. M. Nogiec *et al.* – ‘A Distributed Monitoring and Control System’ – Proceedings of the PAC’97, Vancouver, 1997

- 88) J. M. Nogiec *et al.* – ‘Architecture of a Software Quench Management System’ – Proceedings of the PAC’01, Chicago, 2001
- 89) J.M. Nogiec *et al.* – ‘Architecture of HTS Leads Software Protection System’ – Proceedings of the PAC’99, New York, 1999
- 90) D.F. Orris *et al.* – ‘Voltage spike detection in high field superconducting accelerator magnets’ – IEEE Transactions on Applied Superconductivity, Volume 15, Issue 2, June 2005 Page(s):1205 – 1208
- 91) T. Ogitsu *et al.* – ‘Quench antenna for superconducting particle accelerator magnets’ – IEEE Transactions on Magnetics, Volume 30, Issue 4, Part 2, Jul 1994 Page(s):2273 – 2276
- 92) S. Feher, B. Bordini *et al.* – ‘Sudden Flux Change Studies in High Field Superconducting Accelerator Magnets’ – IEEE Transactions on Applied Superconductivity, Volume 15, Issue 2, Part 2, June 2005 Page(s):1591 – 1594
- 93) B. Bordini, S. Feher *et al.* – ‘SR01 Test Summary Report’ – FNAL Technical Note TD-04-035
- 94) B. Bordini, S. Feher *et al.* – ‘SR02 Summary Report’ – FNAL Technical Note TD-04-060
- 95) S. Feher, B. Bordini *et al.* – ‘HFDA05 Test Summary’ – FNAL Technical Note TD-05-059
- 96) S. Feher, B. Bordini *et al.* – ‘HFDA06 Test Summary’ – FNAL Technical Note TD-05-060
- 97) L. F. Goodrich *et al.* – ‘Superconductor critical current standards for fusion application’ – NISTIR 5027, NIST
- 98) B. Bordini, S. Feher, R. Carcagno, D. Orris – ‘Spike studies using Superconducting strands: Test set up’ – FNAL Technical Note TD-05-029
- 99) P.R. Bevington, D.K. Robinson – ‘Data Reduction and Error Analysis for the Physical Sciences’ – WCB/McGraw-Hill, Boston 1992
- 100) B. Bordini S. Feher – ‘Strand Critical Current Determination by Fitting Voltage Current Measurement Values’ – FNAL Technical Note TD-04-055, 2004
- 101) A. Godeke *et al.* – ‘Scaling of the critical current in ITER type niobium-tin superconductors in relation to the applied field, temperature and uni-axial applied strain’

- IEEE Trans. on Appl. Supercond., Volume 9, Issue 2, Part 1, June 1999 Page(s): 161 – 164
- 102) S. A. Keys D. P. Hampshire – ‘A scaling law for the critical current density of weakly- and strongly-coupled superconductors, used to parameterize data from a technological Nb<sub>3</sub>Sn strand’ – Supercond. Sci. Technol., Vol 16, pag. 1097 – 1108, 2003
- 103) M. Garber *et al.* – ‘The effect of self field on the critical current determination of multifilamentary superconductors’ – IEEE Trans. on Magn., Volume 25, Issue 2, March 1989 Page(s): 1940 – 1944
- 104) B. Bordini and S. Feher – ‘Nb<sub>3</sub>Sn critical surface parameterization estimate’ – FNAL Technical Note TD-05-028
- 105) B. Bordini and S. Feher – ‘Data collection of Modified Jelly Roll and Powder In Tube superconducting strand measured at the Short Sample Test Facility’ – FNAL Technical Note TD-06-015
- 106) B. Bordini and S. Feher – ‘Spike studies using Superconducting strands: Test results of a 1 mm Modified Jelly Roll with a low residual resistivity ratio’ – FNAL Technical Note TD-06-016
- 107) B. Bordini *et al.* – ‘Voltage Spikes in Nb<sub>3</sub>Sn and NbTi Strands’ – IEEE Trans. Appl. Superconduct., Vol. 16, Issue 2, June 2006 Page(s): 366 - 369
- 108) Guritanu *et al.* – ‘Specific heat of Nb<sub>3</sub>Sn: The case for a second energy gap’ – Phys. Rev. B 70, 184526 (2004)
- 109) Bouquet *et al.* – ‘Using specific heat to scan gaps and anisotropy of MgB<sub>2</sub>’ – Physica C 408-410 (2004), pp. 60-62
- 110) M. S. Lubell – ‘Empirical scaling formulas for critical current and critical field for commercial NbTi’ – IEEE Trans. on Magn., Volume 19, Issue 3, May 1983 Page(s): 754 – 757
- 111) R. G. Mints and A. L. Rakhmanov – ‘Critical current of a superconductor’ – Sov. Tech. Phys. Lett., Vol. 2, No. 6, June 1976
- 112) E. J. Kramer – ‘Scaling laws for flux pinning in hard superconductors’ – J. Appl. Phys., Vol. 44, pp. 1360-1370, 1973
- 113) D. Dew-Hughes – ‘Flux pinning mechanisms in type II superconductors’ – Phil. Mag. Vol. 30, pp. 293-305, 1974

114) A. Godeke *et al.* – ‘Toward an accurate scaling relation for the critical current in niobium-tin conductors’ – IEEE Trans. Appl. Supercond., Volume 12, Issue 1, March 2002 Page(s): 1029 – 1032

## Acknowledgments

Working at Fermilab has strongly enriched my mind and character; for this reason I would like to thank all those people who made this experience possible, and helped me to successfully accomplish this work.

First of all, I want to thank those people who have always sustained me in discouraging times: my wife Marina, for her extraordinary love for life and for me; my family, for its endless comforting presence; my friend Cristian Boffo, for his generosity.

Thanks to Prof. Fabio Fineschi and Prof. Bruno Montagnini, my advisors at the University of Pisa, who have always supported this work and have allowed me to carry out my Ph. D. research at Fermilab.

Thanks to Sandor Feher, my supervisor at Fermilab, who not only supervised this work, but also fatherly shared with me his 'rules' of life.

Thanks to Giorgio Ambrosio and Pierre Bauer for the support they provided during the three years I spent at Fermilab.

Thanks to Joe di Marco, Mike Lamm, Darryl Orris, Joe Ozelis, Mike Tartaglia, John Tompkins, and Sasha Zlobin of the Technical Division at Fermilab for their help in correcting this work.

I would also like to thank Emanuela Barzi, Allen Rusy, Daniele Turrioni, Tom Van Raes, and Tom Wokas who helped me in strand measurements at the Engineering Lab of the Technical Division at Fermilab.